Lawrence Berkeley National Laboratory
Recent Work

Title
ENERGY & ENVIRONMENT DIVISION ANNUAL REPORT. ENVIRONMENTAL RESEARCH PROGRAM FY 1982

Permalink
https://escholarship.org/uc/item/03p9w7vh

Authors
Cairns, E.J.
Novakov, Tihomir

Publication Date
1983-07-01

Lawrence Berkeley Laboratory

UNIVERSITY OF CALIFORNIA

ENERGY & ENVIRONMENT DIVISION

FY 1982 Annual Report

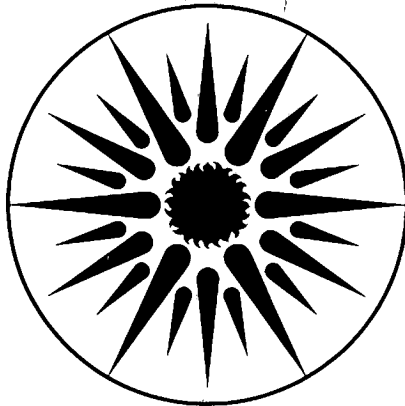ENVIRONMENTAL RESEARCH PROGRAM

July 1983

ENERGY
AND ENVIRONMENT
DIVISION

DISCLAIMER

ENERGY & ENVIRONMENT DIVISION

ANNUAL REPORT

ENVIRONMENTAL RESEARCH PROGRAM
FY 1982

Elton J. Cairns

Head, Energy & Environment Division
and
Associate Director, LBL

Tihomir Novakov

Program Leader, Environmental Research Program

Report Coordinator

Maya Osowitt

Energy and Environment Division
Lawrence Berkeley Laboratory
University of California
Berkeley, California 94720

CONTENTS

Lake Ecotoxicology Research

Trace Element Analysis

ENVIRONMENTAL RESEARCH PROGRAM STAFF

ATMOSPHERIC AEROSOL RESEARCH

William Benner	Lara Gundel	Michael McKinney	Hal Rosen
Ray Dod	Anthony Hansen	Tihomir Novakov[*][t]	Richard Schmidt
Max Dunn	Samuel Markowitz	Roland Otto	Linda Wroth

APPLIED PHYSICS AND LASER SPECTROSCOPY RESEARCH

Nabil Amer[t]	Robert Gerlach	Stanley Kohn	Douglas Wake
Neil Bergstrom	Akio Hitachi	Marjorie Olmstead	Zafer Yasa
Mark Cooper	Ralph Johnson	Andrew Skumanich	

OIL SHALE RESEARCH

Jeremy Cantor	Joe Healy	Linda Maio	Rick Sakaji
Christian Daughton[‡]	Al Hodgson	Kumar Mehta[‡]	Bob Selleck[‡]
Gloria Gill	David Jenkins[‡]	T.N. Narasimhan	Jerry Thomas[t]
Dick Goodman[‡]	Bonnie Jones	Peter Persoff	Neil Thomsen
Bill Hall	Eric Ko	Martin Pollard	Karen Yu
Gloria Harris-Winston	Greg Langlois	Joe Ratigan	

COMBUSTION RESEARCH

Diana Brehob	Gloria Gill	Donald Lucas	Frank Robben
Nancy Brown	Cecile Grant	John Metcalf	Robert Sawyer
Cam Carter	Ralph Greif	Kenneth Metchette	Robert Schefer
Minna Chan	John Hart	Mehdi Namazian[‡]	Lily Shen[‡]
Daih-Yeou Chen	Jean Hertzberg[*]	Izak Namer	Pauline Sherman[§]
Robert Cheng	David Hirvo	Terry Ng	Horton Stewart[‡]
Alexandre Chorin	Kenneth Hom	Antoni Oppenheim	Lawrence Talbot
Patrick Coico	Frank Hurlbut	Patrick Pagni	Chang Tien
Enrique Cuellar	Bruce Ingraham	Gary Parsons	Steve Vosen
John Daily	Claire Johnson[‡]	Richard Peterson	R. Brady Williamson
Derek Dunn-Rankin	Bill Kleiser[‡]	William Pitz	Joan Woodard[§]
Fred Fisher[‡]	John LaFond	Ola Rashed	

SCRUBBER CHEMISTRY RESEARCH

Shih-Ger Chang[t]	Elizabeth Griffiths	Scott Lynn	Robert Demyanovich
David Littlejohn	Thuy Hoang		

LAKE ECOTOXICOLOGY

Charles Blanchard	Gregory Lockett	John Rees	Richard Schneider
John Harte[t]	Harvey Michaels	Ellen Saegebarth	Kathy Tonnessen
Don Levy	Joan Oldfather		

TRACE ELEMENT ANALYSIS

Frank Asaro	Ralph McLaughlin	Anthony Nero	Alexandre Quintanilha
Charles Case	Helen Michel	Mary Quinby-Hunt	Linda Sindelar
Robert Giauque			

---

[*]Program Leader, [t]Group Leader, [‡]University of California, Berkeley, [§]Participating Guest

ENVIRONMENTAL RESEARCH PROGRAM

INTRODUCTION

The primary concern of the Environmental Research Program is the understanding of pollutant formation, transport, and transformation and the impacts of pollutants on the environment. These impacts include global, regional, and local effects on the atmosphere and hydrosphere, and on certain aspects of human health. This multidisciplinary research program includes fundamental and applied research in physics, chemistry, and biology, as well as research on the development of advanced methods of measurement and analysis. During FY 1982, research was concentrated on atmospheric physics and chemistry, applied physics and laser spectroscopy, combustion research, environmental effects of oil shale processing, fresh-water ecology and acid precipitation, trace element analysis for the investigation of present and historical environmental impacts, and a continuing survey of instrumentation for environmental monitoring.

Each of these areas is covered by a different research group or program. Atmospheric physics and chemistry, for example, is the province of the Atmospheric Aerosol Research Group, which has focused its studies on aerosol characterization, formation, and transformation and on the effects of aerosols on precipitation, visibility, and climate. At present, the main research interests of the group involve chemical processes, including those that occur in clouds and fogs, atmospheric aerosol nitrogen chemistry, and the role of particulate carbon in global climate modification. To accomplish these research objectives, the group has developed novel analytical methods, such as a laser transmission method for optical characterization of particles and thermal evolved gas analysis for the characterization of carbonaceous and nitrogenous aerosol species. Members of the group were also the first to apply photoelectron and Raman spectroscopy to aerosol characterization.

The Applied Physics and Laser Spectroscopy Research Group applies advanced laser spectroscopy and condensed-matter physics to energy and environmental problems. Emphasis is on the development of physical methods, as opposed to conventional chemical analysis techniques. The ultrahigh sensitivity, narrow line width, and tunability of lasers and the minimal sample preparation required make it possible for team members to apply such techniques to energy production and to test novel methods for energy conversion, such as photovoltaic solar cells and superionic electrical energy storage devices. The experience of the group accumulated during the past six years will be employed in attacking such significant problems as the increase in global carbon dioxide. Emphasis will be placed on remote sensing.

The LBL Oil Shale Program studies the environmental and waste-treatment problems that would arise from the tremendously large quantities of solid and liquid wastes a commercial-scale shale oil industry would generate. Surface and in-situ oil shale processing will probably create environmental problems through wastewater and solid waste production, emission of atmospheric pollutants during shale disposal, and leaching of organic and inorganic residuals from disposed shale. Developers propose to use process wastewaters to cool the hot processed (spent) shale, moisten it for dust control, and facilitate its compaction, a process called "codisposal." A major task of the oil shale program currently is to delineate the potential problems of such waste codisposal, in particular the estimation of the types and quantitites of uncontrollable air emissions that may result from such use of wastewaters (raw or treated). Its second major task is the development of economical approaches to the treatment of process wastewaters. Because of their turbidity and high concentrations of organic and inorganic solutes, they present tremendous difficulties to any water management scheme that entails reuse or discharge. This research effort is conducted in cooperation with the Sanitary Engineering and Environmental Health Research Laboratory of the University of California.

The Scrubber Chemistry Group has been investigating the chemical character of pollutants generated by the combustion of fossil fuels to develop new, efficient strategies for pollutant

emission control. Current research has been directed toward understanding the kinetics and mechanisms of homogeneous and heterogeneous catalysis of the interactions of sulfur dioxide and nitrogen oxides, both among themselves and with other compounds. When this fundamental chemistry is understood, it will be applied to the development of an efficient, cost-effective scrubber for simultaneous desulfurization and denitrification of flue gases. The same knowledge can also be applied to improving the performance of lime/limestone desulfurization scrubbing systems, currently the most widely used type of scrubber in the utility industry.

Approximately 90% of energy consumption in the United States is attributable to combustion processes. The Combustion Research Group has worked to achieve control over complex combustion processes by acquiring a fundamental understanding of the complex chemical and physical processes that determine combustion efficiency, emissions, and safety. Development of suitable analytical techniques for measuring intermediate and product species formed during the oxidation of fossil fuels and for characterizing turbulence has been a major effort. The characterization and understanding of turbulence and high-temperature chemistry are of high priority in this program. Areas of application which dominate these studies are engine research, pollutant abatement in utilities, control of unwanted fires, and ignition phenomena.

Ecotoxicology is the science that seeks to determine the pathways, fate, and effects of toxic substances in the natural environment. The projects of the Lake Ecotoxicology Research Group focus on one particular type of natural environment, freshwater lakes. Research has proceeded in two converging directions: the development of laboratory microcosms for lake ecotoxicology and the study of acid precipitation in the western United States. The group has demonstrated that lake microcosms can be designed and operated to provide realistic toxic-substance test systems and has applied microcosms to analyze effects of acid precipitation. Field studies on acid precipitation and its effects in the Sierra Nevada and the Colorado Rockies have been another major focus of the group. A combination of microcosm technology and field work is being designed with the goal of predicting the chronology of acidification in the western United States.

Two major projects have occupied members of the Trace Element Analysis Group. The first is the continuation of the survey of instrumentation for environmental monitoring. Commercial publication of that part of the survey dealing with radiation monitoring was completed in 1983. Wiley Interscience is handling the distribution of this 1130-page work. It is expected that material devoted to water monitoring will be updated and published in 1984. The second project is the study of the relationship between massive repetitive life extinctions on the earth and asteroid (or other extraterrestrial) impacts. Studies of this relationship have concentrated on searches for unusually high iridium abundances in geochemical samples from rock layers which are known or expected to mark life-extinction horizons. Geochemical and other tests are made to determine if the iridium-rich rocks are of extraterrestrial origin and hence related to impacts. The nature of the sedimentation of the rocks, the worldwide extent of the extinction horizons and the extent to which the extinctions (as indicated from fossil studies by collaborating paleontologists) are related to impacts are also studied.

During FY 1982, the research groups of the Environmental Research Program conducted the studies described in the short reports that follow. In many cases, more detailed reports have been or will be published.

EVIDENCE FOR PRIMARY OXIDANTS OF SO₂*

SO_2

W.H. Benner, P.M. McKinney, and T. Novakov

A number of pathways by which SO_2 is oxidized in aqueous atmospheric droplets have recently been compared.[1,2] Oxidation occurs either by reaction with gas-phase oxidants like O_3 and H_2O_2 after they have been absorbed into the droplets, or catalytically with trace metals or soot particles. The gas-phase oxidants have been assumed to originate solely from secondary photochemical reactions in the atmosphere. However, we have recently found evidence for combustion-generated (i.e., primary) oxidants of SO_2. In this article, we describe our preliminary observations.

ACCOMPLISHMENTS DURING FY 1982

A schematic sketch of the experimental system is shown in Fig. 1. An axially positioned torch in the cylindrical chimney burns gaseous fuels, such as propane, natural gas, CO, and H_2, in selectable fuel-to-air or fuel-to-O_2 ratios. The flame is electrically ignited and can burn continuously or intermittently (e.g., 5 sec on, 5 sec off). A Fluoropore filter prevents the combustion-generated soot particles from reaching the SO_2 detector (TECO, pulsed fluorescence) or the bubblers. SO_2 can be introduced into the chimney or after the filter.

When SO_2 is introduced into the air flow in the chimney at a rate that maintains its concentration at ~1 ppm, an instantaneous decrease in this concentration is observed when a fuel such as propane (50 ml/min) is burned in the torch. For a diffusion flame, the SO_2 concentration decreases approximately 80%. Combustion of natural gas or tobacco, or pyrolysis of oils, produces similar SO_2 decreases.
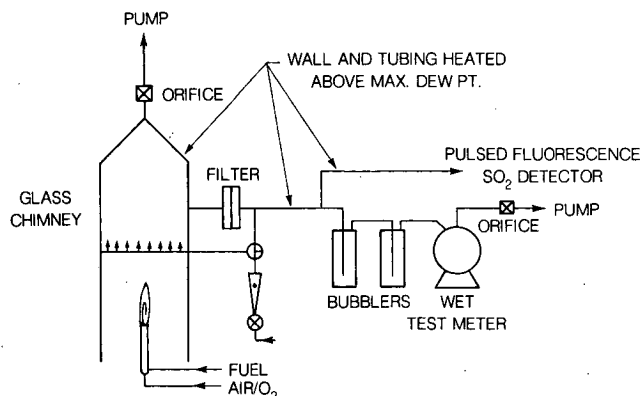
Figure 1. Apparatus for sampling primary oxidants.
(XBL 834-173)

This observation is essentially similar to one we have described in the past[3] and can be explained by one or more of the following processes: (1) SO_2 is scavenged by the condensed combustion-generated water; (2) SO_2 is converted to sulfate by oxidation or adsorption on combustion-generated particles; (3) the SO_2 detector is subject to a negative interference by some of the combustion effluents; or (4) SO_2 reacts in the gas phase with combustion products to produce gaseous sulfur species not detected by the SO_2 detector.

The first possibility was eliminated or at least minimized by maintaining the entire system at a temperature above the maximum measured dew point; furthermore, when H_2 was burned at a flow rate designed to produce the same concentration of H_2O vapor as that produced by the propane flame, only a small (5%) reduction in [SO_2] was noted. The second possibility was eliminated when filter samples collected while a flame was burning showed that particulate sulfur could not account for the observed decrease in [SO_2]. The possibility that the observed SO_2 decrease was caused by species interfering with the SO_2 detector is unlikely. Consultation with the manufacturer of the SO_2 detector (TECO) indicated that no known interfering species cause a decrease in the apparent SO_2 signal: all known interferents, such as fluorescent hydrocarbons, are positive interferents.

This leaves the fourth possibility, a gas-phase reaction between SO_2 and combustion gases, a suggestion that was supported by additional experiments. A

steady (2-min) diffusion flame produced a smaller reduction in [SO_2] than did an intermittent flame (5 sec on, 5 sec off for 4 min) that burned the same total amount of fuel. When propane was premixed with air before combustion, the reduction in [SO_2] was less; and premixing with O_2 caused essentially no reduction in [SO_2]. Results similar to those described thus far were also obtained when SO_2 was added after the filter (Fig. 1).

Further insights were gained by using water bubblers to collect SO_2, the combustion gases, and any SO_2 reaction products (Fig. 1). Ion chromatography was used to analyze the anions in the bubbler solution. When SO_2 alone was drawn through the bubbler, 100% of the expected SO_2 was recovered—95% as S(IV) and 5% as $SO_4^=$. When filtered combustion gases and SO_2 were sampled through the bubbler, 90% of the gas-phase sulfur was recovered, but only 10% of the aqueous S was detected as S(IV); the remaining 90% was $SO_4^=$. (The use of 1% H_2O_2 in the bubbler increased the recovery to 100%, and thus the presence of an undissociated S species in the water bubbler was indicated.) The combustion gases caused a large fraction of the SO_2 to be oxidized to $SO_4^=$.

In addition, filtered combustion gases without added SO_2 were sampled through the bubbler. S(IV) was then added to the bubbler solution so that the diluted final concentration was several ppm. This S(IV), upon immediate analysis, was found to have been oxidized to $SO_4^=$. The fraction of S(IV) that was oxidized in the bubbler can be related to flame conditions and fuel type. For comparable amounts of fuel burned, S(IV) oxidation increases in this order: intermittent flame > steady flame > air-premixed flame > O_2-premixed flame ≈ CO ≈ H_2. The combustion gases contain NO_2, but ion chromatographic analysis of the bubbler solution indicated that NO_2^- was not involved in S(IV) oxidation.

Filtered combustion gases that did not contain added SO_2 were sampled into a bubbler, and 10^{-5} to 10^{-4} molar levels of peroxides were detected via a nonspecific total peroxide technique.[4] A technique[5] that is specific for H_2O_2 showed that a sizable fraction of the total peroxide was H_2O_2.

These bubbler results indicate that (1) combustion is a source of one or more oxidants or of organic species that react with water to produce oxidants for SO_2 and/or S(IV); and (2) there appears to be a reaction intermediate or another sulfur-containing reaction

product that is not dissociated and thus not detectable by ion chromatographic analysis.

We have also conducted some preliminary experiments to determine if automobiles are sources of primary oxidants. Filtered exhaust from several automobiles was sampled through a water bubbler, and analysis showed that

$$S_{SO_4^=}/S_{S(IV)} + S_{SO_4^=} \approx 0.25 \quad .$$

This indicated that one-fourth of the SO_2 released from automobiles was oxidized to $SO_4^=$. (SO_3 would form $SO_4^=$ upon contact with water, but SO_3 is only a few percent of the SO_2 concentration.) When S(IV) was added to the bubbler solution, immediate analysis showed that the added S(IV) could be oxidized to $SO_4^=$. It is not yet known if the $SO_4^=$ collected in the bubbler results only from aqueous reactions or if preceding gas-phase reactions are important. However, the sulfate formation that occurs when S(IV) is added to the sampled exhaust indicates that aqueous reactions are important.

Finally, by using the results of these two steps—the amount of $SO_4^=$ found in a bubbler when filtered automobile exhaust is sampled, plus the amount of $SO_4^=$ that forms when S(IV) is added to the bubbler—we have estimated that the concentration of oxidants in the exhaust is about 1 ppm. Automobiles thus could be a significant source of primary oxidants.

PLANNED ACTIVITIES FOR FY 1983

We are attempting to speciate the various oxidants that can be released by combustion sources. Once this is done, a kinetic study of the SO_2 + oxidant reaction will be started. The ultimate goal is to develop a reaction rate expression.

REFERENCES

1. Middleton, P., Kiang, C.S., and Mohnen, V.A. (1980), "Theoretical Estimates of the Relative Importance of Various Urban Sulfate Aerosol Production Mechanisms," Atmos. Environ. 14, p. 463.

2. Chang, S.-G., Toossi, R., and Novakov, T. (1981), "The Importance of Soot Particles and Nitrous Acid in Oxidizing SO_2 in Atmospheric Aqueous Droplets," Atmos. Environ. 15, p. 1287.

3. Novakov, T., Chang, S.-G., and Harker, A.B. (1974), "Sulfates as Pollution Particulates: Catalytic Formation on Carbon (Soot) Particles," *Science 186*, p. 259.

4. Wolfe, W.C. (1962), "Spectrophotometric Determination of Hydroperoxide in Diethyl Ether," *Anal. Chem. 34*, p. 1328.

5. Zika, R.G., and Saltzman, E.S. (1982), "Interactions of Ozone and Hydrogen Peroxide in Water: Implications for Analysis of H_2O_2 in Air," *Geophys. Res. Lett. 9*, p. 231.

S(IV) OXIDATION BY AMBIENT PARTICULATE MATTER*

W.H. Benner and T. Novakov

Our investigation of SO_2 oxidation in the atmosphere has focused on heterogeneous oxidation pathways.[1-3] We have found that aqueous suspensions of activated carbons (used as model systems to simulate droplets with particulate carbon) and aqueous suspensions of traffic-generated combustion particles collected in a highway tunnel oxidize S(IV) to sulfate. These results suggest that ambient soot particles, and perhaps other ambient particles, can oxidize SO_2 to sulfate. This article describes our current efforts to determine the role of particulate matter in oxidizing SO_2 to sulfate.

ACCOMPLISHMENTS DURING FY 1982

Oxidation of S(IV) by Ambient Particulate Matter

Samples of particulate material, amounting to several grams, were collected continuously over one week from City of Hope, California (Los Angeles air basin) in an electrostatic precipitator. Portions of some samples were multiply extracted in 0.1 *M* NaOH to remove organic material, along with the large amounts of sulfate that were present. With the sulfate removed, S(IV) could be properly separated and detected conductimetrically by ion chromatography (IC).

To determine if these particles can oxidize S(IV), aqueous suspensions of the particulate matter were prepared. S(IV), as a dilute solution of $Na_2S_2O_5$, was added to suspensions of extracted particles, and the [S(IV)] was determined periodically by IC analysis of filtered aliquots. For details of these experiments, see Ref. 1.

The results of the studies with ambient particulate matter are presented in Fig. 1, which shows the rate of S(IV) disappearance in moles S(IV)/gram C·sec, plotted as a function of the [S(IV)]. The rate expression is normalized to the concentration of suspended particulate carbon because we assumed that the catalytic activity is due to particulate carbon (surface-activated graphitic component). In the caption to Fig. 1, the percentage of carbon in each sample is indicated; knowing this percentage, one can calculate the rate based on total weight of suspended particles by multiplying the rate by fraction carbon. Figure 1 also includes a plot for extracted tunnel soot from Brodzinsky et al.[1]
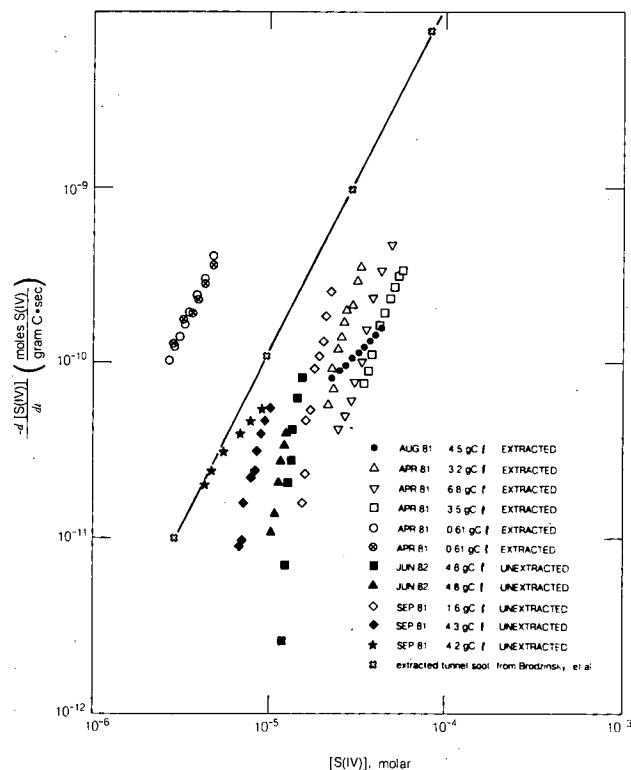

Figure 1. Oxidation of S(IV) by ambient particulate matter. Carbon comprised the following percentages by weight of the particulate matter: August 1981 (extracted), 7.2%; April 1981 (extracted), 9.8%; June 1982 (unextracted), 9.5%; and September 1981 (unextracted), 8.5%.

(XBL 834-176)

The plots in Fig. 1 show that all suspensions of ambient particulate matter oxidize S(IV) to sulfate. The rate of oxidation is variable from batch to batch; and, for some individual samples, the rate was variable from experiment to experiment. The importance of these findings depends on the interpretation one applies to the APR 81 (April 1981) sample. For this sample, relatively large concentrations (3–6 g C/l) of particulate carbon showed a reaction rate slower than that of extracted tunnel soot, while relatively low concentrations (0.61 g C/l) showed a much higher rate of S(IV) oxidation. If the plot of rate vs. [S(IV)] for the low concentration of APR 81 particulate matter was extended and found to have the same general shape as the extracted tunnel soot curve, then the oxidation of SO_2 by ambient particles would be an important reaction pathway for the formation of particulate sulfate; but if this extrapolation fell below the extracted tunnel soot curve, as suggested by the high concentration experiments, then such oxidation would be
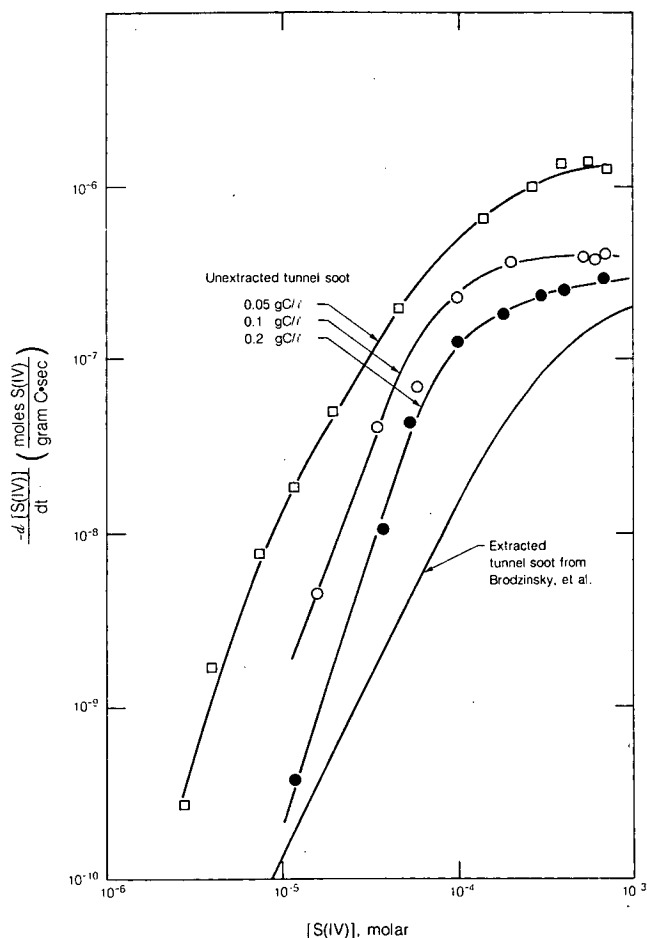
only a minor pathway. This apparent paradox cannot be solved at present, but it led us to re-examine some earlier data and to perform more experiments with tunnel soot suspensions. The results reported in the following section shed some light on the problem.

Oxidation of S(IV) by Unextracted Tunnel Soot

The earlier work done with extracted tunnel soot[1] (reproduced for comparison in Figs. 1 and 2) was conducted with suspensions having drastically different concentrations of particulate carbon (e.g., an order of magnitude between runs). The apparent paradox observed for APR 81 particles (Fig. 1) was not seen in the extracted tunnel soot runs. In fact, normalization of the reaction rate to the particulate carbon concentration in the extracted tunnel soot experiments unified all experimental data into the curve reproduced in Figs. 1 and 2.

S(IV) experiments were conducted with three concentrations of *unextracted* tunnel soot particles to see if normalization to the particulate carbon concentration would again unify the data. The results (Fig. 2) show that the reaction rate was higher than the previous reported rate curve for extracted tunnel soot and that the curve is shifted to higher rates as the particulate carbon concentration is lowered. These results indicate that normalizing the rate of S(IV) disappearance to the particulate carbon concentration may not be entirely appropriate, which supports our findings for the APR 81 particle suspensions.

At least two possibilities are suggested by these results:

1) At high concentrations of particulate carbon, a minor component of the particulate matter desorbs and poisons the catalyst, while at low concentrations of particulate carbon, the concentration of this minor component is too small to cause an effect.

2) There are consecutive and parallel reactions so that one pathway becomes important as the concentration of the catalyst decreases.

Conclusions

These studies show that suspensions of ambient particulate matter can oxidize S(IV) to sulfate. The importance of this reaction pathway in the troposphere is not yet clear. Suspensions of unextracted tunnel soot oxidize S(IV) relatively rapidly, and com-

Figure 2. Oxidation of S(IV) by highway tunnel soot particles. (XBL 834-174)

parison of these reaction rates to the values used in modeling studies[2] indicates that the soot-catalyzed rate may be important due to this unrecognized concentration effect.

PLANNED ACTIVITIES FOR FY 1983

We plan to continue this study and hope to determine the importance of SO_2 oxidation by ambient particulate matter. A problem that has to be overcome is the difficulty of obtaining gram quantities of ambient particulate matter. Electrostatic precipitation of the particles was used in the past, but less artifact-prone samples are needed.

REFERENCES

1. Brodzinsky, R., Chang, S.G., Markowitz, S.S., and Novakov, T. (1980), "Kinetics and Mechanism for the Catalytic Oxidation of Sulfur Dioxide on Carbon in Aqueous Suspension," *J. Phys. Chem. 84*, p. 3354.
2. Chang, S.G., Toossi, R., and Novakov, T. (1981), "The Importance of Soot Particles and Nitrous Acid in Oxidizing SO_2 in Atmospheric Aqueous Droplets," *Atmos. Environ. 15*, p. 1287.
3. Benner, W.H., Brodzinsky, R., and Novakov, T. (1982), "Oxidation of SO_2 in Droplets Which Contain Soot Particles," *Atmos. Environ. 16*, p. 1333.

REAL-TIME MEASUREMENT OF THE ABSORPTION COEFFICIENT OF AEROSOL PARTICLES*†

A.D.A. Hansen, H.J. Rosen, and
T. Novakov

Recent studies have shown that large concentrations of graphitic carbon particles are found in the atmosphere in both urban and remote locations.[1,2] These particles are produced in combustion and have a large optical absorption cross section, on the order of 10 m^2/g. Their presence affects radiation transfer through the atmosphere, causing visibility degradation[3] and possible changes in the regional or global radiation balance.[4] The size of these effects depends critically on both the concentration of the particles and their single-scattering albedo,[5] which is determined by the relative magnitude of the scattering and absorption coefficients. The scattering coefficient is easily measured by the nephelometer.[6,7]

However, measurements of the absorption coefficient of an ambient aerosol are difficult, mainly because of the small magnitude of this coefficient: typically, b_{abs} is ~10^{-3} to 10^{-6} m^{-1}. Measurement systems based on mirror-folded paths[8] and photoacoustic techniques[9] have been developed, but they require sophisticated apparatus that are inconvenient for routine use. In this article, we outline the development of an instrument that measures the attenuation of a light beam transmitted through particles that are being continuously collected on a suitable filter.[10] We have named this instrument the aethalometer, derived from the Greek word αιθαλουν ("to blacken with soot").

ACCOMPLISHMENTS DURING FY 1982

The principle of operation of the aethalometer is illustrated in Fig. 1. The method is based on the laser transmission technique.[11] As predicted theoretically[12] for a deposit of absorbing particles on a diffusely reflecting substrate, the laser transmission technique is sensitive only to absorption, a result confirmed by photoacoustic measurements.[13]

A cellulose fiber filter (e.g., Millipore) is partially covered with a transparent mask so that air is drawn through only a small part of the filter on which the particles are collected. The noncollecting portion of the filter covered by the mask is used as a reference. Light from a stabilized incandescent lamp passes through a 530-nm bandpass filter and is then directed by a quartz light guide to uniformly illuminate the collecting and reference areas of the cellulose filter. The light transmitted through these two portions of the filter is picked up by optical fibers set into the filter support, giving signal and reference beam intensities of I and I_0. The fibers conduct these beams to silicon detectors coupled to a logarithmic ratiometer.[14] The voltage output from this unit is proportional to the optical attenuation, which is defined as $A = -\ln(I/I_0)$ and is due to the collected absorbing particles.
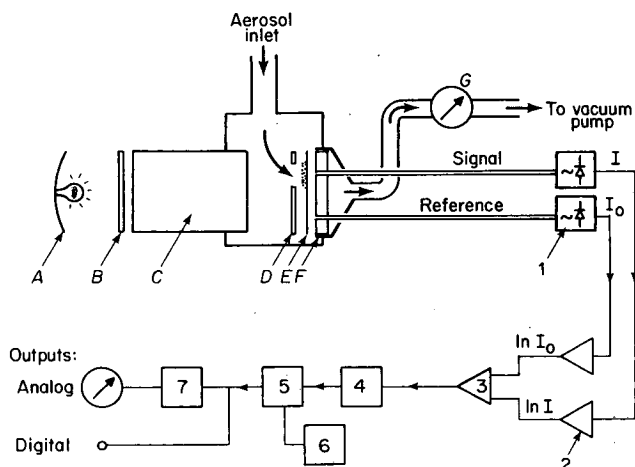
Figure 1. Block diagram of LBL aethalometer. Optical and aerosol collection components: A, light source; B, 530-nm bandpass filter; C, quartz light guide; D, transparent mask; E, filter with particles collected on portion underneath hole in mask; F, filter support with optical fibers set in; G, flowmeter. Electronic system components: 1, silicon photodetectors; 2, logarithmic amplifiers; 3, difference amplifier giving output proportional to $\ln(I/I_0)$; 4, A/D converter; 5, storage and subtraction; 6, variable time base; 7, D/A converter. (XBL 826-722)

If the instantaneous absorption coefficient of the aerosol in the air column being drawn through the filter is $b_a(x,t)$ and v is the airstream velocity at the filter face, the attenuation at time T from the deposit on the filter will be

$$A(T) \propto \int_0^T b_a(x,t) \cdot v dt \quad .$$

Differentiation of the voltage proportional to $A(T)$ will then yield a measure of $b_a(x,t)$. Since the rate of increase of $A(T)$ is rather slow (typically 0.1%/min), we use digital methods to perform the differentiation. At selected time intervals, the signal is digitized and stored. Each result is subtracted from the previous measurement, giving a difference proportional to the average of the absorption coefficient during the averaging time interval. The output is available in digital form for further processing and is also converted back to an analog signal for display on a chart recorder.

The instrument was calibrated by operating it in parallel with a sampler collecting aerosol particles on prefired quartz-fiber filters. It has been shown that the dominant absorbing species in urban aerosols is graphitic carbon,[15] which may be measured on quartz-fiber filters by a combined solvent-extraction and thermal-analysis technique.[16,17] Comparison of the two results enabled us to calibrate the aethalometer output in terms of a concentration of graphitic carbon in micrograms per cubic meter. To calculate the absorption coefficient of this material in suspended form, we used an absorption cross section of 10 m^2/g, which is compatible with reported theoretical[18] and experimental results.[19,20] We then employed the convenient relationship:

[absorption coefficient (units $10^{-6} \ m^{-1}$)]

= [concentration (units $\mu g/m^3$)]

$\times$ [cross section (units m^2/g)].

In the present configuration, the estimated minimum detectable increment in attenuation corresponds to an incremental loading of 10 ng/cm^2 of graphitic carbon in the filter. With an airstream velocity of 2.5 m/sec at the filter face, the sensitivity may be represented by a value of the product [(minimum detectable absorption coefficient) $\times$ (averaging time)] of 4×10^{-4} sec/m. Using an averaging time of 5 minutes, we can detect a graphitic carbon concentration of 0.13 $\mu g/m^3$, which corresponds to an absorption coefficient of $1.3 \times 10^{-6} \ m^{-1}$.

Figure 2 shows an example of the aethalometer output taken when sampling ambient air in Berkeley. It is clear that there is a strong diurnal variation of the absorption coefficient that may be linked to the movement of air masses as well as variations in emissions. In addition, we can see events that may be
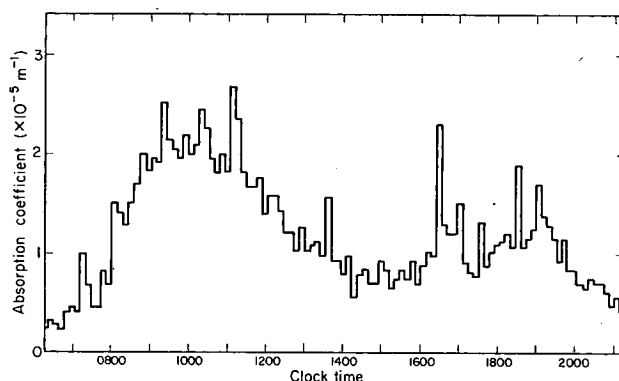

Figure 2. Absorption coefficient vs. clock time at Lawrence Berkeley Laboratory, 1 September 1981. Individual events (e.g., at 1630) may be due to the occasional passage of heavy vehicles on a nearby service road.
(XBL 826-721)

attributable to the passage of individual heavy diesel vehicles on a lightly traveled road some 90 m (100 yards) from the sampling location.

The instrument was also used in the field during an Environmental Protection Agency visibility study in Houston, Texas, in September 1980.[21] Figure 3 shows a result from that study, where the output has been smoothed with a time constant of ~20 min. The figure also shows the simultaneous nephelometer measurement of the scattering coefficient and the calculated single-scattering albedo. It is clear in this case that the magnitudes of the scattering and absorption coefficients are not in constant proportion to one another and that a real-time instrument such as the aethalometer is necessary to determine this variation.

PLANNED ACTIVITIES FOR FY 1983

Work is in progress to improve the stability of the electronic and optical systems and thereby increase the resolution. We are also working on a new filter head that may allow the airstream velocity v to be increased by a factor of 50, which will similarly increase the sensitivity. As there is considerable interest in deploying the aethalometer on an aircraft to determine the vertical profile of aerosol absorption, the instrument is also being strengthened to minimize the effects of vibration.
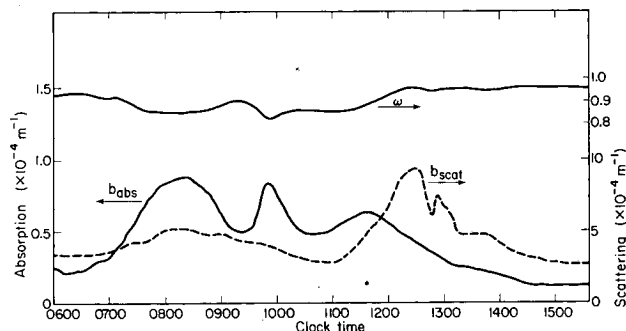
Figure 3. Smoothed data from Houston, Texas, 13 September 1980. Lower curves show absorption coefficient b_{abs} measured by the LBL aethalometer and scattering coefficient b_{scat} measured by a conventional integrating nephelometer vs. clock time. Upper curve shows the variation in single-scattering albedo $\omega = b_{scat}/(b_{scat} + b_{abs})$. Note that absorption and scattering vary most strongly at different times of the day. The absorption peaks, which occur earlier, may correspond to local and regional vehicular emission patterns, while the scattering peak occurs later. Variations in the albedo are significant, although somewhat reduced by the unusually large magnitude of the scattering coefficient. (XBL 826-720)

REFERENCES

1. Novakov, T. (1982) "Soot in the Atmosphere," in *Particulate Carbon: Atmospheric Life Cycle*, G.T. Wolff and R.L. Klimisch, Eds., Plenum, New York, p. 19.

2. Rosen, H., et al. (1982), "Graphitic Carbon in Urban Environments and the Arctic," in *Particulate Carbon: Atmospheric Life Cycle*, G.T. Wolff and R.L. Klimisch, Eds., Plenum, New York, p. 273.

3. Wolff, G.T., Groblicki, P.J., Cadle, S.H., and Countess, R.J. (1982), "Particulate Carbon at Various Locations in the United States," in *Particulate Carbon: Atmospheric Life*, G.T. Wolff and R.L. Klimisch, Eds., Plenum, New York, p. 297.

4. Paltridge, G.W., and Platt, C.M.R. (1976), in *Radiative Processes in Meteorology and Climatology*, Elsevier, Oxford.

5. Chylek, P., and Coakley, J.A. (1974), "Aerosols and Climate," *Science 183*, p. 75.

6. Buettel, R.G., and Brewer, A.W. (1949), "Instruments for the Measurement of Visual Range," *J. Sci. Instrum. 26*, p. 357.

7. Charlson, R.J., Ahlquist, N.C., Selvidge, H., and MacCready, P.B. (1969), "Monitoring of Atmospheric Aerosol Parameters with the Integrating Nephelometer," *J. Air Poll. Cont. Assoc. 19*, p. 943.

8. Rosen, H., Hansen, A.D.A., and Novakov, T. (1980), "An Instrument for the Quasi-Real-Time Measurement of the Optical Absorption Coefficient of Ambient Aerosols," Lawrence Berkeley Laboratory Report LBID-256.

9. Gerber, H.E. (1979), "Portable Cell for Simultaneously Measuring the Coefficients of Light Scattering and Extinction for Ambient Aerosols," *Appl. Opt. 18*, p. 1009.

10. Terhune, R.W., and Anderson, J.E. (1977), "Spectrophone Measurements of the Absorption of Visible Light by Aerosols in the Atmosphere," *Opt. Lett. 1*, p. 70.

11. Rosen, H., and Novakov, T. (1982), "Lawrence Berkeley Laboratory Laser Transmission Method," in *Light Absorption by Aerosol Particles*, H. Gerber, Ed., Spectrum, Hampton, Virginia, p. 321.

12. Rosen, H., and Novakov, T. (1978), "Optical Attenuation: A Measurement of the Absorbing Properties of Aerosol Particles," in *Atmospheric*

Aerosol Research Annual Report, 1977–78, Lawrence Berkeley Laboratory Report LBL-8696, p. 54.

13. Yasa, Z., Amer, N.A., Rosen, H., Hansen, A.D.A., and Novakov, T. (1979), "A Photoacoustic Investigation of Urban Aerosol Particles," Appl. Opt. 18, p. 2528.

14. Optical multimeter, Model 22XL, Photodyne, Inc., Westlake Village, California.

15. Rosen, H., Hansen, A.D.A., Gundel, L., and Novakov, T. (1978), "Identification of the Optically Absorbing Component in Urban Aerosols," Appl. Opt. 17, p. 3859.

16. Novakov, T. (1981), "Microchemical Characterization of Aerosols," in Nature, Aim, and Methods of Microchemistry, H. Malissa, M. Grasserbauer, and R. Belcher, Eds., Springer-Verlag, Vienna, p. 141.

17. Gundel, L., Dod, R., and Novakov, T. (1981), "Determination of Black Carbon by Thermal Analysis," in Energy and Environment Division Annual Report 1980, Lawrence Berkeley Laboratory Report LBL-11990, p. 5-26.

18. Medalia, A.I., and Richards, L.W. (1972), "Tinting Strength of Carbon Black," J. Colloid Interface Sci. 40, p. 223.

19. Truex, T.J., and Anderson, J.E. (1979), "Mass Monitoring of Carbonaceous Aerosols with a Spectrophone," Atmos. Environ. 13, p. 507.

20. Szkarlat, A.C., and Japar, S.M. (1981), "Light Absorption by Airborne Aerosols: Comparison of Integrating Plate and Spectrophone Techniques," Appl. Opt. 20, p. 1151.

21. Dzubay, T.G., et al. (1982), "Visibility and Aerosol Composition in Houston, Texas," Environ. Sci. Technol. 16, p. 514.

THE RELATIONSHIP BETWEEN OPTICAL ATTENUATION AND BLACK CARBON CONCENTRATION FOR CARBONACEOUS PARTICLES*

L.A. Gundel, R.L. Dod,
H.J. Rosen, and T. Novakov

Aerosol particulate material from ambient air and combustion sources usually appears black when collected on filters because of the presence of light-absorbing black carbon.[1] In the atmosphere, this light absorption can degrade visibility[2] and perturb the tropospheric energy balance.[3,4]

Light absorption provides the basis for a fast and nondestructive method for determining concentrations of black carbon on filter samples—the LBL laser transmission technique.[1] This measures the attenuation (ATN) of visible light as it passes through the filter. ATN is defined as $100 \ln I_0/I$, where I_0 and I are the intensities of light transmitted through blank and loaded filters, respectively. When the relationship between ATN and black carbon concentration ([BC]) is known, a good estimate of [BC] can be derived from the simple ATN measurements. For example, if ATN has a linear dependence on [BC], then $[BC] = ATN/\sigma$, where σ is the specific attenuation for black carbon. This application relies on the assumption of similar optical properties for both source and ambient particles.

In this study, we measured [BC] and ATN simultaneously for a large group of source and ambient filter samples. The results were used to calibrate the LBL laser transmission technique and to provide a value for the specific attenuation.

ACCOMPLISHMENTS DURING FY 1982

Samples of ambient aerosol particulate material were collected on prefired quartz-fiber filters in Berkeley and Anaheim, California; Denver, Colorado; Warren, Michigan; and Vienna, Austria. Combustion-source samples were from a natural-gas-fired boiler, a propane burner, and a diesel bus. Samples representing an average motor vehicle population were collected in a highway tunnel and in a parking garage. Before analysis, the samples were sequentially extracted by benzene and a methanol-chloroform mixture (1:2, v:v).[5,6]

Combustion thermal analysis (EGA[†]) with continuous light-absorption[7] monitoring was used to identify and quantitate black carbon (carbon combusted as

[†]Evolved gas analysis—see the article "Qualitative and Quantitative Aspects of Evolved Gas Analysis" for a discussion of this technique.

the light transmission increases), as shown in the shaded areas of Fig. 1. Solvent extraction of the samples does not remove the black carbon (as shown by lack of change in ATN) but does remove nonabsorbing organic materials that can interfere with quantitative determination of the black carbon component.

This method of determining of black carbon was validated by an extensive 11-laboratory round-robin intercomparison.[8] Attenuation measured during thermal analysis, ATN (TA), was validated by comparison to ATN(LBL), measured for the same filters using the LBL laser transmission technique.[1] For 61 extracted filters,

$$ATN(TA) = -2.8 \pm 3.9 + (0.97 \pm 0.02)$$

$$\times ATN(LBL)$$

This is excellent agreement. Estimates of measurement variability and quantitation limits are given below. The limits of detection (LOD) and limits of quantitation (LOQ) are defined as[9] $3s$ and $10s$, where s is the standard deviation for measurements of blanks.

Black carbon:
$$LOD = 0.6 \ \mu g \ cm^{-2} \qquad LOQ = 2.0 \ \mu g \ cm^{-2}$$

ATN (both methods):
$$LOD = 6 \qquad LOQ = 20$$

Ambient black carbon concentrations are given in Table 1. In Berkeley, [BC] ranged from 0.8 to 4.6 μg m^{-3}, with a mean black carbon fraction of 0.20 $\pm$ 0.04 for eleven 24-hour filters. These direct measurements of [BC] are consistent with earlier estimates that used ATN(LBL) for the same locations.[10]
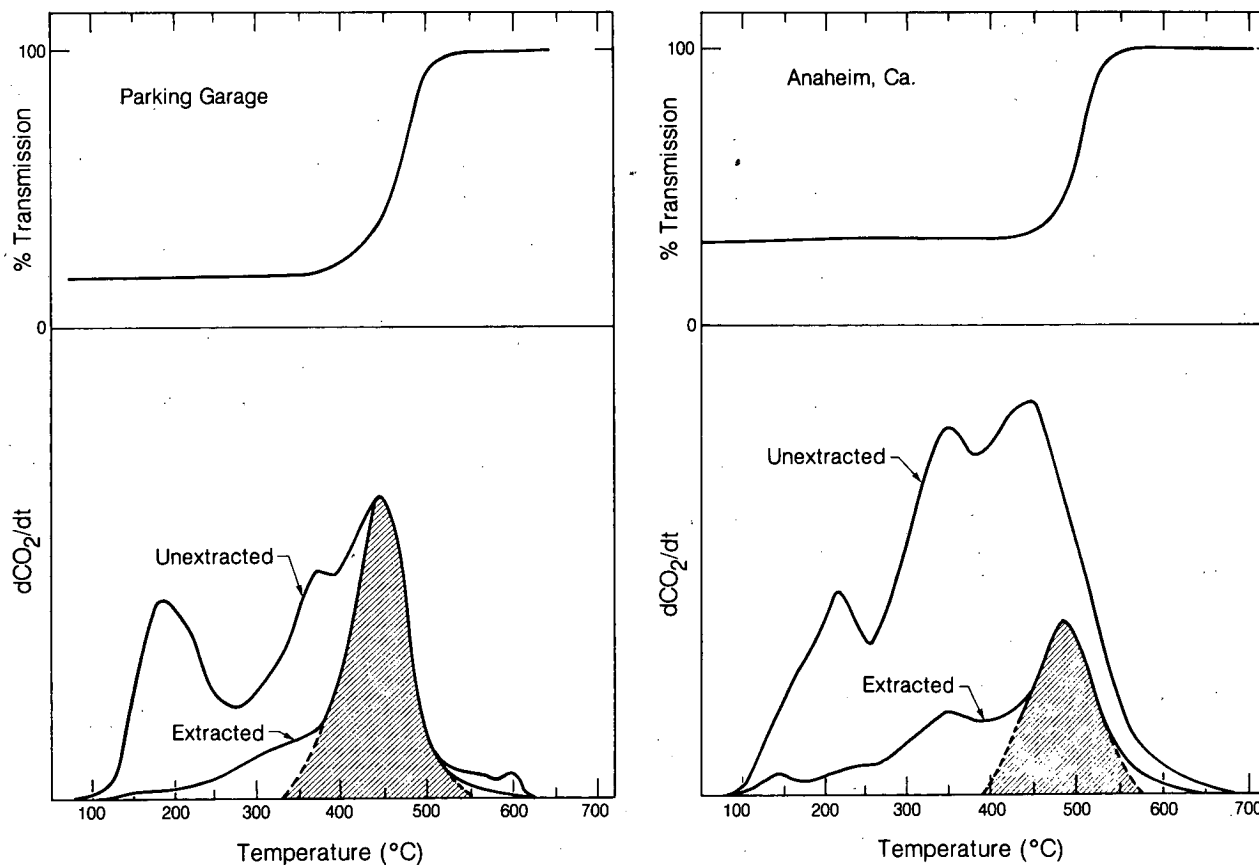

Figure 1. Thermograms of particulate carbon collected in a Berkeley parking garage and in Anaheim, California. Black carbon is represented by the shaded areas. The upper traces show light transmission through the filter samples. (XBL 835-918A)

Table 1. Ambient particulate carbon concentrations.[a]

Site	Date	Range [BC] $\mu g\ m^{-3}$	Range [C_{tot}] $\mu g\ m^{-3}$	Mean [BC]/[C_{tot}]	No. of Samples
Berkeley, CA (LBL)	Sept 79–Oct 81	0.8–4.6	4.4–22.8	0.20±0.04	11
Berkeley, CA (freeway)	Sept–Nov 79	3.1–10.5	10.5–34.0	0.33±0.7	5
Anaheim, CA	Sept–Nov 79	3.9–5.7	20.3–5.2	0.22±0.06	3
Riverside, CA	June 81	1.0–4.7	6.5–24.7	0.17±0.02	4
Denver, CO	Nov 78–May 79	1.3–2.9	7.0–16.6	0.19±0.01	5
Warren, MI[b]	Winter 80–81	2.8–14.5	11.1–42.0	0.30±0.05	3
Vienna, Austria	Sept–Oct 81	6.8–10.6	18.2–35.9	0.32±0.04	6

[a]Black carbon concentrations have been adjusted for losses during extraction. Average BC loss is 7%, as determined from the ratio of ATN values before and after extraction.

[b]These samples were analyzed as part of the General Motors-sponsored intercomparison study of methods for the determination of black carbon.[8]
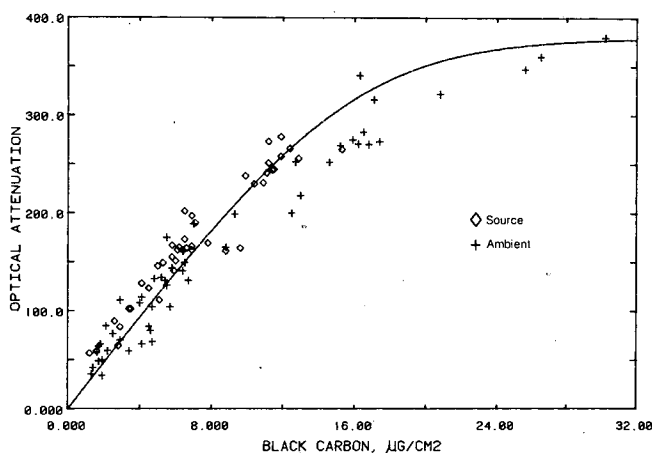
Figure 2. The relationship between optical attenuation and black carbon concentration for source and ambient particles collected on quartz-fiber filters. The line represents Eq. (1) in the text, where $\alpha = 0.02$ and $\sigma = 24.4 \pm 1.5$ cm^2 μg^{-1}. (XBL 834-178)

The relationship between ATN and [BC] is shown in Fig. 2. For source particles where ATN is below 200 and [BC] is below 8 μg cm^{-2}:

$$ATN = (10.6 \pm 16.6) + (24.1 \pm 2.8)[BC]$$

with the correlation coefficient $r = 0.859$. For ambient particles:

$$ATN = (-0.8 \pm 9.8) + (24.1 \pm 2.3)[BC]$$

with $r = 0.893$. There is no significant difference between source and ambient particles in this relationship.

For all data with ATN < 200 and [BC] < 8 μg cm^{-2}:

$$ATN = (-1.6 \pm 8.7) + (25.4 \pm 1.7)[BC]$$

with $r = 0.883$. Since the intercept is not significantly different from zero, the slope of the line is the specific attenuation. Here $\sigma = 25.4 \pm 1.7$.

All data, regardless of sample loading, can be fit to the equation

$$ATN = -100 \ln [(1 - \alpha)\ e^{-\sigma[BC]} - \alpha] \qquad (1)$$

which reflects the observation that a small fraction, α (~ 0.02), of the incident light is conducted along the quartz fibers of the filter without interaction with the particle deposit. Using this equation, we find that specific attenuation is 24.4 ± 1.5 cm^2 μg^{-1} for all data.

PLANNED ACTIVITIES FOR FY 1983

We plan to investigate the influence of particle size and composition on the specific attenuation and to increase our data set with samples collected from other sources and ambient locations.

REFERENCES

1. Rosen, H., Hansen, A.D.A., Gundel, L., and Novakov, T. (1978), "Identification of the Optically Absorbing Component in Urban Aerosols," *Appl. Opt. 17*, p. 3859.
2. Weiss, R.E., et al. (1979), "Studies of the Optical, Physical, and Chemical Properties of Light Absorbing Aerosols," in *Proceedings, Conference on Carbonaceous Particles in the Atmosphere*, Lawrence Berkeley Laboratory Report LBL-9037, p. 257.

3. Porch, W.M., and MacCracken, M.C. (1982), "Parametric Study of the Effects of Arctic Soot on Solar Radiation," *Atmos. Environ. 16*, p. 1365.

4. Cess, R.D. (1982), "Arctic Aerosols: Model Estimates of Interactive Influences upon the Surface-Troposphere Radiation Budget," *Atmos. Environ.* (submitted).

5. Appel, B.R., et al. (1979), "Analysis of Carbonaceous Material in Southern California Atmospheric Aerosols," *Environ. Sci. Technol. 13*, p. 98.

6. Gundel, L.A., and Novakov, T. (1982), "Application of Selective Solvent Extraction to Carbonaceous Aerosols," in *Energy and Environment Annual Report, FY 1981*, Lawrence Berkeley Laboratory Report LBL-13500, p. 4-16.

7. Dod, R.L., Rosen, H., and Novakov, T. (1979), "Optico-Thermal Analysis of the Carbonaceous Fraction of Aerosol Particles," *Atmospheric Aerosol Research Annual Report, 1977-78*, Lawrence Berkeley Laboratory Report LBL-8696, p. 2.

8. Groblicki, P.J., Cadle, S.H., Ang, C.C., and Mullawa, P.A. (1982), *Interlaboratory Comparison of Methods for the Determination of Organic and Elemental Carbon in Atmospheric Particulate Matter*, Report GMR 4054, General Motors Research Laboratory, Warren, Michigan.

9. ACS Committee on Environmental Improvement (1980), "Guidelines for Data Acquisition and Data Quality Evaluation in Environmental Chemistry," *Anal. Chem. 52*, p. 2242.

10. Hansen, A.D.A., et al. (1980), "The Use of an Optical Attenuation Technique to Estimate the Carbonaceous Component of Urban Aerosols," *Atmospheric Aerosol Research, FY 1979*, Lawrence Berkeley Laboratory Report LBL-10735, p. 16.

GRAPHITIC-CARBON-TO-LEAD RATIO AS A TRACER FOR SOURCES OF THE ARCTIC AEROSOL*†

H.J. Rosen, A.D.A. Hansen, and T. Novakov

Recent studies at Barrow, Alaska, indicate the presence of large aerosol concentrations that appear to be characteristic of the Arctic region as a whole.[1-4] If the obvious natural aerosol components (e.g., sea salt and soil) are excluded, the predominant components of the Arctic aerosol are carbon- and sulfur-containing particles. These particles occur at concentrations comparable to those found in urban areas in the continental United States.[1,2]

There is considerable indirect evidence that a major part of the Arctic aerosol is produced from combustion processes. However, the strongest and most direct substantiation of this inference has been provided by the identification of large concentrations of graphitic carbon in the Arctic atmosphere.[1] These graphitic species, which have a structure similar to carbon black, can be produced only by combustion processes. The concentration of these particles at Barrow during the winter and spring approaches those found in urban areas (the concentrations are only a factor of 4 less than the average values found in Berkeley, California, and Gaithersburg, Maryland, and a factor of 10 less than those found in New York City).

Associated with these graphitic species are large optical absorption coefficients (~ 10 m^2 g^{-1}), which could produce a significant perturbation of the heat balance over the Arctic. Preliminary model calculations indicate that present springtime concentrations of graphitic particles could increase the atmospheric heating rate by an amount comparable to that expected from a doubling of the CO_2 concentration.[5,6]

The sources of the Arctic aerosol are unknown at present. Part of the aerosol may come from local Alaskan sources, but there is considerable evidence that a major fraction is due to long-range transport from other industrialized regions,[7,8] with Eurasia suggested as a major source area.[2] Use of the ratio of graphitic carbon to lead as a tracer for the sources of the Arctic aerosol is described here.

ACCOMPLISHMENTS DURING FY 1982

An aerosol sampler has been operating at Barrow since October 1979, collecting parallel filter samples on 47-mm quartz-fiber and Millipore substrates at a flow rate of approximately 1.5 ft^3 min^{-1}. Measurements of graphitic carbon and particulate lead concentrations over eight months—from October 1979 through May 1980—are reported here. The graphitic carbon concentrations were obtained using the LBL laser transmission technique[9] with an empirical calibration curve developed for urban particulates in the United States.[10] Independent measurements of the graphitic carbon concentration by an opticothermal analysis technique are under way. Lead concentrations were determined through x-ray fluorescence analyses, performed by Robert Giauque.

Natural concentrations of particulate lead are very low, and it is usually assumed that in polluted environments the major source is from the burning of leaded gasoline by automobiles. Typical ground-level lead concentrations in urban atmospheres in the United States are ~2 μg m^{-3}. In the Arctic the concentrations are much smaller, as shown in Fig. 1(a), but are probably also combustion-generated since the enrichment factors relative to the earth's average

crustal abundance are large. For comparison, the graphitic carbon concentration as a function of the time of year is shown in Fig. 1(b).

Although both aerosol components show their largest concentrations during the winter and spring, their seasonal variations are quite distinct. Whereas the graphitic carbon concentrations are roughly constant from December through April, the lead concentrations show a rather sharp peak in November and December and relatively low values for the rest of the year. As a result of these differences in behavior, the relative concentrations of graphitic carbon and lead change substantially throughout the year, as shown in Fig. 2. These variations could represent the contributions of different source regions during different times of the year or a seasonal variation in the fuel mix of source regions. It should be emphasized that the results reported here are only for 1 year, and interannual variation due to variability in the air trajectories that arrive at Barrow from year to year could be considerable.

Interpretations of these results are based on several crucial assumptions: (1) the graphitic-carbon-to-lead ratio does not change significantly during transport because of different deposition rates for
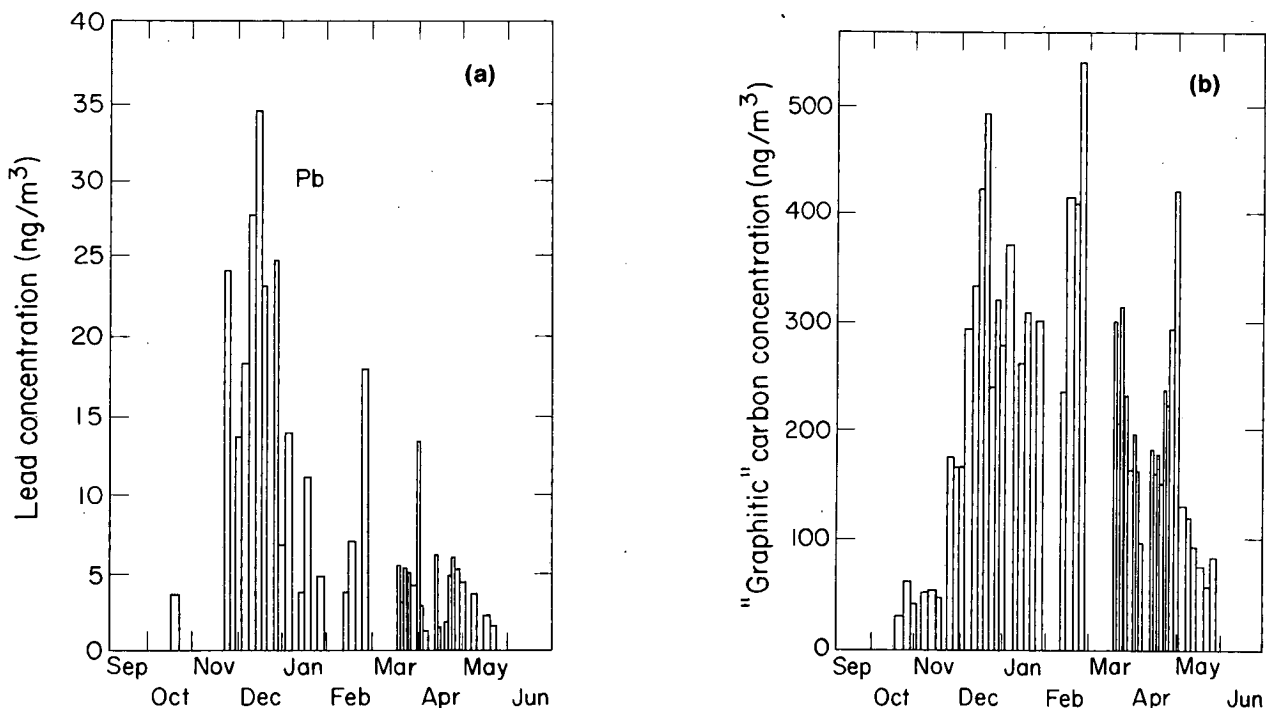

Figure 1. (a) Particulate lead concentration and (b) graphitic carbon concentration, each as a function of the time of year for 1979–1980.   [(a) XBL 827-7185; (b) XBL 827-7186]

particulate lead and graphitic carbon, and (2) source regions may be characterized by ground-level graphitic-carbon-to-lead ratios (i.e., these ratios do not change appreciably with altitude). These assumptions need further investigation.

Finally, we compare the graphitic-carbon-to-lead ratios in the Arctic with typical values in the western and eastern United States. As shown in Fig. 2, the values in the Arctic are considerably larger than those found in the United States, especially during March and April, when the average value is 10 times that found in the eastern U. S. and 30 times that found in the western U. S. If the graphitic-carbon-to-lead ratio in the western U. S. is used to represent a source region dominated by automotive emissions, then these results could imply that source regions of the Barrow aerosol during March and April do not have a large automotive component relative to other soot-generating combustion sources. Such a region could have a large diesel, wood-burning, or stationary-source component relative to automobiles. Furthermore, these results could imply that the United States or other regions with similar fuel mixtures do not contribute significantly to the Arctic haze during these periods of high graphitic-carbon-to-lead ratios.

PLANNED ACTIVITIES FOR FY 1983

The use of the graphitic-carbon-to-lead ratio represents a first attempt to identify the sources of
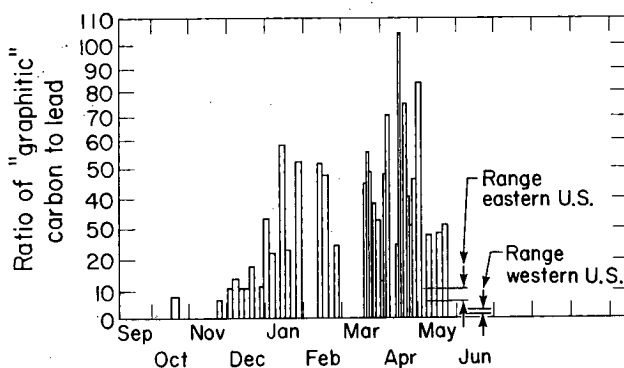
Figure 2. Ratio of concentrations of graphitic carbon to particulate lead as a function of the time of year for 1979–1980. Also shown is the range of values for the western United States (Anaheim, Berkeley, and Fremont, California) and the eastern United States (New York City; Argonne, Illinois; and Gaithersburg, Maryland). The range of values is defined as those values within one standard deviation of the average.   (XBL 827-7100)

the Arctic haze. Future work will extend the technique to other parts of the Arctic and develop new methods of analysis to identify combustion source contributions.

ACKNOWLEDGMENT

REFERENCES

1. Rosen, H., Novakov, T., and Bodhaine, B.A. (1981), "Soot in the Arctic," Atmos. Environ. 15, p. 1371.

2. Rahn, K.A., and McCaffrey, R.J. (1980), "On the Origin and Transport of Winter Arctic Aerosol," Ann. N.Y. Acad. Sci. 338, p. 486.

3. Shaw, G.E. (1981), "Eddy Diffusion Transport of Arctic Pollution from the Mid Latitudes: A Preliminary Model," Atmos. Environ. 15, p. 1483.

4. Bodhaine, B.A., Harris, J.M., and Herbert, G.A. (1981), "Aerosol Light Scattering and Condensation Nuclei Measurements at Barrow, Alaska," Atmos. Environ. 15, p. 1375.

5. Porch, W.M., and MacCracken, M.C. (1982), "Parametric Study of the Effects of Arctic Soot on Solar Radiation," Atmos. Environ. 16, p. 1365.

6. Cess, R.D. (1982), "Arctic Aerosols: Model Estimates of Interactive Influences upon the Surface-Troposphere Radiation Budget," Atmos. Environ. (submitted).

7. Peterson, J.T., Hanson, K.J., Bodhaine, B.A., and Oltmans, S.J. (1980), "Dependence of CO_2, Aerosol, and Ozone Concentrations on Wind Direction at Barrow, Alaska, During Winter," Geophys. Res. Lett. 7, p. 349.

8. Barrie, L.W., Hoff, R.M., and Daggupaty, S.M. (1981), "The Influence of Mid-Latitudinal Pollution Sources on Haze in the Canadian Arctic," Atmos. Environ. 15, p. 1407.

9. Rosen, H., Hansen, A.D.A., Gundel, L., and Novakov, T. (1978), "Identification of the Optically Absorbing Component in Urban Aerosols," Appl. Opt. 17, p. 3859.

10. Gundel, L., Dod, R., and Novakov, T. (1981), "Determination of Black Carbon by Thermal Analysis," Environmental Pollutant Studies, Lawrence Berkeley Laboratory Report LBL-11986, p. 5.

THE OXYGEN CONTENT OF AMBIENT PARTICULATE MATTER*

W.H. Benner, C. Chuang,
A.D.A. Hansen, and T. Novakov

The light-scattering, haze-forming particles of the troposphere can come from primary sources like combustion engines and wind-blown dust or from secondary sources, i.e., chemical reactions that transform gases into particles. Oxygen in the particles can be grouped into several fractions: organic oxygen, carbonates, nitrates, sulfates, silicates, and metal oxides. In general, primary particulate matter contains carbonates, silicates, and metal oxides (from resuspended soil and fly ash) and is likely to contain organic oxygen from incompletely burned fuels. Secondary particulate matter contains sulfates, nitrates, and presumably organic oxygen from photochemically initiated reactions. We are attempting to determine the relative importance of the primary and secondary origins of oxygenated-organic particulate matter; this article describes our initial efforts.

ACCOMPLISHMENTS DURING FY 1982

To determine oxygen in particulate matter, several analytical techniques were combined.[1-5] Figure 1 shows the analytical system. Gas samples were injected into the pyrolysis tube via a septum. A multiport valve changed the direction of flow through the pyrolysis tube. Solid samples and filter samples were loaded into a small platinum boat (formed from 5-mil Pt foil) and placed into the cool zone of the pyrolysis tube during backflushing with N_2 so that room air did not contact the hot carbon. After a sample was loaded, the pyrolysis tube was resealed (at the O-ring seal); any air entrained in the tube was backflushed from the system (~4 min), and the multiport valve was switched. Finally, after the CO detector stabilized, the sample boat was slid into the hot zone with a magnetically moved plunger.
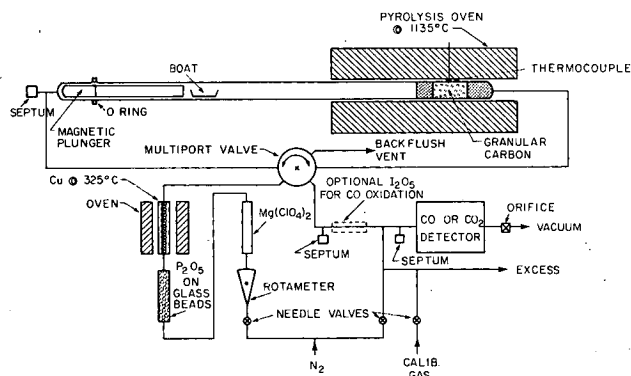
Figure 1. Schematic diagram of oxygen analysis system.
(XBL 833-127)

This method thermally decomposes the sample, and the oxygen-containing decomposition products react with the hot carbon (1130°C) to produce CO. Oxygen can be determined in all materials that decompose at T < 1130°C. In ambient particulate matter, oxygenated organics, nitrates, sulfates, H_2O, adsorbed oxygen-containing gases, and carbonates will decompose; but silica and alumina (Al_2O_3) will not decompose at this temperature. However, silica contains OH functional groups, and these presumably decompose. All samples were dessicated over P_2O_5 to remove H_2O.

A variety of standard compounds, injections of CO_2, and samples of filtered ambient particulate matter were analyzed. Direct injections of CO_2 showed good recovery (100.0%) with a standard deviation (σ) of 0.4%. A number of oxygenated compounds, including ammonium nitrate, ammonium sulfate, 2,4-dihydroxy-benzaldehyde, benzoic acid, m-hydroxybenzoic acid, glutaric acid, myristic acid, phthalic acid, and potassium phthlate (KHP), were analyzed. The recovery for all standards was 101.8 ± 4.5% (n = 65). The analytical limit of detection (LOD) and limit of quantitation (LOQ) for recovery of standards from pieces of quartz-fiber filters are:

$$LOD = blank + 3\sigma_{blank} = 6.9 + 1.2 = 8.1 \ \mu g \ O$$

$$LOQ = blank + 10\sigma_{blank} = 6.9 + 4.0 = 10.9 \ \mu g \ O$$

Figures 2(a) and 2(b) show the linearity and the scatter that can be expected for the analysis of standards prepared by the evaporation of solutions onto 1-cm^2 quartz-fiber discs. Each datum point is the determination of oxygen on a 1-cm^2 disc.

Replicate analyses of two ambient air filter samples are presented in Table 1 to show the applicability of
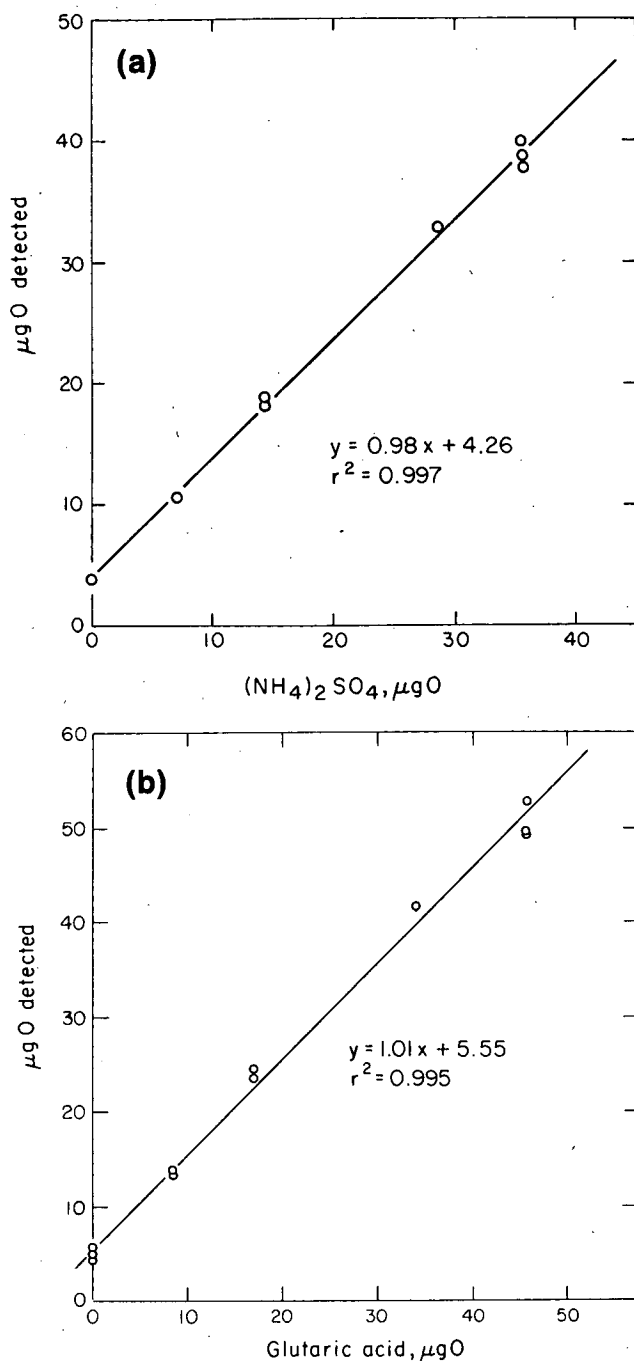
Figure 2. (a) Recovery of oxygen from $(NH_4)_2SO_4$ standards. (b) Recovery of oxygen from glutaric acid standards.   [(a) XBL 833-129; (b) XBL 833-128]

this technique. A high-volume filter sampler ($\sim$1100 liters per minute of ambient air was drawn through 400-cm^2 prefired quartz-fiber filters for several hours) was used to collect samples in Berkeley, California. Multiple 1-cm^2 discs of these filters were dessicated for 12 hours over P_2O_5 and then analyzed for oxygen. Analysis for particulate carbon used a separate tech-

nique.[6] The results indicate that the volumetric flow rates frequently used to sample ambient particulate matter will collect enough oxygenated particulate matter so that 1 cm^2 of filter will give a signal above the LOQ in the nondispersive infrared analysis scheme. Comparison of the carbon loadings in Table 1 of this article and those in Table 2 of Novakov[7] indicates that these loadings are typical for many United States sampling sites.

Table 1. Analysis of filtered ambient particulate matter.

Sample[a]	μg O/cm^2 [b]	μg O/m^3	μg C/cm^2	μg C/m^3
Daytime				
1000–1715 hrs,	20.5			
11 Mar 81	20.3			
		16.3	13.7	11.0
	20.2			
	20.2			
Nighttime				
1800–0600 hrs,	21.0			
11–12 Mar 81		10.1	12.9	6.3
	20.5			

[a]Both samples were collected in Berkeley, California.
[b]Blank corrected replicates.

PLANNED ACTIVITIES FOR FY 1983

The technique described here is being applied to the determination of oxygen in filter samples of ambient particulate matter. Samples from a variety of rural and urban locations have been collected and will be analyzed to determine the parameters (e.g., origin, exposure to photochemical reactive species, exposure to fog, and age) that influence the oxygen content of particles.

REFERENCES

1. Schütze, M. (1939), (*Z. Anal. Chem. 118*, p. 241, 1939), reprinted in *Standard Methods of Chemical Analysis*, Vol. 1 (6th ed.), N.H. Furman, Ed., Van Nostrand, Princeton, p. 780 (1962).

2. Unterzeucher, J. (1940), (*Ber. 73B*, p. 391, 1940), reprinted in *Standard Methods of Chemical Analysis*, Vol. 1 (6th ed.), N.H. Furman, Ed., Van Nostrand, Princeton, p. 780 (1962).

3. Oita, I.J. and Conway, H.S. (1954), "Direct Determination of Oxygen in Organic Substances—Modified Schütze Method," *Anal. Chem. 26*, p. 600.
4. Campanile, V.A., et al. (1951), "Improved Method for Determination of Oxygen," *Anal. Chem. 23*, p. 1421.
5. Uhedova, J. and Rezl, V. (1981), "Determination of Oxygen in Organic Substances by Reaction–Frontal Gas Chromatography," *Anal. Chem. 53*, p. 164.
6. Huffman, Jr., E. (1977), "Performance of a New Automatic Carbon Dioxide Coulometer," *Microchem. J. 22*, p. 567.
7. Novakov, T. (1981), "Microchemical Characterization of Aerosols," in *Nature, Aim and Methods of Microchemistry*, H. Malissa, M. Grasserbauer, and R. Belcher, Eds., Springer-Verlag, Vienna, p. 141.

QUALITATIVE AND QUANTITATIVE ASPECTS OF EVOLVED GAS ANALYSIS*

L.A. Gundel, R.L. Dod, and T. Novakov

Thermal analytical methods, such as thermogravimetric analysis (TGA) and differential scanning calorimetry (DSC), have long been used to provide information about the thermal stability and chemical composition of a variety of materials. Until recently, a method closely related to TGA—evolved gas analysis (EGA)—received relatively little attention. TGA detects the mass loss of a sample as a function of temperature when the sample is heated in an oxidizing or inert atmosphere. EGA, in contrast, determines the rate of evolution of gaseous species from the sample. In EGA, a sample is gradually heated in a stream of oxygen or nitrogen, and the evolved gases are measured by one or more gas-specific

detectors as a function of the sample temperature. For characterizing carbon- and nitrogen-containing materials, it is convenient to use oxygen as the carrier gas with simultaneous detection of CO_2 and NO_x. (A catalyst, such as CuO, is used to convert all carbon- and nitrogen-containing gases to CO_2 and NO_x.)

A plot of concentration of CO_2 and NO_x vs. time or temperature constitutes the EGA thermogram. Thermograms consist of peaks or groups of peaks resulting from the volatilization, decomposition, and combustion of the sample material, thus providing information about the chemical bonding of C and N in the sample. The area under the thermograms is proportional to the concentrations of these elements.

EGA requires no special sample preparation or preseparation and is therefore applicable to both soluble and insoluble sample components. This feature, combined with the high sensitivity of the method, was found to be especially useful in analysis of environmental samples, where some of the most interesting applications have been made. Malissa et al.[1] used conductometric CO_2 and SO_2 detectors to perform simultaneous carbon and sulfur analysis of dust samples. Puxbaum[2] used a TGA system followed by CO_2 and SO_2 detection to analyze aerosol particles and demonstrated the close correspondence between TGA and EGA results for such samples. Malissa et al.[3] used EGA with flame ionization detection to determine volatile aerosol organic materials. Bauer and Natusch[4] used EGA with CO_2 detection to identify carbonate compounds in coal fly ash.

The EGA method was further improved in our laboratory by incorporating continuous monitoring of the light attenuation of the aerosol sample.[5] An examination of the CO_2 and optical thermograms enables the assignment of the CO_2 thermogram peaks that correspond to the optically absorbing black carbon. Because these peaks result from the combustion of black carbon, they are accompanied by a sudden decrease in the sample absorptivity. This apparatus was used to quantitate the black and organic carbon content in aerosol samples[6] and to assess the primary and secondary organic aerosol material.[7]

Recently, we redesigned our EGA system to simultaneously analyze both carbon and nitrogen. This was accomplished by using a chemiluminescent NO_x detector (ThermoElectron Model 14D/E) in series with a nondispersive infrared CO_2 analyzer (MSA Model 202S).[5]

ACCOMPLISHMENTS DURING FY 1982

For individual compounds, EGA, like TGA, may result in single- or multiple-peak thermograms, depending on whether the thermal decomposition occurs in single or multiple stages. With the latter, EGA will give information about both the initial compound and intermediate compounds produced during the heating process. The following examples, obtained with several inorganic nitrogen compounds, illustrate these features of EGA.

NO_x thermograms of NH_4NO_3, NH_4HSO_4, $(NH_4)_2SO_4$, and $NaNO_3$ are shown in Fig. 1. NH_4NO_3, NH_4HSO_4, and $NaNO_3$ result in single-peak thermograms characteristic of single-stage thermal decomposition processes. In contrast, $(NH_4)_2SO_4$ shows a doublet
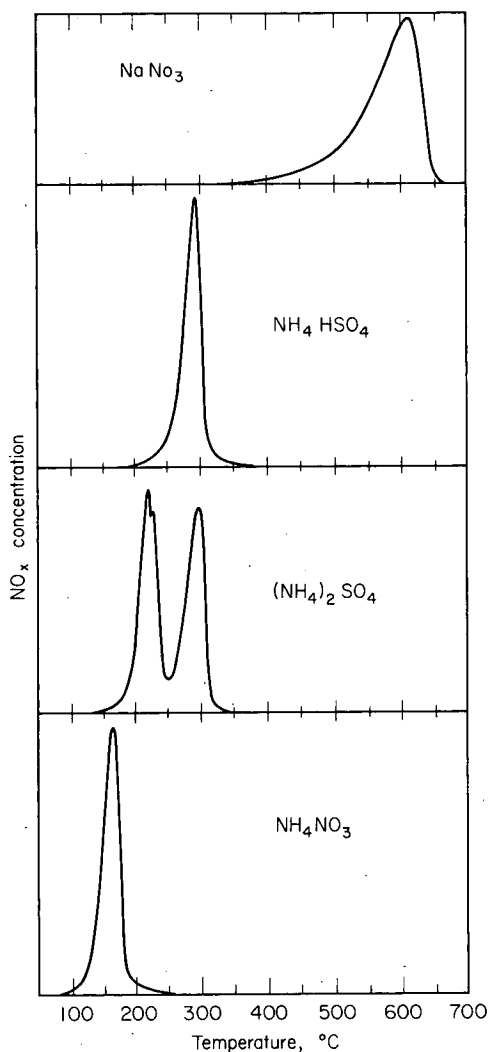
with peaks at 225 and 290°C. The second peak coincides with the NH_4HSO_4 peak. This observation is consistent with a two-stage decomposition process, where one ammonia molecule is released first, leaving a residue of NH_4HSO_4, which decomposes at 290°C. The samples of these compounds, and all others reported here, were prepared for EGA by deposition of aliquots of standard solution onto clean, fired quartz-fiber filters, followed by drying at temperatures between 30 and 50°C before analysis.

A number of organic compounds were also studied. Some examples showing simple, essentially single-peak thermograms are shown in Fig. 2. This figure shows that the peak temperatures are characteristic of the compounds, as are the more detailed features, such as the peak shapes and widths. Examples of organic compounds showing complex thermogram features are shown in Fig. 3. With the exception of brucine, NO_x and CO_2 thermograms show similar features.

It is obvious from these examples that EGA thermograms can be used for qualitatively analyzing different compounds and, with proper standards, for determining specific compounds in a mixture. EGA can also be used for quantitative analysis, provided that the compound does not decompose or sublime at temperatures corresponding to the start of the run. For our samples, this temperature is about 50°C because of the heating of the sample by the catalyst furnace, which is closely coupled to the sample furnace. An example of the quantitative aspect of EGA is shown in Table 1, where carbon and nitrogen recovery as a fraction of the known amounts of C and N are shown. The data show that the carbon recovery is essentially 100%, while the nitrogen recovery depends in some samples on the chemical composition of the sample material.

To illustrate the correspondence between EGA and TGA in Fig. 4, we show the EGA (CO_2) thermogram of potassium hydrogen phthalate (KHP), $KHC_8H_4O_4$. This compound was studied extensively by TGA, and a TGA curve of it (taken from the literature) is shown in the figure for comparison. The following decomposition sequence has been proposed.[8] At lower temperatures (<300°C), water and phthalic anhydride volatilize to form a residue of dipotassium phthalate. This compound then decomposes to form potassium carbonate and elemental carbon. The decomposition of the intermediate species takes place between

Figure 1. NO_x thermograms of some inorganic compounds.
(XBL 8111-1624)
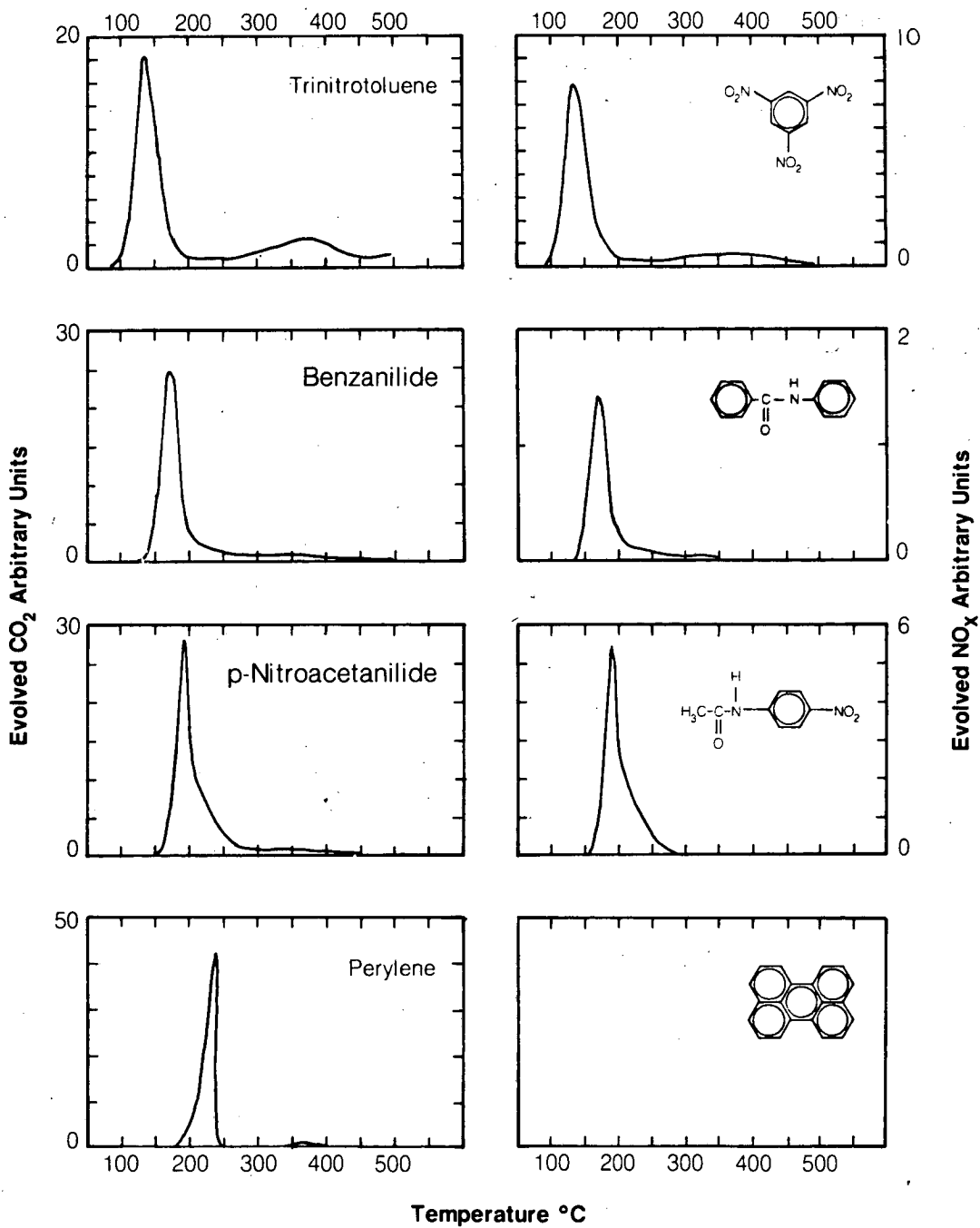
Figure 2. Single-peak thermograms for some organic compounds.   (XBL 834-9403)
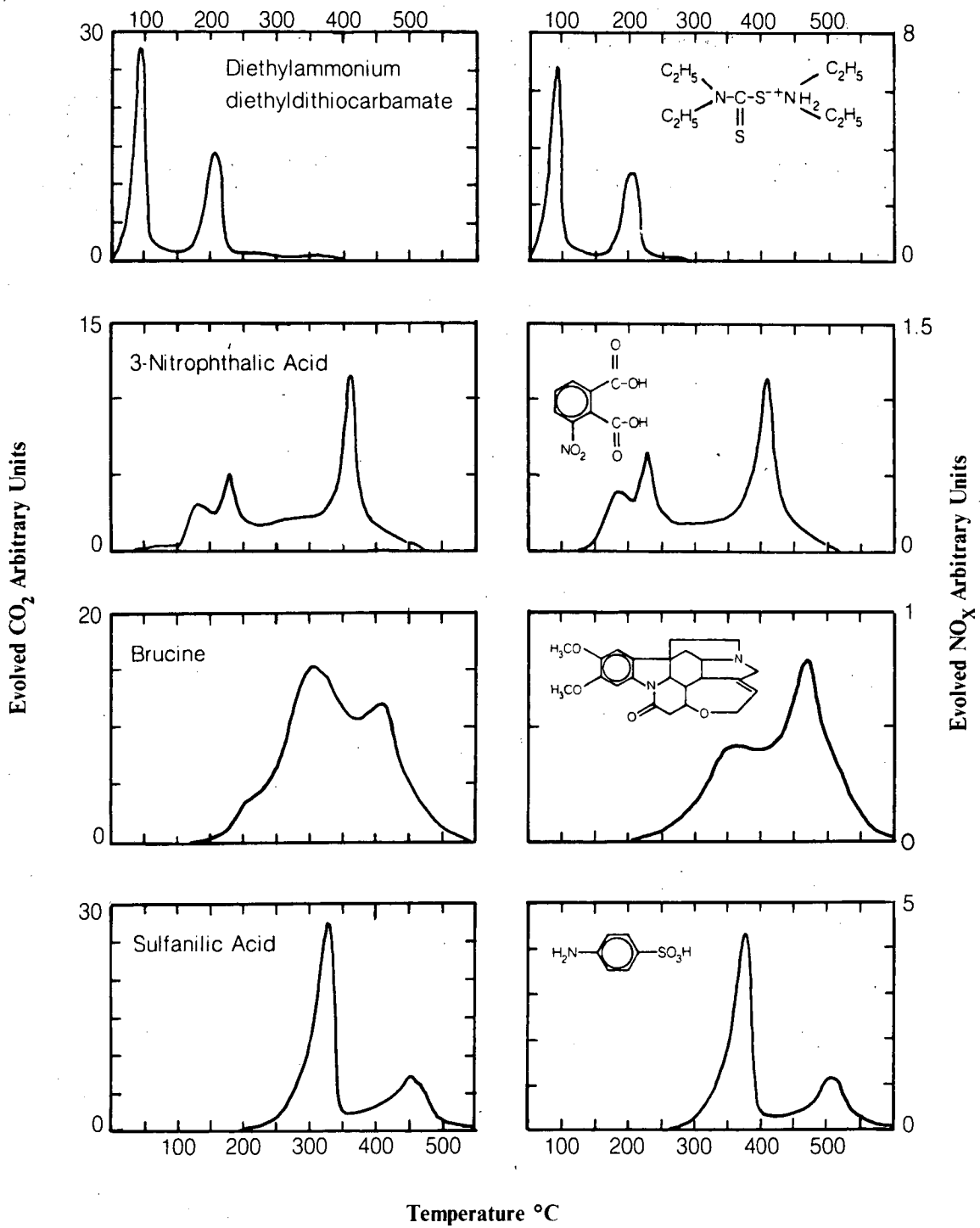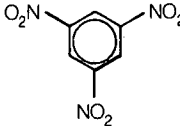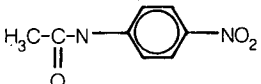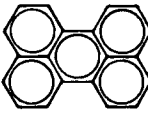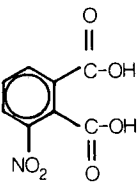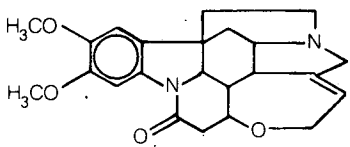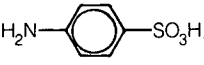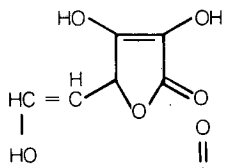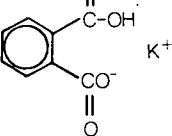
Figure 3. Complex thermograms for some organic compounds.   (XBL 834-9404)

Table 1. Carbon and nitrogen recovery for organic compounds.

Compound	Structure	Carbon Recovery Fraction	Nitrogen Recovery Fraction
Trinitrotoluene		0.989	0.903
p-Nitroacetanilide		1.076	0.753
Perylene		0.977	—
3-Nitrophthalic Acid		0.944	0.889
Brucine		0.924	0.515
Sulfanilic Acid		0.960	0.844
Ascorbic Acid		0.955	—
Potassium Hydrogen Phthalate		1.022	
	Averages	0.981 ± 0.049	0.781 ± 0.160

~325 and 650°C. The combustion of elemental carbon is responsible for the sharp EGA peak at ~475°C, while the KCO_3 decomposes at ~600°C. There is a good correspondence between EGA and TGA for this compound in terms of specific thermogram features and their temperatures. The TGA curve was obtained with a 0.1-g sample in air with a heating rate of 5°C/minute. The carbon content of the EGA sample was 29.6 μg, and the heating rate in oxygen was 10°C/min.

PLANNED ACTIVITIES FOR FY 1983

The second generation of the EGA apparatus will be constructed. The new version will provide hydrogen detection, improved sample handling and throughput, and variable heating rates. A data acquisition and handling system will also be designed.
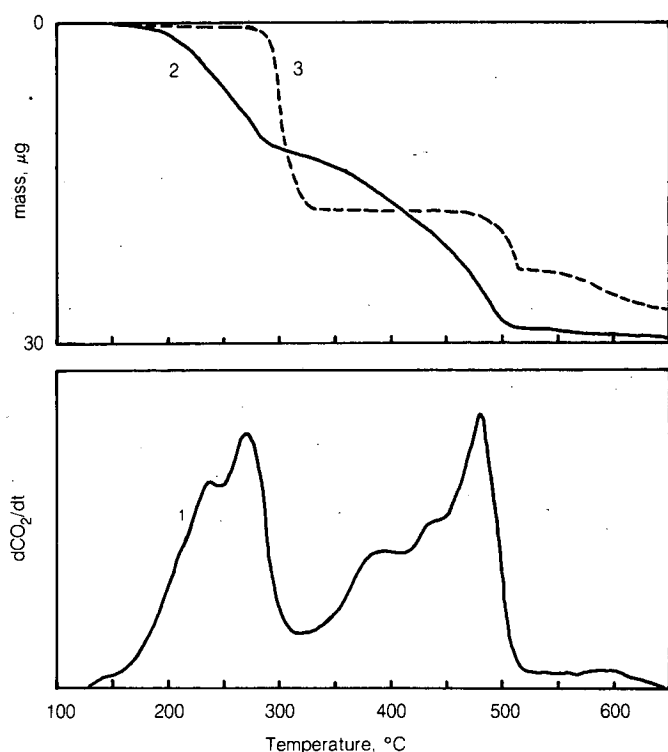
Figure 4. Thermograms of potassium acid phthalate by EGA and TGA methods. Curves are as follows: (1) CO_2 EGA (heating rate: 10°C/min). (2) Integral of curve 1: 29.6 μg carbon. (3) TGA of 0.1-g sample, scaled to fit curve 2 (heating rate: 5°C/min), from Ref. 9.

(XBL 834-9401)

REFERENCES

1. Malissa, H., Puxbaum, H., and Pell, E. (1976), "Zur simultanen relativkonduktometrischen Kohlenstoff- und Schwefelbestimmung in Stäuben," Z. Anal. Chem. 282, p. 109.

2. Puxbaum, H. (1979), "Charakterisierung von Kohlenstoff-, Schwefel- und Stickstoffverbindungen in luftgetragenen Stäuben durch kombinierte thermische und gasanalytische Methoden," Z. Anal. Chem. 299, p. 33.

3. Malissa, H., Puxbaum, H., and Zojer, K. (1981), "Bestimmung flütchtiger organischer Verbindungen in atmosphärischen Aerosolproben durch thermische Desorption und FIG-Detektion," Mikrochemica Acta [Wien] I, p. 1.

4. Bauer, C.F., and Natusch, D.F.S. (1981), "Identification and Quantitation of Carbonate Compounds in Coal Fly Ash," Environ. Sci. Technol. 15, p. 783.

5. Dod, R.L., Rosen, H., and Novakov, T. (1979), "Optico-Thermal Analysis of the Carbonaceous Fraction of Aerosol Particles," Atmospheric Aerosol Research Annual Report 1977–78, Lawrence Berkeley Laboratory Report LBL-8696, p. 2.

6. Gundel, L.A., Dod, R.L., Rosen, H.J., and Novakov, T. (1983), "The Relationship Between Optical Attenuation and Black Carbon Concentration for Carbonaceous Particles," this annual report.

7. Novakov, T. (1982), "Soot in the Atmosphere," in Particulate Carbon: Atmospheric Life Cycle, G.T. Wolff and R.L. Klimisch, Eds., Plenum, New York, p. 19.

8. Wendlandt, W.W. (1974), Thermal Methods of Analysis, Wiley, New York, p. 116.

9. Dupuis, T., and Duval, C. (1958), Mikrochim. Acta. 186.

DETERMINATION OF NON-AMMONIUM, NON-NITRATE NITROGEN IN ATMOSPHERIC AEROSOL PARTICLES*

R.L. Dod, L.A. Gundel, and T. Novakov

It is commonly assumed that NO_3^- and NH_4^+, present as NH_4NO_3, NH_4HSO_4, and $(NH_4)_2SO_4$, are the only nitrogenous species in atmospheric particulate matter. This view was challenged about 10 years ago by the results obtained with a technique, then new, of photoelectron spectroscopy, or ESCA. According to these results,[1] a significant fraction (~50%) of the total reduced nitrogen is present not as ammonium but in a previously unrecognized form, which for simplicity we shall call N_x. It was later postulated that these species consist of particulate amines, amides, and heterocyclic nitrogen compounds.[2]

Until now, there was no direct confirmation of N_x by another analytical method. Commonly used wet chemical determinations are designed for detecting specific ions such as NH_4^+ and are therefore not convenient for detecting an unknown species or group of species. Also, there is evidence that some N_x species can easily be hydrolyzed and detected as ammonium ions.[3] The preferred method for this purpose would be one that is a bulk analytical method (unlike ESCA, which is a surface method) and that does not require any chemical sample preparation or separation. Thermal evolved gas analysis (EGA) is such a method.[4] Its application to filter-collected samples has confirmed the existence of N_x species and could enable their quantitative determination.

ACCOMPLISHMENTS DURING FY 1982

It is obvious from the examples shown in the preceding article[4] that EGA should be able to distinguish common species such as NH_4NO_3 and $(NH_4)_2SO_4$ from those that constitute N_x. To explore this possibility, an ambient sample (collected in Ljubljana, Yugoslavia) was chosen because its ESCA spectrum clearly indicated the presence of both NH_4^+

and N_x with the ratio of NH_4^+ to N_x nitrogen ≈ 1.4. The nitrogen ESCA spectrum of the sample is shown in Fig. 1. The NO_x EGA thermogram of that sample is shown in Fig. 2, together with the thermogram of the $(NH_4)_2SO_4$ standard. It is obvious that the pronounced doublet in the ambient sample corresponds

$$\frac{N(H_4^+)}{N(_x)} \approx 1.4$$

$$\frac{N(H_4^+) \, [(NH_4)_2SO_4]}{N(H_4^+) \text{ OBS.}} \approx 2$$
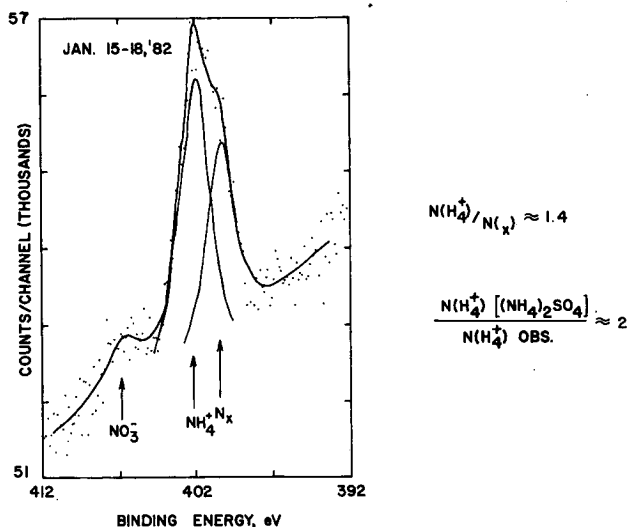
Figure 1. ESCA spectrum (N 1s region) of ambient particulate aerosol sample 111 from Ljubljana, Yugoslavia.

(XBL 834-9174)

to $(NH_4)_2SO_4$, and the small peak at ~150°C to NH_4NO_3. However, in addition to these peaks, a substantial amount of nitrogen is seen in a region from 300 to 500°C, indicated by the crosshatched area in Fig. 2. This nitrogen corresponds to N_x. EGA gives a N_{NH_4}/N_x ratio of ~1.7, which is in reasonable agreement with the ratio derived from ESCA.

A further insight into the nature of N_x is obtained by EGA analysis of an ambient Berkeley sample (Fig. 3). Here the dominant feature of the NO_x thermogram is nitrate. In addition to nitrate, ammonium sulfate or N_x is also seen. N_x here is a relatively small part of the total nitrogen. The N_x peak corresponds closely to the CO_2 peak appearing just before the black carbon peak. Figure 4 shows the thermogram of this sample after sequential extraction with benzene and a methanol/chloroform mixture. It is clear that the extraction has removed most of the N_x, along with the rest of the organic material. This indicates that the N_x species are organic nitrogen compounds associated with relatively high molecular weight organic material.
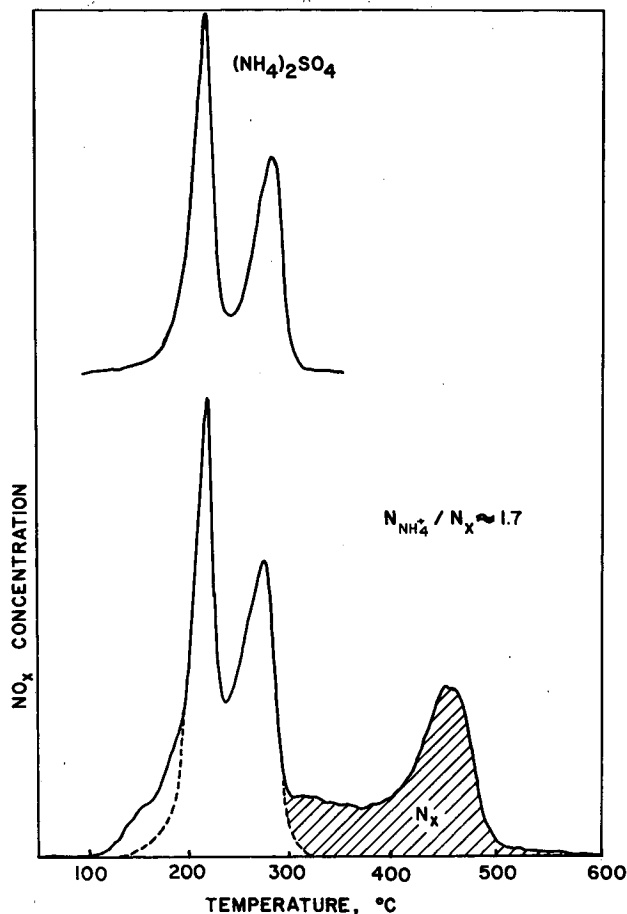
Figure 2. NO_x EGA thermogram of sample 111 from Lju-
bljana, Yugoslavia. (XBL 834-9175)
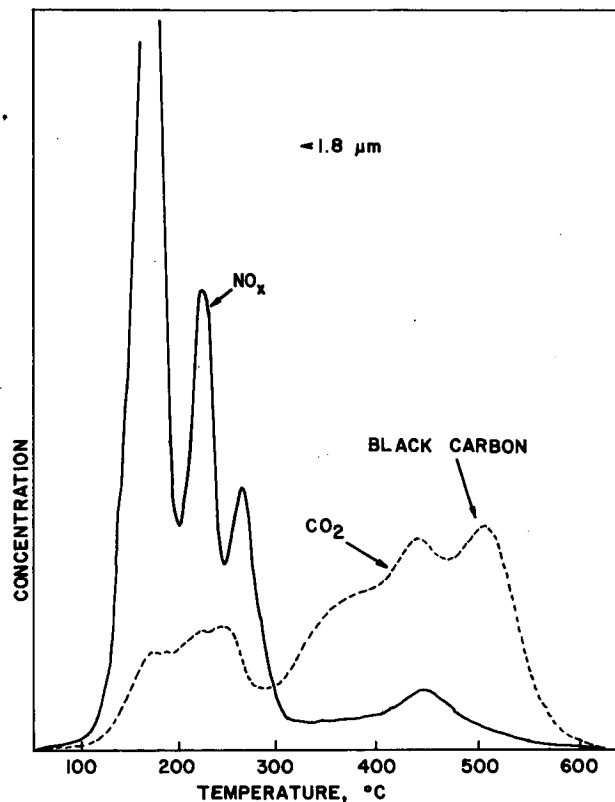
Figure 3. NO_x and CO_2 EGA thermograms of ambient parti-
culate aerosol sample taken 22 October 1981 in Berkeley,
California. (XBL 834-9171)
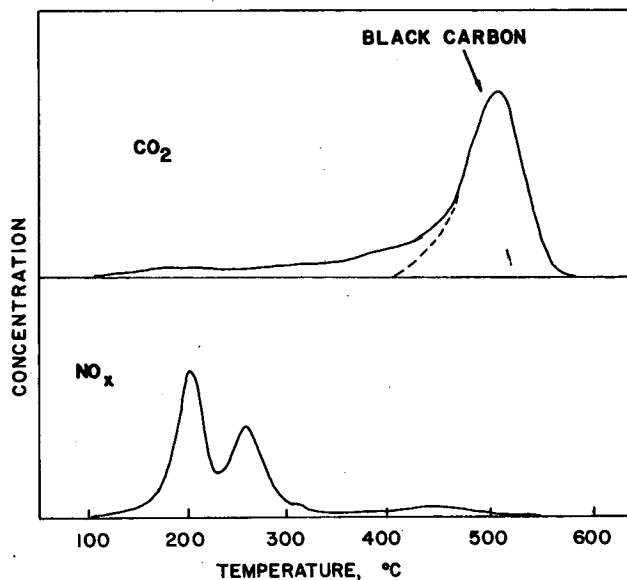
Figure 4. NO_x and CO_2 EGA thermograms of Fig. 3 sample
after sequential solvent extraction. (XBL 834-9172)

PLANNED ACTIVITIES FOR FY 1983

Systematic studies involving ESCA, EGA, and ion
chromatography will be initiated to quantitatively
determine the concentration and structure of N_x
species.

REFERENCES

1. Novakov, T., Mueller, P.K., Alcocer, A.E., and
   Otvos, J.W. (1972), "Chemical Composition of
   Pasadena Aerosol by Particle Size and Time of
   Day: Chemical States of Nitrogen and Sulfur by
   Photoelectron Spectroscopy," *J. Coll. Interface
   Sci. 39*, p. 225.

2. Chang, S.-G., and Novakov, T. (1975), "Forma-
   tion of Pollution Particulate Nitrogen Com-
   pounds by NO-Soot and NH_3-Soot Gas-Particle
   Surface Reactions," *Atmos. Environ. 9*, p. 495.

3. Gundel, L.A., et al. (1979), "Characterization of Particulate Amines," in *Nitrogenous Air Pollutants*, D. Grosjean, Ed., Ann Arbor Science, Ann Arbor, Michigan, p. 211.

4. Gundel, L.A., and Dod, R.L., and Novakov, T. (1983), "Qualitative and Quantitative Aspects of Evolved Gas Analysis," this annual report.

INVESTIGATION OF THE RELATIONSHIP OF PARTICULATE NITROGEN AND SULFATE*

R.L. Dod, W.H. Benner, and T. Novakov

While it is generally known that water extraction of ambient aerosol particulate material usually produces a solution containing ammonium, sulfate, and nitrate ions, what compounds existed in the particles before extraction remains uncertain. We have postulated that, in addition to the simple compounds of these ions, nitrogenous functional groups on the organic and/or elemental carbon present in the particles may act as cationic sites to which sulfate and nitrate are "bonded."

To study this postulated relationship among sulfur, nitrogen, and carbon, we are using a variety of techniques with complementary strengths that help to overcome the limitations of each one alone. X-ray photoelectron spectroscopy (ESCA) can provide relative quantitative information regarding elemental composition as well as oxidation states and can be used without sample preparation.[1] However, ESCA analyzes only the sample surface, and the sample must be in high vacuum and exposed to x radiation for the time (typically tens of minutes) necessary to complete the analysis. ESCA results therefore may not be representative of the bulk composition. Some volatile species could be lost because of the vacuum, and in principle the x-ray bombardment could cause chemical changes in some species.

Combustion thermal analysis (EGA)[2] requires no sample preparation, and the sample is analyzed in an

environment very similar to ambient. The information obtained from EGA regarding quantitation and chemical states of nitrogen often requires supplementary analytical results to be fully explained.

Ion chromatography (IC) is a very sensitive and specific method for determining ionic concentrations in aqueous solution. However, it has the limitations of other wet chemical techniques: some compounds in a solid sample may not be soluble, and others may transform during dissolution. Thus the results of IC analysis may not be totally representative of the original sample.

ACCOMPLISHMENTS DURING FY 1982

A set of 23 ambient-particle filter samples from Anaheim, California; Argonne, Illinois; Gaithersburg, Maryland; New York City, and Ljubljana, Yugoslavia, representing a wide range of total carbon and sulfur concentrations, was assembled for the initial investigation. Fractions of each sample were analyzed by ESCA, EGA, and IC for their sulfur and nitrogen content.

Although these samples were widely disparate in concentration, nearly all exhibited a doublet in their NO_x thermograms similar to that of $(NH_4)_2SO_4$ (Fig. 1).[3] This was usually the dominant feature in the NO_x thermogram, indicating that much of the particulate nitrogen is present either as ammonium sulfate or as a compound in which organic nitrogenous functional groups are bonded to sulfate.[4]

In some samples, nitrate nitrogen is detected by ESCA, but it is lost during exposure of the sample to vacuum for several hours. Accompanying this loss is the simultaneous loss of an equivalent amount of ammonium nitrogen, which is taken as evidence that nitrate is present as the compound NH_4NO_3. For all samples, more nitrate is found by IC than by ESCA, an observation consistent with such volatility. We therefore assume that most, if not all, nitrate is present in these samples as ammonium nitrate.

When the measured ammonium concentration is reduced by the amount necessary to provide counterions for nitrate, the remainder is available to associate with sulfate. This association is indicated by the NO_x EGA results. IC analysis indicates that the average ratio of available ammonium to sulfate for these samples is ~1.5. From ESCA, for the same sample set, the average ratio is ~1.0. If all reduced nitrogen ($NH_4^+ + N_x$) determined by ESCA is taken as ammonium, the average ratio of available ammonium
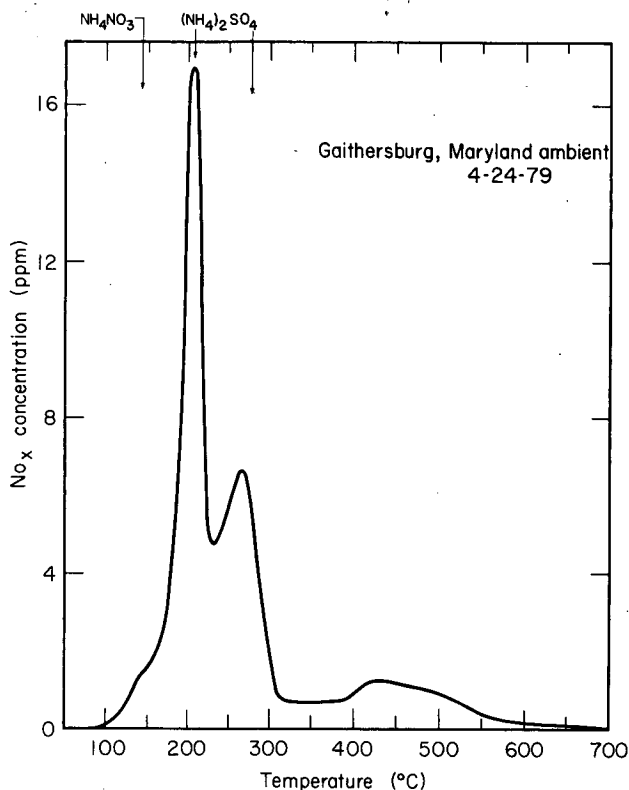
Figure 1. NO$_x$ EGA thermogram showing peak doublet similar to (NH$_4$)$_2$SO$_4$.   (XBL 8111-1622)

to sulfate becomes ~1.6, somewhat larger than—but much closer to—the ratio determined by IC. This implies that much of the N$_x$ is extractable as ammonium, a conclusion consistent with past results.[5]

The observed similarity to ammonium sulfate in the NO$_x$ thermograms of these samples, when considered with the similarity between the concentration of NH$_4^+$ determined by IC and the concentration of total reduced nitrogen determined by ESCA, provides substantial evidence for the formation of ionic compounds between sulfate and organic nitrogenous functional groups.

PLANNED ACTIVITIES FOR FY 1983

We intend to expand our sample set, including standard compounds; to study the effect of heating in ESCA on the samples; and to observe with EGA and IC the effect on the samples of vacuum exposure.

REFERENCES

1. Siegbahn, K., et al. (1967), "ESCA: Atomic, Molecular and Solid State Structure Studied by Means of Electron Spectroscopy," *Nova Acta Regiae Soc. Sci. Ups. Ser IV. 20*, p. 5.

2. Dod, R.L., et al. (1980), "Application of Thermal Analysis to the Characterization of Nitrogenous Aerosol Species," in *Energy & Environment Division Annual Report, 1979*, Lawrence Berkeley Laboratory Report LBL-11650, p. 8-25.

3. Dod, R.L., Gundel, L.A., and Novakov, T. (1983), "Determination of Non-Ammonium, Non-Nitrate Nitrogen in Atmospheric Aerosol Particles," Fig. 2, this annual report.

4. Dod, R.L., and Novakov, T. (1982), "Application of Thermal Analysis and Photoelectron Spectroscopy of the Characterization of Particulate Matter," in *Industrial Applications of Surface Analysis*, L.A. Casper and C.J. Powell, Eds., ACS Symposium Series 199, American Chemical Society, Washington, D.C., p. 397.

5. Gundel, L.A. (1979), "Characterization of Particulate Amines," in *Nitrogenous Air Pollutants*, D. Grosjean, Ed., Ann Arbor Science, Ann Arbor, Michigan, p. 211.

A COMPUTER-BASED CONTROL AND DATA ACQUISITION SYSTEM FOR EVOLVED GAS ANALYSIS*

A.D.A. Hansen, W.H. Benner, and T. Novakov

Ambient aerosol particles are a complex mixture of organic and inorganic chemical compounds, speciation of which can yield information on the origins and atmospheric transformations of the aerosol. The major species of anthropogenic origin are compounds of carbon, hydrogen, oxygen, nitrogen, and sulfur. A powerful analytical tool that is related to other "thermal" methods of physical-chemical analysis and that was first applied to the analysis of aerosol particles by Malissa[1] is the evolved gas analysis (EGA) technique. This technique can identify certain individual compounds and classify broad groups according to the temperatures at which they decompose in either

reactive or inert atmospheres. Considerable development of the method has taken place at LBL and elsewhere, and it has been applied to the analysis of carbon,[2] nitrogen,[3] sulfur,[4] and oxygen[5] compounds. The apparatus must include (1) a temperature-programmed furnace region, in which the sample is heated from room temperature to ~1000°C at a rate of 10 to 30°C per minute, and (2) a data acquisition and reduction system. Early in FY 1982, we decided to automate these otherwise time-consuming functions. Here we outline hardware and software developments that have led to a system fulfilling these requirements.

ACCOMPLISHMENTS DURING FY 1982

Software Development

We decided to develop a system that would control the temperature ramp and would acquire and display the data in a configuration that would be rapidly interchangeable between our different EGA analyzers. The furnaces of these analyzers are totally dissimilar, both in the electrical and thermal characteristics of the heating elements and in the thermal coupling of the furnace to the sample and to the temperature-measuring thermocouple. The temperature-control software must therefore be able to learn the characteristics of each furnace and be self-correcting during each run. The data acquisition and processing requirements are modest: at 10-second intervals as the run progresses, the signal is plotted against temperature on an X–Y recorder while the computer's screen shows temperature control data and provides for operator interaction. At the end of the run, while the oven is cooling down, the data may be processed (e.g., baseline subtraction, calibration factor rescaling, peak integration), replotted in different ways, or recorded on tape. The furnace power is digitally controlled directly and is proportional to a "control number" K calculated by the program. During each run, continuous adjustment of the power control is effected by feedback of a temperature error signal. The power supplied to the furnace in the nth interval at time t is proportional to:

$$K_n = K_n^0 + f \cdot [T_{ramp(t)} - T_{actual\ (t)}] \quad ,$$

where f is the error feedback strength and the sequence of numbers K_n^0 is the previously learned

power control profile. However, due to the imperfect thermal coupling between the furnace heating elements and the sample (usually in a boat in a quartz or ceramic tube), the temperature response of the sample lags relative to the power supplied to the furnace. Thus, at the end of the run, the sequence of control numbers is recomputed retrospectively so that an error in the nth interval is anticipated by adjusting the K_m for $m < n$. These relearned values then form the basis set K_n^0 for the next run. The program can run unattended in a purely "learning" mode so that it can be applied to a furnace-thermocouple combination of unknown electrical and thermal characteristics; after a few cycles, it will have learned the power control profile necessary to achieve the desired temperature ramp to within an acceptable accuracy.

Hardware Development[†]

The equipment used is a commercial microcomputer using the BASIC language, with a multichannel A/D input converter, a semi-intelligent X–Y plotter, a printer, and a serial input/output port. This port transmits the 8-bit control number K (i.e., $0 \le K \le 255$) to the digital power-control interface (DPCI). The isolation provided by this link reduces the coupling of electrical transients and could allow the DPCI to be remotely located.

Development of the DPCI as the means whereby a computer program can rapidly and flexibly control kilowatts of electrical power was essential to this project, since such a unit is not available commercially. The DPCI is therefore able to control AC power from a true zero to full load, limited only by the triac rating.

System Performance

This system has been an integral part of oxygen-EGA development and has demonstrated reliability of temperature control and convenience of use. The adaptive nature of the learning program results in runs from room temperature to 1100°C whose root-mean-square temperature error rarely exceeds 2 degrees, despite changes in experimental conditions and ambient temperatures. The data handling and display routines produce both high-quality graphics and all pertinent numerical information, eliminating the need for further processing.

PLANNED ACTIVITIES FOR FY 1983

Among future software developments is the inclusion of a library of thermograms of standard compounds for quantitative comparison with each sample analysis. Planned hardware developments include the automation of other experimental parameters, such as carrier gas switching, backflushing, sample handling, etc. The field of thermal analysis is expanding rapidly and adds considerably to our understanding of aerosol particles. Automation of the analytical apparatus allows the necessarily large number of samples to be run with minimal manpower demand.

REFERENCES

1. Malissa, H., Puxbaum, H., and Pell, E. (1976), "Zur simultanen relativkonduktometrischen Kohlenstoff und Schwefelbestimmung in Stäuben," *Z. Anal. Chem. 282*, p. 109.

2. Dod, R.L., Rosen, H., and Novakov, T. (1978), "Optico-Thermal Analysis of the Carbonaceous Fraction of Aerosol Particles," *Atmospheric Aerosol Research Annual Report, 1977-78*, Lawrence Berkeley Laboratory Report LBL-8696, p. 2.

3. Dod, R.L., et al. (1980), "Application of Thermal Analysis to the Characterization of Nitrogenous Aerosol Species," *Atmospheric Aerosol Research Report FY 1979*, Lawrence Berkeley Laboratory Report LBL-10735, p. 35.

4. Dod, R.L., and Gundel, L.A., private communication.

5. Benner, W.H. (1983), "The Oxygen Content of Ambient Particulate Matter," this annual report; also Benner, W.H., private communication concerning adaptation of the technique described therein to temperature-programmed EGA.

---

†Details of the hardware invention have been reported to the DOE Office of Patent Counsel.

APPLIED PHYSICS AND LASER SPECTROSCOPY RESEARCH

N.M. Amer,* M.S. Cooper, R.W. Gerlach, A. Hitachi, W. Imler,
M.A. Olmstead, A. Skumanich, D.R. Wake, D. Wei,

The research philosophy of our group is to apply advanced laser spectroscopy and condensed-matter physics to energy and environmental problems. Because of the narrow line width and tunability of lasers, unsurpassed sensitivity and specificity can be achieved in detecting trace contaminants of the environment, for example. The advanced state of condensed-matter physics also makes it possible to apply this knowledge to energy production and to test novel methods of energy conversion such as photovoltaic solar cells, superionic electrical energy storage devices, and the recovery and extraction of oil from abandoned wells and oil shale with lyotropic liquid-crystal emulsifiers.

ACCOMPLISHMENTS DURING FY 1982

LASER PHOTOTHERMAL MEASUREMENTS AND CHARACTERIZATION[†]

Laser photothermal spectroscopies provide powerful tools for detecting trace contaminants in air and water, as well as for investigating the fundamental properties of gaseous, liquid, and solid phases of matter. One goal of this project is to develop ultrasensitive, multiparameter elemental and molecular detectors for characterizing trace constituents, with emphasis on remote sensing. Another is to maintain a state-of-the-art capability in photothermal detection by fully understanding the physics of these techniques. We are also developing, as needed, new or modified laser systems in support of these efforts.

Photothermal Displacement Spectroscopy[‡]

The optical properties of electronic surface states are important for both fundamental and technological reasons, and a variety of optical spectroscopic

techniques have been used to investigate them.[1] Most prominent among these techniques are reflectance and ellipsometric methods. To determine the contribution of surface states, however, the difference between the spectra of clean and intentionally contaminated surfaces must be measured.

We have recently developed a sensitive new technique, photothermal displacement spectroscopy,[2] for directly measuring the optical and thermal properties of surfaces and thin films. The technique, which is relatively easy to implement, is particularly suited for studies requiring wide ranges of pressures and temperatures.

The physical principle underlying photothermal displacement spectroscopy is that when a modulated beam of electromagnetic radiation (a pump beam) is absorbed, heating of the absorbing medium will occur. As the illuminated surface expands with heating, it buckles and is displaced. The magnitude of the displacement is related quantitatively to the optical absorption coefficient.[2]

The surface displacement h is given by

$$h = \alpha_{th}\beta P/(2A\,f\rho C) \tag{1}$$

where

α_{th} = the thermal expansion coefficient of the material,
β = the fraction of absorbed light,
P = the incident power,
f = the modulation frequency,
A = the optically heated area,
ρ = the mass density, and
C = the heat capacity.

An important parameter in photothermal spectroscopy is the thermal diffusion length, L_{th}, which defines the depth within the sample from which the photothermal signal is generated; it is given by

$$L_{th} = (K_{th}/\pi\,f\rho c)^{1/2} \tag{2}$$

where K_{th} is the thermal conductivity of the material. The frequency dependence of the thermal diffusion length is what we exploit to differentiate between sur-

face and bulk contributions to the photothermal signal. It can readily be seen from Eq. (2) that, by increasing the modulation frequency of the pump beam, one can enhance the ratio of surface to bulk contributions.

Figure 1 shows two possible configurations for performing photothermal displacement spectroscopy: a
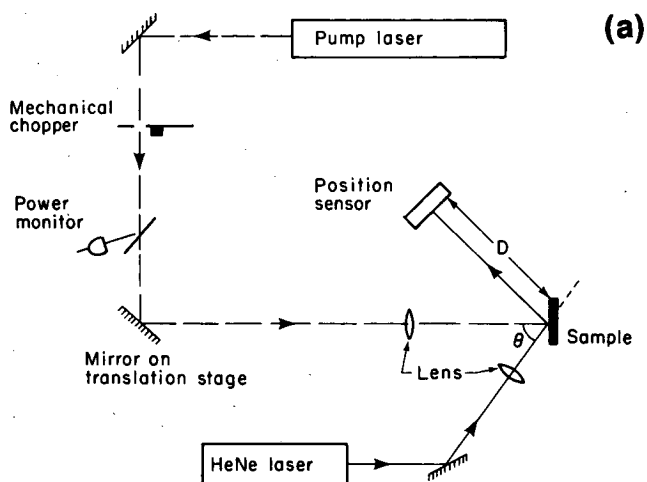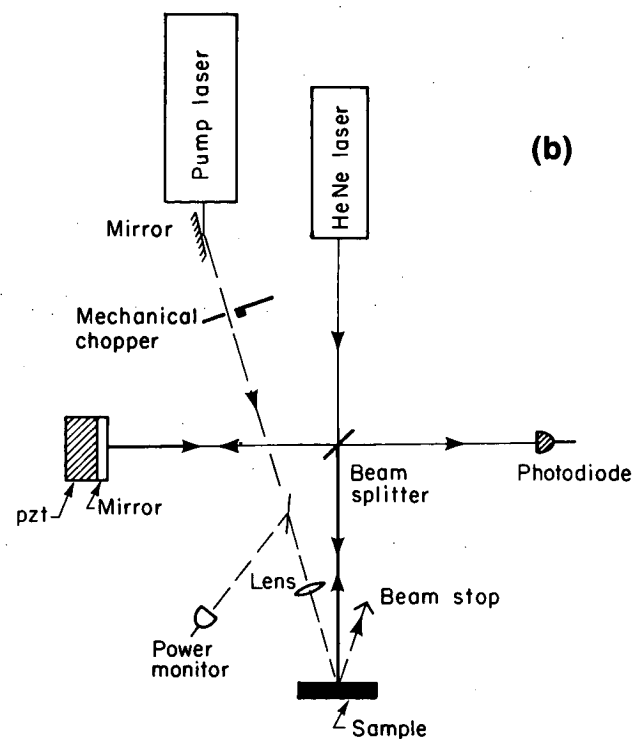
beam deflection scheme that measures the slope of the photoinduced displacement, and an interferometric scheme that measures the displacement itself.

Figure 1(a) shows the details of the beam deflection scheme. The time-dependent change in the slope of the photoinduced surface buckling is measured as a time-dependent change in the deflection angle of a weak probe beam (typically a He-Ne laser), as detected by a position sensor.

The interferometric scheme is shown in Fig. 1(b). The sample of interest serves as one arm of a Michelson interferometer. The position of the mirror in the other arm is modulated to overcome thermally induced drifts and the effect of mechanical vibration on the interferometer.

Both schemes have comparable sensitivities ($\alpha \ell \approx 10^{-6}$), but the beam deflection approach is easier.

To demonstrate the spectroscopic feasibility of this technique, we measured the absorption spectrum of didymium glass in the 700–800 nm range (Fig. 2). Spectra were obtained at atmospheric pressure and at 20 m Torr. To establish that photothermal displacement spectroscopy indeed measures the optical absorption, we also derived the absorption spectrum in this wavelength region by conventional transmission methods.

The ability of the technique to differentiate between surface and bulk absorptions is demonstrated in Fig. 3(a). A 50-Å gold film was evaporated on 2-mm-thick didymium glass. The absorption spectra of gold only and of didymium only are given in Fig. 3(b). In the wavelength region of 700–800 nm, approximately 25% of the incident light is absorbed by the gold film, with didymium having a strong

Figure 1. Two experimental configurations for photothermal displacement spectroscopy: (a) beam deflection scheme; (b) interferometric scheme.

[(a) XBL 831-22; (b) XBL 832-7779]
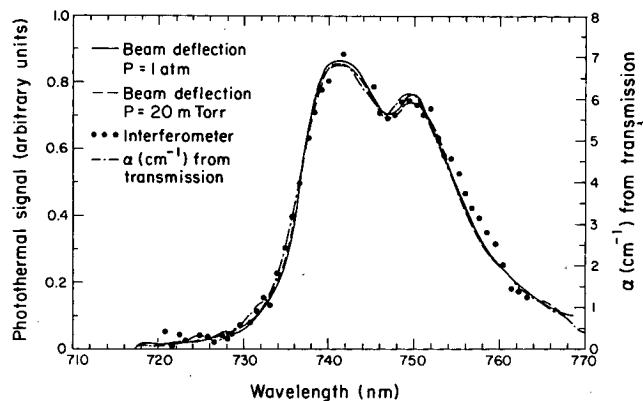
Figure 2. Absorption spectra of didymium.   (XBL 831-20)

absorption peak of ~6.5 cm^{-5} around 740 nm. As shown in Fig. 3(a), at a modulation frequency of 5 Hz, the photothermal signal of the gold-coated didymium is the sum of the featureless gold absorption plus the peaks of the didymium absorption band. As the modulation frequency is increased to 127 Hz, the gold signal decreases by a factor of 2, while the didymium peaks decrease by an additional factor of 2 or 3. Clearly, higher modulation frequencies would still further reduce the substrate (bulk) contribution to the photothermal signal.

In conclusion, this sensitive new photothermal technique[3] directly measures the optical absorption of surfaces and obviates the need for spectra subtraction that is necessary in conventional optical absorption spectroscopy. It is readily suited for ultra-high vacuum studies, requires no mechanical or electrical contacts, and is linear over a wide range of absorption coefficients.
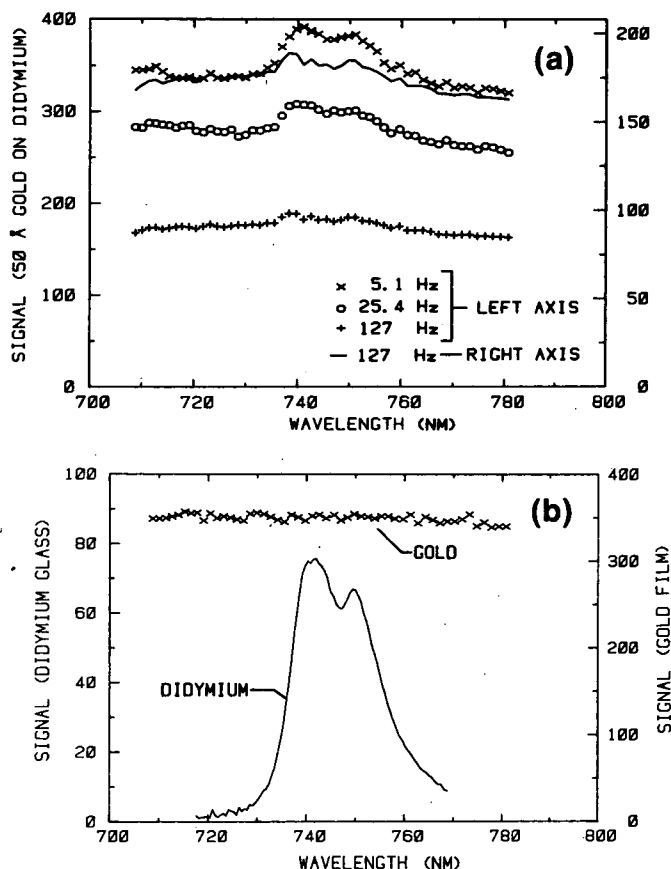
Figure 3. (a) A demonstration of the ability of PDS to differentiate between surface (gold) and bulk (didymium) absorptions; the central peaks represent the didymium contributions, which decrease as the modulation frequency increases. (b) Spectra of 50-Å gold film (top) and of didymium (bottom). [(a) XBL 832-7825; (b) XBL 832-7824]

AMORPHOUS PHOTOVOLTAIC SEMICONDUCTORS*

Amorphous photovoltaic semiconductors, such as hydrogenated amorphous silicon, hold promise for meeting DOE cost and efficiency guidelines for thin-film solar cells before 1990. To achieve the higher conversion efficiencies required, it is necessary to better characterize the unique optical and transport properties of these materials. Photoacoustic and photothermal spectroscopies can provide such elucidation. Of particular interest is the investigation of the optical properties near the so-called bandgap. By combining luminescence studies, photoconductivity, and optical absorption, a full and accurate characterization of the deexcitation of these photoexcited amorphous semiconductors can be achieved.

Experiments investigating the optical properties of amorphous semiconductors are currently under way. These experiments are designed to yield new information on the details of their optical absorption, the nature of the bandgap, and their electronic and transport properties.

Role of Dangling Bond Defects in Early Recombination in Amorphous Silicon[†]:

Dangling bond (DB) defects are the focus of many investigations dealing with tetrahedrally bonded amorphous semiconductors.[4] A DB defect can be pictured as an unsatisfied tetrahedral bond with an unpaired electron, a situation that is disruptive both structurally and electronically. The presence of DB defects correlates strongly with luminescence quenching,[5] short free-carrier lifetime,[6] increased subgap absorption,[7] and the shape of the absorption edge.[8,9] DB defects can be passivated in amorphous silicon (a-Si) by alloying with hydrogen (a-Si:H). The defect density, which is observable by electron spin resonance (ESR), is controlled by material deposition conditions; it is increased with hydrogen evolution and is partially diminished by rehydrogenation.

Strong circumstantial evidence from several experiments indicates that DB defects play an active role in electron hole recombination in amorphous silicon[4]

analogous to that of defects in crystalline materials.[10] In particular, at low temperatures fast recombination by direct tunneling of carriers to DB defects is assumed to be the main mechanism that limits carrier lifetime and quenches luminescence.[5] We have presented evidence that DB defects are not fast recombination centers; instead, the dispersive influence of the exponential distribution of localized states extending into the gap (the band tail) dominates the recombination process in the multiple trapping model (MTM)[11].

Photoexciting carriers across the gap in a-Si:H allows the absorption of infrared radiation (IR) by the nonequilibrium population of electrons and holes, as these carriers make transitions to the extended states deeper in the bands. Similar photoinduced absorption (PA) data have been reported for a-Si:H for times from 0.5 μsec and have been interpreted in terms of multiple trapping.[12,13] Our data span the period from 4 to 500 nsec, when very few carriers have actually recombined, although trapping processes and luminescence quenching have begun and carrier thermalization is important.

We used a 10-Hz Nd:Yag pumped dye laser with 4 nsec (FWHM) pulses of 2.2 eV photons to photoexcite a carrier density of $\sim 10^{18}$ cm^{-3} in a-Si:H. A cw IR beam (0.9 to 1.45 eV) from a filtered tungsten lamp was passed through this carrier population, and changes in the IR transparency were detected by a fast Ge photodiode with a rise time of 1.5 nsec. Changing the spectral width of the IR with a crystalline Si filter had no effect on the PA response. At low temperatures, luminescence is unavoidably emitted into the photodiode optics, but it was separately recorded and subtracted. Data were taken for undoped samples of various defect densities over a temperature range of 10 to 300 K.

Figure 4 shows the PA data for representative a-Si:H samples. The defect density, N_s, is measured by ESR at $g = 2.0055$. A simple power law describes the PA decay of these samples over this time period very well with an exponent of "α". The rate of decay systematically decreases with increasing defect density. This trend is opposite to that expected if DB defects were controlling recombination.

We can, however, successfully interpret these results in terms of a multiple trapping model[11] with a distribution of localized trapping states, $N_t(E)$, whose density declines exponentially into the gap; $N_t(E) = N_0 \exp(-E/E_0)$, where E is the depth of the trap level
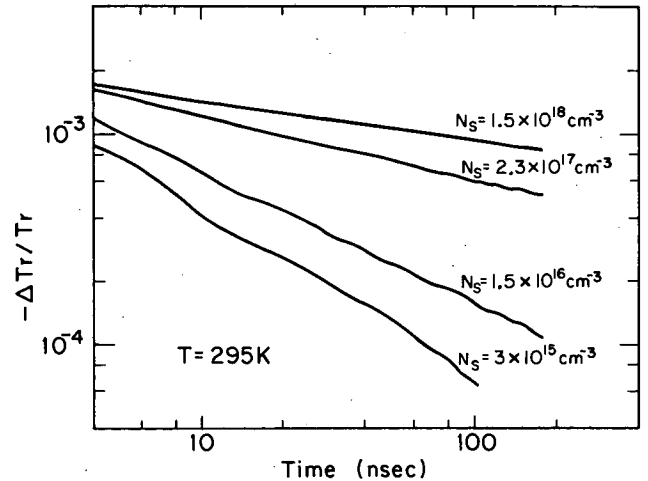
Figure 4. Relative change in transmission (photoinduced absorption) vs. time delay for samples of various defect densities, showing a power-law decay $t^{-\alpha}$.

(XBL 828-4057)

from the band edge and E_0 is the width of this band tail. There is evidence that this is the case not only for a-Si:H but also for a large number of amorphous and disordered crystalline systems. The model implicity assumes that direct transitions either within the band tail or to deep centers are negligible when compared to thermally stimulated transitions to the band edge followed by retrapping. Upon photoexcitation, the carriers are quickly trapped into the band tails,[6] acquiring an exponential energy distribution that parallels the density of trap states. The top of the trapped distribution thermalizes; the level at which thermalization begins, E_d, descends through the distribution as $E_d = k_B T \ln \nu t$, where ν is an attempt-to-escape frequency on the order of 10^{13} sec^{-1}. Below E_d, the probability of thermal release at time t is negligible. The consequence is an exponentially spiked distribution of charge localized (energetically) near E_d. Capture by carriers of opposite charge or deeper levels that are not part of the band tail competes with retrapping; when the probability of capture there exceeds the probability of retrapment at states below E_d, the population in the band tail diminishes as $t^{-\alpha}$, where $\alpha = T/T_0$, and $T_0 = E_0/k_B$. This time dependence is observed from our earliest time of 4 nsec.

The shape of the trap distribution, then, determines the exit rate of the carriers from the band tail. Other experiments have shown that increasing the DB defect density leads to widening of the band edge,

increasing E_o.[8,9] Since E_d descends through the band tail at a rate independent of trap or defect density, a larger fraction of carriers is localized below E_d in a highly defect-dense material than in a low-defect-dense material at comparable times. The high-defect-density material holds carriers in the band tail longer.

A test of this interpretation is to decrease the temperature. In Fig. 5 we plot "α," obtained from the power-law fit to PA at 200 nsec, as a function of temperature for a sample of defect density of 1.5×10^{16} cm^{-3}. As predicted by the MTM, α varies linearly with temperature between 50 and 250 K. A similar temperature dependence has already been observed at longer times.[12] Figure 5 shows that $E_o = 46$ meV or $T_o = 534$ K.

We have also measured E_o directly from optical absorption; Figure 6 compares $k_B T/E_o$ with the "α" from PA. Since the optical absorption data represents a joint density of states involving both the valence and conduction bands, the convolution of a narrow feature of one band with a broad feature of the other band will map out the broad feature in the absorption spectrum. The broader of the two band tails will dominate the optical absorption edge; in a-Si:H, this is the valence band edge.[14] Thus the excellent agreement in Fig. 6 for all but the lowest-defect density samples ($<10^{16}$ cm^{-3}) indicates that the shape of the valence band tail determines the rate of PA decay. O'Connor and Tauc[15] concluded that they
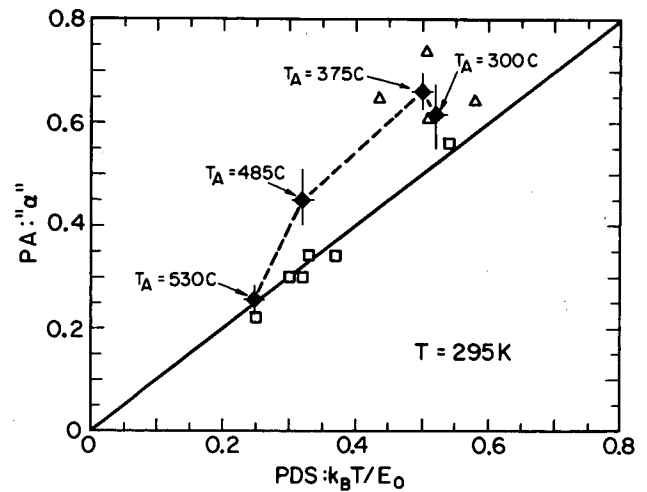
Figure 6. α from a transient photoinduced absorption compared with $k_B T/E_o$ from optical absorption at 295 K. Open symbols represent samples deposited under a range of conditions that vary N_s (ESR), triangles being the "optimal," low-defect-density samples. Solid symbols show the effect of evolving H from a single sample.

(XBL 828-4059)

were not observing electrons in their PA experiments on a-Si:H, and we interpret our similar results as strong and direct evidence that the PA decay is due to hole activity. In the lowest-defect density samples, the PA decays faster than the rate predicted by optical absorption, indicating that hole movement is not the limiting rate that it is in the samples with more defects. This suggests that electron transport assists band-to-band recombination in the samples with lowest defect density and that the faster decay may yield information on the conduction band instead of the valence band.

Figure 4 shows that, at 295 K, the low-defect-density sample relaxes much more quickly than the high-defect-density sample. Below 50 K, both samples relax at about the same rate, $\alpha \approx 0.07$ (very slowly), and the PA signal is approximately equal for all samples near 10 nsec.[16] This is in sharp contrast to luminescence experiments which show that the low-defect-density material has a luminescence quantum efficiency near unity for the 1.4 eV emission while the high-defect-density material has a weaker band at 0.9 eV.[17] One interpretation of this has been that the carriers are rapidly tunneling to the DB defects, which act as nonradiative recombination centers. The PA results indicate that this is not happening. At low T, the highest defect density sample's IR absorption is reduced only 50% at 2 μsecs; yet the luminescence is weak and decays
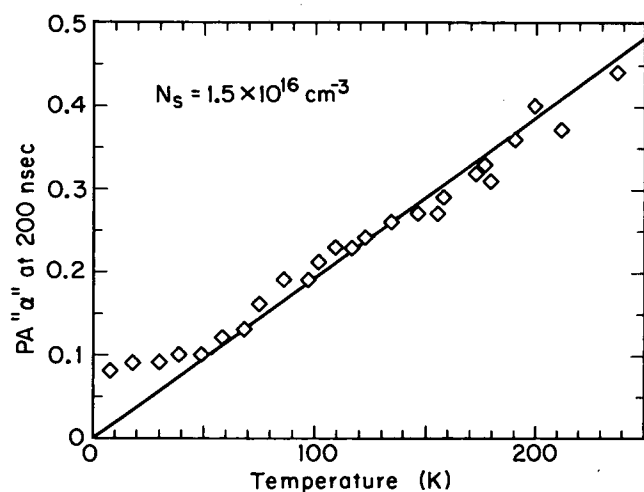

Figure 5. Temperature dependence of α. The weakening of the temperature dependence at low temperature is most likely due to a competing local-to-local recombination process.   (XBL 828-4058)

rapidly. The rate of PA decay correlates better with band-tail widths than with spin density. We conclude that the DB defect is not a rapid recombination center in undoped amorphous silicon, but instead influences the recombination process indirectly by its effect on the width of the band tail.

For the luminescence results, we can only suggest alternative quenching mechanisms such as charged-defect electric field quenching,[18] DB-induced strains, or tightly localized carriers in the higher-defect-density material. We do not completely rule out the possibility that the electrons are rapidly captured by DB defects followed by a slower capture of holes. But serious difficulties exist with all of these suggestions and will be discussed in a future paper.

In order to separate the role of defects from the effects of various deposition conditions used in the samples in Fig. 6, we stepwise-evolved hydrogen from an initially low-defect-density sample by annealing it to temperatures of 300 to 530°C. We directly monitored the optical absorption edge with photothermal deflection spectroscopy[19] and found that the edge widened (E_o increased) as the DB defect density increased, in agreement with Cody et al.[8] The dashed line of Fig. 6 follows the comparison between the PA "α" and $k_B T/E_o$ as the sample is annealed to higher temperatures. The comparison is complicated by the faster decay noted for the lower-defect-density material, but the trend to slower PA decay with increasing E_o is confirmed.

We find it unlikely that PA and luminescence do not arise from the same population of electrons and holes because of the following considerations. (1) Assuming oscillator strengths of unity for the IR cross sections over the bandwidth used, we find a minimum estimate for the population observed when PA is at its highest (earliest) level. We obtain a value from an integrated absorption estimate[20] that is ~80% of that expected from the photoexcited carrier density. Coupled with an estimated luminescence efficiency of 50-100% in low-defect-density material, this argues against separate populations. (2) PA and luminescence have very similar temperature quenching dependences. (3) Similar PA maximum amplitudes near 10 nsec for all the samples support the argument that nearly all of the photoexcited population is being observed. (4) Luminescence recombination kinetics have been observed[21] to change from monomolecular to bimolecular at a photoexcited carrier density N_p of 1-2 $\times$ 10^{18} cm^{-3}. We have discovered[22] a similar change in recombination kinet-

ics at the same density of 1 $\times$ 10^{18} cm^{-3}, where the PA amplitude shifts from $N_p^{0.9}$ to $N_p^{0.5}$ with increasing excitation density. A more extensive study of this transition is in progress.

There may be another deep gap state more important in recombination than the DB since even at $N_s >$ 10^{18} cm^{-3} the recombination is slow. Evidence for other states exists in the light-induced Staebler-Wronski states,[23] the hole trap state deduced from photoconductivity,[24] and the hole trap states observed in a-Si:H:P.[25] The luminescence line due to oxygen is occasionally reported, but other impurities may exist at significant densities in a typical sample. Surface states may also play a role. Clearly, more work is needed.

In conclusion, our PA data show that the band tail of a-Si:H plays a more important role in the early recombination process than does the DB defect density and that DB defects are not fast recombination centers. We suggest another, more important recombination channel may exist, despite the difficulty of reconciling this with non-PA experiments that seem to imply otherwise. Luminescence does not detect carriers that do not radiatively recombine, and photoconductivity does not detect carriers immobilized in deep traps. PA is a complementary probe for studying the time evolution of the carrier population. If the DB defects are not important recombination centers, then other roles proposed for this state[26] must be more fully considered.

The Contribution of the Staebler-Wronski Effect to Gap-State Absorption in Hydrogenated Amorphous Silicon*

Reversible photoinduced changes in hydrogenated amorphous silicon (a-Si:H) have recently attracted attention.[23,27-34] The exact mechanism responsible remains to be fully elucidated. However, it is generally accepted that illumination creates metastable defects, which are annealed away by heating. An interesting question is how these photoinduced changes affect the optical absorption spectrum of the gap states in this material. The answer provides information on the number of states affected and, more important, gives the energy level at which these states reside in the gap. We have employed photothermal deflection spectroscopy[19] to investigate the contribution of these photoinduced defects to gap-state absorption.

The photothermal deflection spectroscopy technique has been described elsewhere.[19] Our samples were undoped, singly doped, and compensated films deposited by glow discharge. The illumination-annealing cycle consisted of exposing the a-Si:H films to 0.5 W/cm² of unfiltered light from a quartz tungsten-halogen lamp. Exposure time was typically 1.5 hours. Annealing was achieved by heating the films at 175°C for 1.5 hours in vacuum and in total darkness.

Figure 7 shows the effect of illumination upon the optical absorption of the undoped material. It can be readily seen that exposure to light enchances gap-state absorption. Furthermore, annealing at 175°C restores the magnitude of this absorption to its original value. Little or no change is seen in the Urbach tail absorption.

We showed earlier that the magnitude of gap-state absorption in a-Si:H correlate directly to the number of spins as determined by ESR and that these states are due to silicon dangling bonds.[7] Since illumination yields a qualitatively similar absorption spectrum, with the only difference being the increase in the absorption of gap-states, one can employ the procedure described in Ref. 7 to calculate the number of photoinduced spins, ΔN_s, in the various samples we investigated. In Fig. 8 we plot the optically-deduced ΔN_s for singly doped and compensated materials as a function of dopant concentration. As can be seen, for singly doped material, the photoinduced spins increase in density with increasing dopant concentration. The compensated material exhibited a light-induced enhancement comparable to that measured in the undoped films.

Figure 8. Photoinduced change in spin density as a function of doping: open squares, boron; open circles, phosphorus; triangle, compensated (10^{-3} P, 10^{-3} B in vapor phase); filled circle, undoped. (XBL 837-10556)

From our results, we deduce that illumination appears to increase the density of those states residing ~1.2–1.3 eV below the conduction band. This conclusion holds for all of our samples, implying that the photoinduced metastable defect is probably the same for the doped and the undoped materials.

Given our earlier finding that the maximum in the density of state 1.2–1.3 eV below the conduction band is due to Si dangling bonds, we tentatively conclude that the observed photoinduced enhancement in gap-state absorption is caused by an increase in the number of these Si dangling bonds. This conclusion is further supported by ESR and field-effect data.[29,33] Illumination apparently break the "weak" Si-Si bonds, which is followed by the relaxation of the surrounding network.

We would like to point out, however, that the photoinduced increase in the density of states near midgap does not uniquely imply the creation of additional dangling bond defects. A shift in the Fermi level, without any increase in the number of gap states, will also result in apparent increase in the number of these states. Clearly, more work is needed in order to understand the origin of the photoinduced metastable gap state.

Figure 7. The effect of illumination on the absorption spectrum of undoped a-Si:H. (XBL 836-10266)

NOVEL LASER SYSTEMS*

Our research activities sometimes require the development of new laser systems to meet a specific need. Of current interest to us is the generation of subpicosecond tunable laser pulses for probing elementary excitation in amorphous photovoltaic semiconductors. We also have a long-standing interest in laser waveguides that would provide high power, compactness, and ruggedness.

Highly Efficient, Widely Tunable Double Mode-Locked Dye Laser†

With the advent of synchronously pumped dye lasers,[35-38] picosecond spectroscopy is becoming widely investigated. Despite the difficulty of achieving subpicosecond operation, these dye lasers have the favorable characteristics of high average output power (~100 mW) and wide tuning range (~600 Å) in the picosecond regime. Conventional passively mode-locked dye lasers,[39-42] on the other hand, while generating shorter pulses, yield low output power (~10 mW) and have a relatively restricted tuning range (~200 Å).

We have developed a passively double mode-locked dye laser that produces subpicosecond pulses (0.5 psec) with high output power (~150 mW) and high conversion efficiency (5-10%) over a wide tuning range (~600 Å). In addition, through double mode-locking,[43,44] a highly synchronous secondary picosecond beam, tunable over a similar range, is generated at longer wavelengths.

Furthermore, we point out that, in the subpicosecond regime, passively mode-locked dye lasers are ultimately more efficient than their synchronously pumped counterparts, as demonstrated below.

A cw Ar^+ laser (5145 Å) pumped rhodamine 6G (R6G) laser is double mode-locked by a mixture of rhodamine 101 (R101) and cresyl violet (CV) in an independently tunable cavity configuration (Fig. 9). The following factors optimize the operation of this laser:

(1) Output coupler M_3 has a transmission value T of 3% to 10%, thus yielding high output coupling efficiency.

(2) The double mode-locking mixture R101/CV has an absorption spectrum that closely matches the gain spectrum of R6G, thus enabling easy tunability over a wide wavelength range.

(3) Cavity length L is kept at about 75 cm to avoid multiple pulse operation.

(4) The R6G jet is placed near the center of the cavity to maximize the gain for single-pulse operation.[45]

(5) The ratio of the radii of curvature R_4/R_1 of mirror M_4 and M_1, respectively, is kept high, resulting in a wide wavelength range of stable mode-locking.

(6) Folding angles are kept to the minimum possible to obtain good astigmatic compensation. Mode structure of the R6G beam is maintained as a good Gaussian.

(7) The angle between the two beams in the R101/CV jet is minimized to obtain maximum overlap.

(8) The thickness of the birefringent tuning filter (LF1) is sufficiently thin (0.375 mm) to suppress a red lasing tendency in the R6G cavity. This also results in less dispersion.

With these conditions satisfied and the cavity lengths matched, this double mode-locked dye laser provides 0.5 psec pulses (yellow) with a wide tuning range (570-630 nm), and high average power (~150 mW for 2-W pump power). Typical efficiencies of 5-10% for pump laser powers of 1-2.5 W are readily obtained, with a weak dependence on pulse width. To our knowledge, this is the highest output power and efficiency for a cw mode-locked subpicosecond dye laser ever reported. Excellent pulse stability and compact autocorrelation tracers are maintained over many hours of operation. Multiple and satellite pulsing problems are readily eliminated. Subpicosecond pulses are obtained near and also significantly above threshold. Finally, picosecond operation remains stable with no need to adjust the pump power or the cavity alignment while the birefringent tuning filter is continuously rotated over nearly the entire tuning range.

Assuming a $sech^2$ pulse shape, we measure a pulsewidth Δt of 500 femtoseconds. Pulsewidth-bandwidth products $\Delta\nu\Delta t$ are typically in the range of 0.5-1.0. Peak powers correspond to ~1.5 kW for a repetition rate of 200 MHz.

Through the double mode-locking process,[43] independently tunable picosecond pulses are synchronously[46,47] generated at a longer wavelength (red), tunable over 630-660 nm. With the output
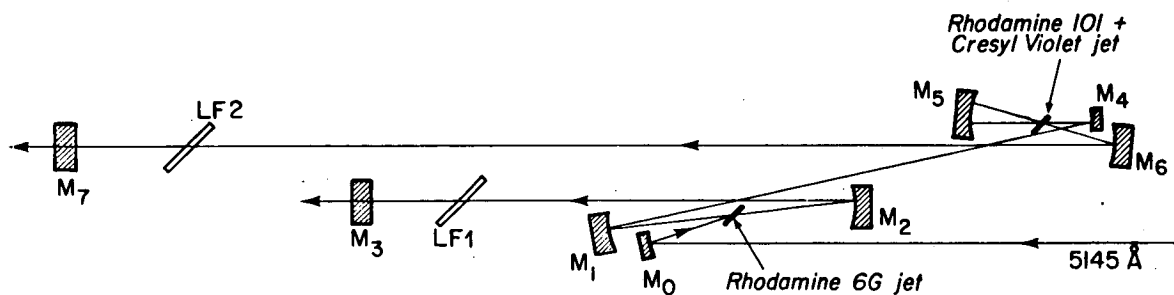
Figure 9. Cavity configuration of the independently tunable double mode-locked dye laser. M_1, M_2 and M_4 are R6G high reflectors (560–650 nm) with radii of curvature $R_1 = R_2 = 10$ cm and $R_4 = 3.5$ cm (or 5 cm). M_5 is a broadband high reflector with $R_5 = 2.5$ cm. M_6 is a red high-reflecting mirror (600–700 nm) with R_6 = 5 cm. M_3 and M_7 are output couplers: M_3 has $T = 3\%$ or 10% and M_7 has $T = 1\%$. LF1 and LF2 are single-plate birefringent filters. (XBL 823-296)

coupler of $T = 1\%$, typical average power for these red pulses was a few mW. The long wavelength limit was set by the coating characteristics on M5. In principle, the tuning range of the red beam should encompass most of the lasing spectrum of the R 101/CV mixture (620 nm–700 nm). In the present work, optimizing the red pulses was not attempted. We observed that as the shorter wavelength (yellow) was tuned towards 630 nm, the mode-locker ceases to lase, with the yellow beam remaining conventionally passively mode-locked.

Double mode-locked operation of this laser depends on the close matching of the lengths of the two cavities. For subpicosecond pulses, cavity lengths needed to be matched to within a few μm. At present, thickness fluctuations of the R6G jet is likely to be the main pulsewidth limiting factor. This independently tunable separate-cavity configuration provides for the correction of the inherent cavity mismatch (due to different group delays of the pulses in various optical elements) present in the collinear cavity configuration previously described.[44] Similar results of pulsewidth (yellow), output power, and tuning range were also obtained in the collinear configuration, indicating a dynamic compensation of the mismatch. The average power in the red beam was higher (~20 mW) in the collinear configuration, as contributed by the R6G gain. However, independent tunability is difficult to obtain. The present configuration also improves on the prism-tuned configuration[48] in that the thickness of the tuning elements can be kept smaller (less dispersion), while the cavity length is kept shorter to avoid multiple pulsing.

The absorption spectrum of the double mode-locking mixture is given in Fig. 10. The peak absorp-

tance corresponds to a single-pass, small-signal absorption of 8% (0.15-mm-thick jet) and a threshold pump power of ≈ 2 W for $T = 3\%$. The corresponding dye concentrations are 1.4×10^{-5} molar for R101 and 1.3×10^{-5} molar for CV. Also shown in Fig. 10 is the emission spectrum of R6G. The excellent matching of the two spectra is important for the demonstrated wide tunability.

In Fig. 11 we plot the output pulse energy and ultimate pulsewidth for an ideal (stable pump pulses, no cavity length perturbation, no dispersion) conventional synchronously pumped dye laser ($T = 50\%$, pump pulsewidth = 100 psec) as a function of cavity
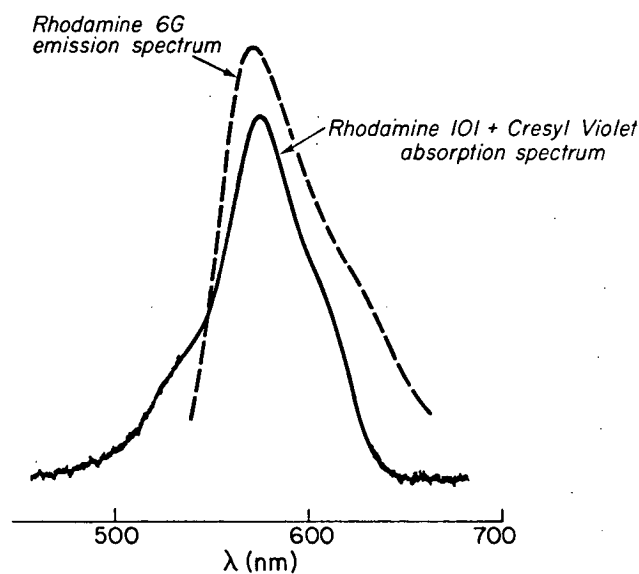
Figure 10. Absorption spectrum of the mode-locking mixture of R101/CV and the emission spectrum of R6G. Peak absorptance of R101/CV is ≈ 0.4 for a 1-mm path length. (XBL 823-295)
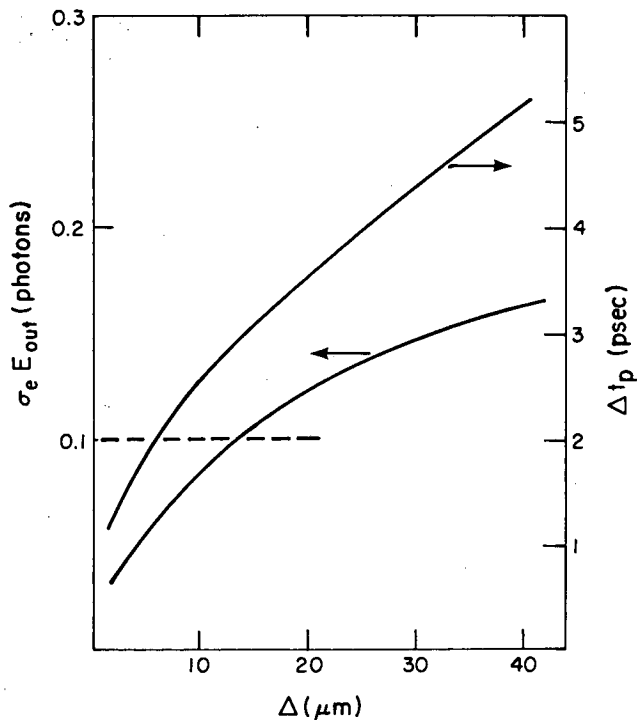
Figure 11. Pulsewidth and energy/pulse for synchronously pumped dye lasers (T = 50%, pump pulsewidth = 100 ps) vs. cavity mismatch. Also shown is a typical output energy value (0.1 photons) for a subpicosecond passively mode-locked dye laser pulse.　　　　　(XBL 823-286)

mismatch.[49] The pulsewidth and energy of the conventional passively mode-locked lasers depend upon parameters such as $S = F\sigma_a/\sigma_e$ (where F is the ratio of the focal spot areas in the two dye jets, σ_a is the absorption cross section of the mode-locking dye, and σ_e is the emission cross section of the laser dye), cavity length, threshold pump power, and the output coupler transmission. A typical energy/pulse for T = 3% under ideal conditions (no triplet losses, etc.) is $\sigma_e E_{out} \approx 0.1$ photons.[45] The corresponding pulsewidth depends on the cavity dispersion but can be in the subpicosecond range. This value is plotted in Fig. 11 as a straight line. It can readily be seen that the pulse energy of synchronously pumped dye lasers decreases significantly as the pulsewidth decreases, to below the pulse energy value for passively mode-locked lasers in the subpicosecond regime.

Hence, Fig. 11 depicts the generally unrecognized fact that, despite its apparent higher losses, the passively mode-locked dye laser has pulse-compression dynamics in its cavity such that *subpicosecond pulses of higher energy can be stably sustained,* as

compared to a conventional synchronously pumped dye laser. In the latter case, only a small fraction of the available gain is usable for sustaining a subpicosecond pulse,[49] the remainder being lost to fluorescence or to the generation of spurious satellite pulses. Pulses of higher energy become stable in a synchronously pumped dye laser cavity only at the expense of a broadened pulsewidth.

The extent of the role of the double mode-locking process (lasing of the mode-locking dye) in the demonstrated high efficiency of our system remains to be fully understood. However, there is a strong indication that this phenomenon enables stable subpicosecond operation at high values of S, which also correspond to higher pulse energies.[46] On the other hand, for conventional passively mode-locked dye lasers, there exists theoretical[45] and experimental evidence that S must not reach very high values, particularly for long cavity lengths; this may result in lower pulse energies. The wide tuning range of our double mode-locked laser provides further evidence in support of this argument.

In summary, a highly efficient cw double mode-locked dye laser has been developed. In addition to generating widely tunable, compact subpicosecond pulses with high power, a highly synchronous and independently tunable pulse is simultaneously generated at a longer wavelength. This two-color cw ultra-short pulsed laser source should prove to be a versatile tool for excite-and-probe experiments in picosecond spectroscopy.

Waveguide Laser Physics

Waveguide gas lasers, in which the beam propagates as a guided wave in a hollow dielectric tube, are of increasing technological and commercial importance. Practical waveguide lasers fall into two categories: (1) internal-mirror lasers, in which the mirrors forming the optical resonator are inside the vacuum enclosure, where they can be placed very close to the ends of the waveguide; and (2) external-mirror lasers, in which the vacuum enclosure terminates in Brewster-angle windows.

The mirrors in internal-mirror lasers can be flat because the beam spreads out very little in propagating the short distances from the ends of the waveguide to the mirrors and back, keeping the diffraction losses very low. However, in external-mirror lasers, short-radius concave mirrors must be used to refocus the diverging beam into the ends of

the waveguide. For CO_2 waveguide lasers, typical mirror radii of curvature are in the 10–40 cm range; these must generally be custom-made and can be quite expensive.

We have investigated, theoretically and experimentally, how low cavity losses might be obtained using ordinary flat mirrors placed significant distances from the ends of the waveguide, as in external-mirror lasers. Our theoretical treatment involves finding the eigenvalues of a matrix describing the effects on the beam of propagating one round trip through the cavity. This matrix is a product of a number of other matrices representing various portions of the round trip, such as one describing the phase shifts and attenuations of the waveguide modes in propagating through the tube, another for transforming the waveguide modes to a set of free-space modes to describe propagation to the mirror and back, and so forth. In a major improvement over previous theoretical analyses of waveguide laser resonators, we have replaced most of the numerical integrations used by previous authors with analytical transformations, greatly reducing the amount of computer time required.

For a wavelength laser cavity formed by flat mirrors at equal distances d from the ends of a hollow circular dielectric waveguide of length L and radius a, operating at wavelength λ and having propagation constant $k = 2\pi/\lambda$, we find that low loss cavity configurations occur along the curves in Fig. 12(a). These curves are labeled with a parameter Re ν_n/ka, which is a measure of the waveguide losses;

$$\nu_n = \frac{\nu^2 + 1}{2(\nu^2 - 1)^{1/2}}$$

where ν is the complex refractive index of the waveguide material. Within the waveguide, the beam propagates mainly as a combination of the HE_{11} and HE_{12} modes. When the beam emerges into the free-space region, these modes couple strongly to the TEM_{00} and TEM_{10} Laguerre-Gaussian modes, respectively, for a particular optimal choice of the spot size w_0. These latter two free-space modes both diverge as they propagate from the waveguide to the mirror and back again, but if they have the proper relative phase when launched, the relative phase shift they undergo in propagating through the free-space region will result in a destructive interference in the outer part of the beam and a constructive interference near the center when the beam reenters the waveguide, so that most of the power is concentrated within a

small radius and couples back into the waveguide. The curves along which cavity losses are minimized are approximately those for which the sum of the HE_{12}–HE_{11} phase shift in the waveguide plus the TEM_{10}–TEM_{00} phase shifts in the free-space regions is 2π (or a multiple thereof). Some experimental points on the optimum d vs. L curve are also included in Fig. 12(a), and it is seen that they agree reasonably well with theory, although they are displaced upward slightly. The parameter ν_n is not known for our laser.

If we calculate the minimum loss along the curves in Fig. 12(a) as a function of the mirror distance d, we obtain the curves in Fig. 12(b). We see that as long as $d/ka^2 \lesssim 0.1$, cavity losses generally remain low, not greatly exceeding the (unavoidable) losses due to the waveguide alone. For a CO_2 waveguide
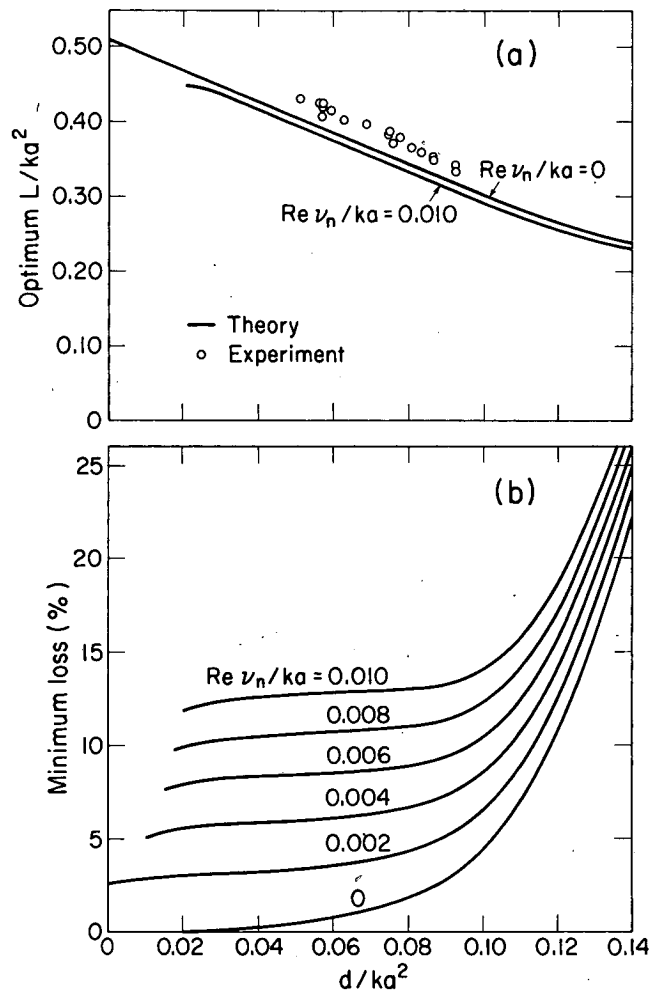
Figure 12. (a) Optimum cavity configuration as a function of d/ka^2; curves from theoretical calculations show good agreement with experimental results. (b) Theoretical minimum diffraction loss along the curves in (a) as a function of mirror distance d. (XBL 836-1868)
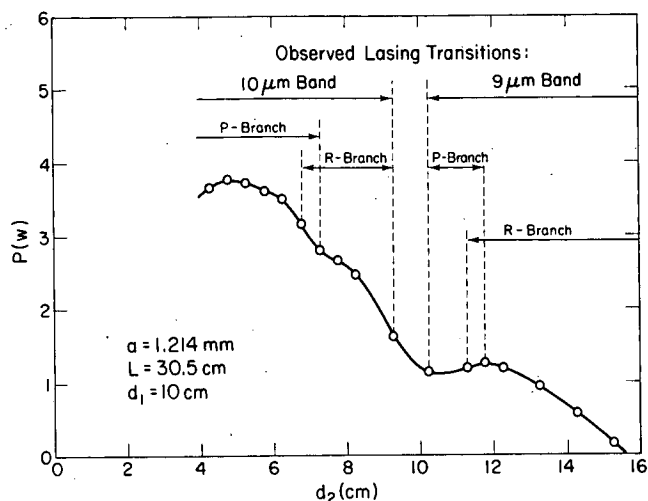
Figure 13. Experimental data showing wavelength selectivity obtained by varying mirror position in an asymmetric cavity. (XBL 836-1869)

laser operating at 10.5 μm and having a typical bore diameter of 2 mm, this corresponds to $d \lesssim 6$ cm, which is a very practical mirror distance for an external-mirror waveguide laser.

We have also analyzed asymmetric laser cavities, for which the mirror distances d_1 and d_2 are unequal. For a given waveguide length L, we find that low losses occur approximately along a straight line: i.e., $d_1 + d_2 =$ constant; we have confirmed this experimentally. We have also found that by varying the position of one of the mirrors, we can exert a coarse wavelength tuning on the cavity, sufficiently selective to determine which of the four possible band-branches in the 9–11 μm region the laser operates on. Some experimental data demonstrating the wavelength selectivity appear in Fig. 13. As we varied one mirror distance d_2 while holding the other distance d_1 fixed, we observed a variation in output power and also a switching by the laser from one branch to another, consistent with the predictions of our theory.

A paper presenting the details of these results will be published shortly. We are also working on extending our theoretical analysis to resonators using curved mirrors, since the greater efficiency of replacing numerical methods with analytical ones will be useful there as well as for flat-mirror resonators.

PLANNED ACTIVITIES FOR FY 1983

In the area of laser photothermal spectroscopy and detection, emphasis will continue to be placed on unambiguous remote sensing of atmospheric constituents. Methods to overcome atmospheric turbulence and speckle will be investigated. Pulsed photothermal displacement spectroscopy will be studied, and extensions of this technique for the study of liquids will be devised. Nonlinear photoacoustic spectroscopy of gases will be initiated.

Research on amorphous semiconductors will focus on the physics of defects in hydrogenated amorphous silicon and germanium. The elucidation of the nature of the metastable photoinduced defects in amorphous silicon will continue to be of interest to us.

A new activity will be the investigation of surface and interface states of semiconductors. In addition, processes at the liquid-semiconductor and gas-semiconductor interfaces will be studied.

Finally, we will continue our research on laser physics and technology with the goal being the production of widely tunable, high-average-power pulses a few femtoseconds wide.

REFERENCES

1. See, for example, H. Lüth (1975), *Appl. Phys. 8*, p. 1.

2. Olmstead, M.A., Amer, N.M., Kohn, S., Fournier, D., and Boccara, A.C., submitted to *Appl. Phys. A*.

3. Other photothermal techniques include photoacoustic spectroscopy—see, for example, *Optoacoustic Spectroscopy and Detection*, Y.-H. Pao, Ed., Academic Press, New York, 1977; W.B. Jackson and N.M. Amer, *J. Appl. Phys. 51*, p. 3343 (1980)—and photothermal deflection spectroscopy (see Ref. 19, below). However, these techniques are not suited for experiments which require UHV or a wide range of temperatures.

4. See, for example, Fritzsche, H. (1980), *Solar Energy Mater. 3*, p. 447, Street, R.A. (1981), *Adv. Phys. 30*, p. 593, and references within.

5. Tsang, C., and Street, R.A. (1979), *Phys. Rev. B 19*, p. 3027; Street, R.A., Knights, J.C., and Biegelsen, D.K. (1978), *Phys. Rev. B 18*, p. 1880.

6. Johnson, A.M., et al. (1981), *Phys. Rev. B 23*, p. 6816.

7. Jackson, W.B., and Amer, N.M. (1982), *Phys. Rev. B 25*, p. 5559.

8. Cody, G., et al. (1981), *Phys. Rev. Lett. 47*, p. 1480.

9. Jackson, W.B. and Amer, N.M. (1982), *J. Phys. (Paris) 42*, p. C4-293.

10. Schockley, W., and Read, T. (1952), *Phys. Rev. 87*, p. 835.

11. Orenstein, J., and Kastner, M.A. (1981), *Phys. Rev. Lett. 46*, p. 1421, and *Solid State. Comm. 40*, p. 85; Tiedje, T., and Rose, A. (1980), *Solid State. Comm. 37*, p. 49.

12. Ray, S., et al. (1981), in *Tetrahedrally Bonded Amorphous Semiconductors—1981*, R.A. Street, D.K. Biegelsen, and J.C. Knights, Eds., AIP Conference Proceedings No. 73, American Institute of Physics, New York, p. 253.

13. Ray, S., Vardeny, Z., and Tauc, J. (1981), *J. Phys. (Paris) 41*, p. C4-555.

14. Tiedje, T., Cebulka, J.M., Morel, D.L., and Abeles, B. (1981), *Phys. Rev. Lett. 46*, p. 1425.

15. O'Connor, P. and Tauc, J. (1980), *Solid State Comm. 36*, p. 947.

16. Wake, D.R., and Amer, N.M., to be published.

17. We have not spectrally resolved the luminescence but have confirmed that the luminescence is quenched in our high-defect-density samples and that the temperature dependence of the high-defect-density luminescence is substantially weaker, as expected.

18. Pankove, J.I., and Carlson, D.E. (1976), *Appl. Phys. Lett. 29*, p. 610, and Engeman, D.E. and Fischer, R. (1977), *Phys. Status Solidi(b) 79*, p. 195; however, R.A. Street has pointed out that charged defects are unlikely to provide sufficiently strong homogeneous fields (private communication).

19. Jackson, W.B., Amer, N.M., Boccara, A.C., and Fournier, D. (1981), *Appl. Optics 20*, p. 1333.

20. Following the procedure of Ref. 9.

21. Rehm, W., and Fischer, R. (1979), *Phys. Status Solidi(b) 94*, p. 595 (1979); Shah, J., Bagley, B.G., and Alexander, F.B., Jr. (1980), *Solid State Comm. 36*, p. 199.

22. Wake, D.R., and Amer, N.M., to be published.

23. Staebler, D.L. and Wronski, C.R. (1980), *J. Appl. Phys. 51*, p. 3262.

24. Persans, P.D., (1980), *Solid State Comm. 36*, p. 851; P.E. Vanier and Griffith, R.W. (1982), *J. Appl. Phys. 53*, p. 3098.

25. Vardeny, Z., Strait, J., Pfost, D., and Tauc, J. (1982), *Phys. Rev. Lett. 48*, p. 1132.

26. Depinna, S.P., Cavenett, B.C., Austin, I.G., and Searle, T.M. (1982), *Solid State Comm. 41*, p. 263.

27. Staebler, D.L., and Wronski, C.R. (1977), *Appl. Phys. Lett. 31*, p. 292.

28. Jousse, D., Basset, R., Deliouibus, S., and Bourdon, B. (1980), *Appl. Phys. Lett. 37*, p. 208.

29. Dersch, H., Stuke, J., and Beichler, J. (1981), *Appl. Phys. Lett. 38*, p. 456.

30. Pankove, J.I. and Berkeyheiser, J.E. (1980), *Appl. Phys. Lett. 37*, p. 705.

31. Lang, D.V., Cohen, J.D., Harbison, J.P., and Sargent, A.M. (1982), *Appl. Phys. Lett. 40*, p. 474.

32. Solomon, I., Dietl, T., and Kaplan, D. (1978), *J. Physique 39*, p. 1241.

33. Goodman, N.B. (1982), *Phil. Mag. B45*, p. 407; Tanielian, M.H., Goodman, N.B., and Fritzsche, H. (1981), *J. Phys. (Paris) 42*, p. C4-293.

34. Morigaki, K., et al. (1980), *Solid State Commun. 33*, p. 851.

35. Heritage, J.P., and Jain, R.K. (1978), *Appl. Phys. Lett. 32*, p. 727.

36. Ferguson, A.I., Eckstein, J.N., and Hansch, T.W. (1978), *J. Appl. Phys. 49*, p. 5389.

37. Kuhl, J., Klingenberg, H., and von der Linde, D. (1979), *Appl. Phys. 18*, p. 279.

38. Ryan, J.P., Goldberg, L.S., and Bradley, D.J. (1978), *Opt. Commun. 27*, p. 127.

39. Ippen, E.P., Shank, C-V., and Dienes, A. (1972), *Appl. Phys. Lett. 21*, p. 348.

40. Ruddock, I.S., and Bradley, D.J. (1976), *Appl. Phys. Lett. 29*, p. 296.

41. Diels, J.C., Van Stryland, E., and Benedict, G. (1978), *Opt. Commun. 25*, p. 93.

42. Rosen, D., et al. (1981), *J. Quantum Electron. QE-17*, p. 2264.

43. Yasa, Z.A., and Teschke, D. (1975), *Appl. Phys. Lett. 27*, p. 446, and Yasa, Z.A. (1975), *J. Appl. Phys. 46*, p. 4895.

44. Yasa, Z.A., Dienes, A., and Whinnery, J.R. (1977), *Appl. Phys. Lett. 30*, p. 24.

45. Yasa, Z.A. (1976), Ph.D. Thesis, University of California, Berkeley.

46. Bourkoff, E., Dienes, A., and Whinnery, J.R. (1979), *Appl. Phys. Lett. 34,* p. 455.

47. Arjavalingam, G., Dienes, A., and Whinnery, J.R. (1982), *Opt. Lett. 7,* p. 193.

48. Bourkoff, E. and Whinnery, J.R. (1979), *Opt. Lett. 4,* p. 179.

49. Yasa, Z.A. and Amer, N.M., to be published.

OIL SHALE WASTEWATER TREATMENT: EFFECT OF OZONATION AND UV IRRADIATION ON BIOREFRACTORY ORGANIC SOLUTES*

B.M. Jones, G.W. Langlois, R.H. Sakaji,
J.F. Thomas, and C.G. Daughton[†]

Wastewaters from the pilot-scale retorting of oil shale have been tremendously variable in their chemical characteristics, but in general retort water is characterized by a complex spectrum of polar and nonpolar organic solutes in extremely high concentrations. The major classes of organic compounds include alkanes, carboxylic acids, polyhydric phenols, and nitrogenous and oxygenated heterocycles. The extreme levels of contaminative organic solutes, the presence of surfactants, suspended oil, tars, and particulates, the possibility of toxicity to microorganisms, the high level of dissolved inorganic salts and gases, and the undersirable color and odor of these wastes—all frustrate both the application of established pollution control technologies and the determination of treatment performance by standard analytical methodologies. To minimize intrasample variation and to allow for interlaboratory comparison of experimental results, our research has concentrated on composited samples of modified in-situ (MIS) retort water and gas condensate from Occidental Oil Shale Company's retort burn No. 6 (Oxy-6).[1]

Biological treatment is the conventional method of removing organic contaminants from a wastewater stream. An acclimated microbial community can convert dissolved organic solutes into cellular biomass, heat, and gases. This scheme can fail, however, if

    (a)   the resultant cells are not separable from the liquid,

    (b)   nutrients essential for growth are not available in the solution,

    (c)   components of the medium are toxic to the microorganisms,

    (d)   the microorganisms are enzymatically incapable of mineralizing the organic material, or

    (e)   many of the compounds are inherently resistant to microbial alteration.

Biological treatment of Oxy-6 retort water is initially limited by inorganic orthophosphate.[1,2] Paradoxically, the nutrient that subsequently limits microbial growth is carbon, even though repeated studies have shown that about half of the dissolved organic carbon (DOC) remains after exhaustive biological treatment[2]; adding trace elements does not elicit further growth or DOC removal. Secondary growth is observed, however, when these same cultures are supplemented with an exogenous source of easily degraded carbon such as aliphatic carboxylic acids.[2] Nitrogen and oxygen heterocycles and aromatic amines have been implicated[3] as the major chemical classes accounting for the extraordinary recalcitrance of organic carbon in the extracellular fluid (i.e., spent retort water) that remains after exhaustive biooxidation. This hypothesis has been strengthened by several reports on the chemical characterization of Oxy-6 retort water extracts[4] indicating the presence of numerous aromatic amines and unsaturated, oxygenated nitrogen heterocycles, each at low part-per-million concentrations.

Successful treatment of oil shale wastewater undoubtedly will require using more than one technology. A particular method may be extremely effective in removing a specific class of organic compounds, but, in a heterogeneous mixture such as retort water, this class may represent only a fraction of the contaminative solutes. Effective treatment will require a combination of methods that yield complementary or enhanced performance when used simultaneously or in sequence. The integration of these processes should be evaluated carefully because the final degree of treatment could be additive (the sum of the individual processes), synergistic (greater than the sum of the processes), antagonistic (lower than any of the processes), or a combination thereof.

Ozonation and ultraviolet (UV) irradiation were investigated as pretreatment methods to augment or

enhance the biological treatment of oil shale wastewaters by mineralizing or oxidatively altering organic solutes that are biorecalcitrant or bactericidal. It was also possible that these processes could, instead, hinder biooxidation by producing toxicants, polymerizing solutes that would ordinarily be biodegradable, or creating a multitude of new solutes, each present at a low concentration; the latter possibility would amplify an already existing problem. The effects of ozonation and UV irradiation could, in any case, be used as a predictor of the maximum capacity of aerobic biooxidation achievable through oxygenases.[5] The extent of oxidation from UV irradiation can also give an indication of the photochemical alterations to be expected during storage of these waters in ponds at the high elevations typical of western oil shale deposits.

BACKGROUND

UV Irradiation

The degradation of organic solutes by exposure to UV radiation occurs by three mechanisms: (1) sufficient radiant energy is absorbed to cleave intramolecular bonds, producing lower-molecular-weight fragments; (2) reactive organic free radicals are generated; and (3) interaction of these free radicals with molecular oxygen produces peroxy and hydroperoxy radicals, which are capable of structural alteration or complete mineralization of the lower-molecular-weight fragments by oxygenation, hydrogen abstraction, or the initiation of chain reactions.[6-8] Furthermore, the photolysis of endogenous organic compounds in natural surface waters has been shown to generate hydroxyl radicals (OH·) and singlet oxygen, both capable of subsequently transforming synthetic organic solutes.[9]

A more efficient use of UV radiation than direct mineralization may be as an aid to biooxidation; thus oxygenated or fragmented, otherwise biorefractory molecules may become amenable to biodegradation. UV radiation has been implicated in the degradation of pesticides in the environment[6] and in aiding the biodegradation of certain synthetic polymers.[10]

Photooxidation characteristically produces a variety of products from a given reactant and each of these products may vary in its susceptibility to microbial metabolism.[11] This plethora of products is especially significant with respect to the photooxidation of oil shale wastewaters. Two factors[12] that exacerbate

the refractory nature of the substituted heterocyclic compounds in spent retort water are (1) the presence of numerous heterocycle homologs and variants, each of which can require a specialized catabolic enzyme system, and (2) the low individual heterocycle concentrations,[4] which, being below the affinity or threshold values, render the enzymes ineffective. Although photooxidation may generate more degradable solutes, it may also exacerbate the purported problems of enzyme specificity and threshold-concentration effects.

Ozonation

Ozone is a very selective and highly versatile oxidizing agent; it is used not only in organic chemistry, but as a disinfectant for potable water and as a wastewater treatment aid. In an aqueous solution, the oxidative capacity of ozone appears to depend on pH and the organic and inorganic solute concentrations. For acidic and slightly alkaline solutions (pH less than 9.0), ozone reacts predominantly as the parent ozone molecule; these reactions are relatively slow and highly specific, depending on the class and bonding structure of the organic reactant. Furthermore, oxidation by ozone is reportedly almost entirely ineffective in highly acidic aqueous solutions (pH below 2.0).[13] In contrast, ozone is catalytically decomposed by hydroxide ion (pH greater than 10.0) to a variety of products, including OH· and superoxide ion.

The hydroxyl radical is the most potent and effective oxidant known to occur in aqueous solutions,[14] having an oxidation potential of 2.8 V (H^+ = 1.0 M) compared with 2.07 V for ozone in acidic solutions and 1.36 V for chlorine gas.[15] At a pH of 10.5, approximately one-half mole of OH· is formed per mole of O_3 decomposed.[14]

Hydroxyl radicals are extremely reactive and easily oxidize organic material; they react with inorganic solutes with little substrate specificity. They are quickly consumed (within microseconds), but their intense reactivity makes them critically important to aqueous ozone chemistry.[16] Hydroxyl radicals are vigorously scavenged by carbonate ion and, to a lesser extent, by bicarbonate species; scavenging accelerates the disproportionation of ozone to its reactive decomposition products,[17] but decreases the oxidative capacity by quenching chain reactions. Free ammonia can be oxidized to nitrate by ozone and OH·, but this reaction will be significant only

when ammonia concentrations are equal to those of carbonate species and organic solutes.[18]

Retort water often contains high ammonia and dissolved inorganic carbon (DIC) concentrations, both of which scavenge or react with ozone or ozone-disproportionation products. Furthermore, substituted nitrogen heterocycles, a major biorefractory organic chemical class is spent retort water, are not particularly susceptible to attack by ozone, unlike most non-nitrogen heterocycles. Pyridine reacts extremely slowly, and ozone preferentially attacks the carbocyclic ring of quinoline.[19]

A preliminary examination of the effect of ozone on Oxy-6 oil-shale retort water showed that high alkalinity interferes with the oxidation of organic compounds; pretreatment with powdered activated carbon (PAC), however, reduces the alkalinity and appears to increase the effectiveness of ozonation.[20] A second study used ozonation and ammonia stripping as preliminary steps before PAC-aided biooxidation of Oxy-6 retort water.[21] The results of these experiments revealed that low dosages of ozone (70 mg/l) appear to slightly increase the biodegradability of Oxy-6 retort water. Ozonation also removes much of the color, indicating that some of the nitrogen heterocycles may have been oxidized. Following extensive integrated treatment, the major portion of the base/neutral organic compounds was not altered or mineralized. The predominant refractory chemical groups were unsaturated, oxygenated nitrogen heterocyles, especially pyrrolidinones, piperidinones, cyclohexanopyrrolidinones, and cyclopentanopiperidinones.

Partial oxidation or cleavage of ozonation of complex high-molecular-weight organic compounds (which are commonly biorefractory) into polar, oxygenated, lower-molecular-weight fragments can substantially affect biodegradability.[22] The benefit of partial oxidation has been shown for nonbiodegradable water-soluble polymers.[23] Ozonation of polyethylene glycol, polyvinyl alcohol, polyvinylpyrrolidone, and sodium polyacrylate reduces the molecular weights and improves biooxidation.

Chemical oxidation by ozone or by ozone-decomposition radicals can also be used to predict the extent of oxidation of biorefractory organic solutes in retort water by acclimated bacteria with competent oxygenase enzyme systems. Ozonation can therefore be viewed as a facile means for predicting the maximum theoretical degree of oxidation that could be effected by aerobic biological treatment.

Combined UV Irradiation/Ozonation

UV radiation catalyzes the disproportionation of ozone into OH·,[19] and superoxide ion, and promotes the production of organic free radicals. In contrast to hydroxide-ion mitigated ozone decomposition, ozone disproportionation by UV radiation is not restricted to the alkaline pH range. The existence of ozone decomposition products at acidic and neutral pH ranges precludes carbonate scavenging and ammonia oxidation due to shifts in the ion equilibria; this is a major advantage of the combined UV/ozone approach. In addition, chemical reactions mediated by UV/ozonation are significantly faster in the acidic than in the basic pH range.[24] Combined UV/ozonation has been reported as superior to either treatment alone for the elimination of biorefractory organic solutes from water and for the treatment of industrial wastewaters.[17,19,25] Mineralization of refractory organic species by simultaneous UV/ozonation has been extensively reviewed.[26]

Combined ultraviolet irradiation and ozonation as a pretreatment to biooxidation may be more economical than complete chemical mineralization of refractory compounds. Structural alterations of solutes effected by a brief exposure to UV/ozone may be sufficient to allow acclimated microorganisms to mineralize a significant portion of the formerly recalcitrant solutes. Preliminary experiments show that some pesticides and industrial wastes can be sufficiently altered by UV/ozone treatment to make them degradable by acclimated soil microbiota.[27] Perhaps the major drawback to this approach with respect to oil shale wastewaters is that, in a manner analogous to UV photolysis, both combined UV irradiation/ozonation, and ozonation alone create multiple products from each oxidizable compound, complicating subsequent treatment.[17,28]

In addition to its role as a pretreatment to biooxidation, the chemical alterations effected by UV/ozonation may also model the degradative potential of microbial systems. If OH· produced by combined UV irradiation/ozonation is unable to completely mineralize refractory organic solutes in a waste stream, then it is unlikely that microbial oxygenases would be effective.

ACCOMPLISHMENTS DURING FY 1982

As part of the Oil Shale Project's waste treatment research, ozonation and UV irradiation were evaluated both for their ability to directly oxidize organic solutes and for their indirect influence on biodegradability through minor structural alterations of refractory compounds in Oxy-6 retort water. Possible mechanisms of organic solute alterations were investigated by determining organic carbon[29] in reverse-phase fractions[30] of time-course samples.

UV Irradiation

Short exposure to intense UV radiation was insufficient to mineralize or alter the recalcitrant compounds in raw or spent retort water. The results of extensive UV irradiation of spent Oxy-6 retort water followed by biological treatment are presented in Fig. 1. The lower graph is the cumulative UV energy sup-
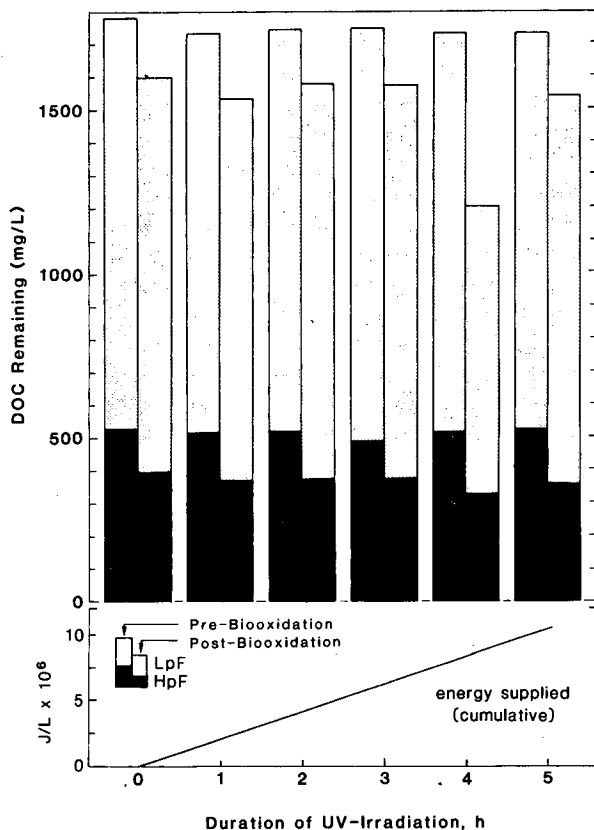

Figure 1. Biooxidation of UV-pretreated spent Oxy-6 retort water. Left bar of each pair shows dissolved organic carbon after UV irradiation; right bar, after subsequent biological treatment. Lower chart shows UV energy supplied. HpF = hydrophilic fraction (polar organic solutes); LpF = lipophilic fraction (nonpolar organic solutes).

(XBL 832-8321)

plied to the photoreactor. Each pair of bars represents a sample withdrawn from the photoreactor at hourly intervals. For each pair, the first bar is the DOC concentration remaining after UV irradiation, and the second bar is the DOC concentration after subsequent biological treatment. The solid portion of each bar is the DOC concentration of the polar organic solutes (hydrophilic fraction, HpF), and the remaining portion is the concentration of the less-polar solutes (lipophilic fraction, LpF).[30] Five hours of intensive irradiation did not mineralize a significant amount of DOC (<2%), remove the chromophoric substances that give retort water its characteristic color, or change the relative polarities of the organic constituents. Furthermore, UV irradiation did not appear to structurally alter the biorefractory organic compounds; biooxidation after photochemical pretreatment did not mineralize additional carbon compared with nonirradiated reinoculated control cultures (i.e., the difference in DOC for each pair of bars was equivalent to the control).

Ultraviolet irradiation of retort water may have been ineffective because of the presence of photooxidation inhibitors.[31] Particulate and colloidal carbonates can protect organic solutes from the effects of UV irradiation,[7] and the high concentrations of these species in this retort water may have prevented photoalterations. In addition, the chromophoric solutes of the water may have absorbed a significant amount of the UV radiant energy, preventing effective penetration into the water.

Ozonation

When low dosages of ozone gas were sparged through raw or spent retort water for short periods, the DOC concentration was not substantially reduced, nor were the structures of the biorefractory organic solutes altered. The effects of extensive ozonation of spent retort water are presented in Fig. 2; the lower graph represents the cumulative amount of ozone consumed. Although 5 hours of ozonation (7.1 mg/l-min) resulted in total ozone consumption and solubilization of more than 1.6 g/l, only a small portion of the DOC was mineralized (4%). This portion, however, was primarily responsible for the color of spent retort water.

In contrast to the low dosages of ozone used in preliminary experiments, extensive ozonation of spent retort water altered a significant portion of the residual organic solutes; 14% of the DOC that was previ-
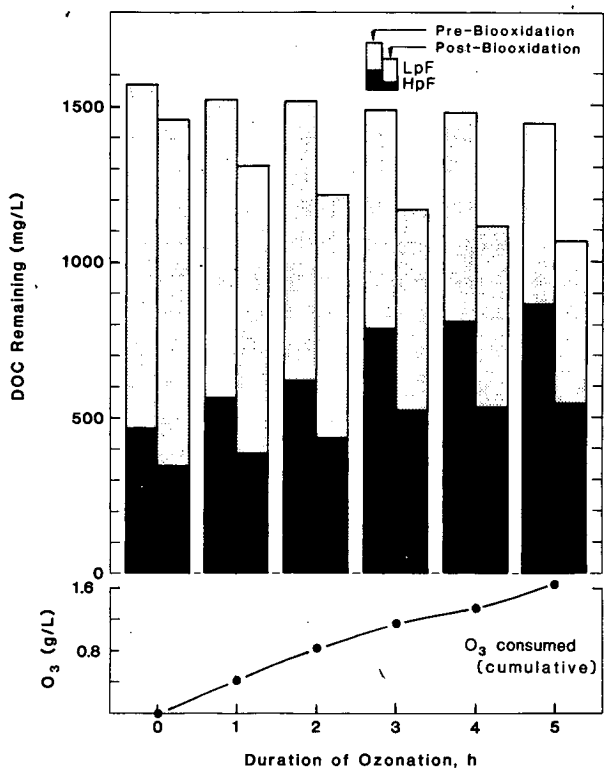
Figure 2. Biooxidation of ozone-pretreated spent Oxy-6 retort water. Bars as in Fig. 1. Lower chart shows ozone consumed. (XBL 832-8322)

ously recalcitrant became amenable to microbial mineralization. Of the DOC converted into biologically oxidizable structures (380 mg/l), approximately 320 mg/l, or 84%, was at the expense of carbon in the HpF. Despite this result, the DOC concentration in the HpF after biological oxidation of the 5-hour, ozone-treated sample was higher than in the time-zero, nonozonated, biologically treated sample (spent retort water); some of the more highly oxidized ozonation products became even less degradable.

Although prolific foaming is a major drawback to ozonation of raw retort water, foaming was not evident, when spent retort water was ozonated. This change probably resulted from the microbial mineralization of aliphatic carboxylic acids, which can act as surfactants. The possibility of excessive consumption of ozone or free radicals by unprotonated ammonia or carbonate ions had been minimized by stripping ammonia from raw retort water by vigorous aeration during primary biooxidation (the ammonia concentration after 100 hours of incubation was reduced from 86 mM to less than 2 mM) and by conducting the experiments at the unaltered pH of retort water, which is below 9.0.

The alteration of the refractory organic compounds and the elimination of the chromophoric substances most likely resulted from direct oxidation by the parent ozone molecule; the solution pH probably precluded the decomposition of ozone by OH⁻ into its highly reactive radicals. The susceptible solutes were gradually modified until the solution was devoid of these compounds, at which point ozone was no longer an effective oxidant.

Combined UV Irradiation/Ozonation

The organic solutes in raw and spent retort water were resistant to mineralization by short exposures to low dosages of ozone in conjunction with UV radiation, and subsequent biooxidation was not improved. In contrast, 6 hours of simultaneous ozonation and UV irradiation of spent retort water mineralized 20% of the organic carbon and appeared to significantly alter the remaining biorefractory compounds. These latter results are presented in Fig. 3; the lower graph shows the cumulative amount of both ozone consumed and UV energy supplied.

Extensive UV/ozone treatment initially either mineralized the LpF organic solutes or transformed them into HpF solutes; oxidation of compounds would
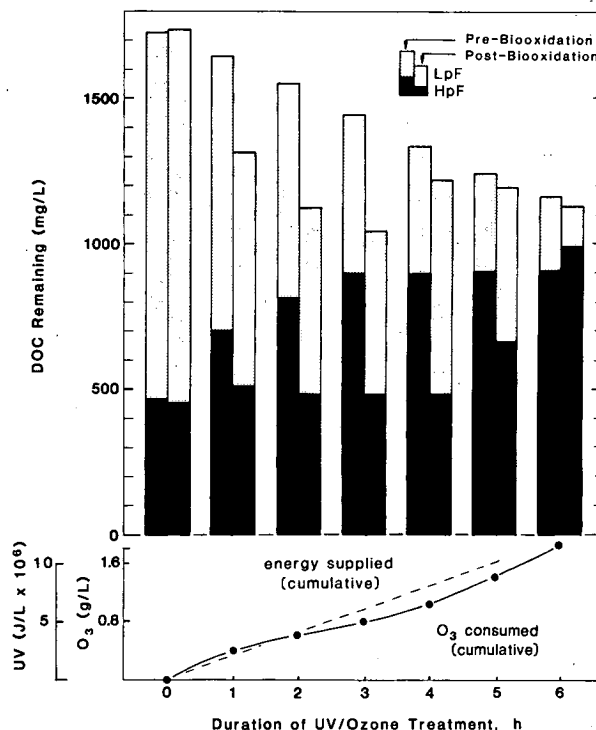

Figure 3. Biooxidation of UV/ozone-pretreated spent Oxy-6 retort water. Lower chart shows cumulative UV energy supplied and ozone consumed. (XBL 832-8323)

be expected to increase their polarities. After 3 hours of treatment, the LpF carbon continued to be mineralized, but further conversion to HpF carbon was not observed. The intense color of the spent retort water was almost entirely eliminated, and the usually persistent odor of the water became almost undetectable.

Three hours of intensive ozonation coupled with UV irradiation also effected considerable structural alterations of the organic solutes in spent retort water so that an acclimated microbial seed was able to use approximately 400 mg/l of DOC that was normally unavailable. This auxiliary biooxidation was entirely at the expense of newly created HpF organic compounds; biodegradability of retort waters seems to correlate with increasing content of HpF organic carbon.[30] The composition of the water following the serial application of biooxidation, three hours of UV/ozonation, and exhaustive secondary biological treatment was similar to that of spent water after 5 hours of ozonation followed by biotreatment.

Simultaneous UV/ozone treatment of spent water beyond 3 hours resulted in a reversal of the trend of increasing biodegradability. Further biodegradable HpF carbon was not generated, and the HpF that remained appeared to become biorefractory. After 6 hours of combined UV/ozonation of spent retort water, only 1% of the DOC was susceptible to microbial attack, although most of the remaining solutes comprised HpF carbon. For the 6-hour sample, the HpF carbon actually increased as a result of secondary biotreatment; the bacteria were growing at the expense of the LpF carbon and apparently altering a portion of this carbon to refractory HpF compounds. Microbial catabolic incompetence may not have been the only factor limiting the degradation of the remaining solutes; increased toxicity, threshold-concentration effects, or the lack of a specific nutrient or enzyme cofactor may have limited further mineralization of the DOC.

The LpF carbon from raw, spent, and UV/ozonated spent retort water was analyzed by gas/liquid chromatography for volatile nitrogenous organic compounds. Six hours of UV/ozonation eliminated most of the lower- and higher-molecular weight volatile nitrogen-containing compounds from the LpF (Fig. 4). In addition, the concentration of the intermediate-molecular-weight nitrogenous compounds in the LpF was greatly reduced. These compounds were either mineralized or transformed into HpF nitrogen-bearing compounds.
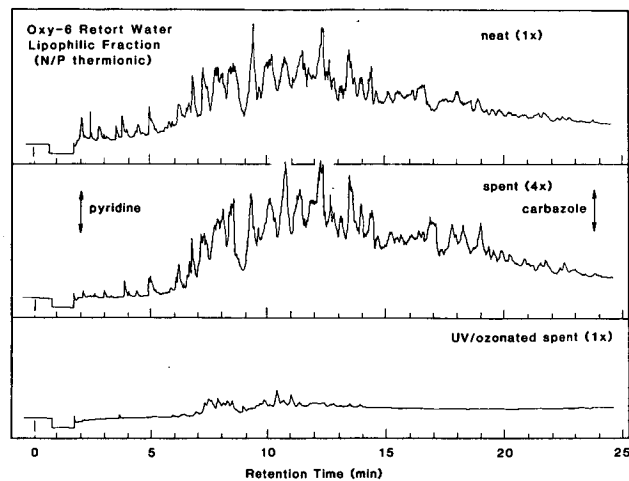
Figure 4. Gas chromatograms of raw, spent, and UV/ozone-treated spent Oxy-6 retort water (nitrogen-selective detection); the UV/ozone treatment has clearly eliminated most of the nitrogen-containing compounds from the lipophilic fraction. (XBL 832-8324)

Extensive UV irradiation combined with ozonation mineralized much of the DOC after 6 hours, but further biological treatment was unsuccessful. Although color and odor were nearly eliminated, 41% of the DOC of raw retort water remained after exhaustive serial treatment by primary biooxidation, UV/ozonation, and secondary biooxidation. The organic solutes that remained appeared to be refractory to both chemical and microbial oxidative alteration or mineralization. Other physicochemical methods that effect complementary treatment may be required to upgrade oil shale wastewaters for reuse or codisposal.

PLANNED ACTIVITIES FOR FY 1983

The nonspecific application of UV irradiation and ozonation may exacerbate the problems of bacterial enzyme specificity and solute threshold-concentration effects by producing a multitude of oxidation products, each varying in its susceptibility to microbial attack. UV irradiation and ozonation should be judged for their combined abilities to mineralize organic material, but their effect on the subsequent biotreatability of residual solutes should not be neglected.

Research will continue on the inability of microorganisms to degrade the organic solutes that remain in spent retort waters. Emphasis will be placed on inducing the enzyme systems required for the catabolism of nitrogen heterocycles. Data from the

exhaustive biotreatment of waters from a range of retorting processes may give an indication of the possible success or reasons for failure of this treatment method.

Fixed-film bioreactors or trickling filters have been used successfully to treat industrial wastes, and they hold promise for upgrading oil shale process waters for reuse. The use of spent or raw shale as a support for a fixed microbial film will be assessed.

Five analytical methods have been validated for oil shale process waters, and detailed operator protocols and background theories have been compiled in a recently completed manual.[32] A prerequisite of continued research on these process waters is the development of valid analytical methods for the determination of specific chemical classes, such as nitrogen heterocycles, and for the determination of solute molecular weight distributions. Such new methods will be reported in a subsequent edition of the manual.

REFERENCES

1. Jones, B.M., Sakaji, R.H., and Daughton, C.G., (1981), "Treatment of Wastewater from Modified In-Situ Oil Shale Retorting," in *Energy and Environment Division Annual Report 1980*, Lawrence Berkeley Laboratory Report LBL-11989.

2. Jones, B.M., Sakaji, R.H., Thomas, J.F., and Daughton, C.G., (1982), "Microbial Aspects of Oil Shale Wastewater Treatment," in *Energy and Environment Division Annual Report 1981*, Lawrence Berkeley Laboratory Report LBL-13500.

3. Daughton, C.G., Sakaji, R.H., and Jones, B.M., (1982), unpublished data, LBL-SEEHRL Oil Shale Waste Treatment Program.

4. Raphaelian, L.A., and Harrison, W., (1981), *Organic Constituents in Process Water from the In-Situ Retorting of Oil from Oil-Shale Kerogen*, Argonne National Laboratory Report ANL/PAG-5.

5. Jones, B.M., Langlois, G.W., Sakaji, R.H., and Daughton, C.G., (1982), "Ozonation and UV Irradiation: Effect on Oil Shale Wastewater Biorefractory Organic Solutes," LBL-SEEHRL Oil Shale Waste Treatment Program, Lawrence Berkeley Laboratory Report, LBID-549.

6. Crosby, D.G., (1972), "Environmental Photooxidation of Pesticides," in *Proceedings of the Conference on the Degradation of Synthetic Molecules in the Biosphere: Natural, Pesticidal, and Various Other Man-Made Compounds*, National Academy of Sciences, Washington, D.C., p. 260.

7. Manny, B.A., Miller, M.C., and Wetzel, R.G., (1971), "Ultraviolet Combustion of Dissolved Organic Nitrogen Compounds in Lake Waters," *Limnol. Oceanog., 16*, p. 71.

8. Plimmer, J.R., (1972), "Principles of Photodecomposition of Pesticides," in *Proceedings of the Conference on the Degradation of Synthetic Molecules in the Biosphere, p. 279.*

9. Mill, T., Hendry, D.G., and Richardson, H., (1980), "Free-Radical Oxidants in Natural Waters," *Science 207*, p. 886.

10. Jones, P.H., et al., (1974), "Biodegradability of Photodegraded Polymers: I. Development of Experimental Procedures," *Environ. Sci. Technol. 8*, p. 919.

11. Bull, A.T., (1980), "Biodegradation: Some Attitudes and Strategies of Microorganisms and Microbiologists," in *Contemporary Microbial Ecology*, D.C. Ellwood, et al., Eds., Academic Press, New York, p. 107.

12. Daughton, C.G., (1981), "Biodegradation of Heterocycles in Synfuel Wastes," Department of Energy Invention Case No. IB-417.

13. Suzuki, J., (1976), "Study on Ozone Treatment of Water-Soluble Polymers: I. Ozone Degradation of Polyethylene Glycol in Water," *J. Appl. Polym. Sci. 20*, p. 93.

14. Hoigné, J. and Bader, H., (1978), "Ozone and Hydroxyl Radical-Initiated Oxidations of Organic and Organometallic Trace Impurities in Water," *ACS Symp. Ser. 82*, p. 292.

15. Peleg, M., (1976), "Review Paper: The Chemistry of Ozone in the Treatment of Water," *Water Res. 10*, p. 361.

16. Hoigné, J. and Bader, H., (1979), "Ozonation of Water: Selectivity and Rate of Oxidation of Solutes," in *Ozone: Science and Engineering*, Vol. 1, Pergamon Press, New York and London, p. 73.

17. Hoigné, J. and Bader, H., (1976), "The Role of Hydroxyl Radical Reactions in Ozonation Processes in Aqueous Solutions," *Water Res. 10*, p. 377.

18. Hoigné, J. and Bader, H., (1978), "Ozonation of Water: Kinetics of Oxidation of Ammonia by

Ozone and Hydroxyl Radicals," *Environ. Sci. Technol. 12*, p. 79.

19. Bailey, P.S., (1982), *Ozonation in Organic Chemistry: Nonolefinic Compounds*, Vol. 2, Academic Press, New York.

20. Sierka, R.A., (1982), "A Preliminary Evaluation of Oil Shale Wastewater Treatment by Ozone and Activated Carbon," in *Fifteenth Oil Shale Symposium Proceedings*, Colorado School of Mines, Golden, Colorado, p. 479.

21. Torpy, M.F., Luthy, R.G., and Raphaelian, L.A., (1982), "Activated-Sludge Treatment and Organic Characterization of Oil Shale Retort Water," in *Fifteenth Oil Shale Symposium Proceedings*, p. 487.

22. Rice, R.G. and Browning, M.E., (1980), *Ozone for Industrial Water and Wastewater Treatment: A Literature Survey*, Environmental Protection Agency Report EPA-600/2-80-060, Washington, D.C.

23. Suzuki, J., Hukushima, K., and Suzuki, S., (1978), "Effect of Ozone Treatment upon Biodegradability of Water-Soluble Polymers," *Environ. Sci. Technol. 12*, p. 1180.

24. Peyton, G.R., Huang, F.Y., Burleson, J.L., and Glaze, W.H., (1982), "Destruction of Pollutants in Water with Ozone in Combination with Ultraviolet Radiation. 1. General Principles and Oxidation of Tetrachloroethylene," *Environ. Sci. Technol. 16*, p. 448.

25. Kuo, P.P.K., Chian, E.S.K., and Chang, B.J., (1977), "Identification of End Products Resulting from Ozonation and Chlorination of Organic Compounds Commonly Found in Water," *Environ. Sci. Technol. 11*, p. 1177.

26. Glaze, W.H., et al., (1980), *Oxidation of Water Supply Refractory Species by Ozone with Ultraviolet Radiation*, Environmental Protection Agency Report EPA-600/2-80-110, Washington, D.C.

27. Kearney, P.C., Plimmer, J.R., and Li, Z.-M., (1982), "UV-Ozonation and Land Disposal of Aqueous Pesticide Wastes," *Fifth International Congress of Pesticide Chemistry Proceedings*, Pergamon Press, London, (in press).

28. Kolonko, K.J., Shapiro, R.H., Barkley, R.M., and Sievers, R.E., (1979), "Ozonation of Caffeine in Aqueous Solution," *J. Org. Chem., 44*, p. 3769.

29. Langlois, G.W., Jones, B.M., Sakaji, R.H., and Daughton, C.G., (1982), "Coulometric Quantitation of Carbon in Oil Shale Process Wastewaters via UV-Peroxydisulfate or High-Temperature Oxidation, in *Quantitation of Oil Shale Wastewater Quality: A Manual of Analytical Methods*, C.G. Daughton, Ed., University of California Sanitary Engineering and Environmental Health Research Laboratory, Richmond, CA, UCB/SEEHRL Report No. 82-6.

30. Daughton, C.G., Jones, B.M., and Sakaji, R.H., (1982), "Rapid Fractionation of Oil Shale Wastewater by Reverse-Phase Separation," in *Quantitation of Oil Shale Wastewater Quality*, UCB/SEEHRL Report No. 82-6.

31. Larson, R.A., (1978), "Environmental Chemistry of Reactive Oxygen Species," *CRC Crit. Rev. Environ. Cont. 8*, p. 197.

32. Daughton, C.G., Ed., (1982), *Quantitation of Oil Shale Wastewater Quality*, UCB/SEEHRL Report 82-6.

THEORETICAL AND EXPERIMENTAL STUDIES OF REACTIONS IMPORTANT IN COMBUSTION*

N.J. Brown, J.A. Miller,[†] and O.M. Rashed

Combustion chemistry consists of complex, multi-step chain mechanisms involving reactive radicals which are present in small concentrations. The complexity of the mechanisms, the inherent difficulties of working in high-temperature environments, and the large number of species involved with the oxidation of a fuel—all make the study of combustion chemistry quite difficult.

Our current research is concerned with the application of theoretical chemical kinetics to study unimolecular and bimolecular reactions important in combustion processes. We also use modeling techniques to extract mechanistic information for catalytic combustion and to acquire a better understanding of combustion inhibition. The theoretical studies are investigated using classical trajectories with realistic potential energy surfaces. Special emphasis is placed upon elucidating the role of molecular angular momentum on intramolecular and intermolecular energy transfer and reactivity. Recently, we have investigated intermolecular energy transfer important in low-pressure-limit unimolecular kinetics and reactivity in a four-center bimolecular system.

ACCOMPLISHMENTS DURING FY 1982

With Dr. James A. Miller of Sandia National Laboratory, we have investigated the low-pressure-limit unimolecular dissociation of HO_2 resulting from collisions with He. A potential energy surface which accounts for the rare-gas/HO_2 interaction has been constructed. The surface with the He atom at infinity is the *ab initio* surface of Melius and Blint[1] that we used in our high-pressure-limit studies.[2] The rare-gas interaction with the three atoms is added to the Melius-Blint surface and is derived from experimental studies of rare-gas scattering. The collisions have been investigated as a function of translational temperature, total molecular internal energy, and total molecular angular momentum. Threshold energy for HO_2 is approximately 47 kcal/mol, and our calculations were performed at molecular internal energies between 30 and 46 kcal/mol. At the termination of each trajectory, the energy transferred into each degree of freedom and the angular momentum transferred are calculated. Averages of these quantities are computed for a given set of trajectories characterized by a common translational temperature, internal molecular energy, and distribution of molecular angular momentum. The energy transfer is also separated into up and down portions, which are also averaged for comparison with commonly used theories. Histograms describing the energy transfer distributions and two-dimensional histograms which provide insight into the energy coupling in the molecule were determined for the various sets. Correlation coefficients were also calculated to provide information on the coupling among the three types of energy.

The most remarkable and somewhat disheartening feature of the energy transfer distributions is that they have very long tails. With the loss-and-gain energy transfer mechanisms, these tails account for the slow convergence of the averages in a particular ensemble. A meaningful average for the kinetic, rotational, and vibrational energy transferred requires on the order of 5000 trajectories. A two-dimensional histogram showing the distribution of the rotational and vibrational energy transferred for an ensemble is shown in Fig. 1. Note that the long tails on the distributions are in conflict with the commonly used exponential-gap model of energy transfer.

The effect of increasing the initial kinetic energy on the energy transfer characteristics is to increase the width of the energy distributions. On the average, kinetic energy is gained in sets of collisions characterized by small values of initial molecular angular momentum (less than $10\hbar$). The average vibrational energy transferred in a collision increases with initial molecular angular momentum for a fixed
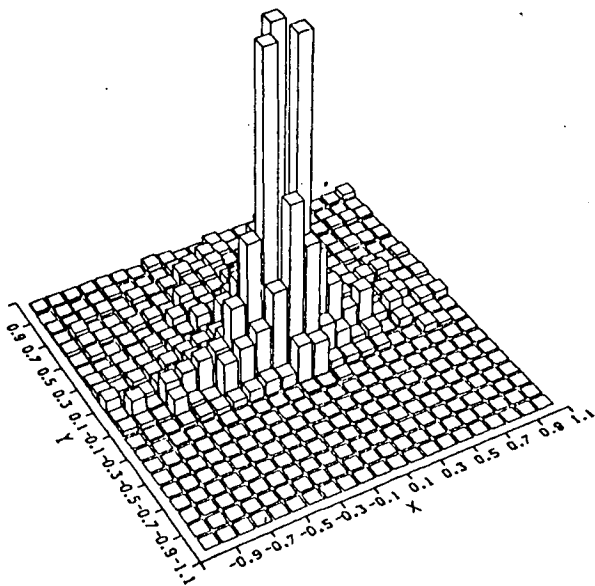
Figure 1. A two-dimensional histogram showing the distribution of energy transferred to the rotational degrees of freedom of HO_2 from collisions with He in an ensemble characterized by a temperature of 800 K, 46 kcal/mol initial molecular energy, and initial angular momentum less than $10\hbar$. The Y-axis indicates change in rotational energy while the X-axis indicates the change in the vibrational energy. The ordinate represents the fractional population of the ensemble.   (XBL 837-10550)

total energy. Energy transfer mechanisms involve energy transfer among kinetic, rotational, and vibrational degrees of freedom. Average angular momentum changes in the molecule were usually less than three angular momentum units.

We began work on a microcanonical transition theory that includes molecular rotation and tunneling corrections. Reliable saddle-point characteristics are needed to use this theory. We are attempting to explore the limitations of this approach and to elucidate its positive attributes. We will use this formalism to compute rate coefficients for molecules of interest in combustion.

We have made progress with our classical dynamics study of the reaction $H_2 + OH \rightarrow H_2O + H$. This work has as its primary objective the determination of the effect of initial rotational energy on reactivity. The potential energy surface used is the analytical form of Schatz and Elgersma[3] of the *ab initio* Walsh and Dunning[4] surface. In the determination of the integration conditions, we began observing some anomalous trajectories in which a rather long-range orbiting type of behavior was noted as the H_2 and OH

were moving apart. Further investigation led to the conclusion that there were some long-range wells in the surface that were artifacts of the analytical fit. This was verified by evaluating the potential energy for several geometries when the reactant molecules were at intermediate distances as well as quite far apart. Subsequent work was concerned with evaluating the effect of anomalous potential surface characteristics on the reactive attributes of the system. At high initial kinetic energies, the potential is suitable for use in dynamics studies. The question of lower initial kinetic energies can only be answered by removing these unusual surface properties and thereby generating a surface with the proper asymptotic behavior while retaining the favorable description at close distances. We are currently exploring this approach. We are also investigating methods for computing the product energy distribution.

Papers describing modeling studies of flame inhibition and catalytic combustion have been completed.[5,6] In the flame inhibition study, the combustion environment was treated as a well-stirred reactor. The inhibitors considered were HCl and HBr, and the combustion mixtures were of hydrogen/oxygen/argon in varying equivalence ratios. Inhibition was investigated as a function of pressure, equivalence ratio, and inhibitor concentration. Inhibitor effectiveness was determined by the competition between the radical-scavenging ability of an inhibitor and the exothermicity of the scavenging reactions. For all cases considered, HBr was more effective in scavenging active radicals than HCl. At 0.01 atmospheres, HCl was a more effective inhibitor in lean and stoichiometric mixtures while HBr was more effective for rich mixtures at 0.01 atmospheres and for all atmospheric pressure mixtures. The effectiveness of HBr over HCl is illustrated in Fig. 2, where blowout residence time is plotted as a function of inhibitor concentration.

The high-temperature oxidation of H_2 on a platinum catalyst in the presence of excess air has been studied over a range of surface temperatures from 450 to 1070 K and equivalence ratios from 0.05 to 0.20. The experimental system considered was the laminar boundary layer of a heated catalytic plate. Under all conditions considered, the surface reaction rapidly became diffusion-limited downstream of the plate-leading edge. A finite-difference scheme was used to model numerically the flow field above the plate surface. This enabled surface reaction rate data to be obtained under conditions in which surface reaction
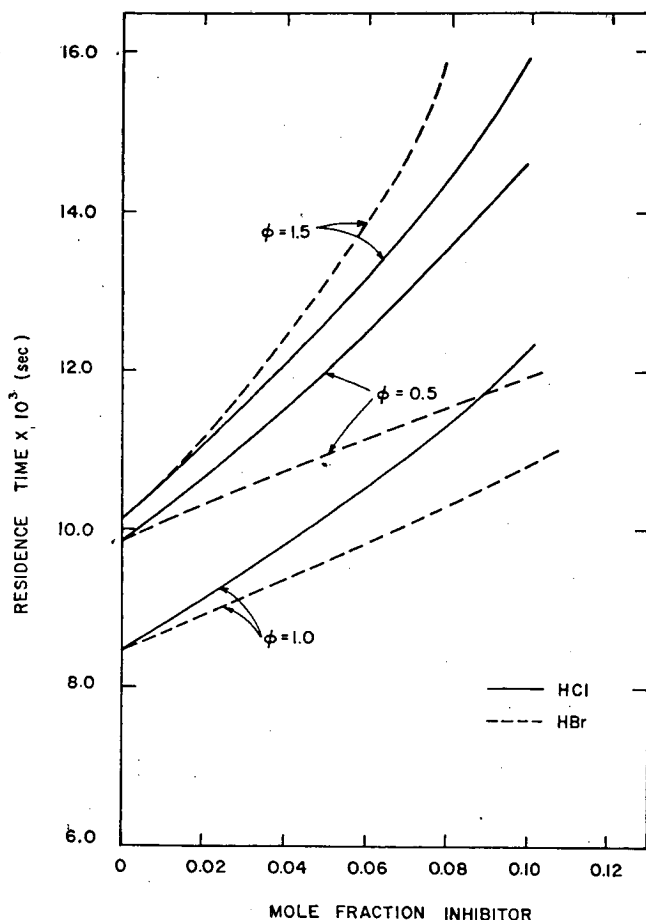
Figure 2. Residence time at blowout (sec) as a function of inhibitor concentration in mole fraction for mixtures at 1.0 atmosphere. Solid lines indicate HCl and dashed lines indicate HBr. (XBL 837-10549)

Figure 3. Surface reaction rate coefficient as a function of inverse temperature for H_2 combustion on a platinum-coated plate for mixtures of various equivalence ratios.

(XBL 832-8284)

rates were significantly influenced by transport effects. On the basis of a one-step model for H_2 oxidation, the data were found to correlate well with a reaction rate expression of the form

$$R_s = 1.4 \times 10^3 \, [H_2]_s \, \exp(-3850/RT)(\text{mol}/\text{cm}^2\text{sec})$$

where R_s is the surface reaction rate and $[H_2]_s$ is the H_2 concentration at the surface. The surface reaction rate coefficient is plotted as a function of inverse temperature in Fig. 3. The effects of the heat and mass transfer on the kinetics were also investigated.

PLANNED ACTIVITIES FOR FY 1983

The analysis of the energy transfer of the He/HO_2 system will be completed. Derived expressions for energy transfer will be compared with models used to describe low-pressure-limit unimolecular kinetics. The analytical representation of the potential surface

for the H_2/OH system will be refitted to give reasonable asymptotic limits, and studies of the bimolecular reaction will continue. Work will begin on the unimolecular kinetics of a four-atom polyatomic molecule. Research will also continue on statistical theories of reactions important in combustion science.

REFERENCES

1. Melius, C.F. and Blint, R.J. (1979), *Chem. Phys. Lett. 264*, p. 183.

2. Miller, J.A. and Brown, N.J. (1982), "The Dynamics of Unimolecular Dissociation of HO_2: Phase Space Sampling, Microcanonical Rate Coefficients and Rotational Effects," *J. Phys. Chem. 86*, p. 772.

3. Schatz, G.C. and Elgersma, H. (1981), *Chem. Phys. Lett. 73*, p. 21.

4. Walsh, S.P. and Dunning, T.H. (1980), *J. Chem. Phys. 72*, p. 1303.

5. Schefer, R.W. and Brown, N.J. (1982), "A Comparative Study of HCl and HBr Combustion Inhibition," *Combustion Sci. Tech., 29*, p. 113.

6. Brown, N.J., Schefer, R.W., and Robben, F. (1983), "High Temperature Oxidation of H_2 on a Platinum Catalyst," accepted for publication in *Combustion and Flame*; Lawrence Berkeley Laboratory Report LBL-13744.

NUMERICAL MODELING OF TURBULENT COMBUSTION*

A.F. Ghoniem, A.J. Chorin, and A.K. Oppenheim

Our approach uses the random vortex method to treat turbulent flow fields associated with combustion. Flame fronts are considered as interfaces between reactants and products propagating with the flow and at the same time advancing in the direction normal to themselves at a specified burning speed. Burning speed is associated with the generation of specific volume (the flame front acting, in effect, as the locus of volumetric sources) to account for the expansion of the flow field from the exothermicity of the combustion process. The model was applied to the flow in a channel equipped with a rearward-facing step. The results we obtained revealed the mechanism of formation of large-scale turbulent structures in the wake of the step, as well as the stabilization of the flame on the outer edges of these eddies.[1]

ACCOMPLISHMENTS DURING FY 1982

We concentrated upon three topics:

(1) Fundamental aspects of the modeling technique.

(2) Application of the model to the formation of a turbulent jet.

(3) Development of an aerodynamic approach to the properties of turbulent flames.

Fundamental Aspects of Modeling

Three problems have been successfully pursued. The first was to develop the random-element method,[2] an application of the random-walk technique to model diffusion of energy. Instead of vortex sheets and vortex blobs, the method uses heat-transfer sheets, or temperature-jump elements, and blobs of internal energy that carry thermal gradients from heat-conducting walls to the interior of the field, redistributing them by diffusion. The fundamental idea behind random-walk modeling of diffusion is the identity between the Green's function representing the solution of the diffusion equation and the probability density function of a Gaussian random variable

with zero mean (see Table 2 in Ref. 3). Preliminary results obtained by this method were presented last year (Fig. 5 in Ref. 3).

The extension of this technique to handle two-dimensional diffusion is presented in Table 1. A one-dimensional approximation close to the walls is employed to implement isothermal boundary conditions, while energy elements are used in the interior to diffuse its energy. Figure 1 compares the temperature profiles along the diagonal of a corner and a square with the corresponding analytical solutions.

The second fundamental problem we solved was the generation of vorticity by the interaction between the pressure field and density gradients—a mechanism important to both flames and buoyancy effects. The motion of the temperature-jump elements, governed by the algorithm of the random-element method, generates elements of vorticity in the interior of the field, while additional elements are generated by the no-slip condition at the walls. Table 2 describes how the random-walk method is used in conjunction with the principle of time splitting to solve the system of equations that describes a natural convection field over a vertical infinite isothermal wall. Figure 2 shows our solution (thick lines) in comparsion to one obtained by a finite-difference technique for two values of the Prandtl number.[4]

The third problem was flame propagation. Our original computations[1] considered the flame as, essentially, a jump in density. Its front was treated, therefore, as an interface propagating as a consequence of advection and self-advancement at a specified normal burning speed. In order to treat flame propagation as the propagation of a reacting surface governed by a chemical reaction proceeding at a finite rate, the problem was recast in terms of a reaction-diffusion equation in temperature. The algorithm of the random-element method was then applied to solve this problem by adjusting the strength of the temperature-jump elements as they move according to the rate of reaction (Table 3). The random-element algorithm was tested by comparing its solution with those of the finite-difference and finite-element methods, demonstrating its capability to calculate flame propagation with proper accuracy. Figure 3 shows the results of numerical computations evaluated for $f(T) = T(1-T)$, when the integration of the reaction part of the equation is done using a first-order Euler scheme in the first case [Fig. 3(a)] and an exact integral in the second case [Fig. 3(b)], both in comparison to the analytical solution.

Table 1. A hybrid scheme for representing two-dimensional diffusion in combustion.

Domain	Boundary $(y < \delta_s)$	Interior $(y > \delta_s)$
Differential	$\dfrac{\partial T}{\partial t} = \alpha \dfrac{\partial^2 T}{\partial y^2}$	$\dfrac{\partial T}{\partial t} = \alpha \nabla^2 T$
Boundary condition	$T = 1$	$T = \delta(y - \delta_s)$
Diffusing element	δT_i	δe_i
Coupling	$\delta e_i = \delta T_i * (y_i - \delta_s)$	$\partial T_i = \pm \delta e_i / \delta_s$
Stochastic solution	$\mathbf{r}_i(t + \Delta t) = \mathbf{r}_i(t) + \eta_i$	$\mathbf{r}_i(t + \Delta t) = \mathbf{r}_i(t) + \eta_i$
Sampling	$T = \dfrac{\Sigma \delta e_i}{\delta_s \cdot dx} + \Sigma \delta T_i H(y - y_i)$	$T = \dfrac{1}{\delta A_i} \Sigma \delta e_i \, \delta(\mathbf{r} - \mathbf{r}_i)$

Note: $\partial_2 = 2\sigma$, the thickness of the one-dimensional diffusion layer; $\partial A_i =$ area element.

Table 2. Pressure-density interaction: Random-walk method.

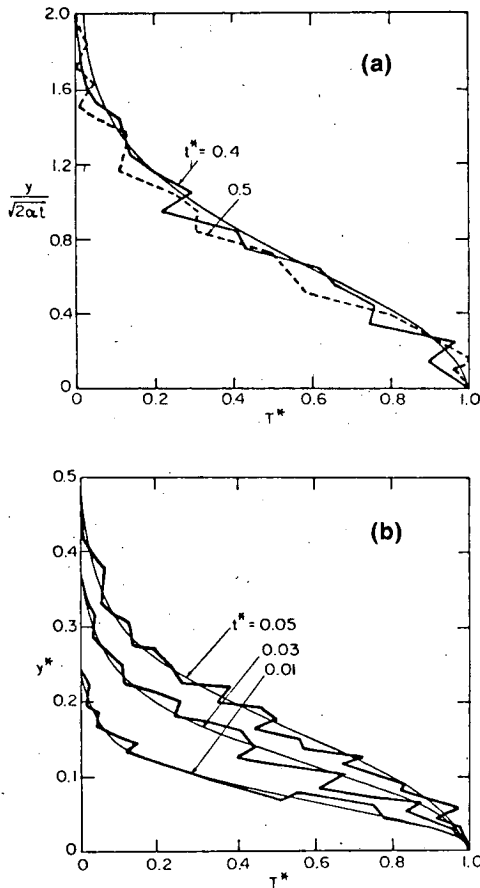|	
Differential equations	$\dfrac{\partial T}{\partial t} = \alpha \dfrac{\partial^2 T}{\partial x^2}$
	$\dfrac{\partial u}{\partial t} = \nu \dfrac{\partial^2 u}{\partial x^2} + g\beta \, (T - T_\infty)$
Initial conditions	$T = 0; \quad u = 0$
Boundary conditions	$x = 0; \quad T = 1; \quad u = 0$
	$x = \infty; \quad T = 0; \quad u = 0$
Fractional steps	$\dfrac{\partial T}{\partial t} = \alpha \dfrac{\partial^2 T}{\partial x^2} \; ; \quad \dfrac{\partial \xi}{\partial t} = \nu \dfrac{\partial^2 \xi}{\partial x^2}$
	$\dfrac{\partial \xi}{\partial t} = g\beta \dfrac{\partial T}{\partial x}$
Vorticity production	$\delta\gamma = g\beta \, \delta T$
	$T = \sum_n \delta T \, H(x - x_i)$
	$\gamma = \sum_N \delta\gamma \, H(x - x_i)$
	$N(t + \Delta t) = N(t) + 2n$

Figure 1. Temperature distribution along the diagonal with two isothermal walls at $T = 1$: (a) for a corner; (b) for a square.   (XBL 832-8042)

Note: $n =$ number of temperature jump elements; $N =$ number of vortex elements.

4-56
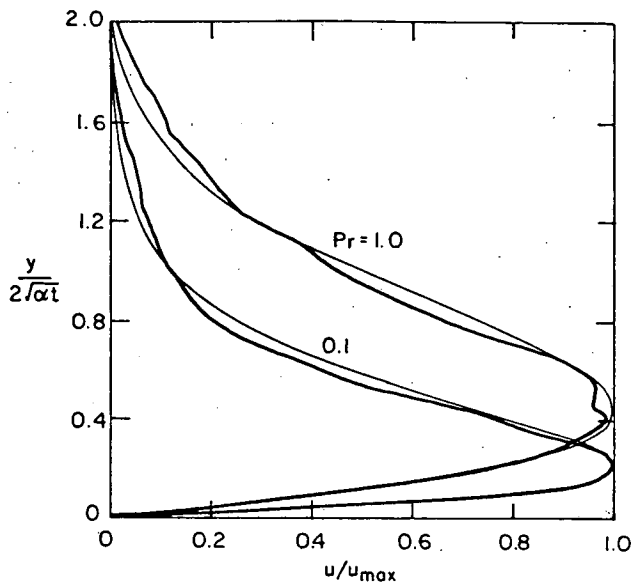
Figure 2. Velocity profiles parallel to a vertical plane set at $T = 1$ in a fluid initially at $T = 0$. (The motion is induced by natural convection.) Thick lines represent our solution (random-element method); thin lines, those of a finite-difference technique. Solutions are for two values of the Prandtl number. (XBL 832-8043)

Table 3. Reaction-diffusion equation.

Differential equation	$\dfrac{\partial T}{\partial t} = \dfrac{\partial^2 T}{\partial x^2} + f(T)$
Initial condition	$T(x,0) = T_o(x)$
Boundary conditions	$T(+\infty,0) = 0; \quad T(-\infty,0) = 1$
Solution:	
Fractional steps	$T(n\Delta t) = [R(\Delta t)\, D(\Delta t)]^n\, T_o$
Reaction	$\dfrac{dT}{dt} = f(T)$
Diffusion	$\dfrac{\partial T}{\partial t} = \dfrac{\partial_2 T}{\partial x^2}$
Deterministic result	$\delta T_i(t + \Delta t) = \delta T_i(t) + f(T_i)\Delta t$
Stochastic result	$T = \Sigma\, \delta T_i\, H(x - x_i)$
	$x_i(t + \Delta t) = x_i(t) + \eta_i$
	$E[\eta] = 0; \quad E[\eta^2] = 2\Delta t$

Figure 3. Temperature profiles in a flame described by a single reaction-diffusion equation: (a) integration of the reaction equation performed by the use of a first-order Euler scheme; (b) numerical solution obtained using exact solution of the reaction equation. Thin curves represent the analytical solution.

(XBL 832-8044)

Application to Turbulent-Jet Formation

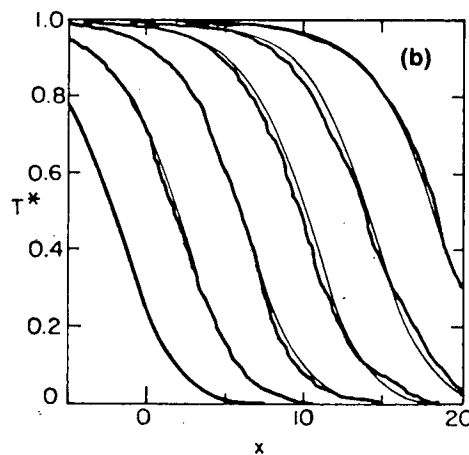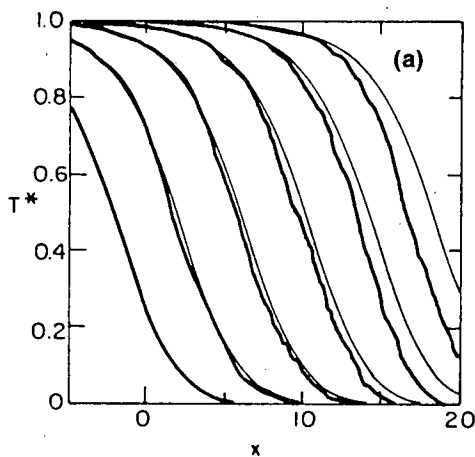The random-vortex method was applied to the problem of the formation of a planar, two-dimensional turbulent jet at high Reynolds numbers. Figure 3 in Ref. 5 describes the elementary processes of the random vortex method and their implementation to solve the convection-diffusion equation. The results, expressed in terms of the development of the vorticity field, are presented in Fig. 4. They reveal the formation of large-scale turbulent eddy structures on both sides of the jet with a potential core inside. A few jet widths downstream, the two layers start to interact, and the flow becomes dominated by the pairing of eddies on both sides. The turbulent eddies grow by entraining the nonturbulent fluid, while, as a result of the interaction between positive and negative vorticity, their trajectories become more and more convoluted. These pictures display a remarkable resemblence to experimental photographs obtained by Dimotakis et al.[6] across the plane of symmetry of an axisymmetric jet.

Aerodynamic Theory

Our numerical modeling studies, supported by experimental observations of turbulent flames, lead to our third topic, the development of an aerodynamic theory of turbulent flame propagation. The theory is based on the concept that the flow field is dominated by a large-scale eddy structure, while the flame front is established at the outer contours of the eddies and acts as a semi-permeable membrane around the burnt gas. We are now studying[7] the aerodynamic patterns produced by the interaction between these eddies and the expansion due to the exothermic effects of the combustion process.

PLANNED ACTIVITIES FOR FY 1983

The next phase of our work will be concerned primarily with applications of the random-walk methods we developed to a variety of problems in turbulent flow and combustion. This effort will be enhanced

Time 14 00   Time 21 00   Time 11 00   Time 44 00   Time 54 00   Time 64 00

Time 53 00   Time 55 00   Time 57 00   Time 59 00   Time 61 00   Time 63 00

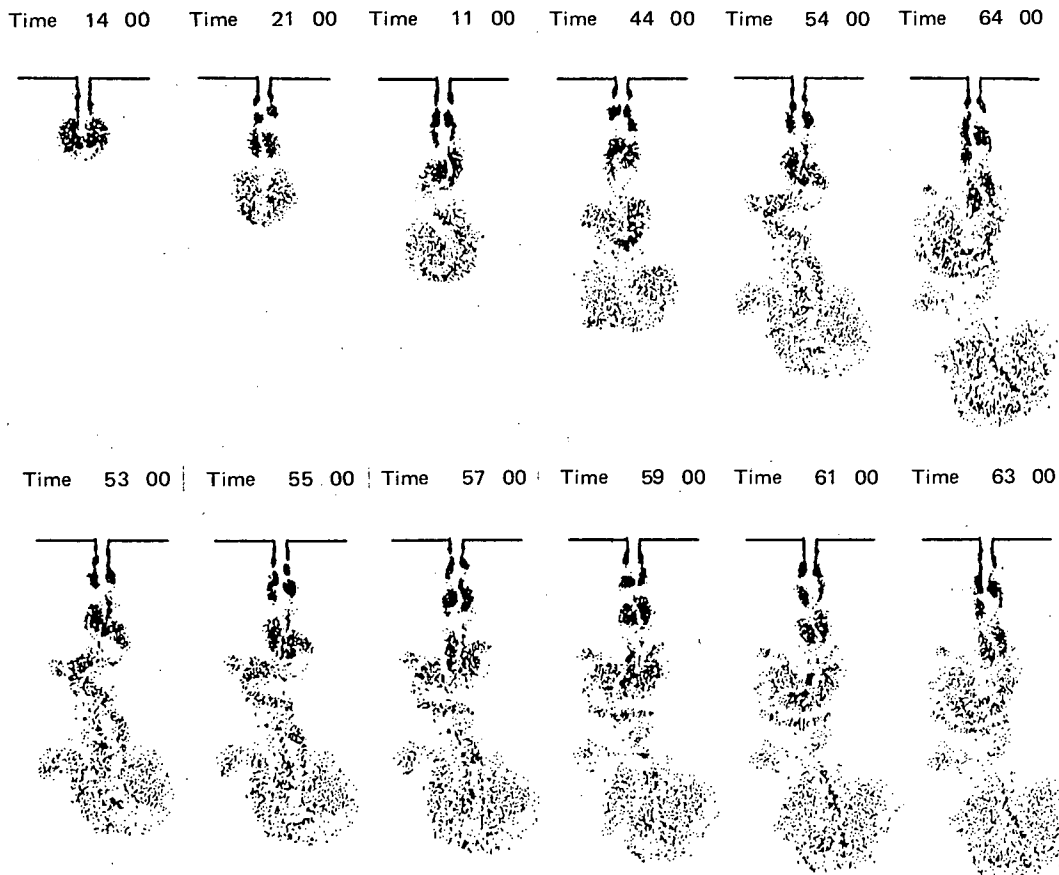Figure 4. Sequential series of computer plots of vortex fields in a turbulent jet at a Reynolds number Re = 10^4.   (XBL 832-8045)

significantly by arrangements to use the Cray computer at the NASA-Ames Research Center.

Of the particular problems we plan to treat, the most prominent are the following:

(1) Inflammation (i.e., the spreading of the flame front in a flow field) of a turbulent jet.

(2) Inflammation of turbulent flow in a channel.

(3) Response of the turbulent combustion system in a channel behind rear-facing steps of various aspect ratios (ratios of step height to channel width) to an increase in the exothermicity of the combustible mixture (corresponding to an increase in the fuel/air ratio); the results should provide specific information on the mechanism of flashback.

(4) Behavior of flames governed by a given reaction-rate law in a two-dimensional flow system.

Concomitantly to numerical modeling, we intend to pursue analytic studies of the rudimentary aerodynamic components of turbulent flames along the lines specified at the end of the last section, i.e., the interaction between eddies and exothermic expansion.

REFERENCES

1. Ghoniem, A.F., Chorin, A.J., and Oppenheim, A.K. (1982), "Numerical Modeling of Turbulent Flow in a Combustion Tunnel," *Phil. Trans. Roy. Soc. Lond. A304*, p. 303.

2. Ghoniem, A.F., and Oppenheim, A.K. (1982), "Random Element Method for Numerical Modeling of Diffusional Processes," in *Eighth International Conference on Numerical Methods in Fluid Dynamics*, Aachen, W. Germany, June 1982, p. 224.

3. Chorin, A.J., Ghoniem, A.F., and Oppenheim, A.K. (1982), "Numerical Modeling of Turbulent Combustion," *Energy and Environment Division Annual Report FY 1981*, p. 4–93.

4. Ghoniem, A.F., and Sherman, F. (1983), "Random Walk Simulation of Diffusion Processes," *J. Comp. Phys.* (in press).

5. Ghoniem, A.F., and Oppenheim, A.K. (1983), "Solution of the Problem of Flame Propagation by the Use of the Random Element Method," presented at the American Institute of Aeronautics and Astronautics 21st Aerospace Sciences Meeting, AIAA Paper No. 83-0600, Reno, Nevada, January 1983.

6. Dimotakis, P.E., Miake-Lye, R.C., and Papantonic, D.A. (1982), "Structure and Dynamics of Round Turbulent Jets," California Institute of Technology Graduate Aeronautical Laboratories, Pasadena, California GALCIT Report FM82-01.

7. Oppenheim, A.K., and Ghoniem, A.F. (1983), "Aerodynamic Features of Turbulent Flames," presented at the American Institute of Aeronautics and Astronautics 21st Aerospace Sciences Meeting, AIAA Paper No. 83-0470, Reno, Nevada, January 1983.

CONTROLLED COMBUSTION*

N.J. Brown, C.D. Carter, K. Hom, F.C. Hurlbut, D. Lucas, A.K. Oppenheim, R.B. Peterson, R.F. Sawyer, and H.E. Stewart

The principal objective of this project is to acquire fundamental knowledge for the development of controlled combustion systems. For power plant and internal combustion engine technologies, such systems offer the prospect of simultaneously maximizing thermal energy conversion efficiency, minimizing pollutant emissions, and optimizing the tolerance to a wide variety of fuels. Of key significance in this respect is the establishment of as homogeneous a combustion process as possible in a lean, gaseous air-fuel mixture—a process that is associated with a distributed, multipoint initiation. A thorough understanding of ignition—the initiation of the self-sustained exothermic process of combustion—is thus essential, and the primary emphasis is therefore placed on an experimental study of the fundamental features of ignition. Using as the test media an assortment of lean gaseous mixtures, ranging from noble gas–diluted hydrogen-oxygen to relatively heavy hydrocarbon vapor–air, all contained in a closed vessel, we employ a variety of ignition methods, including flash photolysis, electric spark discharge, plasma jets, and jets of incomplete combustion products.

The major objective of the experimental program is to determine the particular role played in ignition by active radicals. Consequently, the most important measurement is concerned with their concentration histories. This measurement is accomplished with a high-frequency-response molecular-beam mass spectrometer that has been designed and built especially for this purpose. The results will be interpreted by a thermochemical analysis that follows the theoretical concepts of Semenov[1] and Frank-Kamenetskii[2] for the rationalization of the transient process of ignition in a closed system. This is supplemented by numerical modeling of flame propagation in turbulent flow, carried out by the use of the random-walk methods we have developed in collaboration with their originator, Professor A. Chorin of the University of California, who is actively participating with us in this endeavor.

The operating characteristics of the molecular-beam mass spectrometer have proven most satisfactory after its relocation from the UC Berkeley campus to LBL, and the experimental testing program is in progress, with flash photolysis of NO_2 used to ignite a helium-diluted hydrogen-oxygen mixture. In the concomitant analytical studies, we have been able to deduce the classical ignition limits by appropriate scaling of the thermal relaxation time. The technique we developed for numerical modeling of combustion in a turbulent flow system has recently been published in *Philosophical Transactions of the Royal Society.*

ACCOMPLISHMENTS DURING FY 1982

Our work last year consisted of the development of the theoretical as well as experimental methods of approach. The first was concerned with the fundamental aspects of the thermochemistry of ignition; the second, with a molecular-beam mass spectroscopy of sufficiently high resolution and frequency response to record the variation of active radicals that appear in extremely low concentrations over a submillisecond of time. Progress made in both endeavors is reported here in turn.

Thermochemistry

To formulate the analytical features of ignition, it is sufficient to consider a thermodynamically closed, homogeneous chemical system surrounded by a compressible medium that may absorb the work of expansion and act as a heat sink. The basic theory

of this process has been formulated by Semenov[1] and Frank-Kamenetskii,[2] and some of its analytical features have been included in the recently published textbook of Zeldovich et al.[3] Its essential properties with respect to the case of photoignition have been exposed by Gray and Yang,[4] while the more general case of a thermochemical process has been treated by Guirguis et al.[5] The salient features of this approach have been described in the 1980 Annual Report.[6] A brief rendition is as follows.

The dynamic behavior of the system in the course of ignition can be described by reaction rate expressions, which specify the speed with which molecular species are transformed by chemical reaction, and by the energy conservation equation, including the effect of losses to surroundings.

The solution is expressed in terms of integral curves on a multidimensional phase-space whose coordinates are the temperature and concentrations of all the chemical species participating in the reaction. The results provide a sharp definition for "ignition temperature"—a threshold between ignition and extinction which, for a given chemical system, is a function of the thermal relaxation time (the time constant of temperature decay due to heat transfer losses).

The results we obtained on this basis for the hydrogen-oxygen system are in remarkably good agreement with the classical auto-ignition limits (usually referred to in the literature by the misnomer "explosion limits").

This is in drastic contrast to the views expressed so far in the literature, where each segment has been credited to different effects: the so-called "first explosion limit" at low pressures was believed to be due to quenching by wall effects; the "second explosion limit" at intermediate pressure to the direct effects of chain branching; and the "third explosion limit" to the effects of heat conduction.[7] Thus, getting all three as a consequence of one comprehensive theory is indeed quite an accomplishment.

We are provided, moreover, with a satisfactory demonstration of the physical validity of our relatively simple method of approach and a proof that the *a priori* artificial assumption of a constant relaxation time is in fact quite realistic. Encouraged with these results, we are now ready to tackle the more practical case of heavier hydrocarbon-air mixtures for which there is as yet just a modicum of chemical kinetic-rate data available.

Molecular Beam Mass Spectrometer

This apparatus has been relocated from the UC Berkeley campus to Building 70 of LBL. The move was associated with a number of modifications, as a consequence of which the performance of the system has been significantly improved. Most prominent among them are the following (see Fig. 1):

(1) The beam path was shortened to ~30 cm by the installation of a completely redesigned skimmer support and cone.

(2) A new source nozzle permitting sustained operation at high temperatures and elevated pressures was designed and fabricated.

(3) Pumping capacity was increased by the installation of a 10-inch diffusion pump in the first stage and a 6-inch closed-cycle cryopump in the third stage. The first pump makes it possible to have a source nozzle as large as 0.018 cm in diameter while maintaining a pressure of $\sim 4 \times 10^{-4}$ Torr in the first stage with an atmospheric pressure in the test space. The second greatly reduces the background noise.

(4) A new chopper/trigger pulse system was built to eliminate fluctuations we encountered earlier; these were due to speed variation and mechanical imperfections in the original setup.
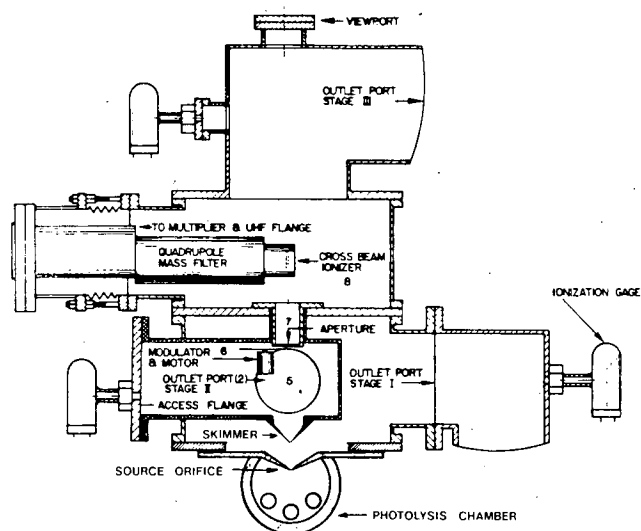
(5) The signal train of the quadrupole was ameliorated by a suitable modification of the electronic circuit.

(6) Test cells for photolysis-induced ignition experiments using high-power flash tubes were designed and constructed—one for molecular-beam sampling, and another for a separate operation using standard measuring techniques and optical diagnostics, such as high-speed schlieren cinematography.

The remodeled apparatus was then subjected to the following performance tests:

(1) Examination of the properties of the molecular beam under the influence of the distance between the source and the nozzle and the alignment of the source cone. A Mach number of ~10 was routinely achieved for air beams at atmospheric pressure and room temperature.

(2) Observation of major effects of ignition in a mixture of $H_2/O_2/NO_2/Ar$ initiated by flash photolysis, particularly the variation of pressure and the time-of-flight signal due to the change of state of inert diluent. This is illustrated by Fig. 2, presenting the pressure transducer and the argon quadrupole signals recorded by our high-speed multichannel analog/digital converter in a 3/61/20 mixture of the constituents specified above at an initial pressure of 0.4 atm.

Figure 1. Molecular-beam mass spectrometer system.
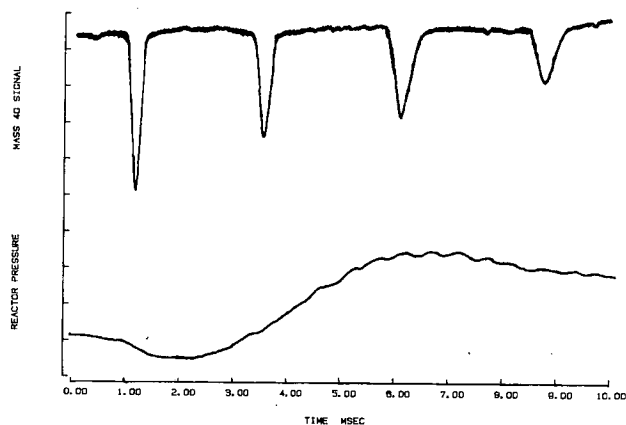(XBL 831-7596)

Figure 2. Argon signal (mass 40) and pressure transducer record in the course of flash photolysis of $Ar/H_2/O_2/NO_2$ mixture at 0.4 atm pressure and room temperature.
(XBL 831-7597)

(3) Investigation of the effects of rapidly vary-ing pressure and temperature on the qua-drupole signal—a necessary prerequisite for the measurement of composition changes using the mass spectrometer, so that such effects could be eliminated. Whereas the influence of pressure has been studied previously,[9] the effects of tempera-ture have so far been unexplored. The pressure effects we observed are in good agreement with previous studies.[10] Some of the results we obtained with different source temperatures are displayed in Fig. 3. The record presents signals of an Ar beam at two source temperatures, 300 K and 900 K, with atmospheric pressure main-tained in both cases. The higher tempera-ture beam arrives at the detector sooner and has a different width. The signals were normalized by their amplitudes, hence their peak values are the same.

To facilitate the interpretation of data provided by the time-of-flight signals, a computer program was developed to calculate the expected beam perfor-mance. Its results are used to fit arrival times and Mach numbers to those measured experimentally. Preliminary tests indicate that sampling from a homo-geneous mixture is not ideal, as evidenced by altera-tions in arrival times due to admixing of cooler gas coming from the boundary layer at the wall of the nozzle. This effect evidently has to be taken into account in concentration measurements.

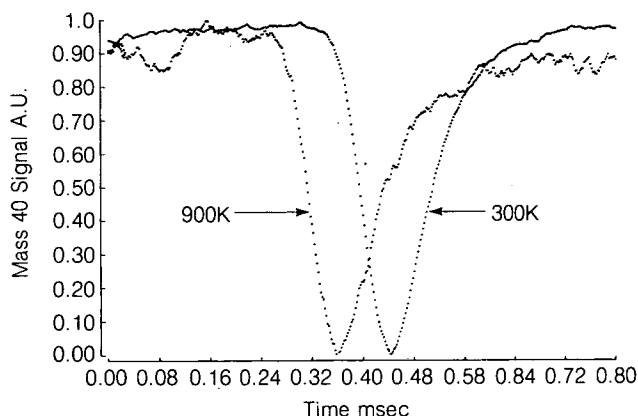In analyzing the effects of beam chopping during a transient event, we have found that it should be pos-sible to attain a time resolution of ~100 microseconds in the course of combustion, when the gas temperature is in excess of 1700 K. This directly contradicts recently published estimates[11] that sug-gested time resolution might be drastically reduced at typical hydrocarbon-air flame temperatures.

PLANNED ACTIVITIES FOR FY 1983

Our objectives for the next phase of these studies will be to:

(1) Apply our theory of ignition to hydrocarbon-air mixtures.

(2) Measure concentration history of chemical species participating in the photolytic igni-tion of $H_2/O_2/NO_2/Ar$ mixtures, and the con-comitant physical properties of the reacting medium contained in the test cell.

Figure 3. Time-of-flight signal of argon beam at 300 and 900 K. (XBL 831-7598)

REFERENCES

1. Semenov, N.N. (1943), "On Types of Kinetic Curves in Chain Reactions. I. Laws of the Auto-catalytic Type," *Comptes Rendus (Doklady) de l'Academie des Sciences de l'URSS 43*(8), p. 342; (1944), "On Types of Kinetic Curves in Chain Reactions. II. Consideration of the Interaction of Active Particles," *Comptes Rendus 44*(2), p. 62; "On types of Kinetic Curves in Chain Reactions. Allowance for Chain Rupture on Walls of Reaction Vessel in the Case of Oxidation of Hydrogen," *Comptes Rendus 44*(6), p. 241; (1958, 1959), *Some Prob-lems in Chemical Kinetics and Reactivity*, M. Boudart, translator, Princeton University Press, Princeton (2 vols.).

2. Frank-Kamenetskii, D.A. (1947, transl. 1955), *Diffusion and Heat Exchange in Chemical Kinet-ics*, N. Thon, translator, Princeton University Press, Princeton, New Jersey.

3. Zeldovich, Ya.B., Barenblatt, G.I., Librovich, V.B., and Machviladze, G.M. (1980), *Mathemati-cal Theory of Combustion and Explosion*, Izdva-telstvo "Nauka," Moscow.

4. Gray, B.F., and Yang, C.H. (1965), "On the Unification of the Thermal and Chain Theories of Explosion Limits," *J. Phys. Chem. 69*(8), p. 2747; Yang, C.H., and Gray, B.F. (1967), "The Determination of Explosion Limits from a Unified Thermal and Chain Theory," in *Eleventh Sympo-*

sium (International) on Combustion, p. 1099, The Combustion Institute, Pittsburgh, Pennsylvania.

5. Guirguis, R.H., Oppenheim, A.K., Karasalo, I., and Creighton, J.R., (1981), "Thermochemistry of Methane Ignition," Prog. Astronaut. and Aeronaut. 76, p. 134.

6. Oppenheim, A.K., Hurlbut, F.C., and Robben, F. (1980), "Ignition Studies," Energy and Environment Division Annual Report 1979, p. 6-5, Lawrence Berkeley Laboratory Report LBL-11650.

7. Gear, C.W. (1971), Numerical Initial Value Problems in Ordinary Differential Equations, Prentice-Hall, Inc., Englewood Cliffs, New Jersey.

8. Lewis, B. and von Elbe, G. (1961), Combustion, Flames and Explosions of Gases, p. 22–70, Academic Press, Inc., New York and London.

9. Young, W.S., Rodgers, W.E., Cullian, C.A., and Knuth, E.L. (1971), "Supersonic Molecular Beams with Cycling-Pressure Sources," AIAA Journal 9, p. 2.

10. Bossel, U. (1968), Investigation of Skimmer Interaction Influences on the Production of Aerodynamically Intensified Molecular Beams, Ph.D. Thesis, University of California, Berkeley.

11. Sloane, T.M., and Ratcliffe, J.W. (1982), Time Resolved Mass Spectrometry of a Propagating Methane-Oxygen-Argon Flame, Western States Section/The Combustion Institute, Paper No. 82-48.

HEAT AND MASS TRANSFER WITH COMBUSTION*

R. Greif, J. Woodard, S. Vosen,
and C. Yen

A major goal of this research has been the experimental and theoretical determination of the variation over time in the heat and mass fluxes during compression and combustion. This is not only of considerable practical importance, but also of fundamental interest since it is anticipated that these results

will elucidate basic aspects of combustion phenomena.

Previously, measurements were carried out in a single-pulse, compression-expansion apparatus built to study reciprocating engine processes under well-controlled laboratory conditions simulating the operation of a spark-ignition engine.[1] Completed studies in the apparatus have included the experimental and theoretical determination of the unsteady wall heat transfer in nonreacting gases during piston compression.[2,3]

That work has been extended to include reacting gases. In view of the complex nature of piston compression processes, it was decided to first carry out measurements during combustion in a shock tube in the end-wall region behind the reflected shock wave.[4,5] This is desirable because, during the pre-ignition period, the free-stream temperature and pressure are constant, and the phenomena during this period are well understood. When ignition occurs, the effects of combustion are clearly displayed, providing a useful basis for appraisal.[4,5]

Here we report on heat and mass transfer studies of reacting gases. This work was conducted in conjunction with flame-propagation studies in two constant-volume cells. The experiments were performed in a new facility constructed for this purpose.

ACCOMPLISHMENTS DURING FY 1982

Pressures, wall temperatures, and schlieren films were obtained simultaneously for a series of combustion processes in which premixed methane and air reacted in a constant-volume chamber.[6] From these data, the temporal variation of the flame speed and the wall heat flux were determined. This portion of the research was carried out in collaboration with Professor R. F. Sawyer and D. Hirvo.[7,8] Data were obtained for equivalence ratios varying from 1.1 to 0.6. The experiments were carried out in a single-pulse compression-expansion apparatus which permitted full optical access to the phenomena.[1] In these experiments, the piston was fully withdrawn so that the test section served as a constant-volume system. The results indicate that side-wall interactions affect flame speed. The wall heat-flux data show that heat transfer varied with distance from the flame; they also show a strong sensitivity to the equivalence ratio. Specifically, for an equivalence ratio of 0.6, the upper wall (at locations far from ignition) reaches a maximum heat flux at significantly later times than the

bottom wall. This is due to the more horizontal orientation of the flame at this equivalence ratio, which is attributed to the effect of buoyancy.[8]

Tests have also been carried out in a new test cell designed and constructed under the supervision of Professor A. K. Oppenheim. The test cell has the approximate shape of two bisecting 9 inch cylinders, 3-1/2 inches in diameter. Optical measurements may be made through 1-1/4 inch quartz windows that lie along the axis of one of the cylinders. Other instrumentation may be mounted through end ports at the ends of the second axis. Four additional ports provide access for a pressure transducer, and a spark plug, an inlet for the combustible gas mixture, and an outlet for the burnt gases. Some tests have been carried out for a methane-air flame encountering a cold, impermeable end wall. Pressures, wall temperatures, and schlieren films have been obtained for these runs. The wall heat flux has also been determined for several conditions.

Preliminary predictions of the unsteady wall heat fluxes have been made by C. Westbrook of the Lawrence Livermore National Laboratory, using the computer program HCT.[9] These calculations show trends very similar to the data. Further work is needed to extend the calculations to conditions corresponding to the test cases.

PLANNED ACTIVITIES FOR FY 1983

Additional experiments will be carried out in the new test cell over a range of pressures and equivalence ratios. Predictions of the wall heat fluxes and the species distributions will also be made, using extended versions of the HCT code. In addition, results will also be obtained on the basis of integral, quasi-steady, and numerical methods. The planned comparison of the theoretical predictions with the data should elucidate fundamental aspects of combustion phenomena. It is also planned to carry out measurements and calculations for reacting gases during piston compression.

REFERENCES

1. Oppenheim, A.K., et al. (1976), "A Cinematographic Study of Combustion in an Enclosure Fitted with a Reciprocating Piston," in *Stratified Charge Engines*, Institute of Mechanical Engineers Conference Publication 1976-11, p. 127.

2. Nikanjam, M., and Greif, R., (1978), "Heat Transfer During Piston Compression," *J. Heat Transfer*, 100, p. 527.

3. Greif, R., Namba, T., and Nikanjam, M. (1979), "Heat Transfer During Piston Compression Including Side Wall and Convection Effects," *Int. J. Heat Mass Transfer, 22*, p. 901.

4. Heperkan, H.A. (1980), "An Experimental and Theoretical Study of Heat Transfer with Combustion," Ph.D. Dissertation, University of California, Berkeley; Lawrence Berkeley Laboratory Report LBL-10868.

5. Heperkan, H., and Greif, R. (1982), "Heat Transfer During the Shock-Induced Ignition of an Explosive Gas," *Int. J. Heat Mass Transfer 25*, p. 267.

6. Woodard, J. B. (1982), "An Experimental and Theoretical Study of Heat Transfer in Constant Volume and Compression-Expansion Systems Including the Effects of Flame Propagation," Ph.D. Dissertation, University of California, Berkeley; Lawrence Berkeley Laboratory Report LBL-14097.

7. Woodard, J.B, Hirvo, D.H., Greif, R., and Sawyer, R.F. (1981), "Wall Heat Transfer and Flame Propagation in a Constant Volume Duct," presented at the Western States Section/The Combustion Institute Fall Meeting, October 19-20, 1981, Tempe, Arizona; Lawrence Berkeley Laboratory Report LBL-13021.

8. Woodard, J.B., Hirvo, D.H., Greif, R., and Sawyer, R.F. (1982), *Flame Propagation, Wall Heat Transfer, and Their Interaction in Lean Premixed Gases*, Lawrence Berkeley Laboratory Report LBL-13950.

9. Westbrook, C.K. Lawrence Livermore National Laboratory, personal communication.

10. Vosen, S. (1983), *Unsteady Heat Transfer During the Interaction of a Laminar Flame with a Cold Wall*, Ph.D. Dissertation, University of California, Berkeley.

FLAME PROPAGATION*

D. Dunn-Rankin and R.F. Sawyer

Operation of internal combustion engines under lean conditions offers the possibility of improved efficiency and reduced emissions. The difficulties associated with lean combustion include reduced flame-propagation speed and flame quenching. This fundamental study of flame propagation under internal combustion conditions is directed at understanding and solving these difficulties.

ACCOMPLISHMENTS DURING FY 1982

A study of approximately two-dimensional flame propagation in a constant-volume enclosure was conducted. The chamber had a square cross section (38 X 38 mm) and variable length. A line ignition source was used to produce a nearly two-dimensional flame. Simultaneous records of pressure versus time and flame position versus time allowed calculation of both flame speed and rate of reactant consumption.

Flame shape and flame location were determined from high-speed schlieren cinematographic records.

Two fuels were used in the study. First, the effect of equivalence ratio on ethylene/air flame propagation was explored. This extended the previous work of Woodard et al.[1] to a new fuel. Second, the effect of chamber length on methane/air flames of unity equivalence ratio was investigated.

Ethylene/air flames demonstrated similar shape development to methane/air flames despite their differing flame speeds (Fig. 1). Duct length greatly influenced flame shape development (Fig. 2). Lean-mixture flame speeds were considerably lower than stoichiometric-mixture flame speeds (Fig. 3). The rate of reactant consumption provided a more reliable measure of flame behavior than did the flame speed when wall effects were significant.

PLANNED ACTIVITIES FOR FY 1983

The flame propagation study will be extended to a compression-expansion environment. The focus will be on lean flame behavior. Provision will be made for laser sheet access through the igniter port. This will allow flow visualization of the unburned gas and definitive location of the flame front.
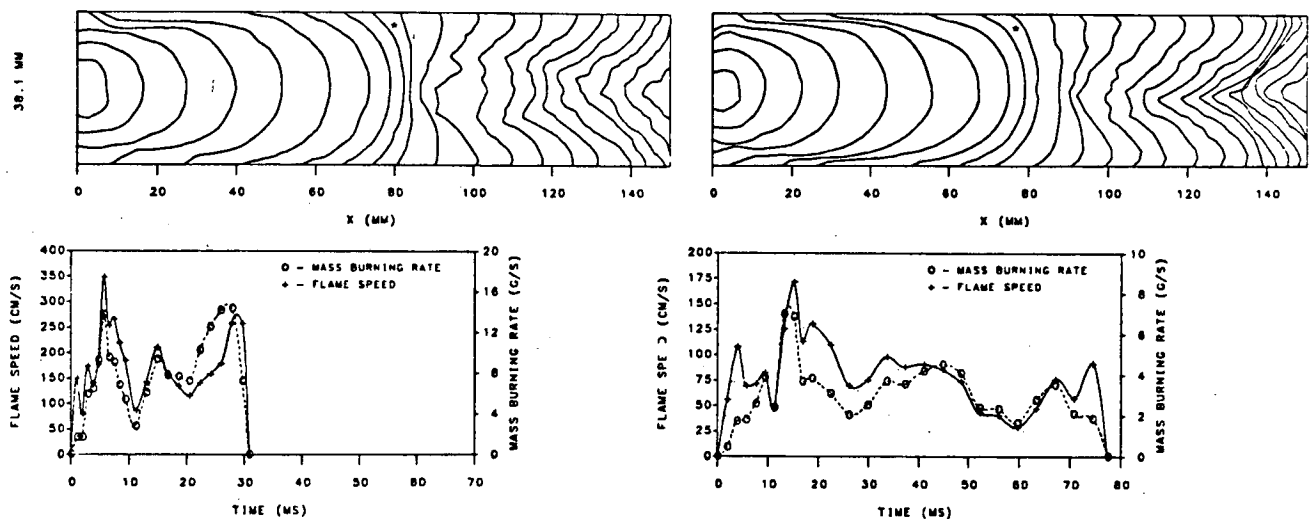

Figure 1. Comparison between ethylene/air (left) and methane/air (right) flame propagation in a constant-volume duct. Upper portions show flame shapes. (XBL 837-10551)

REFERENCE

1. Woodard, J.B., Hirvo, D.H., Greif, R., and Sawyer, R.F. (1981), "Wall Heat Transfer and Flame Propagation in a Constant Volume Duct," Western States Section/The Combustion Institute Paper No. 81-51 and Lawrence Berkeley Laboratory Report LBL-13021.

Figure 2. Flame shape in ducts of different length, for a methane/air flame; equivalence ratio is 1.0.

(XBL 837-10552)

Figure 3. Effect of equivalence ratio on maximum flame speed. (XBL 837-10553)

MEASUREMENT OF COMBUSTION-GENERATED POLLUTANT SPECIES*

N.J. Brown, E. Cuellar, and D. Lucas

Developing analytical techniques and demonstrating their suitability for characterizing combustion emissions is a crucial step in the sequence leading to source emission inventories and assessments of their health effects. Reliable measurement techniques are also needed to understand the mechanisms of pollutant formation and destruction.

Measuring such emissions and understanding their chemistry present particularly difficult analytical problems because of the high temperatures and ambient pressures of combustion processes. Many species are present, and the chemistry of pollutant formation and destruction mechanisms is multistep and frequently dominated by radical species which occur in low concentrations.

Our research is directed toward the development and characterization of techniques to quantify pollutant emissions from combustion systems utilizing synfuels. Emphasis is placed upon the measurement of nitrogen- and sulfur-containing species as well as gas-phase hydrocarbon species which are precursors to soot formation. Measurements of pollutant species are made in premixed laminar flames and in a turbulent-flow reactor in which the well-characterized combustion of prototype synthetic fuels occurs.

We are interested in the development and application of a novel optical absorption technique called tunable atomic line molecular spectroscopy (TALMS) for the measurement of pollutant species in combustion systems. This technique was pioneered at the Lawrence Berkeley Laboratory by Dr. Tetsuo Hadeishi and his co-workers and has been used in the analytical determination of atomic species and small molecules exhibiting sharp rotational electronic structure. The technique is based upon the Zeeman effect and is highly sensitive and selective. A detailed description of TALMS was presented in our earlier work,[4,5] and a summary will be presented below. We have completed a comparative study of nitric oxide measurement in the post-combustion environment of atmospheric pressure, premixed
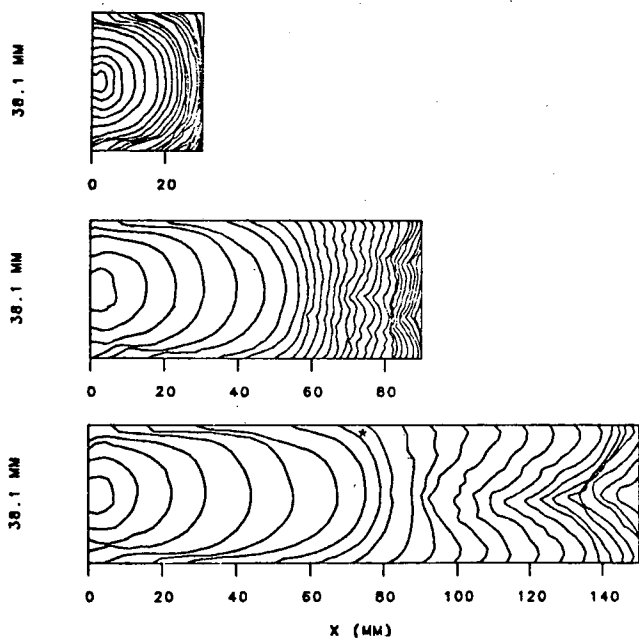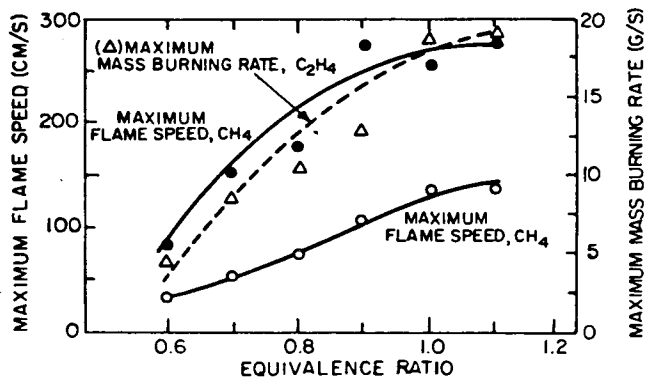
methane-air stoichiometric flames. One of the analytical techniques used is sample extraction with uncooled quartz microprobes, followed by chemiluminescent analysis in a specially constructed analyzer; the other technique is TALMS.

ACCOMPLISHMENTS DURING FY 1982

A schematic diagram of the experimental system is shown in Fig. 1. Methane-air flames were stabilized at atmospheric pressure on a water-cooled, porous-plug, flat-flame burner. The burner was mounted below the optical path of the TALM spectrometer through an opening in the optical bench. A micrometer-driven X-Y-Z translation stage permitted the burner to be moved with respect to the fixed optical beam. Stable methane-air flames were obtained over a wide range of equivalence ratios and total gas flows. We operated the burner at a total flow of 30,000 sccm, corresponding to a linear velocity of 17.7 cm/sec. Stable flames, at this flow, could be obtained at equivalence ratios ranging from 0.75 to 1.5. Radial and axial temperature profiles were measured in the flame with Pt/Pt–13% Rh thermocouples; radial profiles indicated the one-dimensional nature of

the flame, and axial profiles indicated the location of the post-combustion zone.

Gas samples were withdrawn from the flame through a 10-cm long, 1-mm i.d. uncooled quartz probe with an orifice diameter of 314 microns. The probe was mounted on the adjustable stage. A heated Teflon line connected the probe to a valve at the rear of a laboratory-built chemiluminescent gas analyzer (CLA) which measured nitrogen oxides (NO and NO_x). This analyzer is similar to commercially available instruments but incorporates several features that significantly reduce the corrections needed for viscosity and third-body quenching effects. The response of the CLA was measured and found to be linear in NO concentrations to at least 6000 ppm NO.

Koizumi et al[6] have employed TALMS to determine low concentrations of NO in a room-temperature absorption cell with high selectivity and sensitivity, using the accidental near-coincidence between the Cd-ion line at 124.438 nm and a discrete rotational-vibrational line in the $A^2\Sigma^+$ - $X^2\pi$, γ bands of NO. The basis for detection of molecules by tunable atomic line molecular spectroscopy is the splitting and polarization of atomic emission lines by an external magnetic field. By varying the strength of the

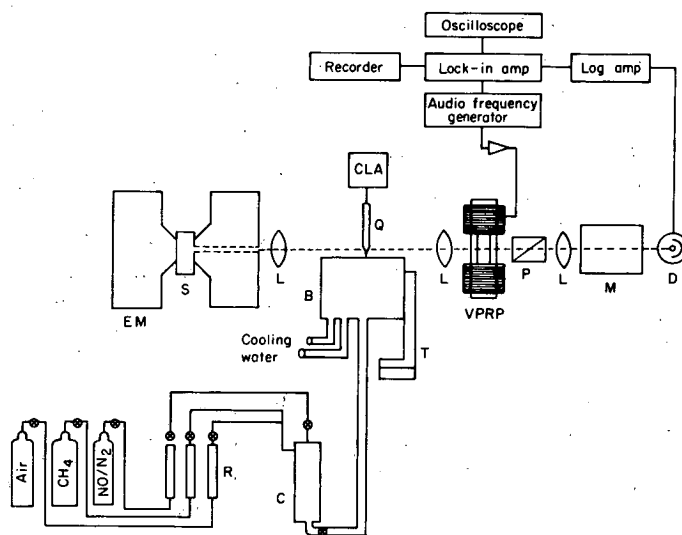Figure 1. Schematic diagram of the experimental apparatus: *EM*, electromagnet; *S*, atomic light source; *L*, quartz lens; *B*, porous plug burner; *T*, X-Y-Z translation stage; *Q*, uncooled quartz probe; CLA, chemiluminescent gas analyzer; *VPRP*, variable phase retardation plate; *M*, monochromator; *D*, photomultiplier tube; *C*, mixing chamber; *R*, rotameters.   (XBL 822-4489)

magnetic field, one of the Zeeman components of the Cd emission lines is tuned into exact coincidence with a discrete rotational-vibrational line of NO. The matching Zeeman component indicates the extent of absorption by NO, while the unmatched component indicates background absorption only. A differential measurement of the matched and unmatched Zeeman components of the Cd emission line provides a quantitative measurement of the NO in the optical path.

The TALM spectrometer is shown schematically in Fig. 1. The lamp consists of a sealed-off quartz U-tube containing a small amount of cadmium metal (natural-abundance Cd) and an inert buffer gas. Nichrome wire heaters wrapped around the U-tube heat the lamp to a few hundred degrees Celsius and provide a small amount of vaporized Cd ($\sim$1 torr), which is excited by an electric discharge through the gas. The lamp is housed between the poles of a Varian electromagnet, and the light, emitted parallel to the magnetic field, is focused with a quartz lens to a 2-mm-diameter spot above the burner surface. The variable phase retardation plate in combination with the linear polarizer allows for the alternate transmission of the matched and unmatched Zeeman components through the monochromator to the detector. The output of the photomultiplier tube is processed electronically and displayed on a strip-chart recorder.

To determine the conditions of maximum sensitivity, the differential absorption between Zeeman components was measured as a function of magnetic field strength, as shown in Fig. 2. Maximum sensitivity was obtained at 11 kilogauss, and all measurements were then taken at this field strength. The response of the TALM spectrometer to increasing NO concentration is shown in Fig. 3. In these experiments, the CH_4 and air were introduced into the gas-mixing chamber, varying amounts of 4.41% NO/N_2 gas were added, and the total mixture was then passed through a 7.5-cm-long flow cell placed in the optical path of the spectrometer. The observed signal was linear in NO concentration to about 1200 ppm NO. At 2000 ppm NO, the transmission through the absorption cell was about 28%, and the observed signal was 10% low with respect to the extrapolated linear response.

Vertical and horizontal profiles of NO concentration were measured, using the uncooled quartz probe and the CLA. Thermal NO is produced by oxidation of atmospheric N_2 via the Zeldovich mechanism, and the
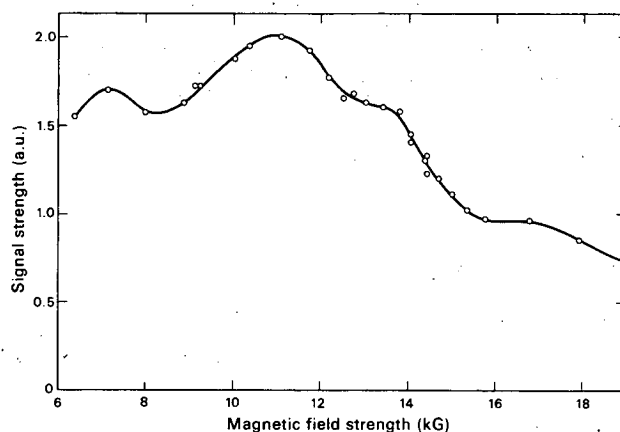

Figure 2. Differential absorption signal from NO as a function of magnetic field strength. Maximum sensitivity was observed at 11 kG. The Cd light source contained natural-abundance cadmium.   (XBL 825-9789)
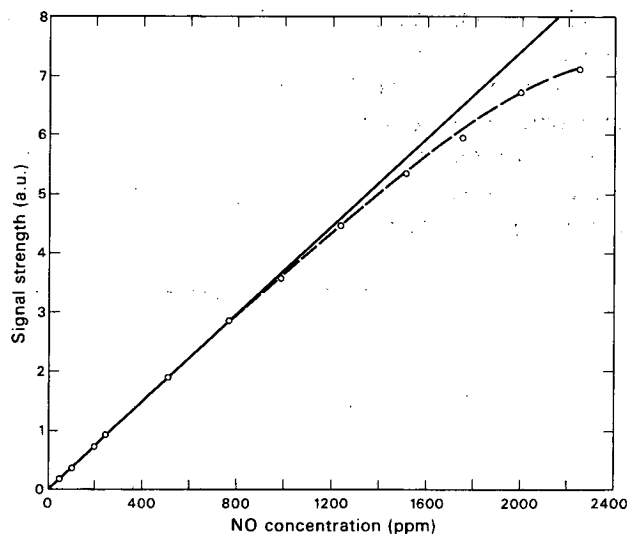
Figure 3. TALMS signal as a function of increasing concentration of NO. Solid line represents the linear response. At 1000 ppm NO, the measured signal is 2.8% below the extrapolated linear response. This deviation from linearity increases to 5.1% at 1500 ppm NO and to 10.4% at 2000 ppm NO.   (XBL 825-9794)

measured values of thermal NO are less than 10 ppm. The results of adding known amounts of NO to the burner and sampling with the probe are shown in Fig. 4. The probe position was kept constant at a height of 5.0 mm above the center of the burner surface. The dashed line represents 100% survival of NO. The survival of NO, defined as the ratio NO measured/NO added, is approximately 80%. The TALMS measure-

Figure 4. Nitric oxide measured vs. NO added as determined with an uncooled quartz probe and the chemiluminescent gas analyzer. The probe is fixed 5.0 mm above the center of the burner. Significant deviation from the dashed line representing 100% NO survival is observed. The thermal NO concentration is 16 ppm. (XBL 825-9793)
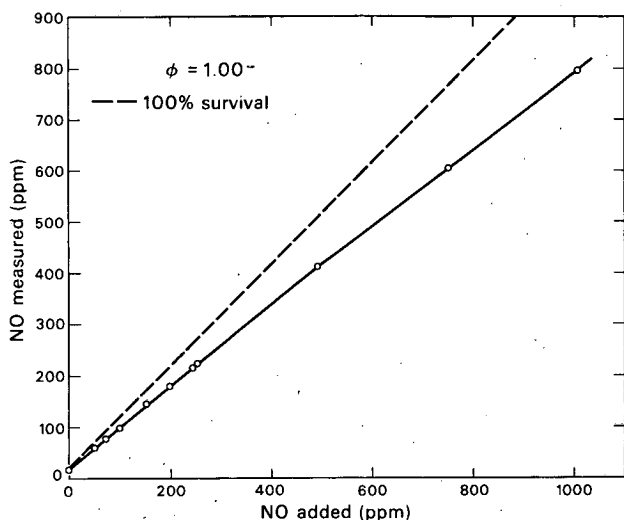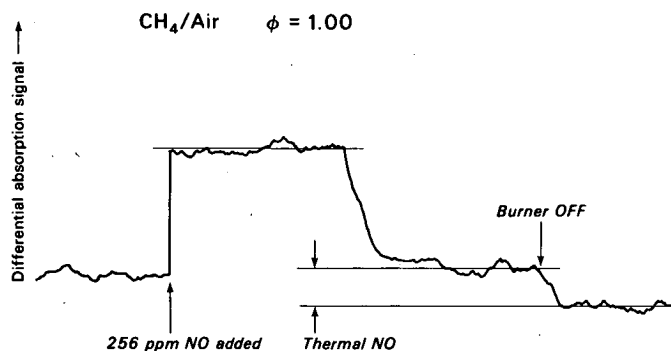

Figure 5. Strip-chart recorder trace showing the differential absorption signal obtained by TALMS. The recorder was stopped when NO was added, and restarted when the signal stabilized (~1 minute later). The maximum differential absorption signal corresponds to 256 ppm added NO plus thermal NO. The decay of this signal corresponds to halting the added NO; turning the burner off results in the loss of thermal NO. (XBL 825-9797)

ments of NO were obtained by doping the burner gases with known amounts of NO. A typical recorder trace of the differential absorption signal observed by thermal NO and added NO is shown in Fig. 5. A range of NO concentrations from 50 to 1000 ppm was added to the burner, and a plot of the observed signal strength as a function of NO added is shown in Fig. 6. Extrapolation to zero doping of NO results in an estimate of the thermal NO.

Table 1 summarizes the data shown graphically in Figs. 4 and 6. In both cases, the experimental points were fitted by a least-squares analysis, and the regression constants obtained were used to calculate the measured NO_{CLA} and NO_{TALMS} for given added NO. The NO_{TALMS} were determined assuming no nitric oxide losses in the flame. At NO concentrations comparable to those used by other experimenters, the ratio NO_{TALMS}/NO_{probe} assumes values similar to those reported in the literature for comparisons between optical and probe measurements. These tabulated ratios would be somewhat smaller, however, if a loss mechanism were assumed for the NO_{TALMS} values. The TALMS technique offers greater sensitivity than previous *in situ* optical measurements of NO. At these lower NO concentrations, the discrepancy between *in situ* and probe measurements is significantly greater.

Figure 6. Signal strength measured by TALMS vs. NO added, for a stoichiometric CH_4-air flame ($\Phi = 1.00$). A least-squares fit of the data points results in the equation $S = 3.07 \times 10^{-4}$ [NO]$_{added}$ + 1.87×10^{-2}, where S is the signal strength in arbitrary units, and the coefficient of correlation is 0.987. (XBL 825-9796)

In a series of separate experiments, measurements of ammonia emissions in the exhaust gases of a lean-burning laboratory combustion tunnel were made with a variety of analytical techniques; a common sampling method allowed for meaningful intercomparisons. Combustion parameters were varied from cold flow conditions to a range of equivalence ratios, sampling techniques, and dopant concentrations. We have reviewed the advantages and disadvantages of these and other techniques in detail in a recent publication.[7]

Table 1. Measured concentrations of NO in the postcombustion environment.

NO$_{added}$ (ppm)	NO$_{CLA}$ (ppm)	NO$_{TALMS}$ (ppm)	$\dfrac{NO_{optical}}{NO_{probe}}$
50	61	110	1.80
75	81	136	1.68
100	100	160	1.60
150	139	210	1.51
200	178	260	1.46
250	217	310	1.43
500	411	560	1.36
750	605	810	1.34
1000	799	1060	1.33
1250	993	1310	1.32
1500	1187	1560	1.31

PLANNED ACTIVITIES FOR FY 1983

Emphasis will be placed upon performing a comparative study of SO$_2$ sulfur dioxide measurements in the postcombustion environment. Sulfur dioxide will be measured with probe sampling and and a continuous gas analyzer that detects the emission from SO$_2$ fluorescence. Quenching measurements for the chaperone gases present in combustion mixtures will be performed. TALMS will also be used to detect SO$_2$. Construction of a molecular-beam sampling system interfaced with a quadrupole mass spectrometer will be initiated. This system will monitor gas-phase hydrocarbon species which are precursors to soot formation in the combustion of alternate fuels.

REFERENCES

1. Hadeishi, T. and McLaughlin, R.D. (1971), "Hyperfine Zeeman Effect: Atomic Absorption Spectrometer for Mercury," *Science 174*, p. 404; Hadeishi, T. (1972), "Isotope Shift Zeeman Effect for Trace-Element Detection: An Application of Atomic Physics to Environmental Problems," *Appl. Phys. Lett. 21*, p. 438.
2. Koizumi, H., Hadeishi, T., and McLaughlin, R.D. (1979), "Detection of Small Molecules by Magnetically Tuned Frequency Modulated Atomic Line Sources," *Appl. Phys. Lett. 34*, p. 382.
3. Koizumi, H., Hadeishi, T. and McLaughlin, R.D. (1979), "A New Technique for the Determination of Isotopic Species Using Zeeman Scanning of an Atomic Line," *Appl. Phys. Lett. 34*, p. 277.
4. Cuellar, E. and Brown, N.J. (1981), "Combustion Diagnostics by Tunable Atomic Line Molecular Spectroscopy," *First Specialists Meeting (International) of the Combustion Institute 2*, p. 545.
5. Cuellar, E. and Brown, N.J. (1982), "Detection of S$_2$ by Magnetic Tuning of a Chromium Atomic Emission Line," *J. Phys. Chem. 86*, p. 1966.
6. Koizumi, H., Hadeishi, T., and McLaughlin, R.D. (1980), "Nitric Oxide Determination by a Zeeman Tuned Frequency Modulated Atomic Line Source," *Anal. Chem. 52*, p. 500.
7. Lucas, D. and Brown, N.J. (1983), "The Measurement of Ammonia in Lean Combustion Exhaust Gases," *Combustion and Flame. 49*, p. 283.

COMBUSTION IN A TURBULENT BOUNDARY LAYER*

R.K. Cheng, F. Robben, and L. Talbot

Combustion in premixed gases sustained in a turbulent boundary layer over a strongly heated surface is a problem with many engineering and fire safety applications. It is also a unique flow configuration for the study of the mutual interaction between combustion and fluid dynamic turbulence. Turbulence structures and their development in isothermal turbulent boundaries have been studied quite extensively in many experimental and theoretical investigations. Since the turbulent boundary layer is well-characterized, the effect of combustion heat release can be readily identified. Also, by adjusting the flow and wall temperatures, a wider range of fuel-to-air ratios can be investigated than is possible with conventional flame configurations.

In FY 1981, we reported density and velocity statistical measurements in isothermal, heated, and

reacting turbulent boundary layers. Some of the conclusions we have drawn are as follows. The large-scale turbulent structures in the layers are found to dominate the development of both the thermal and flame structures within the boundary layer. In the case of the nonreacting layer, strong wall heating is found not to influence the intensity of the root-mean-square (rms) velocity fluctuations throughout the layer, or the Reynolds stress distributions, as compared to the isothermal layer. However, when combustion is present, the Reynolds stress in the wall region is significantly reduced compared with the isothermal layer at the same free-stream Reynolds number.

ACCOMPLISHMENTS DURING FY 1982

Velocity fluctuations and correlations in isothermal, heated, and reacting turbulent boundary layers have been studied in more detail with a two-component laser Doppler velocimetry (LDV) system that allowed simultaneous measurement of two local velocity components. The data were reduced to obtain conditional statistics of the Reynolds stress, which provided further insight into the cause of Reynolds stress reduction by combustion in the wall region.

The experimental conditions of free-stream velocity, U_∞, of 19 m/s, wall temperature, T_w, of 1000 K, and ethylene/air equivalence ratio of 0.35 are similar to those of our previous studies.[1-4] Quantities deduced from the data included two mean velocities, U and V, two rms velocity fluctuation intensities u' and v', the Reynolds stress $-\overline{uv}$, and the third moments $\overline{u^3}$, $\overline{vu^2}$, $\overline{uv^2}$, and $\overline{v^3}$. These results compare well with those we obtained using a single-component LDV system. Since the two-color LDV provides a direct measurement of the velocity correlations, this comparison demonstrates that both techniques are reliable for measurements of velocity correlations, although the indirect method is more time-consuming.

Conditional analysis is a powerful technique for studying the Reynolds stress contribution associated with the movement of the large-scale turbulent structures. By sorting the Reynolds stress contribution into four velocity correlation quadrants according to sign, it has been shown that in the isothermal turbulent boundary layer, the major contributions are due to in-rushing of high-momentum fluid from the free stream towards the wall (inrush) and bursting of low-momentum fluid from the wall region into the

outer region (bursting). Our first concern was to validate the technique by comparing the isothermal layer results with hot-wire measurements reported in the literature, since the two-color LDV technique has not been used extensively for deducing conditioned Reynolds stress statistics. The data were reduced to show the fraction of contributions from each of the four quadrants and analyzed to examine the large contributions of $-\overline{uv}$ in each quadrant (the so-called "hole" analysis). As shown in Fig. 1, our results compared extremely well with typical hot-wire results.

Similar data analyses were made for the heated and the reacting boundary layers. Typical results are shown in Fig. 2. In the heated layer, no significant change in the contributions was observed, except for a slight decrease in the contribution from the burst event at positions close to the end of the heated section. In the reacting layers, contributions in three quadrants remained unchanged, compared to the isothermal and heated layers. At positions near the heated wall, significant reduction was found in the quadrant associated with the burst event. Since the bursting cycle in the reacting layer consisted essentially of inrushing of cold reactants and bursting of hot products, the reduction in the burst quadrant indicated that combustion heat release caused the turbulence fluctuations in the products to be less correlated.
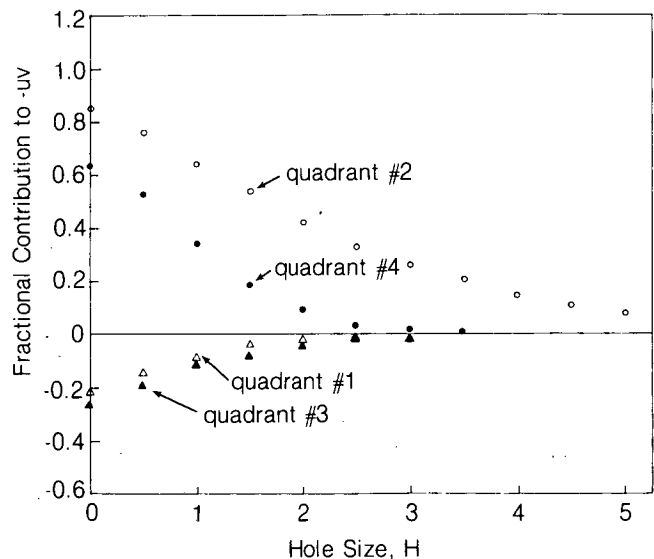

Figure 1. Quadrant analysis of the Reynolds stress in an isothermal turbulent boundary layer at $y/\delta u = 0.7$.
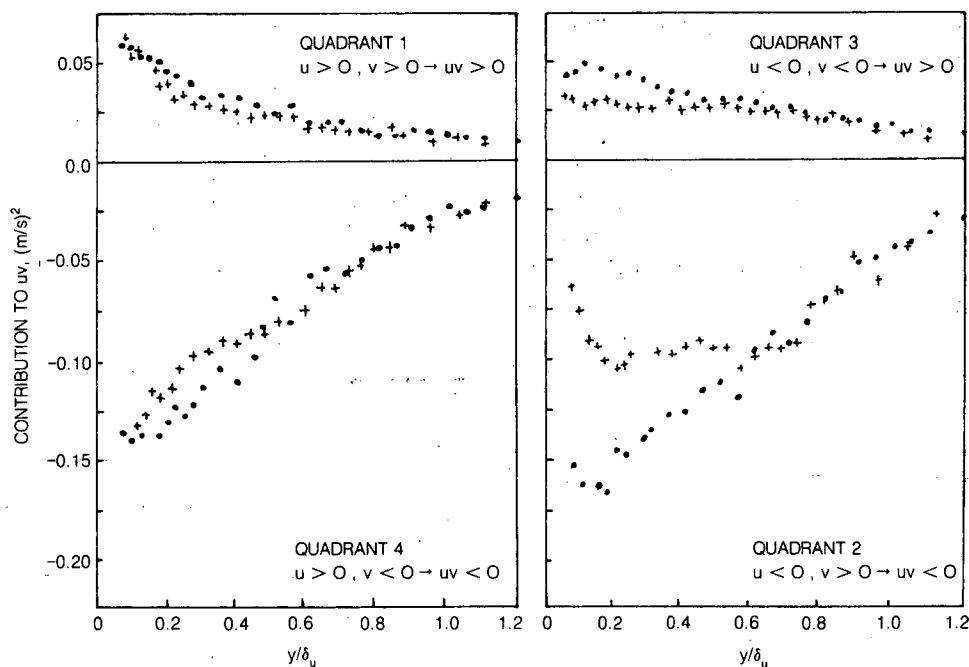
(XBL 834-9425)

Figure 2. Comparison of the contributions of conditional velocity correlations in heated (•) and reacting (+) turbulent boundary layers. (XBL 834-9424)

PLANNED ACTIVITIES FOR FY 1983

In FY 1983, we expect to determine the statistical spatial character of the thermal and flame structures seen in the schlieren movies by using the two-point Reyleigh scattering technique. This technique simultaneously measures the density fluctuations at two points separated by an adjustable distance. These data will be used to obtain spatial and temporal scales of the density fluctuation, their joint probability density functions (jpdf), and higher-order moments. The overall features and development of the thermal and flame structures revealed by schlieren observation can be validated by this quantitative local measurement.

The two-point density correlation is expected to yield a more complete description of the physical processes during ignition and transport of packets of reacting fluid in the heated wall region. This information should provide further insight into the observed reduction of Reynolds stress associated with the bursting event. It will also be of particular interest to determine how strongly the combustion-heat-release-induced local flow acceleration is related to the observed change in turbulence intensities. In a

reacting layer, nonreacting heated fluid and reacting fluid co-exist. Schlieren observations and single-point density statistics cannot differentiate the change in density associated with the two different types of fluid. Analysis of the two-point density correlations should be useful to identify some characteristic features of the reacting fluids and to map the regions where chemical reactions occur; these regions can then be compared with the regions where changes in turbulence intensities take place.

Other useful quantities that can be deduced are the periodicity of the passage of the structures and their overall geometry, such as their inclination with respect to the wall. These results can then be compared with the large-scale turbulent structures reported in many investigations. Such comparisons should show whether or not the thermal and flame structures scale with the same free-stream variables as the large turbulence structures.

REFERENCES

1. Ng, T.T. (1981), *Experimental Study of a Chemically Reacting Turbulent Boundary Layer*, Ph.D. Thesis, Department of Mechanical Engineering,

University of California, Berkeley, Lawrence Berkeley Laboratory Report LBL-13325.

2. Ng, T.T., Cheng, R.K., Robben, F., and Talbot, L. (1982), "Combustion-Turbulence Interaction in the Turbulent Boundary Layer Over a Hot Surface," in Nineteenth Symposium (International) on Combustion, The Combustion Institute, p. 359.

3. Ng, T.T. (1981), "Measurements of Velocity Fluctuation Correlations using a Single-Component Laser Doppler Velocimetry System," submitted to AIAA Journal; Lawrence Berkeley Laboratory Report LBL-13702.

4. Ng, T.T., Talbot, L., Cheng, R.K., and Robben, F. (1982), "The Turbulent Boundary Layer over a Flat Plate with Strong Stepwise Heating," in International Symposium on Application of Laser Doppler Anemometry to Fluid Mechanics, in press.

5. Cheng, R.K., and Ng, T.T. (1983), "The Influence of Combustion on Reynolds Stress in a Strongly Heated Turbulent Boundary Layer," in preparation.

TURBULENT BURNING VELOCITY IN PREMIXED TURBULENT FLAMES*

R.K. Cheng, T.T. Ng, F. Robben, and L. Talbot

The study of turbulent burning velocity is part of our continuing experimental program in premixed turbulent combustion. The overall objective is to investigate the interaction between fluid dynamic turbulence and combustion; together these constitute the majority of combustion phenomena. The flame configuration we have chosen to study is unconfined, rod-stabilized, V-shaped flames propagating in a turbulent flow generated by a grid or perforated plate. This configuration is similar to those found in many practical burners but is more idealized because it is free of geometry and flow constraints. In FY 1981, we reported velocity statistical data obtained by the use of laser Doppler velocimetry (LDV).[1] Reported here

are the turbulent burning velocities deduced from the statistical data.

Turbulent burning velocity, S_t, is a measure of the most significant aspect of turbulent combustion—the increase in flame propagation speed above the laminar burning speed, S_u, due to fluid dynamics turbulence. It is therefore useful both for the design of more efficient combustion systems and for comparison with theoretical predictions. Determination of turbulent burning velocity has been the subject of many experimental investigations, and data obtained in many stabilized and unstabilized flame configurations have been reported. In general, these data show an increase in S_t with increasing turbulence intensity, and many empirical parameters have been used to correlate these data. However, a universally applicable formula has yet to be determined.

ACCOMPLISHMENTS IN FY 1982

The conventional method for deducing the turbulent burning velocity in a V-shaped flame is to measure the velocity and direction of the flow entering the flame region and establish a flame surface representing the overall geometry of the flame brush. This method is not highly accurate because the flame brush is much thicker than the laminar flame thickness and the value of the turbulent burning velocity depends on where the mean flame surface is defined. For example, as demonstrated in Fig. 1, which shows the velocity vectors measured in the flow field of a flame we studied, the S_t determined with respect to the cold boundary would be much larger than the S_t determined with respect to the mean flame surface. Different investigators have used one surface or the other to define the turbulent burning velocity, and as a result, the data in the literature are not very consistent. Shown in Fig. 2 are the turbulent burning velocities determined for our V-shaped flame using the mean flame surface. These data are compared with the correlation obtained by Abdel-Gayed and Bradley.[2] As can be seen, our data are lower than the correlation. Furthermore, some of our results are even lower than the laminar burning velocity.

To improve the accuracy and consistency of these measurements, a method based on an effective flame orientation is proposed. In our turbulent flame with relatively low incident turbulence, the flame sheet is thin and convoluted. This type of turbulent flame is generally classified as wrinkled laminar flame. The
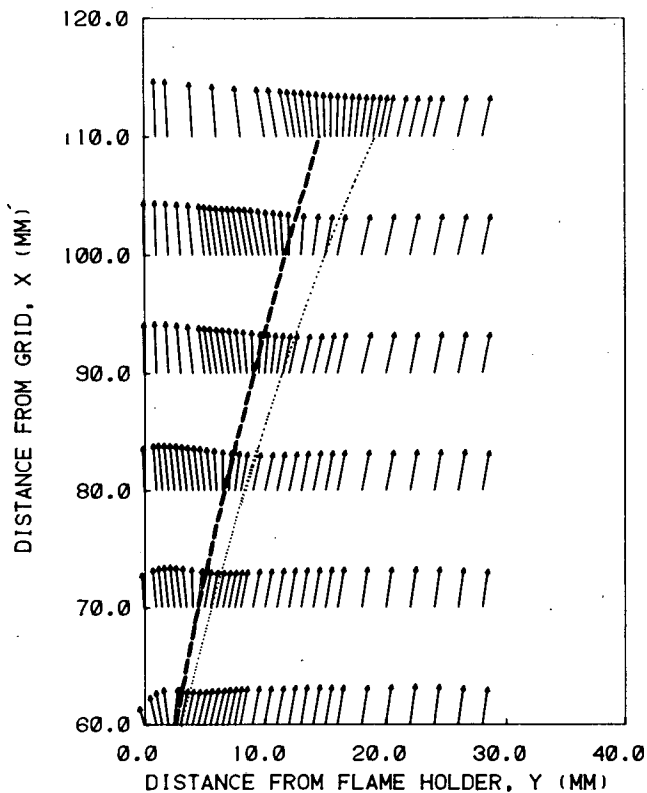
Figure 1. Two-dimensional velocity vectors in the flow field of a V-shaped flame in grid-generated turbulence. Dashed curve represents the time-mean flame surface, dotted curve the cold boundary.   (XBL 834-9423)
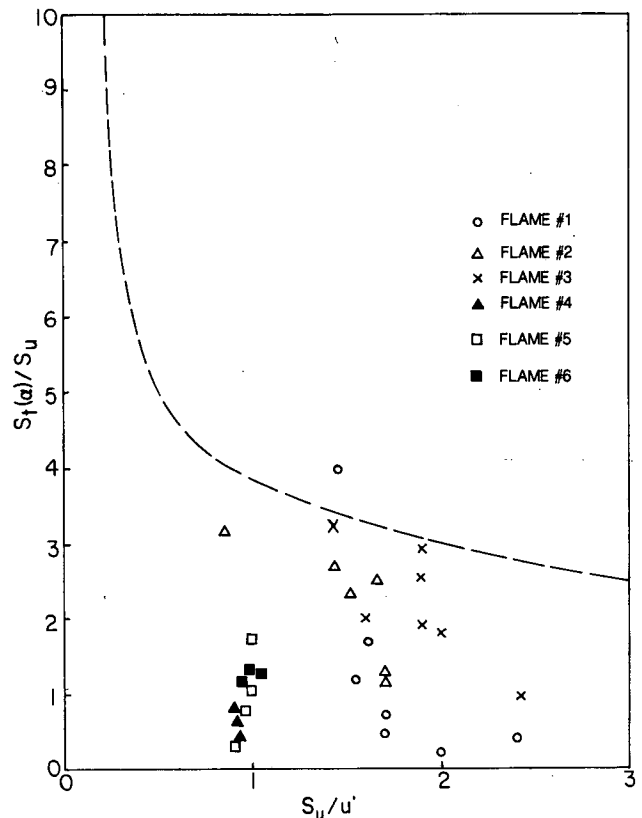

Figure 2. Comparison of turbulent burning velocity, defined with respect to mean flame surface, with correlation of Abdel-Gayed and Bradley[2] (dashed curve).

(XBL 834-9422)

interaction of the thin fluctuating flame sheet with the turbulent flow causes overall flow deflection, as shown in Fig. 1. We have used this fluctuating thin flame phenomenon to explain both the increase in turbulence intensities and Reynolds stress in the flame region.[1]

By applying a conserved tangential velocity criterion to the flow through the flame region, an effective flame orientation for the fluctuating thin flame can be deduced. The turbulent burning velocities defined with respect to this effective flame orientation are shown in Fig. 3. These results compare with Ref. 2 much better than do those shown in Fig. 2. Our analysis demonstrates that for the determination of turbulent burning velocity to be of physical significance, the flame surface criterion is of crucial importance.

PLANNED ACTIVITIES FOR FY 1983

The apparent increase in turbulent intensities in the flame region and the true makeup of the Reynolds stress will be investigated further. A two-color LDV system will be used to measure two velocity components simultaneously. Analysis of the data will enable us to determine the contribution to the turbulent intensities caused by the intermittent measurement of the velocities in the burnt and unburnt states as the thin flame sheet fluctuates past the stationary laser probe. Conditional statistics of the Reynolds stress will be useful to clarify the physical phenomenon causing the increase in Reynolds stress.
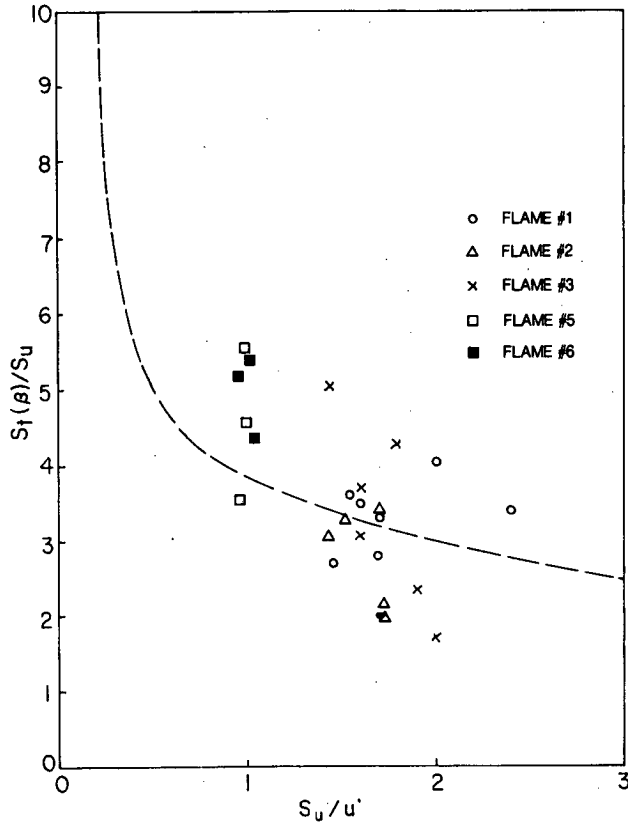
Figure 3. Comparison of turbulent burning velocity, defined with respect to the effect of flame orientation, with the correlation of Abdel-Gayed and Bradley[2] (dashed curve). (XBL 834-9421)

PLASMA IGNITION STUDIES*

A.K. Oppenheim, J. Cavolowsky, C. Edwards, K. Hom, and H.E. Stewart

ACCOMPLISHMENTS DURING FY 1982

Following our earlier investigations of the operating characteristics of jet igniters,[1-4] we have studied the performance of an array of plasma ignition systems in a CFR engine. Included among the igniters were a conventional spark plug, a surface discharge plug, and several types of plasma jet. Information was obtained to determine the specific emissions, mean effective pressure, ignition delay, and duration of the exothermic combustion process. Statistical analysis was performed on the pressure-derived data (mean effective pressure, ignition delay, and combustion duration) in order to quantify the cycle-to-cycle variation in the engine and thus the stability of operation.

The results demonstrate the advantages of enhanced ignition systems over a conventional spark discharge. Figure 1 displays the ignition delay and combustion duration for a typical plasma jet and a standard spark system. It is apparent that the plasma allows for an extension of the lean operating limit of the engine from 0.68 to 0.53 in equivalence ratio. In addition, the plasma jet significantly reduces the ignition delay throughout the lean range of equivalence ratios. Combustion duration remains comparable for the two systems down to an

REFERENCES

1. Cheng, R.K., and Ng, T.T. (1983), "Velocity Statistics in Premixed Turbulent Flames," Combustion and Flame, in press.

2. Abdel-Gayed, R.G., and Bradley, D. (1977), "Turbulent Flame Propagation in Premixed Gases: Theory and Experiment," in Sixteenth Symposium (International) on Combustion, The Combustion Institute, p. 1752.
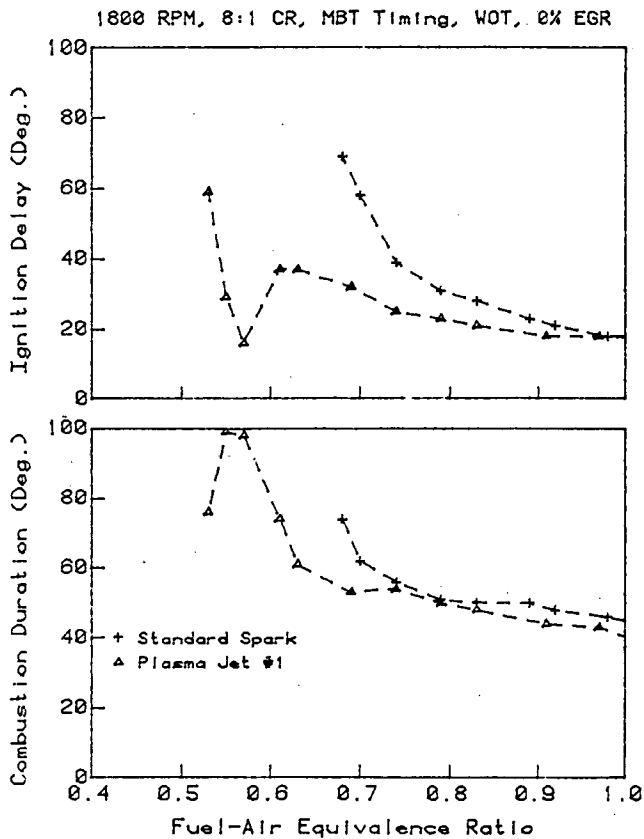
Figure 1. Ensemble-averaged values of ignition delay and combustion duration for the standard-spark and plasma-jet ignitors. (XBL 837-10554)

Figure 2. Ensemble-averaged values of, and cyclic variation in, indicated mean effective pressure for the standard spark and plasma-jet ignitors. (XBL 837-10555)

equivalence ratio of 0.72, after which the plasma jet provides for an extension of ~0.08 in equivalence ratio before exhibiting an increase similar to that of the standard spark.

Figure 2 shows the work output of the two systems expressed in terms of mean effective pressure. Data obtained with plasma jet and standard spark exhibit similar characteristics down to an equivalence ratio of 0.7. At leaner mixtures, the engine run with a standard spark manifests the effects of misfire and soon becomes completely inoperable, as evidenced by the sharp discontinuity in the coefficient of variation. When it is run with a plasma jet, however, misfire does not occur; instead, as the mixture is leaned, the work output decays to zero while the cyclic variation grows to infinity.

Emission characteristics for the two systems remain virtually the same, NO, HC, and CO being primarily a function of equivalence ratio rather than of the particular method of ignition.

PLANNED ACTIVITIES FOR FY 1983

Two phases of investigation are envisaged:
(1) Study of performance of characteristics of plasma jet ignition systems in a CFR engine along the same lines as reported here, but with the addition of exhaust-gas recirculation.
(2) Laser cinematographic study of plasma jet ignition, using a high-pressure combustion cell (bomb) and a single-pulse machine (Mark II).

REFERENCES

1. Weinberg, F.J., Hom, K., Oppenheim, A.K. and Teichman, K. (1978), "Ignition by Plasma Jet," Nature 272, p. 341.
2. Oppenheim, A.K., Teichman, K., Hom, K., and Stewart, H.E. (1978), "Jet Ignition of an Ultra-

Lean Mixture," *SAE Transactions (Sect. 3) 87*, p. 2416.

3. Cetegen, B., Teichman, K.Y., Weinberg, F.J., and Oppenheim, A.K. (1980), "Performance of a Plasma Jet Igniter," Paper No. 800042, presented at the Society of Automotive Engineers Congress and Exposition, Detroit, Michigan, 1980.

4. Dale, J.D. and Oppenheim, A.K. (1981), "Enhanced Ignition for I.C. Engines with Premixed Gases," SAE Technical Paper No. 810146, presented at the Society of Automotive Engineers International Congress and Exposition, Detroit, Michigan, 1981.

Figure 1. Schematic of experimental apparatus for two-point Rayleigh scattering measurements. (XBL 823-8761)

STRUCTURE OF A V-SHAPED TURBULENT FLAME*

M. Namazian, J. Hertzberg, L. Talbot
and F. Robben

In the quest for more efficient combustors, the interaction between turbulence and combustion must be understood at a fundamental level. To accomplish this, the structure of a V-shaped premixed turbulent flame is being studied. Two experimental methods are employed. The first is a two-point Rayleigh scattering technique that gives the density of the gas at two points in space.[1] The second is a visualization of the flame front by light scattering from oil particles fed into the flow.

ACCOMPLISHMENTS DURING FY 1982

Two-Point Rayleigh Scattering

Gas density was measured simultaneously at two separate points in a V-shaped turbulent flame. The measurements were performed by the Rayleigh scattering method. Figure 1 shows a schematic diagram of the premixed combustor and collection optics. We used two independent sets of scattered-
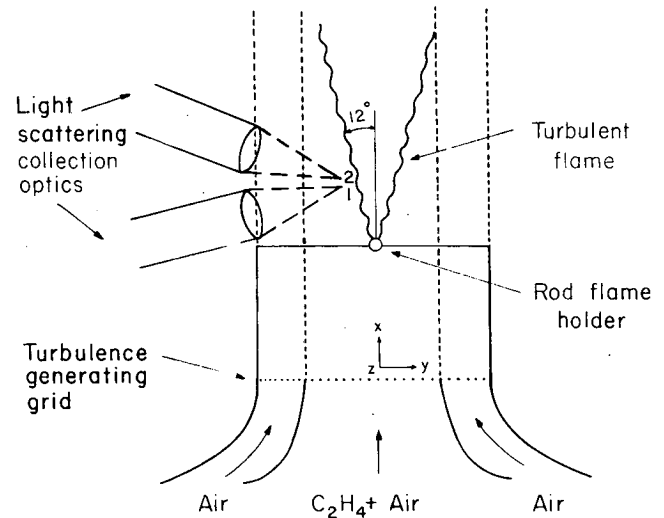
light collection optics plus a method of splitting the laser beam and varying the separation of the two sampled points. As indicated in Fig. 1, the two-point measurements were performed in three directions: x, along the jet; y, normal to the jet and the flame holder; and z, normal to the jet and parallel to the flame holder. In this article, we refer to the two measurement points as points 1 and 2. The two-point density measurements were performed in ethylene-air, at an equivalence ratio of 0.60. The jet velocity was 7 m/sec.

Important information on the structure of the flame can be obtained by analyzing the joint probability density function (jpdf) of the two-point Rayleigh scattering density measurements. Figure 2 shows the jpdf of densities measured at two points separated by 1.2 mm in the y direction; the inset shows the relative position of the sampled points with respect to the flame brush. Note that point 2 lies further into the flame zone than point 1. Also note that the density axes are normalized by the unburned gas density.

Since the laminar flame thickness (about 1 mm) is smaller than the turbulent flame zone (about 5 mm), the jpdf of the densities principally shows the probabilities of finding either burned or unburned gas at the point of measurement. In Fig. 2, the jpdf has three peaks, indicating that the probability of simultaneously finding burned gas at point 1 and unburned gas at point 2 is zero. This result is found to be true for all positions of the two points across the flame.

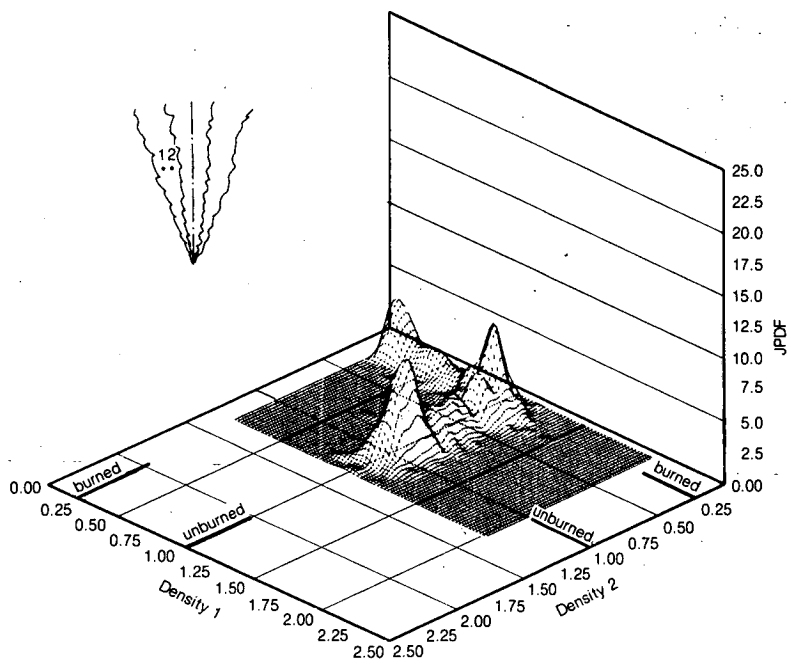For the low-intensity-turbulence regime of the

Figure 2. Joint probability density function of the two-point Rayleigh scattering density measurements. The points 1 and 2 are separated by 1.2 mm across the flame, as shown in the inset.   (XBL 825-9994)

present experiments, it is generally agreed that the physical structure of the turbulent flame zone consists of a wrinkled laminar flame that fluctuates in position and shape. Under these conditions, the wrinkled laminar flame is continuous, with no ruptures or pockets of flame. On the other hand, higher turbulence intensity of sufficient length would cause progressive disintegration of this wrinkled flame, giving rise to discontinuities in the structure and to isolated flamelets. Such flamelets are shown schematically in Fig. 3(a). If the present flame contained flamelets, there should be some cases where burned gas occurs at point 1 and unburned gas at point 2. Since such cases have not been found (the missing peak in Fig. 2), we conclude that there are no flamelets. The same reasoning shows that the present flame cannot be as highly convoluted as sketched in Fig. 3(b). However, the flame orientations sketched in Figs. 3(c), (d), and (e) are possible, and each causes one of the peaks in the jpdf shown in Fig. 2.

For cases where the axis of the points lies either in the flow direction, x, or in the plane of the flame, z, the jpdf's show four peaks, indicating the presence of all possibilities of burned and unburned gas at the sampled points.

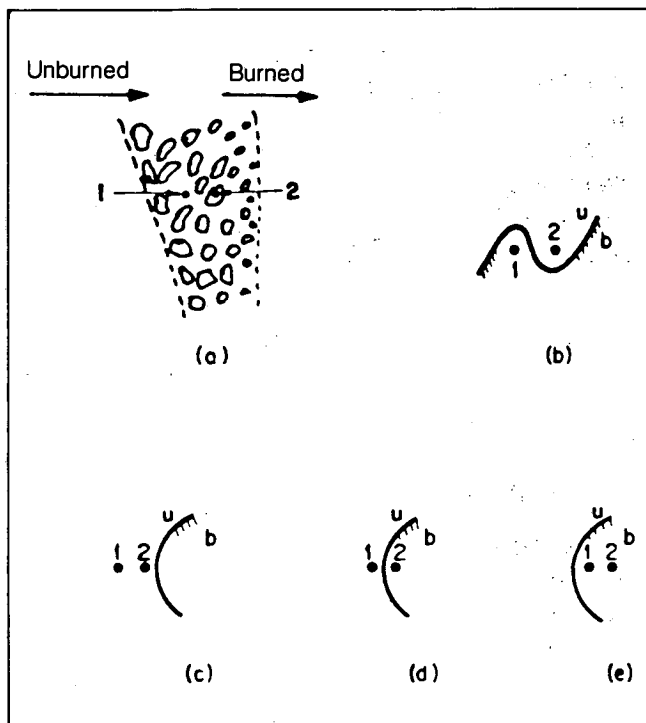We will present below the result of flame-front visualization. This result also supports our conclusion

Figure 3. Examples of possible flame structure and orientation with respect to the two measurement points. Flamelets (a) and convolutions (b) are unlikely in the present flame. The orientations shown in (c), (d), and (e) each contribute to one peak in Figure 2.   (XBL 834-9441)

that the thick flame brush (about 5 mm) consists of a thinner reaction front (about 1 mm) that fluctuates in shape and position. Here, we will present some information on the fluctuation of the reaction front across the flame brush.

Further analysis of the two-point measurements allows the derivation of the probability density function (pdf) for the flame-front position. By measuring the fraction of time that the front was found between the two measurement points and repeating this measurement across the width of the brush, we derived the bell-shaped curve in Fig. 4. The S-shaped curve shows the corresponding mean density profile. The measurements were made 80 mm above the flameholder, and the separation between the two points was 1.2 mm, slightly greater than the laminar flame thickness of I mm.

The pdf of the flame-front position is almost a normal distribution, with the mean at the center of the flame brush. This is also true for experiments at different heights above the flame-holding rod.

Flame-Front Visualization Method

A time-resolved qualitative method of delineating a two-dimensional flame sheet has been developed. As shown in Fig. 5, premixed ethylene and air is seeded with a translucent cloud of oil droplets. The droplets are formed from liquid silicone oil in a sprayer and average 1 micron in diameter. Because of their small size, they are easily convected with the flow. As the cloud passes through the rod-stabilized flame, the droplets evaporate and burn; the burned gases are now transparent. The entire

system is illuminated with a sheet of laser light, created with a simple cylindrical lens. The oil cloud scatters the laser light and essentially "lights up" while the unseeded and the burned regions remain dark. The flame thus appears as the interface between the bright and dark areas.

Because of the intensity of the laser sheet, the result can be photographed and filmed at high speed, providing time resolution. One such photograph is shown in Fig. 6; the equivalence was 0.6 and the jet velocity was 2 m/sec. The flow is turbulent, resulting
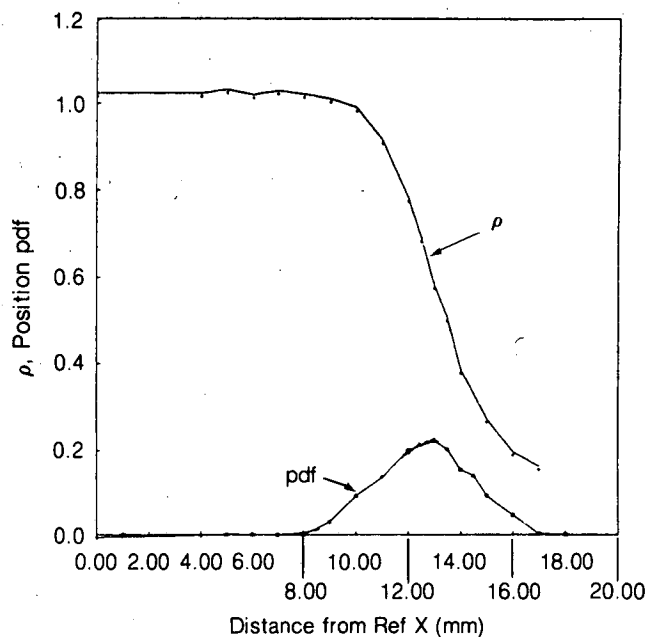

Figure 4. Measured mean density ρ and the pdf of the reaction front position across the flame.   (XBL 834-9442)
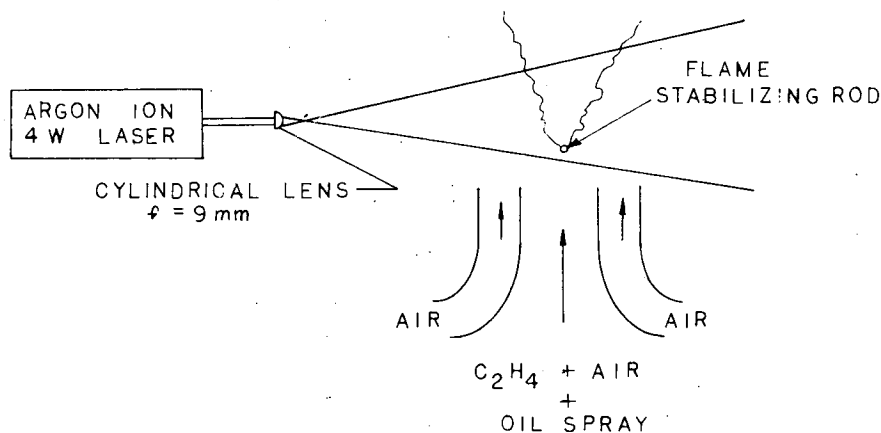

Figure 5. Schematic of the set-up for flame-front visualization. (XBL 834-9443)
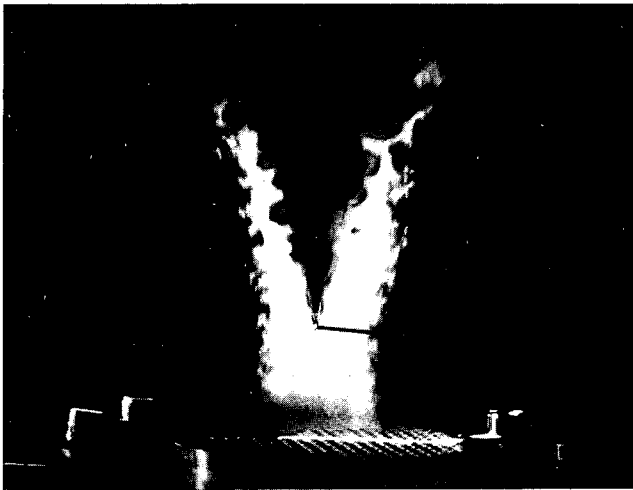
Figure 6. A V-shaped turbulent flame front that has become visible due to the evaporation of oil particulates on the hot side. Unburned areas outside the front are illuminated by particulate scattering of laser light; dark areas within the V are burned. (XBB 8210-9615)

in the irregular appearance of the flame, which is seen as the edges of the V shape. The reaction front appears to be continuous, supporting the results of our two-point density measurements.

PLANNED ACTIVITIES FOR FY 1983

• The structure of a flame with higher incoming turbulence intensity will be studied.

• Further two-point Rayleigh scattering · data, which have already been taken, will be reduced.

• A new program to investigate flame stabilization behind bluff bodies will be started. The basic features of the flame stabilization region will be mapped by first measuring the density and then the velocity of this region. The measurements will also be done near the blow-off velocity.

REFERENCE

1. Namazian, M., Talbot, L., Robben, F. and Cheng, R. K. (1982), "Two-Point Rayleigh Scattering Measurements in a V-shaped Turbulent Flame," in *Nineteenth Symposium (International) on Combustion*, p. 487.

TESTS AND CRITERIA FOR FIRE PROTECTION OF CABLE PENETRATIONS AND ELECTRICAL CABINETS*

R.B. Williamson, F. L. Fisher, and F.W. Mowrer

The spread of fire in nuclear reactors depends critically on the barrier qualities of the cable penetrations in fire-resistant walls and floor/ceiling assemblies. A new ASTM standard, E-814,[1] is now available for the evaluation of "penetration fire stops." This new fire test is similiar to the earlier ASTM E-119, except that it is written specifically to cover assemblies, such as cable and pipe penetration devices, in fire-rated construction. The new standard calls for the pressure differential in the test furnace to be measured and specifies how it should be determined.

The ASTM E-119 Fire Endurance Test Method has been used for seventy years to qualify unpenetrated wall and floor/ceiling assemblies. However, it became evident that there was a need for special attention when such assemblies contained cable penetrations, and the new standard, ASTM E-814, was developed for this purpose. The validation of E-814 and the concept of requiring positive pressure in the test furnace have been the focus of this project for the last four years; recently, a new aspect was added, namely the fire safety of electrical cabinets.

One way the potential spread of fire in nuclear reactors can be controlled is by fire-resistant wall and floor/ceiling assemblies that define "fire areas" or zones. An overriding consideration in the safe operation of nuclear reactors is that all systems and associated circuits used for safe shutdown be free from fire damage. This objective is achieved in part by identifying "redundant" systems necessary for safe shutdown and then assuring that the systems will not be subject to damage from the same fire. This can be accomplished by locating the redundant systems in fire areas separated by fire-rated barriers or, in some instances, by using "substantial physical separation."[2] It has, however, been recognized that:

Unpierced fire barriers offer the best protection of separating redundant trains of

safety-related or safe shutdown equipment. However, these barriers must be pierced for both control and power cables. These penetrations must be sealed to achieve a degree of fire resistance equivalent to that required of the barrier that is unpierced.

(Ref. 2, p. 76608.1)

The fire conditions represented by the E-119 test method are termed "post-flashover" conditions in which fire fully involves a compartment, although the test itself is conducted in a furnace that is not closely controlled by the standard. Under actual conditions, as opposed to laboratory test furnaces, post-flashover fires are characterized by a positive pressure differential between the upper half of the fire compartment and the unexposed face of the wall and floor/ceiling assemblies making up its boundaries. The beginning of this post-flashover period also is characterized by excess amounts of pyrolyzed fuel. Since flames commonly emerge from the doors and windows of both actual and laboratory post-flashover building fires, there is no doubt that these phenomena—postive pressure and excess pyrolyzates—occur.

ACCOMPLISHMENTS DURING FY 1982

A new concept for evaluating penetrations through walls or floor/ceiling assemblies in a true post-flashover compartment fire exposure was discovered during 1981. This concept may have far-reaching consequences for the evaluation of all penetrations of fire-resistive barriers. Many problems with E-119 test furnaces can be attributed to the fact that they are furnaces and not compartments. Thus, by returning to an actual compartment geometry and creating a true post-flashover compartment fire, the pressure differentials, excess pyrolyzates, and other characteristic features of post-flashover fires will be automatically accomplished.

During 1982, we finished instrumenting a pre-flashover room test facility at the University of California's Richmond Field Station for post-flashover experiments. Special attention was paid to developing realistic fire conditions while at the same time retaining control of the fire itself. One objective was to create a controlled amount of excess pyrolyzates in the area of penetration and simultaneously control the temperature of the compartment so as to follow

either the standard or a special time-temperature curve. In addition, a positive pressure differential needed to be created in the upper part of the compartment to duplicate actual fire situations.

To characterize fire conditions within the compartment, an aspirated thermocouple "tree" was constructed and calibrated. This allows for the assessment of the effects of radiation on thermocouples distributed within the compartment. Since radiation is very important in post-flashover fires, aspirated thermocouples may be necessary to characterize them.

A set of pressure probes was installed in the compartment at eight locations from 0.5 m to 2.34 m above the floor level. The associated instrumentation was installed and calibrated to give as accurate a measurement as possible of the differential pressure between the interior of the fire compartment and the external space. Special effort is being made to quantify the accuracy of this measurement. The importance of pressure measurements is well-recognized and is one of the principal reasons for the change from a furnace to a compartment geometry.

An array of 16 thermocouples was placed in the exhaust plenum above the collection hood outside the fire compartment. The measurement of the temperatures within the plenum allows an assessment of the enthalpy flow in the exhaust system; since the energy release in the fire compartment is known, a heat balance can be performed for the experiments. This should be particularly important when correlating these experiments with theoretical models.

The gas-sampling equipment and instrumentation were placed in a protective housing adjacent to the stack above the test compartment. This allows measurement of both the products of combustion and the rate of heat release by the oxygen consumption method.

A set of four experiments (conducted partially under separate sponsorship) were performed in which the special instrumentation described above was monitored to ensure the accuracy and validity of the measurements. A report is being prepared on the results.

A second set of experiments explored methods of producing a controlled post-flashover fire condition on the end wall and ceiling of the test compartment. This entailed placing a "line" burner against the wall and trying to produce a flame zone adjacent to the wall. These experiments proved very discouraging because the flame was not stable and would wander

from side to side. At the beginning of FY 1983, however, a flame holder was installed inside the line burner, and this stabilized the flame.

Another accomplishment was the development of simple microcomputer methods to calculate the expected temperature, pressure, and excess pyrolyzate histories for sample compartments with different fuel loads, using post-flashover fire models. Previous work had led to a post-flashover computer model, COMPF,[3,4] which required a mainframe computer, and we originally intended to download the program to the NOVA-2 minicomputer used in our laboratory for data acquisition and reduction. However, the experimental work took precedence, and the COMPF program was not fully implemented to run under the Data General FORTRAN compiler. As we looked at the problem, it became clear that a much simpler approach would be more effective. This was to use a microcomputer to solve the "closed-form" approximation of Babrauska,[5] which has been shown to be within 3% of the gas temperatures calculated by the numerical methods of COMPF.

By the end of this reporting period, the closed-form calculations had been set up on "Supercalc," the popular microcomputer "spread-sheet" program. The use of the spread sheet to calculate post-flashover fire conditions is very exciting, because it gives the fire protection engineer the benefits of a computer fire model that can be run on a microcomputer.

This is to be the last year for the study of cable penetrations, and a report is being prepared that summarizes our research on this subject. This report will give a detailed analysis on how fire resistance of cable penetrations should be evaluated using the new fire test standard, ASTM E-814, and how this standard relates to other standards, such as IEEE 635.

Another accomplishment was the further development of the probabilistic network approach to modeling fire spread. A Ph.D. thesis entitled *Application of Probabilistic Networks to Fire Protection* was completed in August 1982 by Wai-Ching Teresa Ling. A principal feature of this approach is that fire-resistive elements can be tested under different conditions to provide for a quantitative interpretation of their expected performance under potential fire conditions.

A new topic of research, the assessment of the susceptibility of components within electrical cabinets to damage from a fire either within or outside of the cabinet was started. As of the end of FY 1982, there were no major findings to be reported. This research is being continued in FY 1983.

PLANNED ACTIVITIES FOR FY 1983

The principal research task for this year will be to conduct fire test experiments on electrical cabinets exposed to both interior and exterior fires.

REFERENCES

1. *Annual Book of ASTM Standards*, 1981 ed., American Society for Testing and Materials, Philadelphia, Pennsylvania.
2. "Fire Protection Program for Operating Nuclear Power Plants," 10CFR Part 50, *Federal Register*, *45*, No. 225, p. 76602-76616, Nov. 19, 1980.
3. Babrauskas, V., and Williamson, R.B. (1978), "Post-Flashover Compartment Fires: Basis of a Theoretical Model," *Fire and Materials 2* (2), p. 39.
4. Babrauskas, V., and Williamson, R.B. (1979), "Post-Flashover Compartment Fires— Application of a Theoretical Model," *Fire and Materials 3* (1), p. 1.
5. Babrauskas, V. (1981), "A Closed-Form Approximation for Post-Flashover Compartment Fire Temperatures," *Fire Safety J. 4*, p. 63.

THE EFFECTS OF METAL CHELATES ON WET FLUE GAS SCRUBBING CHEMISTRY*

S.G. Chang, D. Littlejohn, and S. Lynn

Power-plant flue gas frequently contains several hundred ppm NO_x and up to several thousand ppm SO_2. Most of the NO_x is in the form of relatively insoluble NO. Several simultaneous desulfurization and denitrification processes,[1-3] still in the development stage, are based on the addition of metal chelates such as Fe^{2+} (EDTA) to the aqueous scrubbing liquor to promote absorption of NO. These metal chelates can bind NO to form nitrosyl metal chelates, which can in turn react with absorbed SO_2 to produce reduced nitrogen species such as N_2O, N_2, and sulfate while metal chelates are regenerated. Identification of an optimum metal chelate for greater efficiency in removing NO and SO_2 in a wet scrubber requires knowledge of the thermodynamics and kinetics of the coordination of NO to various metal chelates. Knowledge of the kinetics and mechanisms of the reactions between nitrosyl metal chelates and absorbed SO_2 is also needed to calculate the regeneration rate of metal chelates and to control the products of reaction by adjusting the operating conditions.

ACCOMPLISHMENTS DURING FY 82

We have investigated some of the important factors that should be considered in identifying an optimum metal chelate catalyst and in developing an efficient scrubber for the simultaneous desulfurization and denitrification of a power-plant stack gas.

Thermodynamic Equilibrium and Kinetics of NO Absorption

Thermodynamics

Nitric oxide is nonreactive in water (in the absence of oxygen), and the solubility of NO in aqueous solu-

tions is very small. The absorption of NO is enhanced by some water-soluble metal chelate compounds that form complexes with NO.[4] Many studies have been published on the structure of these chelates, but only a few on their thermodynamic properties and reaction rates. Hishinuma et al.[5] and Lin et al.[6] have recently determined the equilibrium constants, enthalpy, and entropy for the coordination of NO to Fe^{2+} (EDTA) and Fe^{2+} (NTA) respectively.

The binding of NO to Fe^{2+}(L) can be expressed by the following reaction:

$$n NO + Fe^{2+}(L) \underset{k_{-1}}{\overset{k_1}{\rightleftarrows}} Fe^{2+}(L)(NO)_n \qquad (1)$$
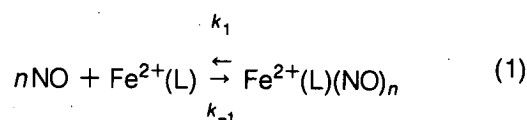
where L is a ligand. The equilibrium constant of this reaction can be written as:

$$K = \frac{k_1}{k_{-1}} = \frac{[Fe^{2+}(L)(NO)_n]}{[NO]^n[Fe^{2+}(L)]} \qquad (2)$$

$$= \frac{[Fe^{2+}(L)(NO)_n]}{[NO]^n[Fe^{2+}(L)]_0 - [Fe^{2+}(L)(NO)_n]}$$

Equation (2) can be rearranged to become

$$\frac{[Fe^{2+}(L)]_0}{[Fe^{2+}(L)(NO)_n]} - 1 = \frac{1}{KH^n p_{NO}^n} \qquad (3)$$

where $[Fe^{2+}(L)]_0$ is the initial concentration of $Fe^{2+}(L)$, $[Fe^{2+}(L)(NO)_n]$ is the concentration of the NO adduct obtained by graphically integrating the outlet NO concentration, p_{NO} is the partial pressure of NO in the gas, and H is the constant for solubility of NO in the water. The experiments were performed at several p_{NO} to calculate n and K, and at several temperatures to evaluate enthalpy and entropy of the reaction (Table 1).

Littlejohn and Chang[4] have recently determined the equilibrium constant for the coordination of NO to $Fe^{2+}(H_2O)_6$, Fe^{2+}(citrate), and $Fe^{2+}(acac)_2$, using a temperature-jump approach (Table 1) similar to that described by Czerlinski and Eigen.[7]

The reciprocal of the relaxation time obtained from the temperature-jump system equals the forward rate constant times the sum of the final equilibrium concentrations of $Fe^{2+}(L)$ and NO plus the backward rate constant.[7] When the reciprocal of the relaxation

Table 1. Kinetic and thermodynamic data for reversible NO coordination to ferrous chelates.

Ferrous chelates	k_1 (moles/lit-sec)	k_{-1} (sec^{-1})	K (liter/mole at 298°K)	H (kcal/mole)	S (e.u)
$Fe^{2+}(H_2O)_5(NO)$	$(7.1 \pm 1.0) \times 10^5$	$(1.5 \pm 0.6) \times 10^3$	$(4.7 \pm 2.0) \times 10^2$		
$Fe^{2+}(citrate)(NO)$	$(4.4 \pm 0.8) \times 10^5$	$(6.6 \pm 2.4) \times 10^2$	$(6.7 \pm 2.0) \times 10^2$		
$Fe^{2+}(acac)_2(NO)$	$(4.0 \pm 3.0) \times 10^2$	24 ± 2	17 ± 14		
$Fe^{2+}(NTA)(NO)$	$\geq 7 \times 10^7$	≥ 35	2.14×10^6	-11.94	-11.0
$Fe^{2+}(EDTA)(NO)$	$\geq 6 \times 10^7$	≥ 60	1.15×10^7	-15.8	-20.7

time is plotted against the final concentrations of $Fe^{2+}(L) + NO$, the slope of the curve gives the forward rate constant (k_1) and the point of interception gives the backward rate constant (k_{-1}).

A comparison of the equilibrium constants of the reactions listed in Table 1 makes it obvious that $Fe^{2+}(EDTA)$ and $Fe^{2+}(NTA)$ have much larger absorption capacities for NO than do $Fe^{2+}(H_2O)_5$, $Fe^{2+}(citrate)$, or $Fe^{2+}(acac)_2$. For an aqueous scrubbing solution initially containing 0.1 mole/liter $Fe^{2+}(NTA)$ at 50°C, $\mu = 0.1$ mole/liter, the fraction of the iron chelate that is converted to $Fe^{2+}(NTA)(NO)$ is about 36% when the solution is in equilibrium with a gas containing 1000 ppm NO at one atmosphere. For a gas containing 100 ppm NO, the conversion is about 5%. Thus, the presence of the iron chelate increases the capacity of the scrubbing solution for NO by a factor of 30,000 or more.

Kinetics

With the temperature-jump technique, Littlejohn and Chang,[4] directly measured the formation and dissociation rate constants of $Fe^{2+}(H_2O)_5NO$, $Fe^{2+}(citrate)NO$, $Fe^{2+}(acac)_2NO$, $Fe^{2+}(EDTA)NO$, and $Fe^{2+}(NTA)NO$ (Table 1). The forward and reverse rate constants for the formation of $Fe^{2+}(citrate)NO$ are somewhat smaller than the values for the $Fe^{2+}(H_2O)_5NO$ complex, while the equilibrium constant is larger. The kinetics for the formation and dissociation of the $Fe^{2+}(acac)_2NO$ complex are much slower than for any other complex studied.

For both $Fe^{2+}(EDTA)NO$ and $Fe^{2+}(NTA)NO$, the relaxation times due to the temperature jump were too short to be measured. However, an upper limit of 10 microseconds was established for the relaxation

times for both complexes. By using this value with the equilibrium constants determined for $Fe^{2+}(EDTA)NO$ by Hishinuma et al.[5] and for $Fe^{2+}(NTA)NO$ by Lin et al.,[6] the lower limits of forward and reverse rate constants were calculated (Table 1).

Thermodynamic Equilibrium and Kinetics of SO$_2$ Absorption

Thermodynamics

Sulfur dioxide is moderately soluble in water; four major S^{4+} species are produced after dissolution of SO_2 in aqueous solutions: $SO_2(aq)$, HSO_3^-, SO_3^{2-}, and $S_2O_5^{2-}$. The equilibrium concentrations of these S^{4+} species depend on both the partial pressure of SO_2 and the pH of the solution. The solubility coefficient of SO_2 is 1.24 mole/liter-atm at 25°C. Hydrated SO_2 can ionize to form bisulfite ion, HSO_3^-, which in turn can undergo further ionization to produce sulfite ion, SO_3^{2-}:

$$SO_2(g) + H_2O \rightleftarrows SO_2(aq) \tag{4}$$

$$SO_2(aq) \rightleftarrows H^+ + HSO_3^- \tag{5}$$

$$(K = 1.27 \times 10^{-2} \text{ mole/liter at 25°C})$$

$$HSO_3^- \rightleftarrows H^+ + SO_3^{2-} \tag{6}$$

$$(K = 6.24 \times 10^{-8} \text{ mole/liter at 25°C})$$

Bisulfite ion is also in equilibrium with the disulfite ion, $S_2O_5^{2-}$:
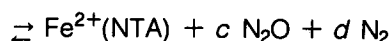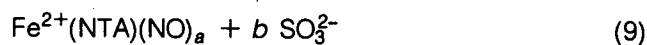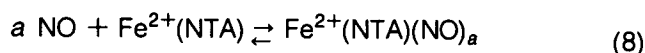
$$2HSO_3^- \rightleftarrows S_2O_5^{2-} + H_2O \tag{7}$$

$$(K = 7 \times 10^{-2} \text{ liter/mole at 25°C})$$

Kinetics

Dissolution of SO_2 can be expressed by Reactions (4)–(7). Reaction (5) proceeds very fast, as can be seen from the rate constant (k_3) and reverse rate constant (k_{-3}) measured by Eigen et al.[8] using a relaxation technique: $k_3 = 3.4 \times 10^6$ sec^{-1} and $k_{-3} = 2.0 \times 10^8$ mole/liter-second at 20°C.

Regeneration Rate of Metal Chelate Catalysts

We have started to investigate the reaction kinetics between Fe^{2+}(NTA)NO and sodium sulfite/bisulfite as a model for the reactions of SO_2-NO-metal chelates in aqueous solutions. The reaction can be expressed as follows:

$$a\ NO + Fe^{2+}(NTA) \rightleftarrows Fe^{2+}(NTA)(NO)_a \tag{8}$$

$$Fe^{2+}(NTA)(NO)_a + b\ SO_3^{2-} \tag{9}$$

$$\rightleftarrows Fe^{2+}(NTA) + c\ N_2O + d\ N_2$$

$$+\ e\ \text{N–S complexes} + f\ SO_4^{2-}$$

The experiments were performed under O_2-free conditions to avoid oxidation of Fe^{2+}, NO, and S^{4+}. The concentration of Fe^{2+}(NTA)NO was monitored by visible-absorption spectrometry during the course of the reaction. A spectrum of the Fe^{2+}(NTA)NO complex is shown in Fig. 1 and has been found to obey Beer's law over the concentration range (10^{-4} mole/liter to 10^{-3} mole/liter) employed in the experiments. The rate of disappearance of Fe^{2+}(NTA)NO in the presence of SO_3^{2-} or HSO_3^- has been found to have a second-order dependence on the concentration of Fe^{2+}(NTA)NO and a first-order dependence on the concentration of SO_3^{2-} or HSO_3^-. The rates can be expressed as follows:

$$\frac{-d[Fe^{2+}(NTA)NO]}{dt} \tag{10}$$

$$= (k_7[SO_3^{2-}] + k_7'[HSO_3^-])\ [Fe^{2+}(NTA)NO]^2$$

Tentative values for k_7 and k_7' have been obtained. At pH 8.0, $k_7 = 3.16 \times 10^3$ (liter/mole)^2/sec; and at pH 3.5, $k_7' = 4.3 \times 10^2$ (liter/mole)^2/sec. These values were obtained at 20°C. The dependence of

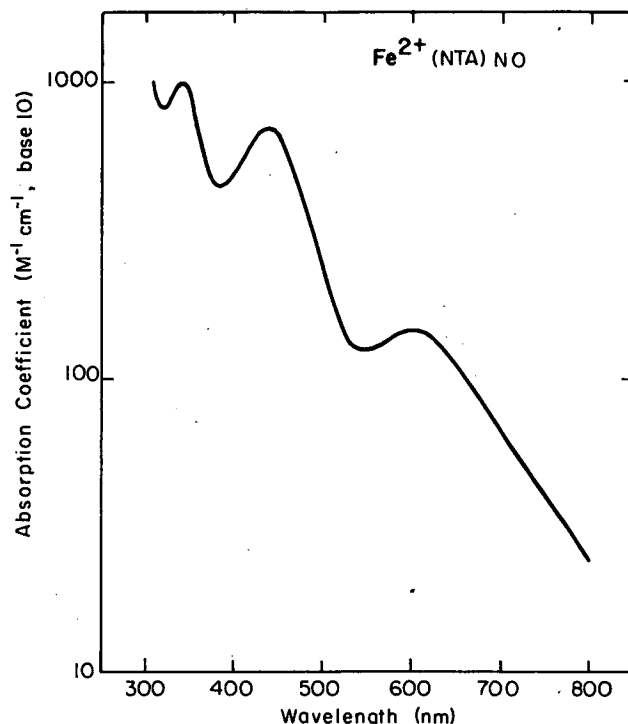

Figure 1. An absorption spectrum of Fe^{2+}(NTA)NO from 800 to 300 nm.　　　　　(XBL 816-5927)

the reaction rate on ionic strength at conditions near neutral pH was found to be negligible.

Identification of Reaction Products

The intermediate and final products that can be formed from the reaction of SO_2, NO, and ferrous chelates in aqueous solutions have not yet been well characterized, although a few compounds such as SO_4^{2-}, N_2O, and some N–S complexes (sulfamate[9] and amine disulfonate[1,2]) have been found. It is necessary to identify such intermediate and final products so that reaction kinetics and mechanisms can be characterized and, from this knowledge, an optimum stack gas scrubber developed. To this end, we have begun to develop analytical techniques so that species can be directly, rapidly, and quantitatively determined and the mass balances of the reactions between nitrosyl metal chelates and SO_2 in aqueous solutions performed. Laser Raman spectroscopy appears to have the potential to identify the species present in mixtures of SO_2, NO, and metal chelates efficiently and unambiguously.

The first step in the identification process is to acquire Raman spectra[10] of potential reaction products so that the relative scattering efficiencies and

Raman shifts will be known. The species studied to date, along with their Raman shifts and scattering efficiencies relative to sulfate ion, are shown in Table 2.

Laser Raman spectroscopy has been used to detect the products of the reactions of $Fe^{2+}(NTA)NO$ with sulfite ion and $Fe^{2+}(H_2O)_5NO$ with bisulfite ion. Figures 2(a) and 2(b) are Raman spectra of amine disulfonate (ADS) and sulfamate (SFA) respectively. Sulfate ion was added to the solutions as a reference so that the relative scattering efficiencies could be obtained. The ADS peak is at 1084 cm^{-1}, the SFA peak is at 1049 cm^{-1}, and the SO_4^{2-} peak is at 981 cm^{-1}.

Figure 2(c) is a spectrum of a solution with initial concentrations of 0.037 mole/liter $Fe^{2+}(H_2O)_5NO$ and 0.19 mole/liter bisulfite ion at pH ~4. The 985 cm^{-1} sulfate peak is from the ferrous sulfate used to prepare the solution and the sulfate created as a reaction product. The peak due to ADS is apparent at 1087 cm^{-1}. The peak at 1052 cm^{-1} could be from both SFA and disulfite ions. The species responsible for some of the other peaks present, such as the 1245 and 1280 cm^{-1} peaks, have not yet been identified. The solution is colorless after the completion of the reaction. The 488 nm Ar$^+$ laser line was used to obtain the spectra.

Figure 2(d) is a spectrum of $Fe^{2+}(NTA)NO$ and sulfite ion at pH 8.3, with initial concentrations of

Table 2. Raman shifts and scattering efficiencies of some species relative to sulfate ion.

Compound	Raman shift (cm^{-1})	Relative scattering efficiency (SO_4^{2-} = 1.00)
SO_4^{2-}	985	1.00
SO_3^{2-}	~970	0.067
NO_2^-	818/1332	0.0235/0.055
NO_3^-	1050	0.42
N_2O	1285	0.08
$HN(SO_3)_2^{2-}$(ADS)	1087	0.025
$H_2NSO_3^-$(SFA)	1052	0.18

INTENSITY (ARBITRARY UNITS)

RAMAN SHIFT (CM^{-1})
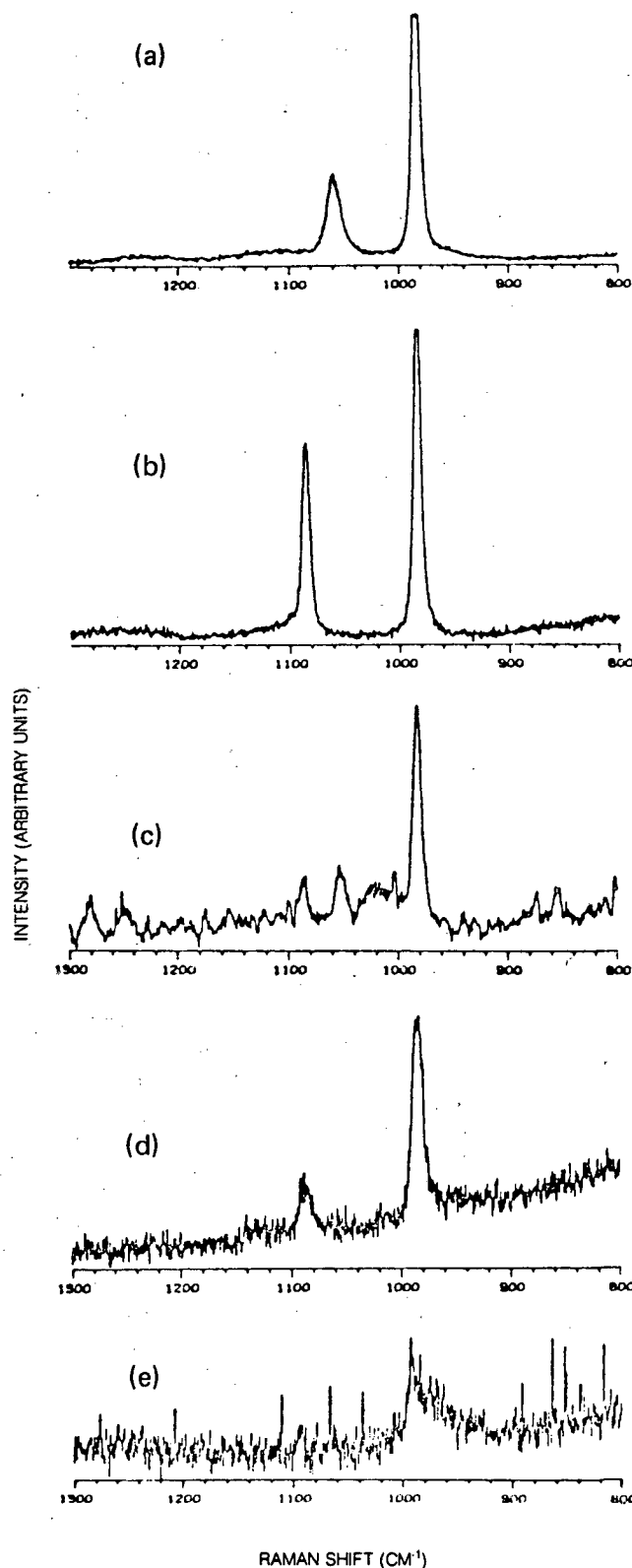
Figure 2. Raman spectra of (a) sulfamates(SFA), (b) aminedisulfonates (ADS), and reaction mixtures of (c) $Fe^{2+}(H_2O)_5NO$ with HSO_3^-, and (d) and (e) $Fe^{2+}(NTA)NO$ with HSO_3^- and SO_3^{2-}, respectively. (XBL 835-9685)

4-86

0.043 mole/liter and 0.100 mole/liter, respectively. Additional sulfate ion was added to the solution at the time of mixing, making a total of 0.091 mole/liter sulfate added to the solution. The peak due to ADS is prominent at 1087 cm^{-1}. Since the solution is basic, ADS will not be rapidly hydrolyzed to form SFA. The reacted solution absorbs strongly in the blue region of the spectrum, so the 647 nm Kr^+ laser line was used for this spectrum.

Figure 2(e) is a spectrum of an initial concentration of 0.012 mole/liter Fe^{2+}(NTA)NO and 0.100 mole/liter sulfite ion at pH ~7. The 985 cm^{-1} sulfate peak overlaps with the broader sulfite peak centered at 970 cm^{-1}. The peaks ascribed to ADS and SFA are weak but visible at 1087 and 1052 cm^{-1}. While the reacted solution does absorb in the blue region of the spectrum, the absorption is sufficiently weak to allow the 488 nm Ar^+ laser line to be used. The sharp spikes in the spectrum are due to noise in the laser output.

Implications for Scrubber Design

The results of these studies show the technical feasibility of designing and operating a scrubber capable of removing both NO_x and SO_x well enough to meet national air quality standards.

NO Removal

The data given in Table 1 show that Fe^{2+} chelated by either NTA or EDTA reacts rapidly with NO under scrubber conditions. A large fraction of the iron chelate is converted to the nitrosyl complex when equilibrated with NO at concentrations commonly found in stack gases. The rate constant for forming NO complexes is so large that for either chelating agent the reaction is effectively instantaneous. Since NTA costs less per pound than EDTA and has a lower

molecular weight, it appears to be the agent of choice at this time.

SO$_2$ Removal

The reaction between the NO complexes and HSO_3^- is too slow to affect the rate of absorption of SO_2. One must, instead, depend upon the buffering capacity of the solution for absorbing SO_2, and upon subsequent reaction for removing it from the solution. As shown in Table 3, the pH of the solution in the scrubber is thus advantageously kept in the range of 5 to 7. However, examination of the acid constants of NTA[11] (pK_{a_1} = 1.97; pK_{a_2} = 2.57; and pK_{a_3} = 9.81) shows that the NTA cannot provide buffering in this pH range. The buffering must, therefore, be provided by adding some other soluble base to the scrubbing solution. Ammonia, sodium carbonate, sodium citrate and sodium phosphate are examples of bases that may be useful.

Solution Regeneration

To be economically attractive, a scrubbing solution must be regenerable with little or no loss of active ingredients. For a scrubbing solution containing Fe^{2+}(NTA) together with an appropriate buffer, regeneration will be a complex process. Neumann and Lynn[12] have shown that Fe^{2+}(NTA) reacts rapidly with oxygen to form Fe^{3+}(NTA). The fraction of Fe^{2+} oxidized will depend on the O_2 content of the flue gas. Besides removing the absorbed NO and SO_2, the regeneration must then reduce the Fe^{3+} back to Fe^{2+}. Lynn and Dubs[13] found that H_2S reacts stoichiometrically with Fe^{3+}(NTA) to form Fe^{2+}(NTA) and elemental sulfur in the pH range 3.5 to 4.5. When the pH of the solution is above 7.0, some thiosulfate and polythionates may be formed. Neumann and Lynn[12] showed that the rate of the absorp-

Table 3. Equilibrium concentration of sulfites (mole/liter) at P_{SO_2} = 100 ppm at 25°C.

Sulfites	pH 7	pH 6	pH 5	pH 4	pH 3
$SO_2 \cdot H_2O$	1.24×10^{-3}	1.24×10^{-3}	1.24×10^{-3}	1.24×10^{-3}	1.24×10^{-3}
HSO_3^-	$1.58 \times 10^{+2}$	$1.58 \times 10^{+1}$	1.58	1.58×10^{-1}	1.58×10^{-2}
SO_3^-	$9.82 \times 10^{+1}$	9.82×10^{-1}	9.82×10^{-3}	9.82×10^{-5}	9.82×10^{-7}
$S_2O_5^=$	$1.75 \times 10^{+3}$	$1.75 \times 10^{+1}$	1.75×10^{-1}	1.75×10^{-3}	1.75×10^{-5}

tion of H_2S by Fe^{3+}(NTA) solution indicated the rate of reaction to be effectively instantaneous in the pH range 3.5 to 4.5. Absorption rates and reaction products in the pH range 5 to 7 must still be determined.

Several methods are available for removing the absorbed SO_2 from the scrubber liquid during regeneration. One approach is to add lime and precipitate a mixture of $CaSO_3$ and $CaSO_4$. This would require technology similar to that used in the various double-alkali processes for SO_2 scrubbing. Thorough washing of the precipitate to avoid excessive loss of scrubber-liquid chemicals would be required. A second approach is to react dissolved SO_2 with H_2S to form elemental sulfur. The technology for this approach has been demonstrated in the citrate process of the U.S. Bureau of Mines and Stauffer Chemical's AquaClaus process. With this approach, a salable form of sulfur is produced, and costs may be reduced as a result. The reaction of H_2S and HSO_3^- in the presence of chelated iron compounds has not yet been studied.

PLANNED ACTIVITIES FOR FY 1983

We plan to determine quantitatively the amounts of the observed products that are produced by the reactions of ferrous nitrosyl complexes with sulfite and bisulfite ions. We also plan to study the interaction of H_2S with this system.

REFERENCES

1. Yaverbaum, L.H. (1979), *Nitrogen Oxides Control and Removal, Recent Developments*, Noyes Data Corporation, Park Ridge, New Jersey.
2. Martin, A.E., Ed. (1981), *Emission Control Technology for Industrial Boilers*, Noyes Data Corporation, Park Ridge, New Jersey.
3. Chang, S.G., Littlejohn, D., and Lin, N.H. (1982), "Kinetics of Reactions in a Wet Flue Gas Simultaneous Desulfurization and Denitrification System," in *Flue Gas Desulfurization*, ACS Symposium Series 188, American Chemical Society, Washington, D.C.
4. Littlejohn, D., and Chang, S.G. (1982), "Kinetic Study of Ferrous Nitrosyl Chelates," *J. Phys. Chem. 86*, p. 537.
5. Hishinuma, Y., et al. (1979), "Reversible Binding of NO to Fe(II)EDTA," *Bull. Chem. Soc. Japan 52*, p. 2863.
6. Lin, N.H., Littlejohn, D., and Chang, S.G. (1982), "The Thermodynamics and Kinetics of the Coordination of NO to Fe^{+2}(NTA) in Aqueous Solutions," *I&EC Process Res. Dev. 21*, p. 725.
7. Czerlinski, G., and Eigen, M. (1959), "Eine Temperatursprungmethode zur Untersuchung Chemischer Relaxation," *Z. Elektrochem. 63*, p. 652.
8. Eigen, M. (1961), "Investigation on Rapid Reactions by Means of Relaxation Spectrometry," *Suomen Kemistilekti 34A*, p. 25.
9. Sawai, K. and Gorai, T. (1976), "Simultaneous Removal of Sulfur Dioxide and Nitrogen Oxides from Flue Gases by the CEC Method," *Kyusan to Kogyo*, p. 187.
10. Littlejohn, D., and Chang, S.G., (1982), "Identification of Species in a Wet Flue Gas Desulfurization and Denitrification System by Laser Raman Spectroscopy," submitted for publication in *Environ. Sci. Tech.*, Lawrence Berkeley Laboratory Report LBL-14756.
11. Pietrezyk, D.J., and Frank, C.W. (1974), *Analytical Chemistry*, Academic Press, New York, p. 453.
12. Neumann, D.W., and Lynn, S. (1981), "Oxidative Absorption of H_2S and O_2 by Iron Chelate Solutions," presented at the AIChE Annual Meeting, New Orleans, and submitted for publication to *AIChE Journal*.
13. Lynn, S., and Dubs, B.J.-L., U.S. Patent No. 4,278,646, July 1981.

THE REACTION OF FERROUS NITROSYL COMPLEXES WITH SULFITE AND BISULFITE IONS*

D. Littlejohn, E. Griffiths, and S.G. Chang

Untreated flue gases from coal-fired power plants contain substantial amounts of sulfur dioxide (SO_2) and nitrogen oxides (NO_x). A number of control strategies are being developed to reduce the concentrations of these pollutants to acceptable levels.[1] Since SO_2 is fairly soluble in water, it can be effectively removed by scrubbing the flue gases with aqueous

solutions. Nitric oxide (NO) is the major constituent of nitrogen oxides; the rest of the NO_x consists mainly of nitrogen dioxide (NO_2). While NO_2 is readily dissolved in aqueous solutions, NO is relatively insoluble. One promising technique for enhancing the solubility of NO is to use ferrous chelates to form ferrous nitrosyl complexes in aqueous solutions.

A scrubbing process based on this procedure must be able to regenerate the ferrous chelate so that it may absorb more NO. One method of regeneration is to react the ferrous nitrosyl compound with the dissolved SO_2, which exists as bisulfite (HSO_3^-) and sulfite ($SO_3^=$) ions, depending on the pH of the solution.[2] These ions will be referred to collectively as S(IV). The behavior of this reaction needs to be known so that a scrubber based on this method can be properly designed.

ACCOMPLISHMENTS DURING FY 1982

We have begun a systematic study of the reaction of ferrous nitrosyl complexes with S(IV) and have obtained a preliminary rate expression. We have also identified the major products of the reaction.

Kinetic Studies

The ferrous nitrosyl complexes were prepared under oxygen-free conditions.[3] Concentrations of the complexes were determined spectrophotometrically. Solutions of the ferrous nitrosyl complexes were mixed with degassed solutions of S(IV) ions. After mixing, the concentration of the complexes was monitored over time, using its visible absorption band. Solutions were prepared such that the concentration of S(IV) was much greater than that of the ferrous nitrosyl complex. Most of the work has involved the two complexes that bind NO most efficiently: Fe(II)(NTA)NO[4] and Fe(II)(EDTA)NO.[5] Kinetic studies have been done at 25°C for Fe(II)(NTA)NO, and at 25°C and 55°C for Fe(II)(EDTA)NO. Analysis of the kinetic data was done using values of the change with time in [Fe(II)(L)NO] (L representing the chelate in use), dc/dt, obtained from the initial decay of the ferrous nitrosyl complex.

Determination of Reaction Products

Gaseous products of the reaction were analyzed by gas chromatographic and mass spectrometric techniques. The solutions containing the reaction mixture were kept in a sealed container under an argon atmo-

sphere. Gas samples were withdrawn after allowing the reaction to go to completion and permitting the solution to equilibrate with the gas above it.

Other products remaining in solution were measured either spectrophotometrically or by laser Raman spectroscopy (LRS). Not all of the product compounds can be easily determined by spectrophotometric methods. The major limitations of LRS are its relatively low sensitivity and the difficulty of working with strongly colored solutions. Practically all product compounds can be determined by LRS, however, if their concentrations are sufficiently high.[6]

Results and Discussion

Kinetic Results

Values of dc/dt obtained from experiments were used to obtain rate information on the reaction. Figure 1 illustrates the dependence of the reaction rate on the pH of the solution containing Fe(II)(NTA)NO + S(IV). The data were obtained from experiments using [Fe(II)(NTA)NO] at 2.5×10^{-4} M and [S(IV)] at $\sim 4 \times 10^{-2} M$. The decrease in rate at pH below 3 is attributed to two factors: the decreasing fraction of S(IV) in the form of HSO_3^-, and the decreasing ability of Fe(II)(NTA) to bind with NO.[4] The increase in rate around pH 6 is due to the increasing fraction of S(IV) as $SO_3^=$. The cause of the decrease in rate above pH 7 is currently not well understood, but may be due to OH^- complexing with Fe(II)(NTA)NO and inhibiting the reaction.

Plots of log (dc/dt) vs. log (S(IV)) have been used to determine the rate dependence on S(IV). Within the accuracy of our results, we find first order dependence on S(IV) throughout the pH range of 4 to 8.
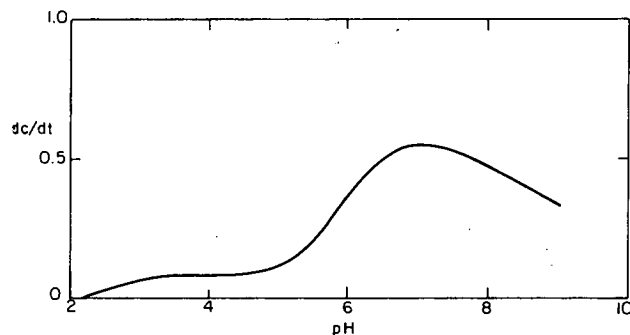

Figure 1. Dependence of reaction rate (dc/dt) on pH for [Fe(II)(NTA)NO] $\approx 2.5 \times 10^{-4}$ M and [S(IV)] $\approx 4 \times 10^{-2}$ M.

This is true for both ferrous nitrosyl complexes. This appears to be valid over a S(IV) range of 0.01 to 0.1 M when [S(IV)] > [Fe(II)(L)NO].

Plots of log (dc/dt) vs. log (Fe(II)(L)NO) were used to determine the dependence of the reaction rate on the ferrous nitrosyl complex concentration. A representative plot is shown in Fig. 2. At high pH conditions where $SO_3^=$ is the only S(IV) species, there is a first order dependence on Fe(II)(L)NO over a concentration range of 10^{-3} M to 10^{-4} M. Above 10^{-2} M in Fe(II)(L)NO concentration, the dependence appears to approach zero order. At low pH conditions, where HSO_3^- is the only S(IV) species, there appears to be zero order dependence on Fe(II)(L)NO at all concentrations studied (10^{-4} M to 10^{-2} M).

A study done on ionic strength dependence at pH 7, where both HSO_3^- and $SO_3^=$ are present, found no dependence on ionic strength over the range of $\mu = 0.01$ to $\mu = 1.0$.

From our results, we have obtained the following rate expressions:

Fe(II)(NTA)NO at 25°C:

$$\{d[Fe(II)(NTA)NO]\}/dt = 1.2 \times 10^{-5} \text{ sec}^{-1}[HSO_3^-]$$
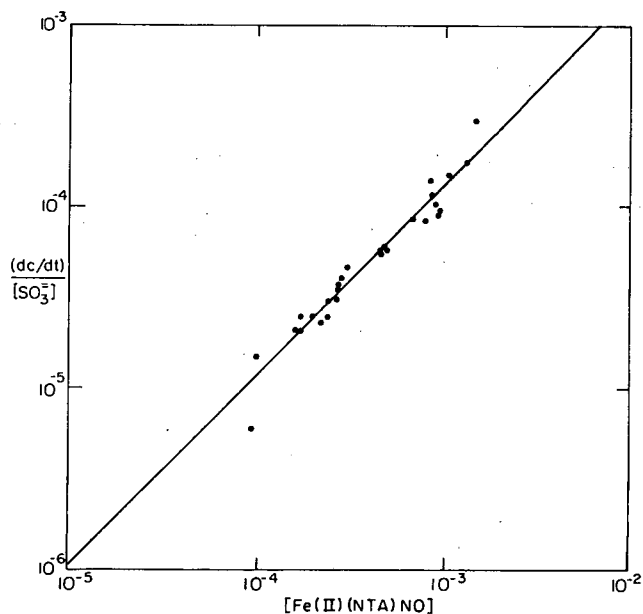
$$+ 0.13M^{-1}\text{sec}^{-1}[Fe(II)(NTA)NO][SO_3^-]$$

(valid for pH $\approx$ 3 to 8, [Fe(II)(NTA)NO] $\approx 10^{-4}$ to 10^{-3} M, [S(IV)] $\approx$ 0.01 to 0.1 M).

Fe(II)(EDTA)NO:

$$\{-d[Fe(II)(EDTA)NO]\}/dt$$

$$= k_1[HSO_3^-] + k_2[Fe(II)(EDTA)NO][SO_3^=]$$

where k_1 at 25°C = 5.62×10^{-5} sec^{-1}, and k_2 at 25°C = 0.175 M^{-1} sec^{-1}; k_1 at 55°C = 9.00×10^{-5} sec^{-1}, and k_2 at 55°C = 0.60 M^{-1} sec^{-1}. (pH range $\approx$ 4 to 8.5, [Fe(II)(EDTA)NO] = 10^{-4} to 10^{-3} M, [S(IV)] 10^{-3} to 10^{-1} M.)

Reaction Products

Nitrous oxide (N_2O) and nitrogen gas (N_2) were found to be among the major nitrogen-containing products of the reaction of ferrous nitrosyl complexes with S(IV). Nitrous oxide was analyzed by both gas chromatographic and mass spectrometric techniques, and N_2 was analyzed by mass spectrometry alone.

The fraction of nitrogen that is NO converted to N_2O is affected by pH and the concentration of the ferrous nitrosyl complex. Figure 3 shows the pH dependence for N_2O production for [Fe(II)(NTA)NO] $< 5 \times 10^{-3}$ M when reacted with excess S(IV). The fraction of N_2O produced decreases as the

Figure 2. Reaction rate dependence on Fe(II)(NTA)NO: log $\{(dc/dt)/[SO_3^=]\}$ vs. log $\{[Fe(II)(NTA)NO]\}$ at pH $\geq$ 8. Slope = 1.06 ± 0.05.
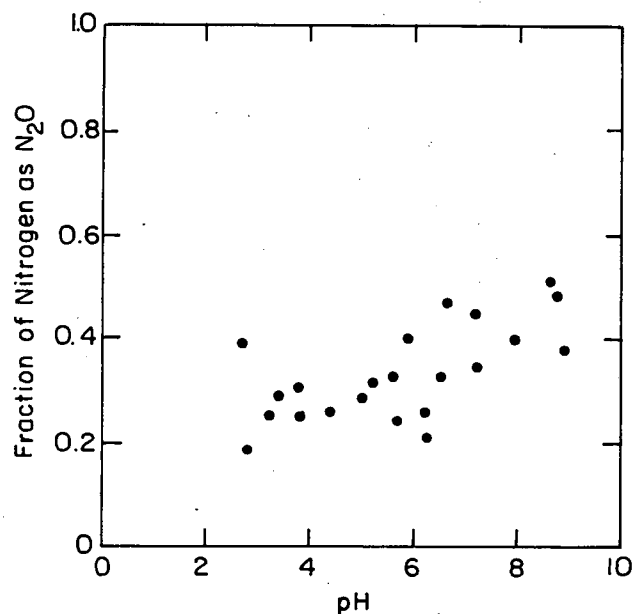
(XBL 832-5297)

Figure 3. pH dependence on N_2O production for reaction of Fe(II)(NTA)NO + S(IV). [Fe(II)(NTA)NO] $< 5 \times 10^{-3}$ M.

(XBL 823-5380)

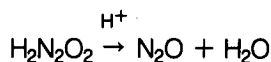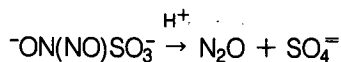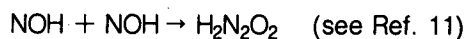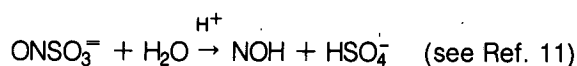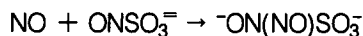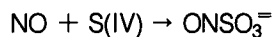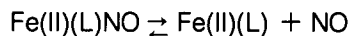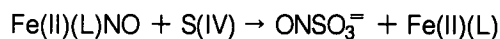Fe(II)(NTA)NO concentration is raised above this level. Similar behavior is observed for Fe(II)(EDTA)NO.

Nitrogen gas appears to be an important nitrogen-containing product, although the effects of pH and concentration on its production have not yet been determined. Its concentrations have been found to be much higher than those of N_2O at the Fe(II)(NTA)NO concentrations estimated to occur in this type of scrubber.

Hydroxylamine disulfonate (HADS) was found to be another reaction product. HADS can react with S(IV) and can hydrolyze to form other compounds.[2] HADS determinations were made by LRS and by oxidation of HADS to nitrosodisulfonate (NDS), which can be measured by its optical absorption.[7] A limited number of measurements on HADS indicate that it and the compounds it forms in the reaction mixture also contain a substantial fraction of the nitrogen originally in the form of NO.

Sulfate ion ($SO_4^=$) appears to be the major product into which S(IV) is converted. It has been observed by LRS and by wet analytical methods.

Spectra taken several days after mixing Fe(II)(L)NO with S(IV) under alkaline conditions show the appearance of the characteristic spectra of Fe(III)(NTA)OH$^-$ and Fe(III)(EDTA)OH$^-$.[8] This indicates that Fe(II) is slowly being oxidized to Fe(III). The reaction continues to occur long after the primary reaction has gone to completion. The oxidizing agent has not yet been identified.

From studies of reactions of similar compounds[9,10] and knowledge of the reaction products, a tentative reaction scheme can be proposed:

$$Fe(II)(L)NO + S(IV) \rightarrow ONSO_3^= + Fe(II)(L)$$

$$Fe(II)(L)NO \rightleftharpoons Fe(II)(L) + NO$$

$$NO + S(IV) \rightarrow ONSO_3^=$$

$$NO + ONSO_3^= \rightarrow {}^-ON(NO)SO_3^=$$

$$S(IV) + ONSO_3^= \rightarrow HADS$$

$$ONSO_3^= + H_2O \xrightarrow{H^+} NOH + HSO_4^- \quad \text{(see Ref. 11)}$$

$$NOH + NOH \rightarrow H_2N_2O_2 \quad \text{(see Ref. 11)}$$

$${}^-ON(NO)SO_3^= \xrightarrow{H^+} N_2O + SO_4^=$$

$$H_2N_2O_2 \xrightarrow{H^+} N_2O + H_2O$$

$$H_2N_2O_2 \rightarrow N_2 + 2OH \quad \text{(see Ref. 10)}$$

Not included in this scheme are reactions in which HADS is converted into other nitrogen-sulfur compounds. These are discussed in detail elsewhere.[2]

PLANNED ACTIVITIES FOR FY 1983

We plan to extend the range of concentrations of S(IV) and Fe(II)(L)NO under study to develop a more complete rate expression. A mass balance for the nitrogen-containing products will be made, and the factors influencing the relative amounts of these compounds will be determined. With this knowledge, it will be possible to develop an efficient system for simultaneous desulfurization and denitrification of power-plant flue gases.

REFERENCES

1. Yaverbaum, L.H. (1979), "Nitrogen Oxides Control and Removal, Recent Developments," Noyes Data Corp., Park Ridge, New Jersey.

2. Chang, S.G., Littlejohn, D., and Lin, N.H. (1982), "Kinetics of Reactions in a Wet Flue Gas Simultaneous Desulfurization and Denitrification System," in *Flue Gas Desulfurization*, ACS Symposium Series 188, American Chemical Society, Washington, D.C.

3. Littlejohn, D. and Chang, S.G., (1982), "Kinetic Study of Ferrous Nitrosyl Complexes," *J. Phys. Chem. 86*, p. 537.

4. Lin, N.H., Littlejohn, D., and Chang, S.G. (1982), "Thermodynamics and Kinetics of the Coordination of NO to Fe(II)NTA in Aqueous Solutions," *I & EC Proc. Design Dev. 21*, p. 725.

5. Hishinuma, Y., et al. (1979), "Reversible Binding of NO to Fe(II)EDTA," *Bull. Chem. Soc. Japan 52*, p. 2863.

6. Littlejohn, D., and Chang, S.G. (1983), "Identification of Species in a Wet Flue Gas Desulfurization and Denitrification System by Laser Raman Spectroscopy," submitted to *Environ. Sci. Tech.*

7. Oblath, S.B. (1981), *Kinetics of the Reduction of Nitrite Ion by Sulfur Dioxide in Aqueous Solution*, Ph.D. Thesis, Chemistry Department, University of California, Berkeley.

8. Jones, S.S., and Long, F.A. (1952), "Complex

lons From Iron and Ethylenediaminetetraacetate: General Properties and Radioactive Exchange," *J. Phys. Chem. 56*, p. 25.

9. Nunes, T.L., and Powell, R.E. (1970), "Kinetics of the Reaction of Nitric Oxide with Sulfite," *Inorg. Chem. 9*, p. 1916.

10. Buchholz, J.R., and Powell, R.E., (1963), "The Decomposition of Hyponitrous Acid. I. The Non-Chain Reaction," *J. Amer. Chem. Soc. 85*, p. 509.

11. Oblath, S.B., Markowitz, S.S., Novakov, T., and Chang, S.G. (1982), "Kinetics of the Initial Reaction of Nitrite Ion in Bisulfite Solutions," *J. Phys. Chem. 86*, p. 4853.

IDENTIFICATION OF SPECIES IN A WET FLUE GAS DESULFURIZATION AND DENITRIFICATION SYSTEM BY LASER RAMAN SPECTROSCOPY*

D. Littlejohn and S.G. Chang

Several wet processes[1,2] for simultaneous removal of SO_2 and NO_x from power-plant flue gases are based on injecting a gaseous oxidant such as O_3 into the flue gas to selectively oxidize the relatively insoluble NO to the more soluble NO_2. The flue gas is subsequently passed to a NO_2/SO_2 absorber. The major fraction of the absorbed NO_x in these processes has been found to be in the form of nitrogen-sulfur complexes,[1-8] which are the compounds produced in the reaction between nitrite and bisulfite ions.

Some of the reactions that can occur in this system are illustrated in Fig. 1. The intermediate species nitrosulfonic acid (HO_3SNO) has never been identified, but its existence has been inferred from the behavior of the nitrite ion–bisulfite ion reaction. Some of the compounds identified in the figure are abbreviated as follows: HADS for hydroxylamine disulfonate (disulfonic acid at low pH), HAMS for hydroxylamine monosulfonate, HA for hydroxylamine, ATS for amine trisulfonate (trisulfonic acid at low pH),

ADS for amine disulfonate, and SA for sulfamic acid.

In studying these processes to determine an optimum design and operating condition for scrubbers, one problem is to detect quantitatively all the species present under a wide range of solution conditions. Our work is intended to overcome this difficulty.
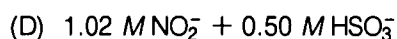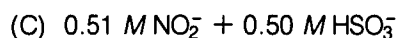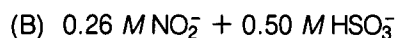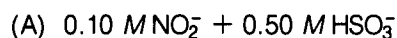
ACCOMPLISHMENTS DURING FY 1982

Using laser Raman specrsocopy, we have investigated the reaction system of nitrite ions and bisulfite ions in aqueous solutions. The reaction products have been identified, and the effect of reactant concentrations and solution pH has been studied.

The Raman system has been described in detail elsewhere.[9] Spectra were obtained using the 488.0 nm argon ion laser line as the exciting light. Raman spectra were obtained for the reactants and potential reaction products. For most species, the relative molar intensity (RMI) was determined as follows:

$$RMI = \frac{H_i/C_i}{(981\ cm^{-1}\ H_{sulfate})/(C_{sulfate})}$$

where H_i is the ion peak height, C_i is the ion molarity, $H_{sulfate}$ is the sulfate ion peak height, and $C_{sulfate}$ is the sulfate ion molarity. The Raman shifts and relative molar intensities are given in Table 1.

The solutions containing the reaction mixtures of nitrite ions and bisulfite or sulfite ions were prepared in a vacuum line to prevent oxidation of the sulfur (IV) species to sulfate ion. The solutions were transferred to 8-mm-diameter Pyrex tubes under an argon atmosphere and sealed, after which Raman spectra were obtained. To investigate the nitrite ion–bisulfite ion reaction, four solutions with varying nitrite ion–bisulfite ion ratios were prepared. The initial pH of the solutions was about pH 4, and the initial concentrations were:

(A) $0.10\ M\ NO_2^- + 0.50\ M\ HSO_3^-$

(B) $0.26\ M\ NO_2^- + 0.50\ M\ HSO_3^-$

(C) $0.51\ M\ NO_2^- + 0.50\ M\ HSO_3^-$

(D) $1.02\ M\ NO_2^- + 0.50\ M\ HSO_3^-$

A solution containing $1.02\ M\ NO_2^-$ and $0.50\ M\ SO_3^=$ was also prepared at pH 10 for an investigation of the reaction at high pH conditions.

HSO₃⁻ over arrows, reaction scheme:

$$HNO_2 \rightleftarrows HO_3SNO \rightleftarrows (HO_3S)_2NOH \rightleftarrows (HO_3S)_3N$$

Nitrous acid — Nitrosulfonic acid — Hydroxylamine disulfonic acid — Amine trisulfonic acid

$NO + HSO_4^-$

$H_2N_2O_2$ Hyponitrous acid ⟵ $(HO_3S)NHOH$ Hydroxylamine monosulfonate ⟶ $NH(HSO_3)_2$ Amine disulfonate

HSO_4^-

N_2O

NH_2OH Hydroxylamine ⟶ $SO_2 \cdot H_2O$ ⟶ $(NH_2)(HSO_3)$ Sulfamic acid

$SO_2 \cdot H_2O$ / H^+ HNO_2

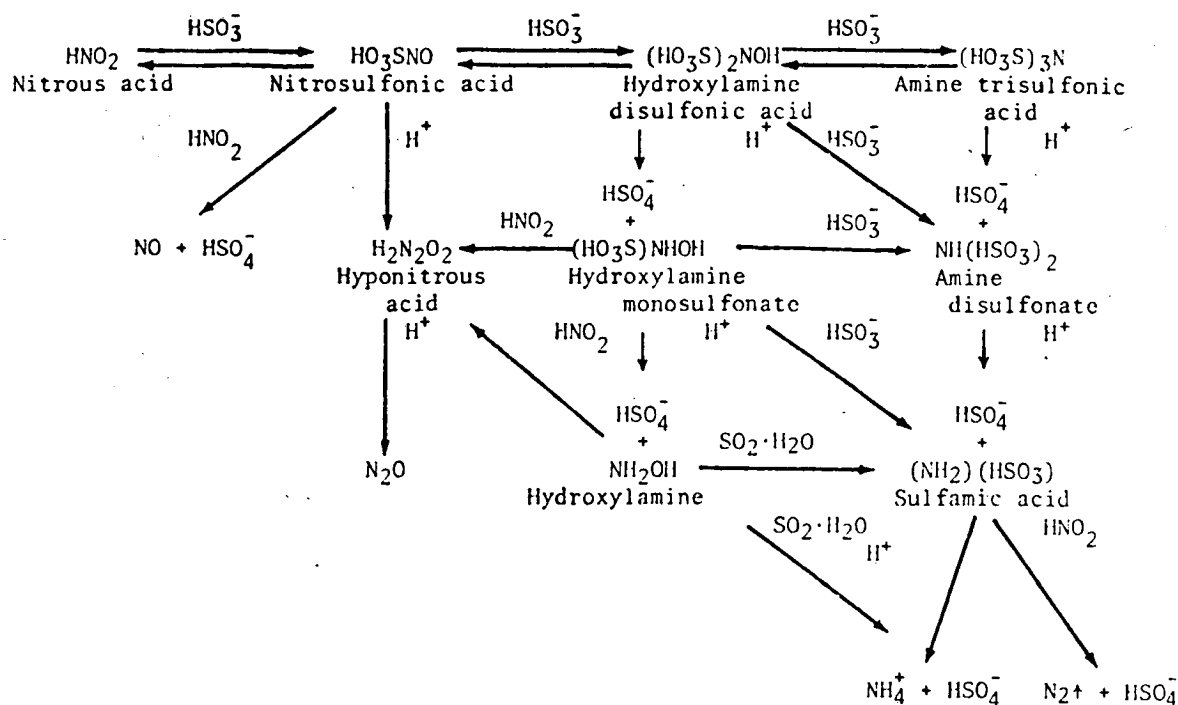$NH_4^+ + HSO_4^-$ $N_2\uparrow + HSO_4^-$

Figure 1. Reactions that occur in the nitrogen oxyacid–sulfur oxyacid system.   (XBL 8112-13061)

Results and Discussion

Raman spectra of the four nitrite ion–bisulfite ion solutions taken 24 hours after mixing are shown in Fig. 2. The spectrum of mixture A in Fig. 2(a) shows the presence of sulfite ion ($SO_3^=$) at 970 cm⁻¹ (the shoulder on the 980 cm⁻¹ peak), sulfate ion ($SO_4^=$) at 980 cm⁻¹, bisulfite ion (HSO_3^-) at 1025 cm⁻¹, disulfite ion ($S_2O_5^=$) at 1050 cm⁻¹, HADS at 1085 cm⁻¹, and ATS at 1100 cm⁻¹. Since bisulfite ion and disulfite ion exist in equilibrium in solution, the 1050 cm⁻¹ peak is attributed to disulfite ion, and not to nitrate ion. The spectrum of mixture B, shown in Fig. 2(b), is less complicated, with sulfite ion at 970 cm⁻¹, HADS at 1085 cm⁻¹, and ATS at 1100 cm⁻¹. Sulfate ion is much less prominent in the spectrum of mixture B. The spectra of mixtures C and D are similar to that of mixture B, except for increasingly strong nitrite bands at 820 cm⁻¹ and 1240 cm⁻¹ and an increasingly weak ATS band. The 1240 cm⁻¹ band of nitrite ion is broad and overlaps with the 1330 cm⁻¹ nitrite band.

Figure 2(a) shows that some of the bisulfite ion has been converted to sulfite ion. In Figs. 2(b), (c), and (d), all the bisulfite ion has been converted into sulfite ion. This is due to the reaction producing HADS:

$$NO_2^- + 2HSO_3^- \rightarrow (^-O_3S)_2NOH + OH^-$$
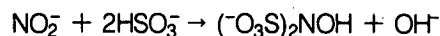
The occurrence of the hydrolysis reactions will cause a decrease in pH. For example, the hydrolysis of HADS and ATS produce H⁺:

$$(^-O_3S)_2NOH + H_2O \rightarrow (^-O_3S)NHOH + SO_4^= + H^+ ;$$

$$(^-O_3S)_3N + H_2O \rightarrow (^-O_3S)_2NH + SO_4^= + H^+ .$$
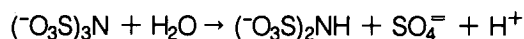
The hydrolysis reactions in this reaction scheme are all hydrogen-ion catalyzed and are slower than the initial reaction between nitrite ion and bisulfite ion.

In mixture A, the nitrite ion–bisulfite ion ratio is much less than 1:2, the stoichiometry of the initial reaction to produce HADS. Under these conditions, the kinetics of the system will be considerably different than in mixtures B, C, and D. In this situation, the amount of HADS produced should be limited by the amount of nitrite ion present. Since bisulfite ion should remain after the nitrite ion has been consumed, it can react with HADS to produce ATS. There should be less hydroxyl ion produced than in the other mixtures, so that the hydrogen ion–catalyzed hydrolysis reactions should occur more rapidly. The relative amount of ATS in Fig. 3(a) is much larger than in the other spectra. Sulfate ion is

Table 1. Raman shifts and relative molar intensities of species studied in this investigation.

Species	Raman shift (cm^{-1})	Relative molar intensity[a]
NO_2^-	818	0.053
	1240	~0.025
	1331	0.125
NO_3^-	1050	0.95
$NO_2O_2^=$	692[b]	weak[b]
	1115[b]	weak[b]
	1383[b]	strong[b]
N_2O	1285	~0.18
$SO_3^=$	967	0.12
HSO_3^-	1023	0.10
$SO_4^=$	~455	~0.07
	981	1.00
$S_2O_5^=$	1055	~0.9
HSO_4^-	1050	0.05
HADS	~700	~0.20
	1084	1.43
HAMS	~420	~0.13
	~760	~0.08
	1058	0.48
HA (pH $\leq$ 7)	1004	0.21
HA (pH $\geq$ 9)	918	0.09
ATS	1097	0.10
ADS	1084	0.056
SA (pH $\leq$ 1)	1063	c
SA (pH $\geq$ 3)	1049	0.41

[a] $SO_4^=$ cm^{-1} line = 1.000.
[b] From Ref. 10.
[c] No value obtained.

produced only by the hydrolysis reactions, according to the reaction scheme in Fig. 1. The sulfate ion peak at 980 cm^{-1} is much more prominent in Fig. 3(a) than in the other figures, indicating that more hydrolysis has occurred. Since no HAMS is apparent at 1060 cm^{-1}, the sulfate ion must be due to the hydrolysis of ATS to ADS. The 1085 cm^{-1} peak is, therefore, due to both ADS and HADS.

The spectra of mixtures B, C, and D did not display much change with time since the hydrolysis reactions are fairly slow. The spectra of mixture A did change

considerably; the change with time is shown in Fig. 3, over the range of 900 to 1300 cm^{-1}. The times after mixing and the number of scans for the spectra are: Fig. 3(a)—20 min. and 1 scan; Fig. 3(b)—2 hours and 1 scan; Fig. 3(c)—24 hours and 4 scans, Fig. 3(d)—105 days and 4 scans. In the first spectrum in Fig. 3(a), HADS is prominent at 1085 cm^{-1}. The presence of ATS is indicated by the peak at 1100 cm^{-1}, and HSO_3^- and $S_2O_5^=$ are visible at 1025 and 1050 cm^{-1}. There is weak evidence for $SO_3^=$ and $SO_4^=$ at 960 and 980 cm^{-1}. In Fig. 3(b), the ATS and sulfate ion peaks have become more prominent. In Fig. 3(c), the ATS
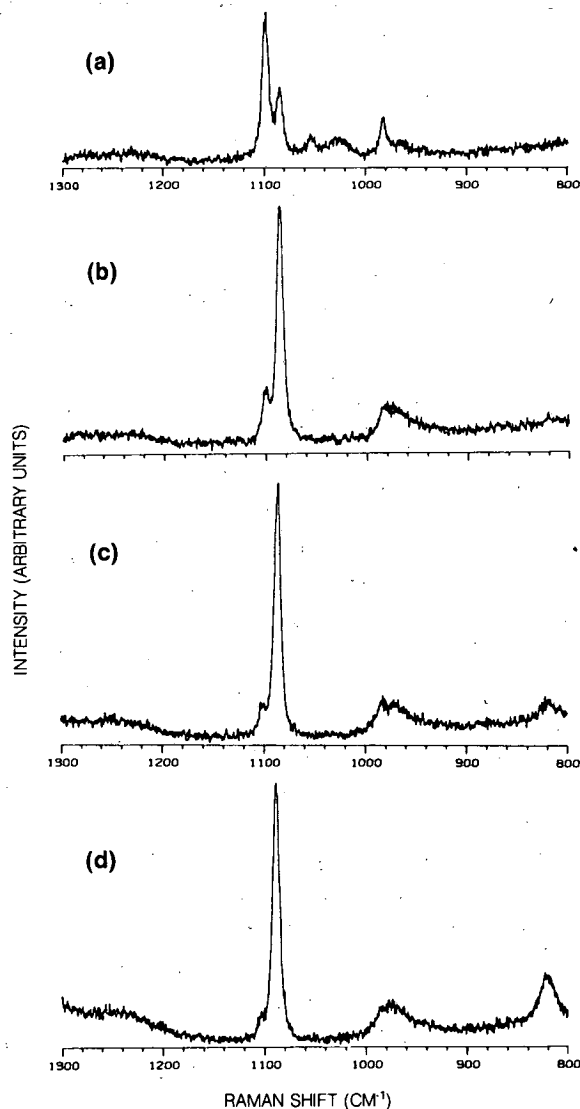

Figure 2. Raman spectra of nitrite ion–bisulfite ion mixtures taken 24 hours after mixing: (a) 0.10 M NO_2^- + 0.50 M HSO_3^-; (b) 0.26 M NO_2^- + 0.50 M HSO_3^-; (c) 0.51 M NO_2^- + 0.50 M HSO_3^-; (d) 1.02 M NO_2^- + 0.50 M HSO_3^-.
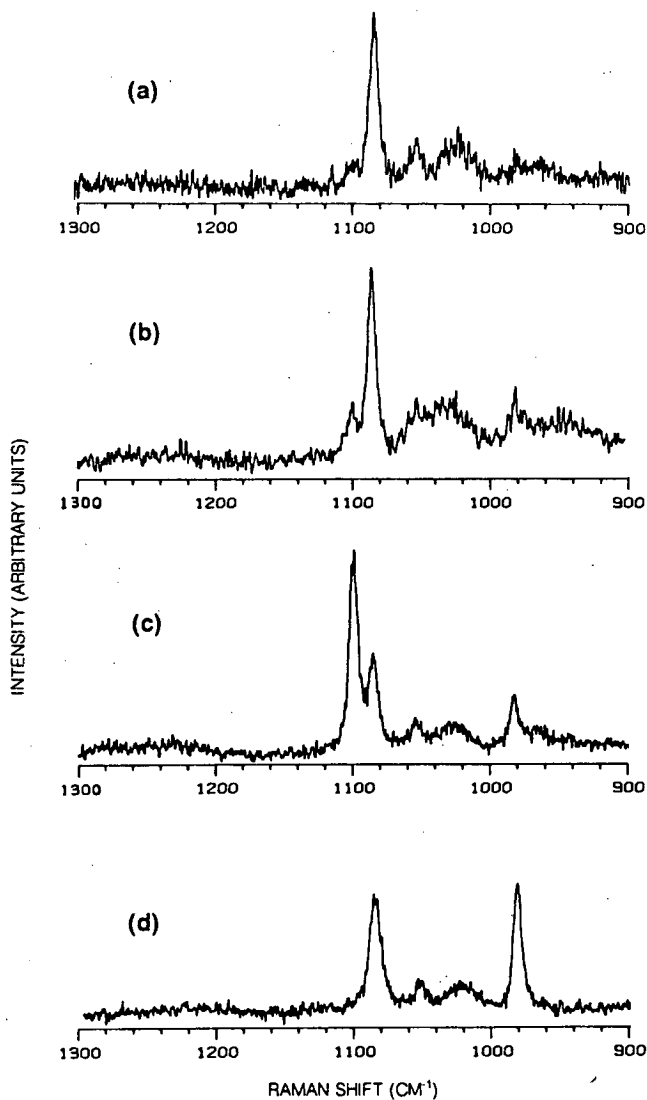
(XBL 828-10805)

Figure 3. Raman spectra of 0.10 M nitrite ion–0.50 M bisulfite ion mixture: (a) 20 minutes after mixing; (b) 2 hours after mixing; (c) 24 hours after mixing; (d) 105 days after mixing. (XBL 828-10831)

peak is very prominent, the HADS/ADS peak is smaller, sulfate ion is larger, and sulfite ion is still present. In Fig. 3(d), the peak due to ATS is absent, the 1085-cm^{-1} peak is due solely to ADS (because of the absence of the 700-cm^{-1} HADS peak), and the 970-cm^{-1} SO$_3^=$ peak is absent.

The chemistry occurring in mixture A is consistent with the reaction scheme shown in Fig. 1. The reaction producing HADS is fairly rapid and was essentially completed by the time the first spectrum was taken. The conversion of HADS to ATS has started as well. The second spectrum shows further conver-

sion of HADS to ATS. Hydrolysis is also occurring as evidenced by the growth of the sulfate ion peak at 980 cm^{-1}. The size of the sulfite ion peak relative to the bisulfite ion peak has increased from Fig. 3(a), indicating that the solution has become more basic from the production of HADS. In Fig. 3(c), much of nitrogen from the nitrite ion is in the form of ATS, with the rest as ADS and a little HADS. Considerable hydrolysis of ATS has occurred, shown by the growth of the sulfate ion peak. The solution is at a higher pH than it was originally, as indicated by the presence of sulfite ion as well as bisulfite ion. In the last spectrum, all the ATS has been hydrolyzed to ADS, and hydrolysis of ADS to SA is beginning. The hydrolysis rate of ADS is much slower than that of ATS, so evidence of its occurrence will be much slower in appearing.

Mixtures B, C, and D all show the presence of sulfite ion and nitrite ion in solution 24 hours after mixing, indicating that the reaction between them and the reaction between HADS and sulfite ion is fairly slow. This was confirmed by preparing a solution of 1.02 M nitrite ion and 0.50 M sulfite ion at pH 10. A Raman spectrum obtained shortly after mixing showed no evidence of any reaction products, and a spectrum taken one week later (Fig. 4) showed no change. From this, we conclude that the reaction between sulfite ion and nitrite ion occurs very slowly, if at all. This is consistent with the reaction mechanism proposed by Oblath et al.[5] and by Seel et al.[11] for bisulfite ion in HADS and ATS production.

We have confirmed the accuracy of the reaction scheme shown in Fig. 1. These results are of great value in developing and improving wet flue gas scrubber systems. Our work indicates that, for optimum scrubber operation, the SO$_2$/NO$_x$ ratio in the flue gases should be large enough that the ratio of bisulfite ion to nitrite ion in solution is greater than 2. The results also show that the pH of the scrubbing solution should be mildly acidic, so that bisulfite ion is the dominant form of sulfur oxyanion in solution. These scrubber conditions will permit optimum conversion of SO$_2$ and NO$_x$ into other compounds.

PLANNED ACTIVITIES FOR FY 1983

Laser Raman spectroscopy holds promise for studying other reactions occurring in aqueous solutions. Among the reactions of interest are the reactions of ferrous nitrosyl complexes with sulfite and bisulfite ions and the oxidation of sulfite and bisulfite ions by
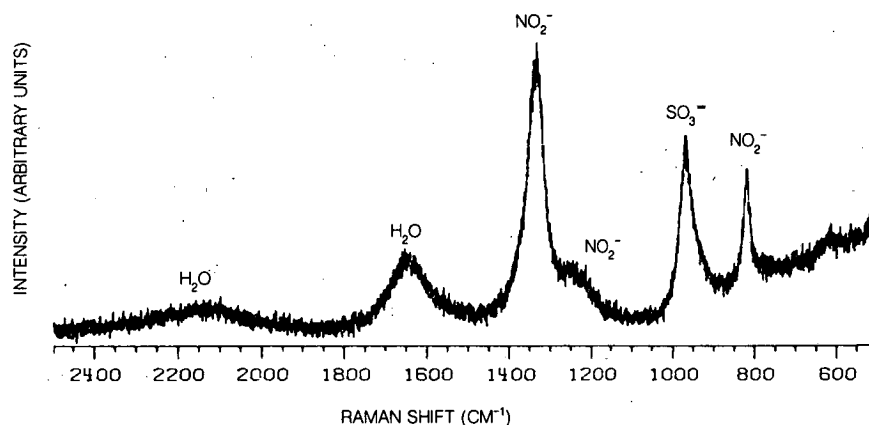
Figure 4. Raman spectrum of a 1.02 *M* nitrite ion–0.50 *M* sulfite ion mixture taken one week after mixing.
(XBL 828-10803)

dissolved oxygen in aqueous solutions. Iron and manganese ions appear to catalytically affect the latter reactions, and their influence is especially worthy of study.

REFERENCES

1. Chang, S.G., et al. (1982), *Flue Gas Desulfurization,* ACS Symposium Series 188, American Chemical Society, Washington, D.C.

2. Martin, A.E. (1981), *Emission Control Technology for Industrial Boilers,* Park Ridge, New Jersey, Noyes Data Corp.

3. Yaverbaum, L.H. (1979), *Nitrogen Oxide Control and Removal, Recent Developments,* Park Ridge, New Jersey, Noyes Data Corp.

4. Chang, S.G., et al. (1981), "The Importance of Soot Particles and Nitrous Acid in Oxidizing SO_2 in Atmospheric Aqueous Droplets," *Atmos. Environ. 15,* p. 1287.

5. Oblath, S.B., et al. (1981), "Kinetics of the Formation of Hydroxylamine Disulfonate by Reaction of Nitrite with Sulfites," *J. Phys. Chem. 85,* p. 1017.

6. Gomiscek, S. et al. (1981), "Kinetics of the Reaction Between Hydroxylamine and Sodium Bisulfite," *J. Phys. Chem. 85,* p. 2567.

7. Oblath, S.B. et al. (1983), "Reaction of Nitrite Ion with Hydroxylamine-N-Sulfonate in Aqueous Solution," *Inorg. Chem. 22,* p. 579.

8. Oblath, S.B. (1981), *Kinetics of the Reduction of Nitrite Ion by Sulfur Dioxide in Aqueous Solution,* Ph.D. Thesis, Chemistry Department, University of California, Berkeley, Lawrence Berkeley Laboratory Report LBL-13026.

9. Littlejohn, D., and Chang, S.G. (1983), "Identification of Species in a Wet Flue Gas Desulfurization and Denitrification System by Laser Raman Spectroscopy," submitted to *Environ. Sci. & Tech.*

10. Rauch, J.E., and Decius, J.C. (1966), *Spectrochim. Acta 22,* p. 1963.

11. Seel, V.F. et al. (1956), "Kinetik und Chemismus der Raschigschen Hydroxylamin-Synthese," *Z. Anorg. Allg. Chem. 284,* p. 101.

REALISM AND REPLICABILITY OF LENTIC MICROCOSMS AS A FUNCTION OF WATER AGITATION

*J. Harte, D.J. Levy, G.P. Lockett,
J.M. Oldfather, J.T. Rees,
E.I. Saegebarth, and R.A. Schneider*

Microcosms can be defined as experimental units containing inorganic and biological materials from, and exhibiting important processes occurring in, a whole ecosystem. Traditionally, microcosms have been used in chemical uptake studies, enrichment studies, and primary productivity measurements. Such applications are typically of short duration (4 to 48 hours) and are carried out in small samples, of a few liters volume or less, from a natural system. More recently, larger microcosms have been proposed for longer-term studies to determine the effects of pollutants on ecosystem functions and species composition.[1-3] A potential obstacle to such applications is that over longer time periods (weeks or months), microcosms may replicate poorly and their chemical and biotic behavior may diverge from the natural system from which they were derived. The results reported here contribute to our understanding of the potential for such divergence.

In a series of experiments, we have been analyzing how the design of lentic (freshwater) microcosms and the conditions under which they are operated affect their replicability and realism.[4,5] A partial list of the factors that can affect lentic microcosm replicability and realism includes: container size and shape, light and temperature levels, rate of water agitation, rate of hydraulic flow-through, presence or absence of macroflora and macrofauna, and presence or absence of algal wall growth.[4-6] It has been demonstrated that the degree of water agitation in estuarine microcosms effects significantly the degree to which these systems simulate the estuary from which they were derived.[6] In the present experiments,[7] the ability of lentic freshwater microcosms to replicate well and to simulate accurately the pelagic epilimnion of a stratified reservoir is explored as a function of the degree of water agitation. Lessons learned from earlier studies concerning tank size, water temperature control, and the need to prevent algal wall growth are incorporated into the experimental design.

ACCOMPLISHMENTS DURING FY 1982

In 1981, two experiments, lasting 7 and 5 weeks respectively, were carried out. The water source and field-comparison system was Briones Reservoir in Contra Costa County, California. Experiment I (June 6–July 20) used water taken in equal amounts from depths of 5 and 8 m. The epilimnion depth of the reservoir was 8 to 10 m, and the depth-integrated temperature increased from 18.5°C to ~20.5°C over the course of the experiment. Experiment II (October 21–November 23) used water taken in equal amounts from 0, 5, and 10 m. The epilimnion depth was 15-20 m, and the depth-integrated temperature decreased from 17.6°C to 15°. In both experiments, water was obtained approximately 100 m from the nearest shore, using a 12-liter Van Dorn bottle.

The water was placed in a large mixing tank in the laboratory, then siphoned into cylindrical Nalgene tanks (diameter = 33.0 cm; height = 70.5 cm), which were filled with 58 liters of water. (Experiment I had 6 tanks, Experiment II had 12.) Previous work had demonstrated that microcosms 50 liters or larger best simulate relatively isolated pelagic surface water.[5]

In Experiment I, two levels of agitation—A and D—were examined, while in experiment II, four levels of agitation—A, B, C, and D—were examined. Three replicate tanks were used to study each level of agitation. In Experiment I, systems A were not agitated while systems D were agitated by Pyrex stirring propellers (4 blades; $r = 2.5$ cm) inserted to a depth of 15 cm and rotated at ~600 rpm by standard stirring motors. Motors were on during light periods and off during dark periods. In Experiment II, systems A were not agitated. Systems B were agitated by air bubbling out of a capillary tube at a rate of 1 liter/min.; the tube extended 15 cm below the water surface. Systems C were agitated by slowly rotating (75 rpm) flat Lucite paddles (20 cm × 7.5 cm × 0.5 cm)

inserted to a depth of 23 cm. Systems D were agitated by rapidly rotating (600 rpm) Teflon stirring propellers (3 blades, $r = 2.2$ cm) inserted to a depth of 23 cm. The stirring motors in systems C and D were on continuously.

Sampling was done weekly in both the reservoir and the microcosms, and always within a day of each other. In the reservoir, sampling was done from a small aluminum boat at approximately the same position from which the microcosm water was drawn. The variables measured included phytoplankton and zooplankton (number density by genus), ammonia, dissolved silica, pH, total organic carbon, dissolved organic carbon, temperature, light levels, and water agitation rate (the last by measuring the rate of dissolution of small gypsum blocks suspended in the reservoir and in the microcosms).

In both experiments, the dissolution rate in the most vigorously agitated microcosms, systems D, most nearly matched that measured in the reservoir epilimnion. The dissolution rate in the least agitated microcosms, systems A, was on the order of one-tenth that measured in the most agitated microcosms.

Nearly all chemical measurements showed good replication within a set of microcosms ($x^2 \leq 6.00$ and/or coefficient of variation ≤ 0.10). In the microcosms, the chemical variables in both experiments did not depend strongly on the level of agitation, whereas the taxonomic variables in the microcosms did exhibit definite trends as a function of agitation. The taxonomic variables in sets of microcosms with no agitation (systems A) and agitation accomplished by bubbling (systems B) exhibited slightly better replication than did the mechanically agitated microcosms (systems C and D).

Time-averaged values of the taxonomic variables were used to compare quantitatively each set of microcosms with the reservoir. A variable in a set of microcosms was considered to exhibit good tracking if it replicated well with the set ($x^2 \leq 6.00$), and if its mean value (averaged over the set of microcosms) was close ($|t| \leq 2.92$, d.f. $= 2$) to the depth-averaged value observed in the reservoir epilimnion. By these criteria, the taxonomic variables in Experiment I tracked poorly with only 17% of the taxonomic data entries satisfying them in the mechanically agitated systems. Nonetheless, for 5 weeks the major population changes exhibited by the dominant phytoplankton and zooplankton in the reservoir were well followed by these variables in the microcosms. In Experiment II, the unagitated and bubbled systems tracked the reservoir quite well, while the mechanically agitated systems did not (the above tracking criteria were satisfied by 79%, 69%, 21%, and 14% of the taxonomic data entries in systems A, B, C, and D respectively). A further indication that important relationships in the reservoir during Experiment I were also present in the microcosms is the fact that the identical functional and numerical relationship between SiO_2 concentrations and total diatom volume observed in the reservoir was observed in the microcosms.

This work can be compared to another set of experiments, similar in design to ours, which investigated the effects of mechanical agitation on microcosms derived from one point in Narragansett Bay.[6] This study concluded that the level of mechanical agitation in estuarine microcosms should be set to match the dissolution rate in the field system being investigated. This conclusion was based on the assumption that the matching of physical parameters, in particular the gypsum dissolution rate, is more important than achieving maximum realism of biological population densities.

The matching of lake or estuarine turbulence levels in microcosms is a desirable goal, but we urge that some caution be exercised in interpreting gypsum dissolution rates too literally. In particular, water movement in the reservoir can be characterized by scales of motion ranging from the small (e.g., small-scale turbulence) to the large (e.g., wind-driven currents). The dissolution rates of the tethered gypsum blocks measured in the reservoir may reflect increased dissolution due to large-scale motion not present in the microcosms. Thus, by matching gypsum dissolution rates, it is possible that microturbulence in the microcosms is set well above the value in the natural system.

We conclude that freshwater microcosms designed to mimic the pelagic epilimnion of a lentic body can be run for periods of 3 to 6 weeks with statistically acceptable replicability and realism. In most cases, gentle, nonmechanical agitation is the most successful technique for insuring good tracking and replicability. Gypsum dissolution rates very likely do not provide a realistic measure of biologically-relevant turbulence.

PLANNED ACTIVITIES FOR FY 1983

Further studies to determine how microcosm design and operating conditions affect replicability and realism of performance are planned. In particular, studies on appropriate procedures for including benthic sediments in microcosms will be continued and the results analyzed according to the statistical criteria developed for the water agitation research.

An application of lentic microcosms to determine effects of prolonged darkness on aquatic food chains is planned. In addition, an application of microcosms to determine the effects of trace metals on phosphatase activity will be carried out. A successful model for describing mineralization processes in lakewaters,[8] previously developed from microcosm studies[9] of nitrogen cycling will be extended to describe the phosphorous cycle. Finally, the development of soil microcosms for use in acid deposition research is also planned.

REFERENCES

1. Pilson, M.E.Q., Oviatt, C.A., and Nixon, S.W. (1980), "Annual Nutrient Cycles in a Marine Microcosm," in *Microcosms in Ecological Research*, J.P. Giesy, Jr., Ed., Technical Information Center, U.S. Department of Energy, Oak Ridge, Tennessee, CONF-781101, p. 753.

2. Giesy, J.P., Jr., Ed. (1980), *Microcosms in Ecological Research*, Technical Information Center, U.S. Department of Energy, Oak Ridge, Tennessee, CONF-781101.

3. National Academy of Sciences (1981), *Testing for Effects of Chemicals on Ecosystems. A Report by the Committee to Review Methods for Ecotoxicology*, National Academy Press, Washington D.C., pp. 62–77.

4. Harte, J., Levy, D., and Rees, J. (1983), "Pelagic Diatom Populations in Lentic Freshwater Microcosms," *Int. Rev. der Gesamten Hydrobiol.,* in press.

5. Harte, J., Levy, D., Rees, J., and Saegebarth, E. (1981), "Assessment of Optimum Aquatic Microcosm Design for Pollution Impact Studies," Electric Power Research Institute Report EA-1989, Palo Alto, California.

6. Perez, K.T., et al. (1977), "The Importance of Physical and Biotic Scaling to the Experimental Simulation of a Coastal Marine System," *Helgolander wiss. Meeresunters 30*, p. 144.

7. Harte, J., et al. (1983), "Realism and Replicability of Freshwater Lentic Microcosms as a Function of Water Agitation," submitted to *Freshwater Biology*, Lawrence Berkeley Laboratory Report LBL-16133.

ACID PRECIPITATION AND SURFACE-WATER VULNERABILITY ON THE WESTERN SLOPE OF THE HIGH COLORADO ROCKIES*†

*J. Harte, G.P. Lockett,
R.A. Schneider, H. Michaels,
and C. Blanchard*

Acid precipitation has been a subject of intense research for more than a decade, since it was discovered and documented in Scandinavia and in the northeastern United States. Defined as a precipitation with a pH substantially below 5.65 (the normal equilibrium value) and composed primarily of dilute sulfuric and nitric acids (which come from the burning of fossil fuels), acid precipitation has also been reported in several locations in the western states, most notably in central and southern California[1,2] and on the eastern slope of the Colorado Rockies.[3] We report here on the site-specific incidence and potential effects of acid precipitation on the western slope of the Rockies.

Increased fossil fuel consumption in California, the Great Basin, or in the upper or lower Colorado River drainage regions could subject the western slope of the Rockies to acidic precipitation. For that reason, this investigation was designed to obtain reliable baseline data on precipitation and surface water chemistry on the western slope. Such data provide a means of assessing the present sensitivity of watersheds in the region to acidification and will

allow future determination of a possible worsening trend in precipitation quality.

Our study site (Fig. 1) is a remote and relatively pristine high-elevation watershed located in the Elk Mountains of west-central Colorado and includes the entire upstream drainage. It is largely on land owned by The Nature Conservancy and is called the Galena Mountain/Mexican Cut Preserve. The study to date includes 21 non-consecutive months of observations over a 26-month period.

The two major results reported here are evidence for numerous storm events with pH considerably below 5.6 and evidence of very poorly buffered surface waters, as measured by titratable alkalinity. In addition, biological species likely to be sensitive to acidification have been located at the site, and preliminary censuses of these populations have been carried out.

ACCOMPLISHMENTS DURING FY 1982

Table 1 shows time averages of precipitation pH. In Figs. 2 and 3, the pH values of the individual storm samples are plotted against the amount of precipita-
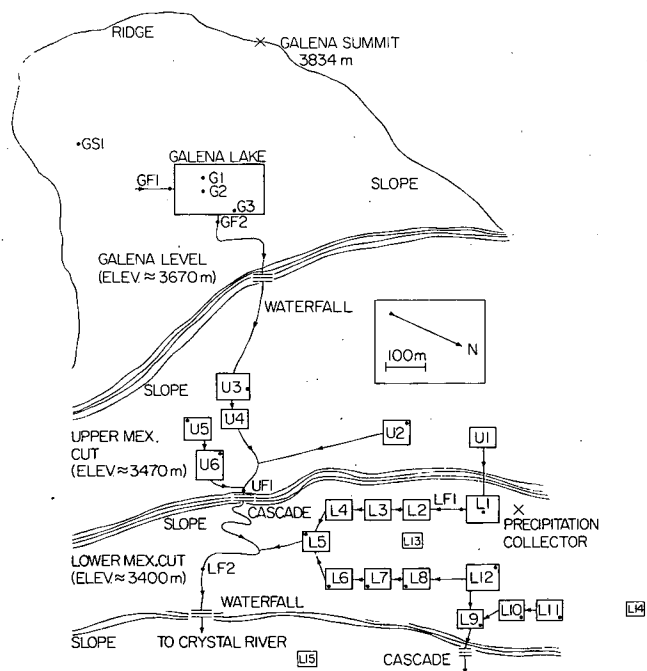

Figure 1. A schematic map of the Galena Mountain/Mexican Cut watershed. Sampling sites are indicated by dots, the lake, tarn, and ponds by boxes, and connecting streams by lines with arrows in the direction of flow.

(XBL 825-674)

Table 1. Precipitation acidity averages, with and without a precipitation-amount weighting factor (centimeters of precipitation).

Period	N^a	Average[b] precipitation pH with P_i weighting factor	Average[c] precipitation pH without P_i weighting factor
Summer 1980	4		4.35
Winter 1980-81	35	4.28	4.17
Summer 1981	14	4.68	4.64
Winter 1981-82	24	5.12	5.09
		4.55	4.40
Total N		73	77

[a]Number of samples

[b]Average precipitation pH is expressed by the formula

$$-\log \left\{ \sum_{i=1}^{N} [H_i^+] \, P_i \Big/ \sum_{i=1}^{N} P_i \right\}$$

where P_i is the precipitation amount.

[c]Average pH without rainfall amount factor is expressed by the formula

$$-\log \sum_{i=1}^{N} \frac{[H_i^+]}{N}$$

tion and the time between an event and its predecessor. Figure 2 shows that both the very high and the very low pH measurements correspond to samples with a relatively small amount of precipitation. Figure 3 suggests a weak inverse relationship between pH and sample interval. A considerable amount of scatter is evident in these plots. Measurement of anion correlations indicates that the most acidic winter events show a slight tendency toward higher nitrate-to-sulfate ratios.

For several rain events, we measured the pH immediately afterwards and then one to three days later in samples sealed in glass flasks after initial measurement. In all cases, the pH rose from one-half to one pH unit during that interval, presumably because of the presence of buffering agents in the samples. Rain splash on the dusty ground near the collector was one likely source for such agents. We note, in addition, that the generally alkaline soils at lower elevations in the western United States could
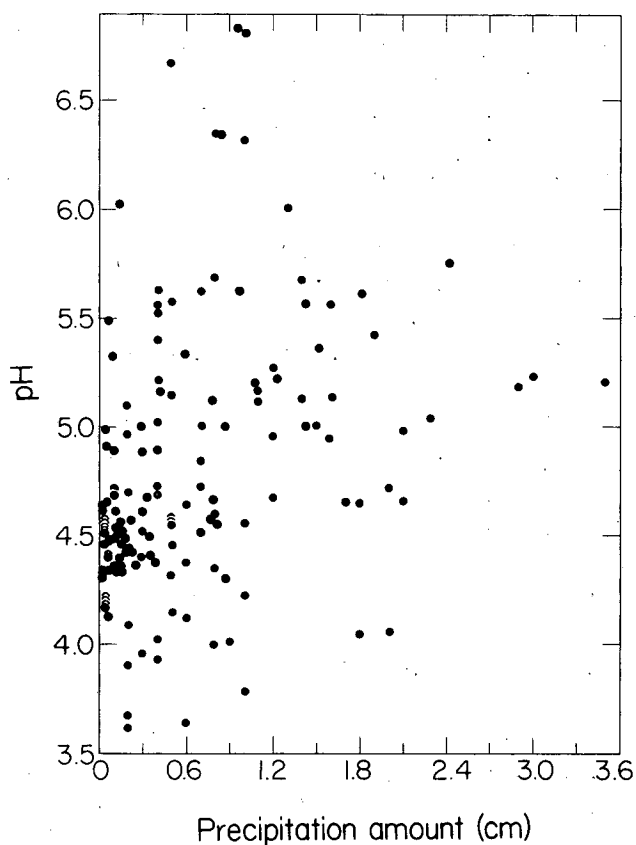
Figure 2. Precipitation pH vs. precipitation amount.
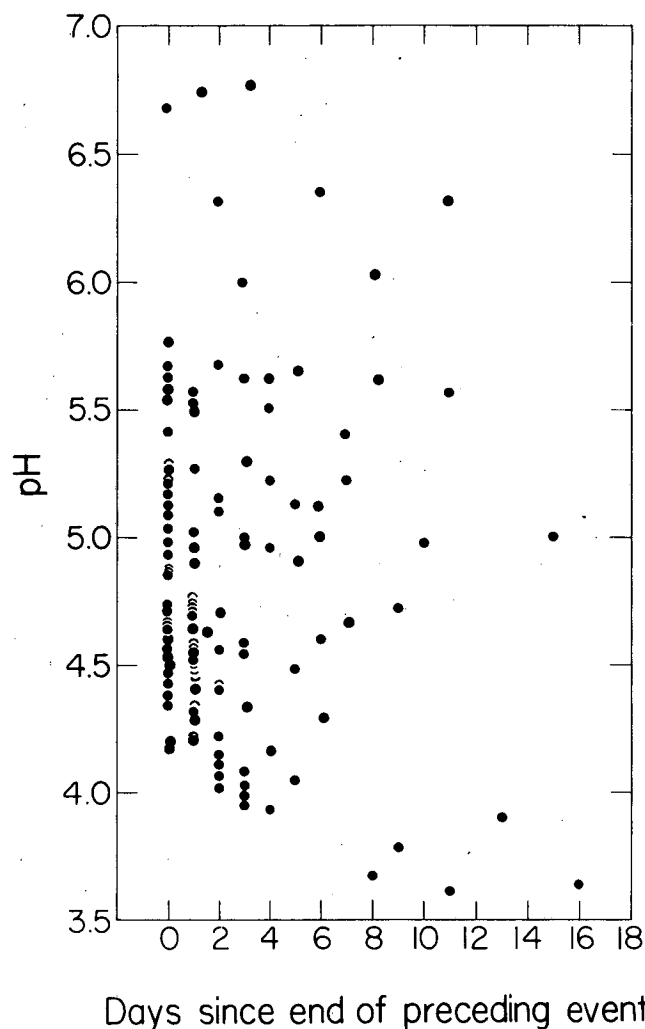(XBL 825-669)

Days since end of preceding event

Figure 3. Precipitation pH vs. time between sampled events, rounded off to the nearest day. Sample collection always occurred either in the midst of a storm or immediately after precipitation ceased. (XBL 825-673)

be the source of buffering agents in precipitation even at higher elevations. Calcium plus magnesium concentrations measured in the summer 1981 precipitation samples (for which rain splash was eliminated) ranged from 9.0 to 18.2 microequivalents per liter, supporting this speculation and suggesting that the precipitation pH could have been lower than measured had partial neutralization not occurred. The presence of buffering materials in the precipitation may account for the spread in Fig. 3; long intervals between storms can allow acidic materials to build up in the atmosphere under some circumstances, alkaline agents under others.[4]

Surface waters were also measured for pH, alkalinity, and calcium and magnesium concentrations. In Fig. 4, the plot of pH vs. alkalinity for the surface-water samples shows that all of the data lie below the theoretical curve. The formula for this curve is $[H^+] + [alkalinity] = 10^{-11.5}/[H^+]$. It is derived under the assumption that all the alkalinity is due to the bicarbonate system, and is based on the standard equilibrium relations for atmospheric

CO_2 (at 3500 m) and aqueous OH^-, CO_3^{2-}, HCO_3^{2-}, CO_2, and H^+. The figure suggests that other sources of alkalinity besides bicarbonate are present. For those samples for which calcium and magnesium concentrations were measured, a linear regression of alkalinity against the sum of the calcium and magnesium concentrations (expressed as microequivalents/liter) yields:

$$alkalinity = 10.6 + 0.65\,([Ca] + [Mg])\ ,$$

with $r = 0.97$, $n = 30$. This suggests that a portion of the bicarbonate alkalinity associated with the calcium and magnesium is gone, but that other sources of buffering, perhaps of organic origin, are present.
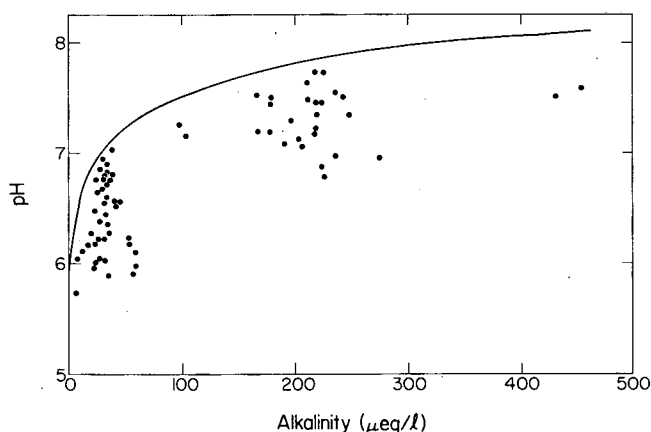
Figure 4. Plot of pH vs. alkalinity for all surface-water samples. The curve expresses a theoretical relationship between pH and carbonate-bicarbonate alkalinity.

(XBL 825-672)

A species of salamander, *Ambystoma tigrinum*, inhabits many of the ponds in the Mexican Cut. Censusing has been carried out over two summers in pond L1 (see Fig. 1) and for all ponds in 1981. Because this species belongs to the same genus as the acid-sensitive spotted salamander (*Ambystoma maculatum*) of the Adirondacks[5] it may serve as a valuable biological indicator of a decreasing trend in surface water pH during snow melt, when routine measurements are extremely difficult to carry out. Other populations at the site that may serve as useful indicators are cutthroat trout (*Salmo clarki*), lichens, and several species of *Daphnia*, including *D. pulex*, which may be sensitive to declining pond-water pH.[6]

Our results provide evidence of acidic precipitation in the west Elk Mountains of Colorado. The period of study was too short to allow estimation of a temporal trend in the total acidity or the ionic composition of the samples, but our sampling and chemical analysis of precipitation at the site are continuing, and we expect to be able to characterize such trends after several more years of investigation.

In several respects, the precipitation data presented here differ qualitatively from those in the northeastern United States. Comparing winter snow with summer rain events, we find the variation in pH from storm to storm considerably greater in winter than in summer at our site. The 15 precipitation samples with lowest pH all occurred in winter, as did the 19 events with highest pH. Elsewhere, the most acidic events and the widest range of pH values appear to occur in summer.[7]

The considerable amount of scatter when pH is regressed against the logarithm of precipitation amount ($r = 0.25$, $n = 71$) or against the interval between samples ($r = 0.3$, $n = 65$) is also in contrast to observations in the northeastern U.S., where pH tends to be more positively correlated with precipitation amount and negatively with storm interval.[7-9]

Precipitation data from the eastern states indicate typical annually averaged nitrate-to-sulfate (equivalents) ratios of 0.4,[8,10] in contrast to our measured value of 0.9. In this respect, our results are more typical of the western U.S.[1-3]

In the eastern U.S., precipitation events in the colder months tend to have a significantly higher nitrate-to-sulfate ratio than those in the warmer months. Our data show no significant trend of that sort; during the summer of 1981, the average nitrate-to-sulfate ratio differed from the summer-plus-winter average by less than 3%.

Our data differ also from measurements for the northeastern U.S. in the large ammonium concentrations we observed. In this respect, our data are similar to those taken in the southwestern U.S.[4] For those samples in which sulfate, nitrate, and ammonium were measured (summer 1981), $[NH_4^+]$ averages 15.0 $\mu eq/l$, $[SO_4^{2-}]$ averages 20.9 $\mu eq/l$, $[NO_3^-]$ averages 17.3 $\mu eq/l$, and $[H^+]$ averages 23.1 $\mu eq/l$. The ammonium-to-sulfate ratio of 0.72 is considerably higher than in the northeastern U.S., where the ratio of ammonium-to-sulfate in precipitation averages about 0.2.[7,9,10] Our results are suggestive of aerosol composition characterized by roughly equal parts of $(NH_4)_2SO_4$ and NH_4HSO_4. However, we are not suggesting that the precipitation resembles aerosol in other respects. In particular, for our summer 1981 samples, the ratio of $[H^+]$ to $[SO_4^{2-}]$ is 1.1 and the ratio of $[NO_3^+]$ to NH_4^- is 1.2. Both ratios are considerably higher than for aerosols in the northeastern U.S., where 0.2 and 0.04, respectively, are typical values.[11]

The variations in $[NH_4^+]$ and $[H^+]$ measurements from event to event in summer 1981 can be about equally well explained by variation in the nitrate and sulfate concentrations separately. In particular, linear regression yields:

$[NH^+] = 0.79 [SO_4^{2-}] - 1.20$, $r = 0.80$, $n = 13$;

$$[NH^+] = 0.94\ [NO_3^-] - 1.00\ ,\ r = 0.87\ ,\ n = 13\ ;$$

$$[H^+] = 0.63\ [SO_4^{2-}] + 10.7\ ,\ r = 0.73\ ,\ n = 14\ ;$$

and

$$[H^+] = 0.74\ [NO_3^-] + 10.9\ ,\ r = 0.79\ ,\ n = 14\ ,$$

where all concentrations are expressed as micro-equivalents per liter.

This discussion is based on comparisons of concentrations. Volume-weighted comparisons would yield the same qualitative results. A safe generalization is that the precipitation chemistry at our site on the western slope of the Colorado Rockies bears a closer resemblance to the precipitation chemistry in California and the southwestern United States than it does to the precipitation chemistry in the northeastern U.S. and Scandinavia.

The surface-water and soil analyses indicate that some of the water bodies in this high-elevation watershed are quite vulnerable to acidification. In particular, the alkalinities of Galena Lake and of ponds L6, L8, L9, L10, L11, and L12 average below 60 μeq/liter. Other ponds have considerably higher alkalinity. In some of the ponds below timberline with alkalinity above 60 μeq/l, relatively high biological productivity could be a contributing factor. However, the two ponds with the highest alkalinity in the watershed—ponds U5 and U6, with alkalinities of 462 and 902 μeq/l, respectively—are above timberline in the upper Cut and had considerably less visible accumulations of water-column organic materials by midsummer than did the ponds below timberline, such as pond L1. Organic acids from conifers surrounding the ponds in the lower Cut are a minor cause of the lower pH and alkalinity found there, whereas ground water in contact with subterranean limestone is the major cause of the high alkalinity seen in ponds U5 and U6.

A watershed is at risk from acid precipitation when three criteria are met: acid precipitation is falling in the watershed, buffering agents are present only in low concentrations, and sensitive biological species inhabit the site. All three criteria are satisfied in the Galena Mountain/Mexican Cut Preserve; if precipitation in the region continues to be acidic in the future, chemical and biological transformations can be anticipated.

PLANNED ACTIVITIES FOR FY 1983

A continuation of the collection and analysis of baseline data is planned. A careful statistical treatment of surface water alkalinity changes over time will be carried out to determine whether acidic precipitation has resulted in the decline of watershed buffering capacity. A mathematical model will be constructed for predicting the chronology of watershed acidification (i.e., the period over which alkalinity will gradually decline to zero, when surface-water pH will plummet).

Research on snow melt dynamics and its relation to the spring "acid pulse" is also planned for the Sierra Nevada, where our earlier work[12] indicated high vulnerability of surface waters to acid deposition. Finally, a policy-oriented paper will be prepared on acid precipitation risks in the developing nations; this will be based in part on results of our field research in China.[13]

REFERENCES

1. Liljestrand, H.M., and Morgan, J.J. (1978), *Environ. Sci. Technol. 12*, p. 1271.
2. McColl, J.G. (1980), "A Survey of Acid Precipitation in Northern California," California Air Resources Board, Sacramento, California, Final Report for Contract A7-149-30.
3. Lewis, W.M., and Grant, M.C. (1979), *Ecology, 60*, p. 1093.
4. Dawson, G.A. (1978), *Atmos. Environ. 12*, p. 1991.
5. Pough, F.M. (1974), *Science 192*, p. 68.
6. Davis, P. and Ozborn, G.W. (1969), *Canad. J. of Zoology 47*, p. 1173.
7. Johannes, A.M., Altwicker, E.R., and Clesceri, N.L. (1981), *Characterization of Acidic Precipitation in the Adirondack Region*, Electric Power Research Institute Report EA-1826, Palo Alto, California.
8. Baker, M., Caniparoli, D., and Harrison, H. (1981), *Atmos. Environ. 15*, p. 43.
9. Raynor, G.S., and Hayes, J.V. (1981), *Water, Air, Soil Pollut. 15*, p. 229.
10. McNaughton, D.J. (1981), *Atmos. Environ. 15*, p. 1075.
11. Johnson, S.A., et al. (1981), *The Map's Aerosol Acidity Network: A Progress Report and Data Summary*, Argonne National Laboratory Report ANL-81-63.

12. Tonnessen K. and Harte, J. (1982), "Acid Rain and Ecological Damage: Implications of Sierra Nevada Lake Studies," *Publ. Aff. Rep. 23*, p. 1.

13. Harte, J. (1983), *Atmos. Envir. 17*, p. 403.

SURVEY OF INSTRUMENTATION FOR ENVIRONMENTAL MONITORING*

*M. Quinby-Hunt, R. McLaughlin, A. Quintanilha,
G. Morton, and C. Case*

The environmental impact of pollutants resulting from current and future technological development is of continuing concern to responsible societies. Governments are increasingly aware that an accurate analysis of such effects is required if efficient and effective measures are to be taken to correct or prevent the potentially dangerous consequences of trace contaminants and other hazards of new processes and materials. Fortunately, instruments and techniques are continuously being developed that allow the rapid characterization and quantification of most pollutants associated with established and developing technologies.

Over the past 12 years, the Environmental Instrumentation Survey has collected information on instrumentation for environmental monitoring. The Survey reviews three major areas: (1) environmental information about the constituents to be monitored; (2) analytical techniques; and (3) commercial instrumentation. The first area gives an overview of the sources, characteristics, and effects of a wide variety of environmental constituents and pollutants; it also provides information on regulatory means of control. The second area describes and evaluates those analytical techniques currently used, including "standard," "reference," and developing methods for the identification and quantification of pollutants. The third area gives a detailed description of commercially available analytical instrumentation; these

instrument notes cover modes of operation, ranges, performance, features, options available, and cost.

The inclusion of these three distinct areas into a single source has proven to be extremely valuable to many workers because it facilitates and expedites the choice of appropriate instrumentation by the laboratories concerned (state, federal, industrial, and those of other institutions).

The work has been subdivided into four major fields: Radiation, Water, Air, and Biomedical Monitoring. Wiley Interscience has published the Radiation volume[1] and has contracted to publish the second, Water.

ACCOMPLISHMENTS DURING FY 1982

Radiation

The Radiation volume was completely rewritten and will be commercially published by Wiley Interscience in April 1983 as a volume of 1130 + xix pages; all 20 chapters were updated and carefully edited prior to publication. The instrument notes were completely revised so that the latest information (up to January 1983) could be included for each manufacturer.

Water

We have completed new sections on bacteria, residues (solids), halogens, and cyanide, and an update on asbestos. These sections contain descriptions of instrumental techniques, including ion chromatography, ion-selective electrodes, and electron-microscope methods for monitoring asbestos. Three sections on organics in water (phenolics, pesticides, and petrochemicals) have been updated.

Air (Particulates)

Sections on neutron activation techniques for measurement of trace metals in airborne particulate

matter and x-ray spectrometry and diffractometry have been reviewed, and a new section on the composition of atmospheric particulate matter is currently being reviewed.

PLANNED ACTIVITIES FOR FY 1983

Water

A contract has been negotiated with Wiley Interscience for publication of the Water volume by mid-1984. The book will consist of four sections: inorganic, organic, biological, and physical measurements. Chapter topics include:

Inorganic

Major anions
Trace metals
Nutrient elements
Dissolved gases
Strong oxidizing agents
Alkalinity and pH

Organic

Organic carbon
Phenolics
Pesticides
Oil and grease
Halogenated hydrocarbons
Surfactants

Biological

Biomass indicators
Microbiological
    constituents
Biological oxygen demand

Physical

Temperature
Turbidity
Solids
Asbestos
Color, taste, and odor
Radiation

A new section on biomass indicators such as chlorophylls, phaeophytins, and adenosine triphosphate is in preparation. This is important because biomass indicators can provide important information on the effects that effluents from facilities such as petroleum refineries and nuclear power plants have on the water into which they are released. A new section on turbidity is planned, and new sections are being prepared on strong oxidizing agents and on color, taste, and odor.

Instrument notes will be completely revised and expanded to include all the current manufacturers in this field.

Radiation

The Radiation volume is scheduled to be published in April 1983.

Air

Contingent on funding, this volume will be updated and edited for publication.

REFERENCE

1. Environmental Instrumentation Survey, Lawrence Berkeley Laboratory (1983), *Instrumentation for Environmental Monitoring: Vol. 1, Radiation*, 2nd ed., John Wiley and Sons, New York.

CURRENT STATUS OF THE IMPACT THEORY OF MASS EXTINCTION

H.V. Michel, F. Asaro, W. Alvarez, and L.W. Alvarez

Two geological boundaries, the Permian-Triassic and the Cretaceous-Tertiary, and a more recent boundary between the Eocene and Oligocene stages are being investigated for geochemical anomalies associated with impacts and extinctions.

ACCOMPLISHMENTS DURING FY 1982

Eocene-Oligocene Boundary

Five new iridium anomalies in deep-sea cores associated with microtektites (34 million years old) from the North American strewn tektite field have been discovered. The site locations and the excess Ir

abundances (expressed in nanograms per cm^2) were Deep-Sea Drilling Project sites 167 (>0.8), 166 (2), and 69A (29) in the Central Pacific, DSDP 94 (~45) in the Gulf of Mexico, and DSDP 216 (4) in the Indian Ocean. These data, together with two earlier Ir anomalies[1,2] found in the Caribbean Sea (one by ourselves and the other by another group) and associated with extinctions of radiolaria, indicate an equatorial distribution over halfway around the world (Fig. 1). The ratios of iridium, chromium, and nickel in DSDP 69A are close to the values expected for chondritic meteorites. This work reinforces the association of microtektites, impacts, iridium anomalies, and extinctions.

Permian-Triassic Boundary

Sensitive measurements of Ir and other elements were made on a suite of samples from near the Permian-Triassic boundary (about 230 million years old) in five locations in China. There were two sites near Nanking, two near Changsingh, and one near Kweiyang, a span of 1300 kilometers. The boundary should have either a volcanic or an extraterrestrial-

impact source, since clay minerology studies indicated it was an altered glass. No Ir was detected in any of the five samples within an overall upper limit of 0.008 parts per billion. At present, the best explanation for the origin of the boundary is volcanic.[2]

Cretaceous-Tertiary Boundary

New Ir anomalies in the Cretaceous-Tertiary (C-T) boundary (about 65 million years old) were identified in deep-sea cores from DSDP sites 530A, 527, 528, and 529 in the South Atlantic Ocean. About 30 elements were measured in suites of samples from each site. This work demonstrated that, almost without exception, every continuously deposited Cretaceous-Tertiary boundary contains an Ir anomaly.

Correlation of data on plankton, brachiopods, ammonites, bivalves, and cheilostome bryozoans show that they (as well as nannoplankton and foraminifera) became extinct suddenly at the C-T boundary.

In a collaboration with W. Clemens, a new continental Ir anomaly at Lance Creek near Lusk, Wyoming, was identified. This anomaly is close (within 20 cm) to the geological C-T boundary, i.e., the base of
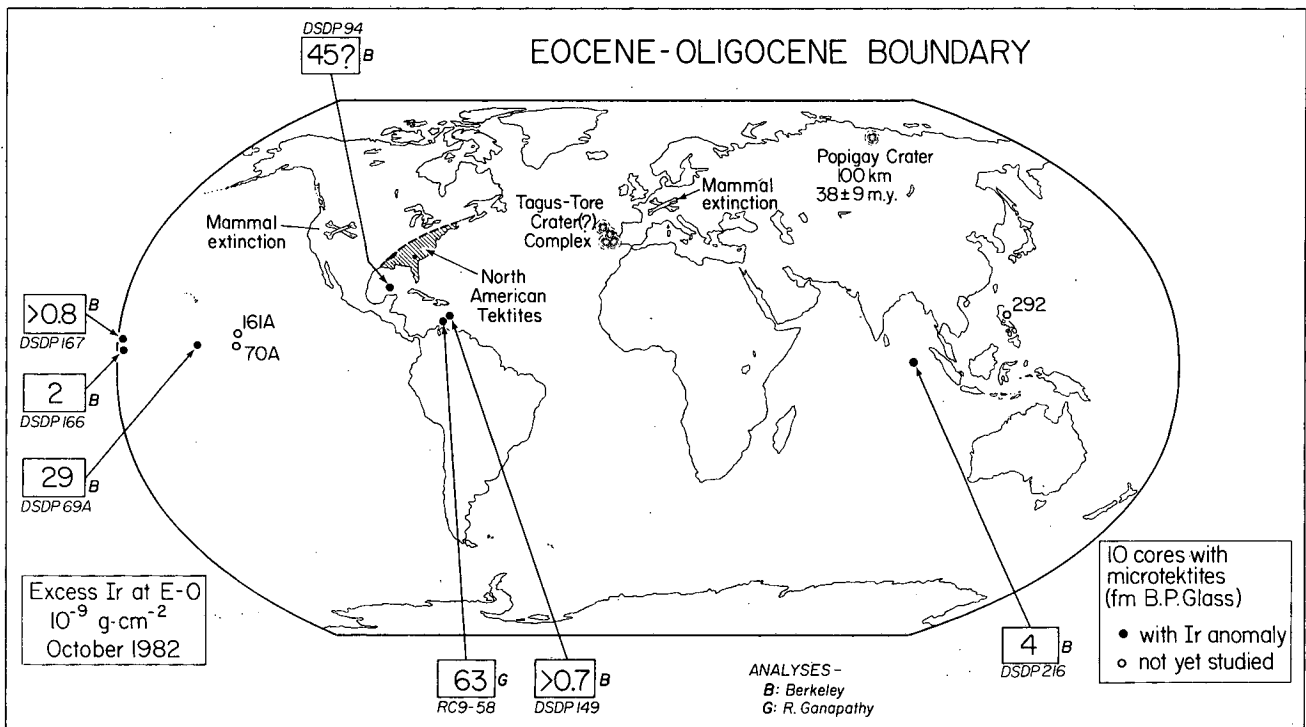

Figure 1. Sites of iridium anomalies at the Eocene-Oligocene boundary, by Deep-Sea Drilling Project (DSDP) site number (known as of October 1982). Boxes indicate excess Ir abundances in nanograms per square centimeter. (XBL 8210-2946)

the lowest Tertiary coal layer. Continental Ir anomalies which are in agreement with the geological boundary have been found in Montana and Wyoming by us and in New Mexico and Colorado by others. Since all C-T Ir anomalies following an extraterrestrial impact would have been deposited at the same time, such anomalies could be used as precise relative time markers.

Statistical analysis of most of the pertinent dinosaur stratigraphic data has shown that the dinosaurs became extinct in western North America suddenly at the C-T boundary. Because of the small number of dinosaur fossils compared to the much more numerous smaller fossils of marine organisms, there is an uncertainty of about 30,000 years in the estimated time of extinction of the dinosaurs. Because of our work, more precise characterizations of dinosaur stratigraphic positions are being made, and more precise data will be forthcoming.

Fourteen black shales from three deep-sea cores were studied, but no Ir was detected in any sample. This demonstrated that highly organic reducing environments do not automatically produce Ir anomalies.

A detailed stratigraphic profile was measured for ~30 elements in the Stevns Klint C-T sediments in Denmark. There was an obvious shift in position of the various elements (on the order of a few centimeters) in the boundary layer. The work strongly suggests that Ir (a very noble element) is, nonetheless, mobile in deep sea sediments. Previous work of ours had shown that the Au/Ir and Pt/Ir ratios in bulk samples from the center of the boundary agreed exactly with comparable data on Type I carbonaceous chondrites, but that the Ni/Ir ratio was ~20% too low in the C-T material. The present work, however, shows that there is no Ni deficit in the boundary and that the Ni has only been shifted in position with respect to the Ir (Fig. 2).

Studies of many elements in mineral fractions have shown that Cretaceous-Tertiary Ir is not particularly concentrated by pyrite or glauconite, although it is associated with pyrite-bearing clays. In collaboration with A. Montanari, however, we found that Ir is concentrated strongly in magnetite from one Italian C-T section.[3] It is preferentially found in the fine clay fractions; it is also found in the silt-size silicate fractions, but not in silt-size quartz fractions. Iridium anomalies associated with 13 new marine C-T sections in Italy were found. In the sand fraction of these and other C-T clay layers containing the Ir anomaly, evidence of diagenetically altered microtektites,[3,4] i.e., impact debris, was found. Thus, the impact source of the C-T Ir anomaly is again confirmed.

Summary

Over 43 C-T Ir anomalies (Fig. 3) have now been detected throughout the world, 30 of these by the present researchers and their collaborators. The worldwide distribution of the C-T Ir anomaly has thus been amply confirmed, as has its extraterrestrial-impact origin. The correlation of Ir anomalies (and hence impacts) with the C-T extinctions has also been confirmed.

The repetitive nature of the Ir anomaly has also been confirmed in at least one other geological layer (from the Eocene-Oligocene Ir anomaly). Not all major mass extinctions, however, are necessarily due to impacts: no Ir was associated with the biggest of all (the Permian-Triassic).

Figure 2. Deviations of siderophile abundances in Stevns Klint section from C1 chondrite expectations (normalized by iridium).   (XBL 827-943)

PLANNED ACTIVITIES FOR FY 1983

The iridium and other geochemical anomalies will be searched for in Eocene-Oligocene boundary sediments from the Apennines in Italy. The intention is to
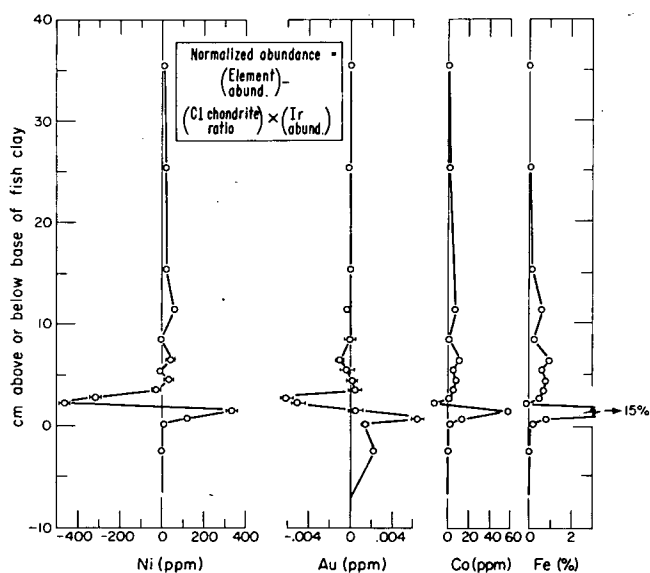
establish a precise time marker for relating marine taxa extinctions in that region to those already studied in seven equatorial sites. Extensive studies will also be made of geochemical anomalies associated with the Cretaceous-Tertiary boundary (65 million years ago) in Montana, Wyoming, and Canada in order to precisely relate the times of extinction of different land taxa.

REFERENCES

1. Alvarez, W., Asaro, F., Michel, H.V., and Alvarez, L.W. (1982), "Iridium Anomaly Approximately Synchronous with Terminal Eocene Extinctions," *Science 216*, p. 286.

2. Asaro, F., Alvarez, L.W., Alvarez, W., and Michel, H.V. (1982), "Geochemical Anomalies Near the Eocene/Oligocene and Permian/Triassic Boundaries," Geological Society of America Special Paper 190, p. 517.

3. Montanari, A., et al. (1983), "Spheroids at the Cretaceous-Tertiary Boundary: Probable Origin as Authigenically Altered Microtektites," submitted to *Geology*.

4. Montanari, A., et al. (1982), "Micropaleontological, Mineralogic and Chemical Analysis of C-T Boundary Clay in the Northern Apennines," *GSA Abstracts with Program 14*(7), p. 569.
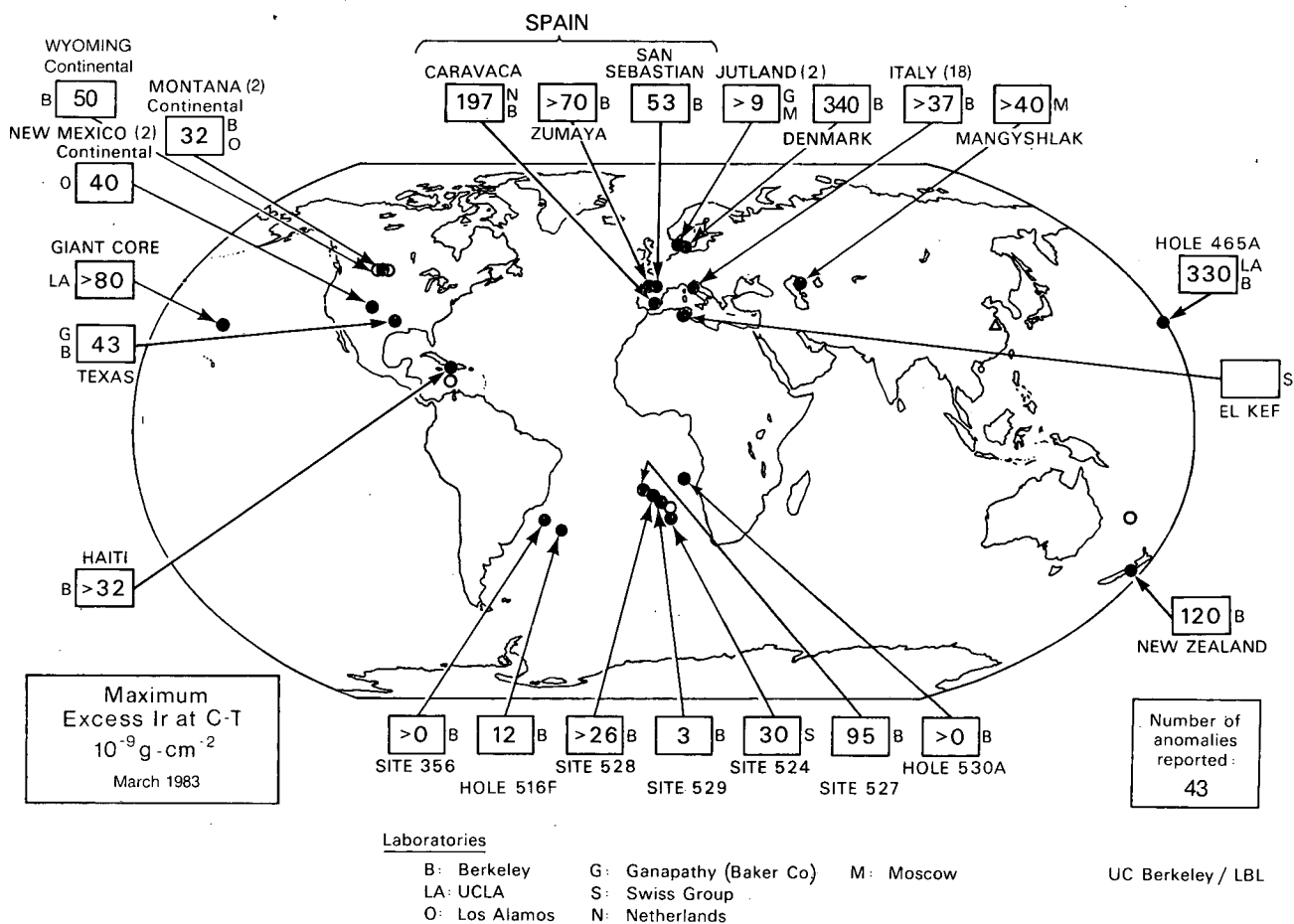
Figure 3. Sites of Cretaceous-Tertiary iridium anomalies known as of March 1983 (43 in all). Boxes indicate maximum excess Ir abundances in nanograms/cm^2. Laboratories performing the analyses are also indicated. (XBL 833-94)